

# Global Carbon Budget 2022

Pierre Friedlingstein<sup>1,2</sup>, Michael O'Sullivan<sup>1</sup>, Matthew W. Jones<sup>3</sup>, Robbie M. Andrew<sup>4</sup>, Luke Gregor<sup>5</sup>, Judith Hauck<sup>6</sup>, Corinne Le Quéré<sup>3</sup>, Ingrid T. Luijkx<sup>7</sup>, Are Olsen<sup>8,9</sup>, Glen P. Peters<sup>4</sup>, Wouter Peters<sup>7,10</sup>, Julia Pongratz<sup>11,12</sup>, Clemens Schwingshackl<sup>11</sup>, Stephen Sitch<sup>1</sup>, Josep G. Canadell<sup>13</sup>, Philippe Ciais<sup>14</sup>, Robert B. Jackson<sup>15</sup>, Simone Alin<sup>16</sup>, Ramdane Alkama<sup>17</sup>, Almut Arneth<sup>18</sup>, Vivek K. Arora<sup>19</sup>, Nicholas R. Bates<sup>20,21</sup>, Meike Becker<sup>8,9</sup>, Nicolas Bellouin<sup>22</sup>, Henry C. Bittig<sup>23</sup>, Laurent Bopp<sup>2</sup>, Frédéric Chevallier<sup>14</sup>, Louise P. Chini<sup>24</sup>, Margot Cronin<sup>25</sup>, Wiley Evans<sup>26</sup>, Stefanie Falk<sup>11</sup>, Richard A. Feely<sup>16</sup>, Thomas Gasser<sup>27</sup>, Marion Gehlen<sup>14</sup>, Thanos Gkritzalis<sup>28</sup>, Lucas Gloor<sup>29,30</sup>, Giacomo Grassi<sup>17</sup>, Nicolas Gruber<sup>5</sup>, Özgür Gürses<sup>6</sup>, Ian Harris<sup>31</sup>, Matthew Hefner<sup>32,33</sup>, Richard A. Houghton<sup>34</sup>, George C. Hurtt<sup>24</sup>, Yosuke Iida<sup>35</sup>, Tatiana Ilyina<sup>12</sup>, Atul K. Jain<sup>36</sup>, Annika Jersild<sup>12</sup>, Koji Kadono<sup>35</sup>, Etsushi Kato<sup>37</sup>, Daniel Kennedy<sup>38</sup>, Kees Klein Goldewijk<sup>39</sup>, Jürgen Knauer<sup>40,41</sup>, Jan Ivar Korsbakken<sup>4</sup>, Peter Landschützer<sup>12,28</sup>, Nathalie Lefèvre<sup>42</sup>, Keith Lindsay<sup>43</sup>, Junjie Liu<sup>44</sup>, Zhu Liu<sup>45</sup>, Gregg Marland<sup>32,33</sup>, Nicolas Mayot<sup>3</sup>, Matthew J. McGrath<sup>14</sup>, Nicolas Metzler<sup>42</sup>, Natalie M. Monacci<sup>46</sup>, David R. Munro<sup>47,48</sup>, Shin-Ichiro Nakaoka<sup>49</sup>, Yosuke Niwa<sup>49,50</sup>, Kevin O'Brien<sup>51,16</sup>, Tsuneo Ono<sup>52</sup>, Paul I. Palmer<sup>53,54</sup>, Naiqing Pan<sup>55,56</sup>, Denis Pierrot<sup>57</sup>, Katie Pocock<sup>26</sup>, Benjamin Poulter<sup>58</sup>, Laure Resplandy<sup>59</sup>, Eddy Robertson<sup>60</sup>, Christian Rödenbeck<sup>61</sup>, Carmen Rodriguez<sup>62</sup>, Thais M. Rosan<sup>1</sup>, Jörg Schwinger<sup>63,9</sup>, Roland Séférian<sup>64</sup>, Jamie D. Shutler<sup>1</sup>, Ingunn Skjelvan<sup>63,9</sup>, Tobias Steinhoff<sup>65</sup>, Qing Sun<sup>66</sup>, Adrienne J. Sutton<sup>16</sup>, Colm Sweeney<sup>48</sup>, Shintaro Takao<sup>49</sup>, Toste Tanhua<sup>65</sup>, Pieter P. Tans<sup>67,68</sup>, Xiangjun Tian<sup>69</sup>, Hanqin Tian<sup>56</sup>, Bronte Tilbrook<sup>70,71</sup>, Hiroyuki Tsujino<sup>50</sup>, Francesco Tubiello<sup>72</sup>, Guido R. van der Werf<sup>73</sup>, Anthony P. Walker<sup>74</sup>, Rik Wanninkhof<sup>57</sup>, Chris Whitehead<sup>75</sup>, Anna Willstrand Wranne<sup>76</sup>, Rebecca Wright<sup>3</sup>, Wenping Yuan<sup>77</sup>, Chao Yue<sup>78</sup>, Xu Yue<sup>79</sup>, Sönke Zaehle<sup>61</sup>, Jiye Zeng<sup>49</sup>, Bo Zheng<sup>80</sup>

<sup>1</sup> Faculty of Environment, Science and Economy, University of Exeter, Exeter EX4 4QF, UK

<sup>2</sup> Laboratoire de Météorologie Dynamique / Institut Pierre-Simon Laplace, CNRS, Ecole Normale Supérieure / Université PSL, Sorbonne Université, Ecole Polytechnique, Paris, France

<sup>3</sup> Tyndall Centre for Climate Change Research, School of Environmental Sciences, University of East Anglia, Norwich Research Park, Norwich NR4 7TJ, UK

<sup>4</sup> CICERO Center for International Climate Research, Oslo 0349, Norway

<sup>5</sup> Environmental Physics Group, ETH Zürich, Institute of Biogeochemistry and Pollutant Dynamics and Center for Climate Systems Modeling (C2SM), Zurich, Switzerland

<sup>6</sup> Alfred-Wegener-Institut Helmholtz-Zentrum für Polar- und Meeresforschung, Postfach 120161, 27515 Bremerhaven, Germany

<sup>7</sup> Wageningen University, Environmental Sciences Group, P.O. Box 47, 6700AA, Wageningen, The Netherlands

<sup>8</sup> Geophysical Institute, University of Bergen, Bergen, Norway

<sup>9</sup> Bjerknes Centre for Climate Research, Bergen, Norway

<sup>10</sup> University of Groningen, Centre for Isotope Research, Groningen, The Netherlands

<sup>11</sup> Ludwig-Maximilians-Universität Munich, Luisenstr. 37, 80333 München, Germany

<sup>12</sup> Max Planck Institute for Meteorology, Hamburg, Germany

<sup>13</sup> CSIRO Oceans and Atmosphere, Canberra, ACT 2101, Australia

<sup>14</sup> Laboratoire des Sciences du Climat et de l'Environnement, LSCE/IPSL, CEA-CNRS-UVSQ, Université Paris-Saclay, F-91191 Gif-sur-Yvette, France

<sup>15</sup> Department of Earth System Science, Woods Institute for the Environment, and Precourt Institute for Energy, Stanford University, Stanford, CA 94305–2210, United States of America

<sup>16</sup> National Oceanic & Atmospheric Administration, Pacific Marine Environmental Laboratory (NOAA/PMEL), 7600 Sand Point Way NE, Seattle, WA 98115, USA

<sup>17</sup> Joint Research Centre, European Commission, Ispra, Italy

<sup>18</sup> Karlsruhe Institute of Technology, Institute of Meteorology and Climate Research/Atmospheric Environmental Research, 82467 Garmisch-Partenkirchen, Germany

54 <sup>19</sup> Canadian Centre for Climate Modelling and Analysis, Climate Research Division, Environment  
 55 and Climate Change Canada, Victoria, BC, Canada  
 56 <sup>20</sup> Bermuda Institute of Ocean Sciences (BIOS), 17 Biological Lane, St. Georges, GE01, Bermuda  
 57 <sup>21</sup> Department of Ocean and Earth Science, University of Southampton, European Way,  
 58 Southampton, SO14 3ZH, UK  
 59 <sup>22</sup> Department of Meteorology, University of Reading, Reading, UK  
 60 <sup>23</sup> Leibniz Institute for Baltic Sea Research Warnemuende (IOW), Seestrassse 15; 18119 Rostock,  
 61 Germany  
 62 <sup>24</sup> Department of Geographical Sciences, University of Maryland, College Park, Maryland 20742,  
 63 USA  
 64 <sup>25</sup> Marine Institute, Galway, Ireland  
 65 <sup>26</sup> Hakai Institute, Heriot Bay, BC, Canada  
 66 <sup>27</sup> International Institute for Applied Systems Analysis (IIASA), Schlossplatz 1  
 67 A-2361 Laxenburg, Austria  
 68 <sup>28</sup> Flanders Marine Institute (VLIZ), InnovOceanSite, Wandelaarkaai 7, 8400 Ostend, Belgium  
 69 <sup>29</sup> Lamont-Doherty Earth Observatory and Department of Earth and Environmental Sciences,  
 70 Columbia University, New York, NY, USA  
 71 <sup>30</sup> Open Earth Foundation, Marina del Rey, CA, USA  
 72 <sup>31</sup> NCAS-Climate, Climatic Research Unit, School of Environmental Sciences, University of East  
 73 Anglia, Norwich Research Park, Norwich, NR4 7TJ, UK  
 74 <sup>32</sup> Research Institute for Environment, Energy, and Economics, Appalachian State University,  
 75 Boone, North Carolina, USA  
 76 <sup>33</sup> Department of Geological and Environmental Sciences, Appalachian State University, Boone,  
 77 North Carolina, USA  
 78 <sup>34</sup> Woodwell Climate Research Center, Falmouth, MA 02540, USA  
 79 <sup>35</sup> Atmosphere and Ocean Department, Japan Meteorological Agency, Minato-Ku, Tokyo 105-  
 80 8431, Japan  
 81 <sup>36</sup> Department of Atmospheric Sciences, University of Illinois, Urbana, IL 61821, USA  
 82 <sup>37</sup> Institute of Applied Energy (IAE), Minato-ku, Tokyo 105-0003, Japan  
 83 <sup>38</sup> National Center for Atmospheric Research, Climate and Global Dynamics, Terrestrial Sciences  
 84 Section, Boulder, CO 80305, USA  
 85 <sup>39</sup> Utrecht University, Faculty of Geosciences, Department IMEW, Copernicus Institute of  
 86 Sustainable Development, Heidelberglaan 2, P.O. Box 80115, 3508 TC, Utrecht, the Netherlands  
 87 <sup>40</sup> Hawkesbury Institute for the Environment, Western Sydney University, Penrith, New South  
 88 Wales, Australia  
 89 <sup>41</sup> Climate Science Centre, CSIRO Oceans and Atmosphere, Canberra, ACT, Australia  
 90 <sup>42</sup> LOCEAN/IPSL laboratory, Sorbonne Université, CNRS/IRD/MNHN, Paris, France  
 91 <sup>43</sup> National Center for Atmospheric Research, Climate and Global Dynamics, Oceanography  
 92 Section, Boulder, CO 80305, USA  
 93 <sup>44</sup> Jet Propulsion Laboratory, California Institute of Technology, Pasadena, CA, USA  
 94 <sup>45</sup> Department of Earth System Science, Tsinghua University, Beijing, China  
 95 <sup>46</sup> University of Alaska Fairbanks, College of Fisheries and Ocean Sciences, PO Box 757220,  
 96 Fairbanks, AK, USA  
 97 <sup>47</sup> Cooperative Institute for Research in Environmental Sciences, University of Colorado, Boulder,  
 98 CO, 80305, USA  
 99 <sup>48</sup> National Oceanic & Atmospheric Administration/Global Monitoring Laboratory (NOAA/GML),  
 100 Boulder, CO, 80305, USA  
 101 <sup>49</sup> Earth System Division, National Institute for Environmental Studies (NIES), 16-2 Onogawa,  
 102 Tsukuba Ibaraki, 305-8506, Japan  
 103 <sup>50</sup> Meteorological Research Institute, 1-1 Nagamine, Tsukuba, Ibaraki, 305-0052 Japan  
 104 <sup>51</sup> Cooperative Institute for Climate, Ocean and Ecosystem Studies (CICOES), University of  
 105 Washington, Seattle, WA, USA  
 106 <sup>52</sup> Japan Fisheries Research and Education Agency, 2-12-4 Fukuura, Kanazawa-Ku, Yokohama 236-  
 107 8648, Japan  
 108 <sup>53</sup> National Centre for Earth Observation, University of Edinburgh, UK  
 109 <sup>54</sup> School of GeoSciences, University of Edinburgh, UK  
 110 <sup>55</sup> College of Forestry, Wildlife and Environment, Auburn University, Auburn, AL 36849, USA  
 111 <sup>56</sup> Schiller Institute for Integrated Science and Society, Department of Earth and Environmental  
 112 Sciences, Boston College, Chestnut Hill, MA 02467, USA  
 113

<sup>57</sup> National Oceanic & Atmospheric Administration/Atlantic Oceanographic & Meteorological Laboratory (NOAA/AOML), Miami, FL 33149, USA

<sup>58</sup> NASA Goddard Space Flight Center, Biospheric Sciences Laboratory, Greenbelt, Maryland 20771, USA

<sup>59</sup> Princeton University, Department of Geosciences and Princeton Environmental Institute, Princeton, NJ, USA

<sup>60</sup> Met Office Hadley Centre, FitzRoy Road, Exeter EX1 3PB, UK

<sup>61</sup> Max Planck Institute for Biogeochemistry, P.O. Box 600164, Hans-Knöll-Str. 10, 07745 Jena, Germany

<sup>62</sup> University of Miami, RSMAS, 4600 Rickenbacker Causeway, Miami, FL 33149, USA

<sup>63</sup> NORCE Norwegian Research Centre, Jahnebakken 5, 5007 Bergen, Norway

<sup>64</sup> CNRM, Université de Toulouse, Météo-France, CNRS, Toulouse, France

<sup>65</sup> GEOMAR Helmholtz Centre for Ocean Research Kiel, Düsterbrookweg 20, 24105 Kiel, Germany

<sup>66</sup> Climate and Environmental Physics, Physics Institute and Oeschger Centre for Climate Change Research, University of Bern, Bern, Switzerland

<sup>67</sup> National Oceanic & Atmospheric Administration, Global Monitoring Laboratory (NOAA GML), Boulder, CO 80305, USA

<sup>68</sup> Institute of Arctic and Alpine Research, University of Colorado, Boulder, CO 80309, USA

<sup>69</sup> Institute of Tibetan Plateau Research, Chinese Academy of Sciences, Beijing 100101, China

<sup>70</sup> CSIRO Oceans and Atmosphere, PO Box 1538, Hobart, Tasmania 7001, Australia

<sup>71</sup> Australian Antarctic Partnership Program, University of Tasmania, Hobart, Australia

<sup>72</sup> Statistics Division, Food and Agriculture Organization of the United Nations, Via Terme di Caracalla, Rome 00153, Italy

<sup>73</sup> Department of Earth sciences, Faculty of Science, Vrije Universiteit, Amsterdam, the Netherlands

<sup>74</sup> Environmental Sciences Division and Climate Change Science Institute, Oak Ridge National Laboratory, Oak Ridge, TN, 37831, USA

<sup>75</sup> Sitka Tribe of Alaska, 456 Katlian Street, Sitka, Alaska 99835, USA

<sup>76</sup> Swedish Meteorological and Hydrological Institute, Sven Källfeltsgata 15, 426 68 Västra Frölunda, Sweden

<sup>77</sup> School of Atmospheric Sciences, Sun Yat-sen University, Zhuhai, Guangdong 510245, China.

<sup>78</sup> Institute of Soil and Water Conservation, Northwest A&F University, Yangling, Shaanxi 712100, P.R. China

<sup>79</sup> School of Environmental Science and Engineering, Nanjing University of Information Science and Technology (NUIST), China

<sup>80</sup> Institute of Environment and Ecology, Tsinghua Shenzhen International Graduate School, Tsinghua University, Shenzhen 518055, China

*Correspondence to:* Pierre Friedlingstein (p.friedlingstein@exeter.ac.uk)

## Abstract

Accurate assessment of anthropogenic carbon dioxide (CO<sub>2</sub>) emissions and their redistribution among the atmosphere, ocean, and terrestrial biosphere in a changing climate is critical to better understand the global carbon cycle, support the development of climate policies, and project future climate change. Here we describe and synthesise data sets and methodology to quantify the five major components of the global carbon budget and their uncertainties. Fossil CO<sub>2</sub> emissions (E<sub>FOS</sub>) are based on energy statistics and cement production data, while emissions from land-use change (E<sub>LUC</sub>), mainly deforestation, are based on land-use and land-use change data and bookkeeping models. Atmospheric CO<sub>2</sub> concentration is measured directly, and its growth rate (G<sub>ATM</sub>) is computed from the annual changes in concentration. The ocean CO<sub>2</sub> sink (S<sub>OCEAN</sub>) is estimated with global ocean biogeochemistry models and observation-based data-products. The terrestrial CO<sub>2</sub> sink (S<sub>LAND</sub>) is estimated with dynamic global vegetation models. The resulting carbon budget imbalance (B<sub>IM</sub>), the difference between the estimated total emissions and the estimated changes in the atmosphere, ocean, and terrestrial

biosphere, is a measure of imperfect data and understanding of the contemporary carbon cycle. All  
 uncertainties are reported as  $\pm 1\sigma$ .  
 For the year 2021,  $E_{FOS}$  increased by 5.1% relative to 2020, with fossil emissions at  $10.1 \pm 0.5 \text{ GtC yr}^{-1}$  ( $9.9 \pm 0.5 \text{ GtC yr}^{-1}$  when the cement carbonation sink is included),  $E_{LUC}$  was  $1.1 \pm 0.7 \text{ GtC yr}^{-1}$ , for a total  
 anthropogenic  $\text{CO}_2$  emission (including the cement carbonation sink) of  $10.9 \pm 0.8 \text{ GtC yr}^{-1}$  ( $40.0 \pm 2.9 \text{ GtCO}_2$ ). Also, for 2021,  $G_{ATM}$  was  $5.2 \pm 0.2 \text{ GtC yr}^{-1}$  ( $2.5 \pm 0.1 \text{ ppm yr}^{-1}$ ),  $S_{OCEAN}$  was  $2.9 \pm 0.4 \text{ GtC yr}^{-1}$  and  
 $S_{LAND}$  was  $3.5 \pm 0.9 \text{ GtC yr}^{-1}$ , with a  $B_{IM}$  of  $-0.6 \text{ GtC yr}^{-1}$  (i.e. total estimated sources too low or sinks too high).  
 The global atmospheric  $\text{CO}_2$  concentration averaged over 2021 reached  $414.71 \pm 0.1 \text{ ppm}$ . Preliminary data for  
 2022, suggest an increase in  $E_{FOS}$  relative to 2021 of +1.1% (0% to 1.7%) globally, and atmospheric  $\text{CO}_2$   
 concentration reaching 417.3 ppm, more than 50% above pre-industrial level (around 278 ppm). Overall, the  
 mean and trend in the components of the global carbon budget are consistently estimated over the period 1959-  
 2021, but discrepancies of up to  $1 \text{ GtC yr}^{-1}$  persist for the representation of annual to semi-decadal variability in  
 $\text{CO}_2$  fluxes. Comparison of estimates from multiple approaches and observations shows: (1) a persistent large  
 uncertainty in the estimate of land-use changes emissions, (2) a low agreement between the different methods  
 on the magnitude of the land  $\text{CO}_2$  flux in the northern extra-tropics, and (3) a discrepancy between the different  
 methods on the strength of the ocean sink over the last decade. This living data update documents changes in  
 the methods and data sets used in this new global carbon budget and the progress in understanding of the  
 global carbon cycle compared with previous publications of this data set. The data presented in this work are  
 available at <https://doi.org/10.18160/GCP-2022> (Friedlingstein et al., 2022b).



## Executive Summary

**Global fossil CO<sub>2</sub> emissions (including cement carbonation) further increased in 2022, being now slightly above their pre-COVID-19 pandemic 2019 level.** The 2021 emission increase was 0.46 GtC yr<sup>-1</sup> (1.7 GtCO<sub>2</sub> yr<sup>-1</sup>), bringing 2021 emissions to  $9.9 \pm 0.5$  GtC yr<sup>-1</sup> ( $36.1 \pm 1.8$  GtCO<sub>2</sub> yr<sup>-1</sup>), slightly below the emissions level of 2019 ( $9.9 \pm 0.5$  GtC yr<sup>-1</sup>,  $36.2 \pm 1.8$  GtCO<sub>2</sub> yr<sup>-1</sup>). Preliminary estimates based on data available suggest fossil CO<sub>2</sub> emissions continued to increase in 2022, by 1.1% relative to 2021 (0% to 1.7%), bringing emissions at 10.0 GtC yr<sup>-1</sup> ( $36.5$  GtCO<sub>2</sub> yr<sup>-1</sup>), slightly above the 2019 level.

Emissions from coal, oil, and gas in 2022 are expected to be above their 2021 levels (by 0.8%, 2.2% and 1.1% respectively). Regionally, emissions in 2022 are expected to have been decreasing by 1.5% in China (3.0 GtC, 11.1 GtCO<sub>2</sub>), and 1% in the European Union (0.8 GtC, 2.8 GtCO<sub>2</sub>), but increasing by 1.6% in the United States (1.4 GtC, 5.1 GtCO<sub>2</sub>), 5.6% in India (0.8 GtC, 2.9 GtCO<sub>2</sub>) and 2.5% for the rest of the world (4.2 GtC, 15.5 GtCO<sub>2</sub>).

**Fossil CO<sub>2</sub> emissions decreased in 24 countries during the decade 2012-2021.** Altogether, these 24 countries contribute to about 2.4 GtC yr<sup>-1</sup> (8.8 GtCO<sub>2</sub>) fossil fuel CO<sub>2</sub> emissions over the last decade, about one quarter of world CO<sub>2</sub> fossil emissions.

**Global CO<sub>2</sub> emissions from land-use, land-use change, and forestry (LUC) averaged at  $1.2 \pm 0.7$  GtC yr<sup>-1</sup> ( $4.5 \pm 2.6$  GtCO<sub>2</sub> yr<sup>-1</sup>) for the 2012-2021 period with a preliminary projection for 2022 of  $1.0 \pm 0.7$  GtC yr<sup>-1</sup> ( $3.6 \pm 2.6$  GtCO<sub>2</sub> yr<sup>-1</sup>). A small decrease over the past two decades is not robust given the large model uncertainty.** Emissions from deforestation, the main driver of global gross sources, remain high at  $1.8 \pm 0.4$  GtC yr<sup>-1</sup> over the 2012-2021 period, highlighting the strong potential of halting deforestation for emissions reductions. Sequestration of  $0.9 \pm 0.3$  GtC yr<sup>-1</sup> through re-/afforestation and forestry offsets one half of the deforestation emissions. Emissions from other land-use transitions and from peat drainage and peat fire add further, small contributions. The highest emitters during 2012-2021 in descending order were Brazil, Indonesia, and the Democratic Republic of the Congo, with these 3 countries contributing more than half of the global total land-use emissions.

**The remaining carbon budget for a 50% likelihood to limit global warming to 1.5°C, 1.7°C and 2°C has respectively reduced to 105 GtC (380 GtCO<sub>2</sub>), 200 GtC (730 GtCO<sub>2</sub>) and 335 GtC (1230 GtCO<sub>2</sub>) from the beginning of 2023, equivalent to 9, 18 and 30 years, assuming 2022 emissions levels.** Total anthropogenic emissions were 10.9 GtC yr<sup>-1</sup> (40.0 GtCO<sub>2</sub> yr<sup>-1</sup>) in 2021, with a preliminary estimate of 10.9 GtC yr<sup>-1</sup> (40.1 GtCO<sub>2</sub> yr<sup>-1</sup>) for 2022. The remaining carbon budget to keep global temperatures below these climate targets has shrunk by 32 GtC (121 GtCO<sub>2</sub>) since the IPCC AR6 Working Group 1 assessment, based on data up to 2019. Reaching zero CO<sub>2</sub> emissions by 2050 entails a total anthropogenic CO<sub>2</sub> emissions linear decrease by about 0.4 GtC (1.4 GtCO<sub>2</sub>) each year, comparable to the decrease during 2020, highlighting the scale of the action needed.

**The concentration of CO<sub>2</sub> in the atmosphere is set to reach 417.3 ppm in 2022, 51% above pre-industrial levels.** The atmospheric CO<sub>2</sub> growth was  $5.2 \pm 0.02$  GtC yr<sup>-1</sup> during the decade 2012-2021 (48% of total CO<sub>2</sub> emissions) with a preliminary 2022 growth rate estimate of around 5.5 GtC yr<sup>-1</sup> (2.6 ppm).

**The ocean CO<sub>2</sub> sink resumed a more rapid growth in the past two decades after low or no growth during the 1991-2002 period.** However, the growth of the ocean CO<sub>2</sub> sink in the past decade has an uncertainty of a factor of three, with estimates based on data products and estimates based on models showing an ocean sink trend of +0.7 GtC yr<sup>-1</sup> decade<sup>-1</sup> and +0.2 GtC yr<sup>-1</sup> decade<sup>-1</sup> since 2010, respectively. The discrepancy in the trend originates from all latitudes but is largest in the Southern Ocean. The ocean CO<sub>2</sub> sink was  $2.9 \pm 0.4$  GtC yr<sup>-1</sup> during the decade 2012-2021 (26% of total CO<sub>2</sub> emissions), with a similar preliminary estimate of 2.9 GtC yr<sup>-1</sup> for 2022.

**The land CO<sub>2</sub> sink continued to increase during the 2012-2021 period primarily in response to increased atmospheric CO<sub>2</sub>, albeit with large interannual variability.** The land CO<sub>2</sub> sink was  $3.1 \pm 0.6$  GtC yr<sup>-1</sup> during the 2012-2021 decade (29% of total CO<sub>2</sub> emissions), 0.4 GtC yr<sup>-1</sup> larger than during the previous decade (2000-2009), with a preliminary 2022 estimate of around 3.4 GtC yr<sup>-1</sup>. Year to year variability in the land sink is about 1 GtC yr<sup>-1</sup> and dominates the year-to-year changes in the global atmospheric CO<sub>2</sub> concentration, implying that small annual changes in anthropogenic emissions (such as the fossil fuel emission decrease in 2020) are hard to detect in the atmospheric CO<sub>2</sub> observations.

## 1 Introduction

The concentration of carbon dioxide (CO<sub>2</sub>) in the atmosphere has increased from approximately 278 parts per million (ppm) in 1750 (Gulev et al., 2021), the beginning of the Industrial Era, to  $414.7 \pm 0.1$  ppm in 2021 (Dlugokencky and Tans, 2022); Figure 1). The atmospheric CO<sub>2</sub> increase above pre-industrial levels was, initially, primarily caused by the release of carbon to the atmosphere from deforestation and other land-use change activities (Canadell et al., 2021). While emissions from fossil fuels started before the Industrial Era, they became the dominant source of anthropogenic emissions to the atmosphere from around 1950 and their relative share has continued to increase until present. Anthropogenic emissions occur on top of an active natural carbon cycle that circulates carbon between the reservoirs of the atmosphere, ocean, and terrestrial biosphere on time scales from sub-daily to millennia, while exchanges with geologic reservoirs occur at longer timescales (Archer et al., 2009).

The global carbon budget (GCB) presented here refers to the mean, variations, and trends in the perturbation of CO<sub>2</sub> in the environment, referenced to the beginning of the Industrial Era (defined here as 1750). This paper describes the components of the global carbon cycle over the historical period with a stronger focus on the recent period (since 1958, onset of atmospheric CO<sub>2</sub> measurements), the last decade (2012-2021), the last year (2021) and the current year (2022). Finally, it provides cumulative emissions from fossil fuels and land-use change since the year 1750 (the pre-industrial period), and since the year 1850 (the reference year for historical simulations in IPCC AR6) (Eyring et al., 2016).

We quantify the input of CO<sub>2</sub> to the atmosphere by emissions from human activities, the growth rate of atmospheric CO<sub>2</sub> concentration, and the resulting changes in the storage of carbon in the land and ocean reservoirs in response to increasing atmospheric CO<sub>2</sub> levels, climate change and variability, and other anthropogenic and natural changes (Figure 2). An understanding of this perturbation budget over time and the underlying variability and trends of the natural carbon cycle is necessary to understand the response of natural sinks to changes in climate, CO<sub>2</sub> and land-use change drivers, and to quantify emissions compatible with a given climate stabilisation target.

The components of the CO<sub>2</sub> budget that are reported annually in this paper include separate and independent estimates for the CO<sub>2</sub> emissions from (1) fossil fuel combustion and oxidation from all energy and industrial processes; also including cement production and carbonation ( $E_{FOS}$ ; GtC yr<sup>-1</sup>) and (2) the emissions resulting from deliberate human activities on land, including those leading to land-use change ( $E_{LUC}$ ; GtC yr<sup>-1</sup>); and their partitioning among (3) the growth rate of atmospheric CO<sub>2</sub> concentration ( $G_{ATM}$ ; GtC yr<sup>-1</sup>), and the uptake of CO<sub>2</sub> (the ‘CO<sub>2</sub> sinks’) in (4) the ocean ( $S_{OCEAN}$ ; GtC yr<sup>-1</sup>) and (5) on land ( $S_{LAND}$ ; GtC yr<sup>-1</sup>). The CO<sub>2</sub> sinks as defined here conceptually include the response of the land (including inland waters and estuaries) and ocean (including coastal and marginal seas) to elevated CO<sub>2</sub> and changes in climate and other environmental conditions, although in practice not all processes are fully accounted for (see Section 2.7). Global emissions and their partitioning among the atmosphere, ocean and land are in balance in the real world. Due to the combination of imperfect spatial and/or temporal data coverage, errors in each estimate, and smaller terms not included in our budget estimate (discussed in Section 2.7), the independent estimates (1) to (5) above do not necessarily add up

to zero. We therefore (a) additionally assess a set of global atmospheric inversion system results that by design close the global carbon balance (see Section 2.6), and (b) estimate a budget imbalance ( $B_{IM}$ ), which is a measure of the mismatch between the estimated emissions and the estimated changes in the atmosphere, land and ocean, as follows:

$$B_{IM} = E_{FOS} + E_{LUC} - (G_{ATM} + S_{OCEAN} + S_{LAND}) \quad (1)$$

$G_{ATM}$  is usually reported in  $\text{ppm yr}^{-1}$ , which we convert to units of carbon mass per year,  $\text{GtC yr}^{-1}$ , using  $1 \text{ ppm} = 2.124 \text{ GtC}$  (Ballantyne et al., 2012; Table 1). All quantities are presented in units of gigatonnes of carbon ( $\text{GtC}$ ,  $10^{15} \text{ gC}$ ), which is the same as petagrams of carbon ( $\text{PgC}$ ; Table 1). Units of gigatonnes of  $\text{CO}_2$  (or billion tonnes of  $\text{CO}_2$ ) used in policy are equal to 3.664 multiplied by the value in units of  $\text{GtC}$ .

We also quantify  $E_{FOS}$  and  $E_{LUC}$  by country, including both territorial and consumption-based accounting for  $E_{FOS}$  (see Section 2), and discuss missing terms from sources other than the combustion of fossil fuels (see Section 2.7, Appendix D1 and D2).

The global  $\text{CO}_2$  budget has been assessed by the Intergovernmental Panel on Climate Change (IPCC) in all assessment reports (Prentice et al., 2001; Schimel et al., 1995; Watson et al., 1990; Denman et al., 2007; Ciais et al., 2013; Canadell et al., 2021), and by others (e.g. Ballantyne et al., 2012). The Global Carbon Project (GCP, [www.globalcarbonproject.org](http://www.globalcarbonproject.org), last access: 25 September 2022) has coordinated this cooperative community effort for the annual publication of global carbon budgets for the year 2005 (Raupach et al., 2007; including fossil emissions only), year 2006 (Canadell et al., 2007), year 2007 (GCP, 2008), year 2008 (Le Quéré et al., 2009), year 2009 (Friedlingstein et al., 2010), year 2010 (Peters et al., 2012b), year 2012 (Le Quéré et al., 2013; Peters et al., 2013), year 2013 (Le Quéré et al., 2014), year 2014 (Le Quéré et al., 2015a; Friedlingstein et al., 2014), year 2015 (Jackson et al., 2016; Le Quéré et al., 2015b), year 2016 (Le Quéré et al., 2016), year 2017 (Le Quéré et al., 2018a; Peters et al., 2017), year 2018 (Le Quéré et al., 2018b; Jackson et al., 2018), year 2019 (Friedlingstein et al., 2019; Jackson et al., 2019; Peters et al., 2020), year 2020 (Friedlingstein et al., 2020; Le Quéré et al., 2021) and more recently the year 2021 (Friedlingstein et al., 2022a; Jackson et al., 2022). Each of these papers updated previous estimates with the latest available information for the entire time series.

We adopt a range of  $\pm 1$  standard deviation ( $\sigma$ ) to report the uncertainties in our estimates, representing a likelihood of 68% that the true value will be within the provided range if the errors have a Gaussian distribution, and no bias is assumed. This choice reflects the difficulty of characterising the uncertainty in the  $\text{CO}_2$  fluxes between the atmosphere and the ocean and land reservoirs individually, particularly on an annual basis, as well as the difficulty of updating the  $\text{CO}_2$  emissions from land-use change. A likelihood of 68% provides an indication of our current capability to quantify each term and its uncertainty given the available information. The uncertainties reported here combine statistical analysis of the underlying data, assessments of uncertainties in the generation of the data sets, and expert judgement of the likelihood of results lying outside this range. The limitations of current information are discussed in the paper and have been examined in detail elsewhere (Ballantyne et al., 2015; Zscheischler et al., 2017). We also use a qualitative assessment of confidence level to characterise the annual estimates from each term based on the type, amount, quality, and consistency of the evidence as defined by the IPCC (Stocker et al., 2013).

This paper provides a detailed description of the data sets and methodology used to compute the global carbon budget estimates for the industrial period, from 1750 to 2022, and in more detail for the period since 1959. This paper is updated every year using the format of ‘living data’ to keep a record of budget versions and the changes in new data, revision of data, and changes in methodology that lead to changes in estimates of the carbon budget. Additional materials associated with the release of each new version will be posted at the Global Carbon Project (GCP) website (<http://www.globalcarbonproject.org/carbonbudget>, last access: 25 September 2022), with fossil fuel emissions also available through the Global Carbon Atlas (<http://www.globalcarbonatlas.org>, last access: 25 September 2022). All underlying data used to produce the budget can also be found at <https://globalcarbonbudget.org/> (last access: 25 September 2022). With this approach, we aim to provide the highest transparency and traceability in the reporting of CO<sub>2</sub>, the key driver of climate change.

## 2 Methods

Multiple organisations and research groups around the world generated the original measurements and data used to complete the global carbon budget. The effort presented here is thus mainly one of synthesis, where results from individual groups are collated, analysed, and evaluated for consistency. We facilitate access to original data with the understanding that primary data sets will be referenced in future work (see Table 2 for how to cite the data sets). Descriptions of the measurements, models, and methodologies follow below, and detailed descriptions of each component are provided elsewhere.

This is the 17th version of the global carbon budget and the 11th revised version in the format of a living data update in Earth System Science Data. It builds on the latest published global carbon budget of Friedlingstein et al. (2022a). The main changes are: the inclusion of (1) data to year 2021 and a projection for the global carbon budget for year 2022; (2) the inclusion of country level estimates of ELUC; (3) a process-based decomposition of ELUC into its main components (deforestation, re/afforestation and wood harvest, emissions from organic soils, and net flux from other transitions).

The main methodological differences between recent annual carbon budgets (2018-2022) are summarised in Table 3 and previous changes since 2006 are provided in Table A7.

### 2.1 Fossil CO<sub>2</sub> emissions (E<sub>FOS</sub>)

#### 2.1.1 Historical period 1850-2021

The estimates of global and national fossil CO<sub>2</sub> emissions (E<sub>FOS</sub>) include the oxidation of fossil fuels through both combustion (e.g., transport, heating) and chemical oxidation (e.g. carbon anode decomposition in aluminium refining) activities, and the decomposition of carbonates in industrial processes (e.g. the production of cement). We also include CO<sub>2</sub> uptake from the cement carbonation process. Several emissions sources are not estimated or not fully covered: coverage of emissions from lime production are not global, and decomposition of carbonates in glass and ceramic production are included only for the “Annex 1” countries of the United Nations Framework Convention on Climate Change (UNFCCC) for lack of activity data. These omissions are considered to be minor. Short-cycle carbon emissions - for example from combustion of biomass - are not included here but are accounted for in the CO<sub>2</sub> emissions from land use (see section 2.2).

Our estimates of fossil CO<sub>2</sub> emissions are derived using the standard approach of activity data and emission factors, relying on data collection by many other parties. Our goal is to produce the best estimate of this flux, and we therefore use a prioritisation framework to combine data from different sources that have used different methods, while being careful to avoid double counting and undercounting of emissions sources. The CDIAC-FF emissions dataset, derived largely from UN energy data, forms the foundation, and we extend emissions to year Y-1 using energy growth rates reported by BP energy company. We then proceed to replace estimates using data from what we consider to be superior sources, for example Annex 1 countries' official submissions to the UNFCCC. All data points are potentially subject to revision, not just the latest year. For full details see Andrew and Peters (2021).

Other estimates of global fossil CO<sub>2</sub> emissions exist, and these are compared by Andrew (2020a). The most common reason for differences in estimates of global fossil CO<sub>2</sub> emissions is a difference in which emissions sources are included in the datasets. Datasets such as those published by the energy company BP, the US Energy Information Administration, and the International Energy Agency's 'CO<sub>2</sub> emissions from fuel combustion' are all generally limited to emissions from combustion of fossil fuels. In contrast, datasets such as PRIMAP-hist, CEDS, EDGAR, and GCP's dataset aim to include all sources of fossil CO<sub>2</sub> emissions. See Andrew (2020a) for detailed comparisons and discussion.

Cement absorbs CO<sub>2</sub> from the atmosphere over its lifetime, a process known as 'cement carbonation'. We estimate this CO<sub>2</sub> sink, from 1931, onwards as the average of two studies in the literature (Cao et al., 2020; Guo et al., 2021). Both studies use the same model, developed by Xi et al. (2016), with different parameterisations and input data, with the estimate of Guo and colleagues being a revision of Xi et al (2016). The trends of the two studies are very similar. Since carbonation is a function of both current and previous cement production, we extend these estimates to 2022 by using the growth rate derived from the smoothed cement emissions (10-year smoothing) fitted to the carbonation data. In the present budget, we always include the cement carbonation carbon sink in the fossil CO<sub>2</sub> emission component (E<sub>FOS</sub>).

We use the Kaya Identity for a simple decomposition of CO<sub>2</sub> emissions into the key drivers (Raupach et al., 2007). While there are variations (Peters et al., 2017), we focus here on a decomposition of CO<sub>2</sub> emissions into population, GDP per person, energy use per GDP, and CO<sub>2</sub> emissions per energy. Multiplying these individual components together returns the CO<sub>2</sub> emissions. Using the decomposition, it is possible to attribute the change in CO<sub>2</sub> emissions to the change in each of the drivers. This method gives a first order understanding of what causes CO<sub>2</sub> emissions to change each year.

### **2.1.2 2022 projection**

We provide a projection of global CO<sub>2</sub> emissions in 2022 by combining separate projections for China, USA, EU, India, and for all other countries combined. The methods are different for each of these. For China we combine monthly fossil fuel production data from the National Bureau of Statistics, import/export data from the Customs Administration, and monthly coal consumption estimates from SX Coal (2022), giving us partial data for the growth rates to date of natural gas, petroleum, and cement, and of the consumption itself for raw coal. We then use a regression model to project full-year emissions based on historical observations. For the USA our projection is taken directly from the Energy Information Administration's (EIA) Short-Term Energy Outlook (EIA, 2022), combined with the year-to-date growth rate of cement clinker production. For the EU we use

monthly energy data from Eurostat to derive estimates of monthly CO<sub>2</sub> emissions through July, with coal emissions extended through August using a statistical relationship with reported electricity generation from coal and other factors. Given the very high uncertainty in European energy markets in 2022, we forego our usual history-based projection techniques and use instead the year-to-date growth rate as the full-year growth rate for both coal and natural gas. EU emissions from oil are derived using the EIA's projection of oil consumption for Europe. EU cement emissions are based on available year-to-date data from three of the largest producers, Germany, Poland, and Spain. India's projected emissions are derived from estimates through July (August for oil) using the methods of Andrew (2020b) and extrapolated assuming normal seasonal patterns. Emissions for the rest of the world are derived using projected growth in economic production from the IMF (2022) combined with extrapolated changes in emissions intensity of economic production. More details on the EFOS methodology and its 2022 projection can be found in Appendix C.1.

## **2.2 CO<sub>2</sub> emissions from land-use, land-use change and forestry (ELUC)**

### **2.2.1 Historical period 1850-2021**

The net CO<sub>2</sub> flux from land-use, land-use change and forestry (ELUC, called land-use change emissions in the rest of the text) includes CO<sub>2</sub> fluxes from deforestation, afforestation, logging and forest degradation (including harvest activity), shifting cultivation (cycle of cutting forest for agriculture, then abandoning), and regrowth of forests (following wood harvest or agriculture abandonment). Emissions from peat burning and drainage are added from external datasets, peat drainage being averaged from three spatially explicit independent datasets (see Appendix C.2.1).

Three bookkeeping approaches (updated estimates each of BLUE (Hansis et al., 2015), OSCAR (Gasser et al., 2020), and H&N2017 (Houghton and Nassikas, 2017)) were used to quantify gross sources and sinks and the resulting net ELUC. Uncertainty estimates were derived from the Dynamic Global vegetation Models (DGVMs) ensemble for the time period prior to 1960, using for the recent decades an uncertainty range of  $\pm 0.7$  GtC yr<sup>-1</sup>, which is a semi-quantitative measure for annual and decadal emissions and reflects our best value judgement that there is at least 68% chance ( $\pm 1\sigma$ ) that the true land-use change emission lies within the given range, for the range of processes considered here. This uncertainty range had been increased from 0.5 GtC yr<sup>-1</sup> after new bookkeeping models were included that indicated a larger spread than assumed before (Le Quéré et al., 2018). Projections for 2021 are based on fire activity from tropical deforestation and degradation as well as emissions from peat fires and drainage.

Our ELUC estimates follow the definition of global carbon cycle models of CO<sub>2</sub> fluxes related to land-use and land management and differ from IPCC definitions adopted in National GHG Inventories (NGHGI) for reporting under the UNFCCC, which additionally generally include, through adoption of the IPCC so-called managed land proxy approach, the terrestrial fluxes occurring on land defined by countries as managed. This partly includes fluxes due to environmental change (e.g. atmospheric CO<sub>2</sub> increase), which are part of S<sub>LAND</sub> in our definition. This causes the global emission estimates to be smaller for NGHGI than for the global carbon budget definition (Grassi et al., 2018). The same is the case for the Food Agriculture Organization (FAO) estimates of carbon fluxes on forest land, which include both anthropogenic and natural sources on managed land (Tubiello et al., 2021). We map the two definitions to each other, to provide a comparison of the anthropogenic carbon budget to the official country reporting to the climate convention.

## 2.2.2 2022 Projection

We project the 2022 land-use emissions for BLUE, the updated H&N2017 and OSCAR, starting from their estimates for 2021 assuming unaltered peat drainage, which has low interannual variability, but adjusting the highly variable emissions from peat fires, tropical deforestation and degradation as estimated using active fire data (MCD14ML; Giglio et al., 2016). More details on the  $E_{LUC}$  methodology can be found in Appendix C.2

## 2.3 Growth rate in atmospheric CO<sub>2</sub> concentration ( $G_{ATM}$ )

### 2.3.1 Historical period 1850-2021

The rate of growth of the atmospheric CO<sub>2</sub> concentration is provided for years 1959-2021 by the US National Oceanic and Atmospheric Administration Global Monitoring Laboratory (NOAA/GML; Dlugokencky and Tans, 2022), which is updated from Ballantyne et al. (2012) and includes recent revisions to the calibration scale of atmospheric CO<sub>2</sub> measurements (Hall et al., 2021). For the 1959-1979 period, the global growth rate is based on measurements of atmospheric CO<sub>2</sub> concentration averaged from the Mauna Loa and South Pole stations, as observed by the CO<sub>2</sub> Program at Scripps Institution of Oceanography (Keeling et al., 1976). For the 1980-2020 time period, the global growth rate is based on the average of multiple stations selected from the marine boundary layer sites with well-mixed background air (Ballantyne et al., 2012), after fitting a smooth curve through the data for each station as a function of time, and averaging by latitude band (Masarie and Tans, 1995). The annual growth rate is estimated by Dlugokencky and Tans (2022) from atmospheric CO<sub>2</sub> concentration by taking the average of the most recent December-January months corrected for the average seasonal cycle and subtracting this same average one year earlier. The growth rate in units of ppm yr<sup>-1</sup> is converted to units of GtC yr<sup>-1</sup> by multiplying by a factor of 2.124 GtC per ppm, assuming instantaneous mixing of CO<sub>2</sub> throughout the atmosphere (Ballantyne et al., 2012; Table 1).

Since 2020, NOAA/GML provides estimates of atmospheric CO<sub>2</sub> concentrations with respect to a new calibration scale, referred to as WMO-CO<sub>2</sub>-X2019, in line with the recommendation of the World Meteorological Organization (WMO) Global Atmosphere Watch (GAW) community (Hall et al., 2021). The "X" in the scale name indicates that it is a mole fraction scale, how many micro-moles of CO<sub>2</sub> in one mole of (dry) air. The word "concentration" only loosely reflects this. The WMO-CO<sub>2</sub>-X2019 scale improves upon the earlier WMO-CO<sub>2</sub>-X2007 scale by including a broader set of standards, which contain CO<sub>2</sub> in a wider range of concentrations that span the range 250-800 ppm (versus 250–520 ppm for WMO-CO<sub>2</sub>-X2007). In addition, NOAA/GML made two minor corrections to the analytical procedure used to quantify CO<sub>2</sub> concentrations, fixing an error in the second virial coefficient of CO<sub>2</sub> and accounting for loss of a small amount of CO<sub>2</sub> to materials in the manometer during the measurement process. The difference in concentrations measured using WMO-CO<sub>2</sub>-X2019 versus WMO-CO<sub>2</sub>-X2007 is ~+0.18 ppm at 400 ppm and the observational record of atmospheric CO<sub>2</sub> concentrations have been revised accordingly. The revisions have been applied retrospectively in all cases where the calibrations were performed by NOAA/GML, thus affecting measurements made by members of the WMO-GAW programme and other regionally coordinated programmes (e.g., Integrated Carbon Observing System, ICOS). Changes to the CO<sub>2</sub> concentrations measured across these networks propagate to the global mean CO<sub>2</sub> concentrations. The re-calibrated data were first used to estimate  $G_{ATM}$  in the 2021 edition of the global carbon budget (Friedlingstein et al., 2022a). Friedlingstein et al. (2022a) verified that the change of



scales from WMO-CO2-X2007 to WMO-CO2-X2019 made a negligible difference to the value of  $G_{ATM}$  ( $-0.06$   $GtC\ yr^{-1}$  during 2010-2019 and  $-0.01\ GtC\ yr^{-1}$  during 1959-2019, well within the uncertainty range reported below).

The uncertainty around the atmospheric growth rate is due to four main factors. First, the long-term reproducibility of reference gas standards (around  $0.03\ ppm$  for  $1\sigma$  from the 1980s; Dlugokencky and Tans, 2022). Second, small unexplained systematic analytical errors that may have a duration of several months to two years come and go. They have been simulated by randomising both the duration and the magnitude (determined from the existing evidence) in a Monte Carlo procedure. Third, the network composition of the marine boundary layer with some sites coming or going, gaps in the time series at each site, etc (Dlugokencky and Tans, 2022). The latter uncertainty was estimated by NOAA/GML with a Monte Carlo method by constructing 100 "alternative" networks (Masarie and Tans, 1995; NOAA/GML, 2019). The second and third uncertainties, summed in quadrature, add up to  $0.085\ ppm$  on average (Dlugokencky and Tans, 2022). Fourth, the uncertainty associated with using the average  $CO_2$  concentration from a surface network to approximate the true atmospheric average  $CO_2$  concentration (mass-weighted, in 3 dimensions) as needed to assess the total atmospheric  $CO_2$  burden. In reality,  $CO_2$  variations measured at the stations will not exactly track changes in total atmospheric burden, with offsets in magnitude and phasing due to vertical and horizontal mixing. This effect must be very small on decadal and longer time scales, when the atmosphere can be considered well mixed. The  $CO_2$  increase in the stratosphere lags the increase (meaning lower concentrations) that we observe in the marine boundary layer, while the continental boundary layer (where most of the emissions take place) leads the marine boundary layer with higher concentrations. These effects nearly cancel each other. In addition the growth rate is nearly the same everywhere (Ballantyne et al, 2012). We therefore maintain an uncertainty around the annual growth rate based on the multiple stations data set ranges between  $0.11$  and  $0.72\ GtC\ yr^{-1}$ , with a mean of  $0.61\ GtC\ yr^{-1}$  for 1959-1979 and  $0.17\ GtC\ yr^{-1}$  for 1980-2020, when a larger set of stations were available as provided by Dlugokencky and Tans (2022). We estimate the uncertainty of the decadal averaged growth rate after 1980 at  $0.02\ GtC\ yr^{-1}$  based on the calibration and the annual growth rate uncertainty but stretched over a 10-year interval. For years prior to 1980, we estimate the decadal averaged uncertainty to be  $0.07\ GtC\ yr^{-1}$  based on a factor proportional to the annual uncertainty prior and after 1980 ( $0.02 * [0.61/0.17]\ GtC\ yr^{-1}$ ).

We assign a high confidence to the annual estimates of  $G_{ATM}$  because they are based on direct measurements from multiple and consistent instruments and stations distributed around the world (Ballantyne et al., 2012; Hall et al., 2021).

To estimate the total carbon accumulated in the atmosphere since 1750 or 1850, we use an atmospheric  $CO_2$  concentration of  $278.3 \pm 3\ ppm$  or  $285.1 \pm 3\ ppm$ , respectively (Gulev et al., 2021). For the construction of the cumulative budget shown in Figure 3, we use the fitted estimates of  $CO_2$  concentration from Joos and Spahni (2008) to estimate the annual atmospheric growth rate using the conversion factors shown in Table 1. The uncertainty of  $\pm 3\ ppm$  (converted to  $\pm 1\sigma$ ) is taken directly from the IPCC's AR5 assessment (Ciais et al., 2013). Typical uncertainties in the growth rate in atmospheric  $CO_2$  concentration from ice core data are equivalent to  $\pm 0.1$ - $0.15\ GtC\ yr^{-1}$  as evaluated from the Law Dome data (Etheridge et al., 1996) for individual 20-year intervals over the period from 1850 to 1960 (Bruno and Joos, 1997).

### 2.3.2 2022 projection

We provide an assessment of  $G_{ATM}$  for 2022 based on the monthly calculated global atmospheric  $CO_2$  concentration (GLO) through August (Dlugokencky and Tans, 2022), and bias-adjusted Holt–Winters exponential smoothing with additive seasonality (Chatfield, 1978) to project to January 2023. Additional analysis suggests that the first half of the year (the boreal winter-spring-summer transition) shows more interannual variability than the second half of the year (the boreal summer-autumn-winter transition), so that the exact projection method applied to the second half of the year has a relatively smaller impact on the projection of the full year. Uncertainty is estimated from past variability using the standard deviation of the last 5 years' monthly growth rates.

## 2.4 Ocean $CO_2$ sink

### 2.4.1 Historical period 1850-2021

The reported estimate of the global ocean anthropogenic  $CO_2$  sink  $SO_{CEAN}$  is derived as the average of two estimates. The first estimate is derived as the mean over an ensemble of ten global ocean biogeochemistry models (GOBMs, Table 4 and Table A2). The second estimate is obtained as the mean over an ensemble of seven observation-based data-products (Table 4 and Table A3). An eighth product (Watson et al., 2020) is shown, but is not included in the ensemble average as it differs from the other products by adjusting the flux to a cool, salty ocean surface skin (see Appendix C.3.1 for a discussion of the Watson product). The GOBMs simulate both the natural and anthropogenic  $CO_2$  cycles in the ocean. They constrain the anthropogenic air-sea  $CO_2$  flux (the dominant component of  $SO_{CEAN}$ ) by the transport of carbon into the ocean interior, which is also the controlling factor of present-day ocean carbon uptake in the real world. They cover the full globe and all seasons and were recently evaluated against surface ocean carbon observations, suggesting they are suitable to estimate the annual ocean carbon sink (Hauck et al., 2020). The data-products are tightly linked to observations of  $fCO_2$  (fugacity of  $CO_2$ , which equals  $pCO_2$  corrected for the non-ideal behaviour of the gas; Pfeil et al., 2013), which carry imprints of temporal and spatial variability, but are also sensitive to uncertainties in gas-exchange parameterizations and data-sparsity. Their asset is the assessment of interannual and spatial variability (Hauck et al., 2020). We further use two diagnostic ocean models to estimate  $SO_{CEAN}$  over the industrial era (1781-1958).

The global  $fCO_2$ -based flux estimates were adjusted to remove the pre-industrial ocean source of  $CO_2$  to the atmosphere of  $0.65 \text{ GtC yr}^{-1}$  from river input to the ocean (Regnier et al., 2022), to satisfy our definition of  $SO_{CEAN}$  (Hauck et al., 2020). The river flux adjustment was distributed over the latitudinal bands using the regional distribution of Aumont et al. (2001; North:  $0.17 \text{ GtC yr}^{-1}$ , Tropics:  $0.16 \text{ GtC yr}^{-1}$ , South:  $0.32 \text{ GtC yr}^{-1}$ ), acknowledging that the boundaries of Aumont et al (2001; namely  $20^\circ\text{S}$  and  $20^\circ\text{N}$ ) are not consistent with the boundaries otherwise used in the GCB ( $30^\circ\text{S}$  and  $30^\circ\text{N}$ ). A recent study based on one ocean biogeochemical model (Lacroix et al., 2020) suggests that more of the riverine outgassing is located in the tropics than in the Southern Ocean; and hence this regional distribution is associated with a major uncertainty. Anthropogenic perturbations of river carbon and nutrient transport to the ocean are not considered (see section 2.7 and Appendix D.3).

We derive  $S_{OCEAN}$  from GOBMs by using a simulation (sim A) with historical forcing of climate and atmospheric  $CO_2$ , accounting for model biases and drift from a control simulation (sim B) with constant atmospheric  $CO_2$  and normal year climate forcing. A third simulation (sim C) with historical atmospheric  $CO_2$  increase and normal year climate forcing is used to attribute the ocean sink to  $CO_2$  (sim C minus sim B) and climate (sim A minus sim C) effects. A fourth simulation (sim D; historical climate forcing and constant atmospheric  $CO_2$ ) is used to compare the change in anthropogenic carbon inventory in the interior ocean (sim A minus sim D) to the observational estimate of Gruber et al. (2019) with the same flux components (steady state and non-steady state anthropogenic carbon flux). Data-products are adjusted to represent the full ice-free ocean area by a simple scaling approach when coverage is below 99%. GOBMs and data-products fall within the observational constraints over the 1990s ( $2.2 \pm 0.7 \text{ GtC yr}^{-1}$ , Ciais et al., 2013) after applying adjustments.  $S_{OCEAN}$  is calculated as the average of the GOBM ensemble mean and data-product ensemble mean from 1990 onwards. Prior to 1990, it is calculated as the GOBM ensemble mean plus half of the offset between GOBMs and data-products ensemble means over 1990-2001.

We assign an uncertainty of  $\pm 0.4 \text{ GtC yr}^{-1}$  to the ocean sink based on a combination of random (ensemble standard deviation) and systematic uncertainties (GOBMs bias in anthropogenic carbon accumulation, previously reported uncertainties in  $fCO_2$ -based data-products; see Appendix C.3.3). We assess a medium confidence level to the annual ocean  $CO_2$  sink and its uncertainty because it is based on multiple lines of evidence, it is consistent with ocean interior carbon estimates (Gruber et al., 2019, see section 3.5.5) and the interannual variability in the GOBMs and data-based estimates is largely consistent and can be explained by climate variability. We refrain from assigning a high confidence because of the systematic deviation between the GOBM and data-product trends since around 2002. More details on the  $S_{OCEAN}$  methodology can be found in Appendix C.3.

#### **2.4.2 2022 Projection**

The ocean  $CO_2$  sink forecast for the year 2022 is based on the annual historical and estimated 2022 atmospheric  $CO_2$  concentration (Dlugokencky and Tans 2021), the historical and estimated 2022 annual global fossil fuel emissions from this year's carbon budget, and the spring (March, April, May) Oceanic Niño Index (ONI) (NCEP, 2022). Using a non-linear regression approach, i.e., a feed-forward neural network, atmospheric  $CO_2$ , ONI, and the fossil fuel emissions are used as training data to best match the annual ocean  $CO_2$  sink (i.e. combined  $S_{OCEAN}$  estimate from GOBMs and data products) from 1959 through 2021 from this year's carbon budget. Using this relationship, the 2022  $S_{OCEAN}$  can then be estimated from the projected 2021 input data using the non-linear relationship established during the network training. To avoid overfitting, the neural network was trained with a variable number of hidden neurons (varying between 2-5) and 20% of the randomly selected training data were withheld for independent internal testing. Based on the best output performance (tested using the 20% withheld input data), the best performing number of neurons was selected. In a second step, we trained the network 10 times using the best number of neurons identified in step 1 and different sets of randomly selected training data. The mean of the 10 trainings is considered our best forecast, whereas the standard deviation of the 10 ensembles provides a first order estimate of the forecast uncertainty. This uncertainty is then combined with the  $S_{OCEAN}$  uncertainty ( $0.4 \text{ GtC yr}^{-1}$ ) to estimate the overall uncertainty of the 2022 projection.

## 2.5 Land CO<sub>2</sub> sink

### 2.5.1 Historical Period

The terrestrial land sink ( $S_{\text{LAND}}$ ) is thought to be due to the combined effects of fertilisation by rising atmospheric CO<sub>2</sub> and N inputs on plant growth, as well as the effects of climate change such as the lengthening of the growing season in northern temperate and boreal areas.  $S_{\text{LAND}}$  does not include land sinks directly resulting from land-use and land-use change (e.g., regrowth of vegetation) as these are part of the land-use flux ( $E_{\text{LUC}}$ ), although system boundaries make it difficult to attribute exactly CO<sub>2</sub> fluxes on land between  $S_{\text{LAND}}$  and  $E_{\text{LUC}}$  (Erb et al., 2013).

$S_{\text{LAND}}$  is estimated from the multi-model mean of 16 DGVMs (Table A1). As described in Appendix C.4, DGVMs simulations include all climate variability and CO<sub>2</sub> effects over land. In addition to the carbon cycle represented in all DGVMs, 11 models also account for the nitrogen cycle and hence can include the effect of N inputs on  $S_{\text{LAND}}$ . The DGVMs estimate of  $S_{\text{LAND}}$  does not include the export of carbon to aquatic systems or its historical perturbation, which is discussed in Appendix D3. See Appendix C.4 for DGVMs evaluation and uncertainty assessment for  $S_{\text{LAND}}$ , using the International Land Model Benchmarking system (ILAMB; Collier et al., 2018). More details on the  $S_{\text{LAND}}$  methodology can be found in Appendix C.4.

### 2.5.2 2022 Projection

Like for the ocean forecast, the land CO<sub>2</sub> sink ( $S_{\text{LAND}}$ ) forecast is based on the annual historical and estimated 2022 atmospheric CO<sub>2</sub> concentration (Dlugokencky and Tans 2021), historical and estimated 2022 annual global fossil fuel emissions from this year's carbon budget, and the summer (June, July, August) ONI (NCEP, 2022). All training data are again used to best match  $S_{\text{LAND}}$  from 1959 through 2021 from this year's carbon budget using a feed-forward neural network. To avoid overfitting, the neural network was trained with a variable number of hidden neurons (varying between 2-15), larger than for  $S_{\text{OCEAN}}$  prediction due to the stronger land carbon interannual variability. As done for  $S_{\text{OCEAN}}$ , a pre-training selects the optimal number of hidden neurons based on 20% withheld input data, and in a second step, an ensemble of 10 forecasts is produced to provide the mean forecast plus uncertainty. This uncertainty is then combined with the  $S_{\text{LAND}}$  uncertainty for 2021 (0.9 GtC yr<sup>-1</sup>) to estimate the overall uncertainty of the 2022 projection.

## 2.6 The atmospheric perspective

The world-wide network of in-situ atmospheric measurements and satellite derived atmospheric CO<sub>2</sub> column ( $x\text{CO}_2$ ) observations put a strong constraint on changes in the atmospheric abundance of CO<sub>2</sub>. This is true globally (hence our large confidence in  $G_{\text{ATM}}$ ), but also regionally in regions with sufficient observational density found mostly in the extra-tropics. This allows atmospheric inversion methods to constrain the magnitude and location of the combined total surface CO<sub>2</sub> fluxes from all sources, including fossil and land-use change emissions and land and ocean CO<sub>2</sub> fluxes. The inversions assume  $E_{\text{FOS}}$  to be well known, and they solve for the spatial and temporal distribution of land and ocean fluxes from the residual gradients of CO<sub>2</sub> between stations that are not explained by fossil fuel emissions. By design, such systems thus close the carbon balance ( $B_{\text{IM}} = 0$ ) and thus provide an additional perspective on the independent estimates of the ocean and land fluxes.

This year's release includes nine inversion systems that are described in Table A4. Each system is rooted in Bayesian inversion principles but uses different methodologies. These differences concern the selection of atmospheric CO<sub>2</sub> data or xCO<sub>2</sub>, and the choice of a-priori fluxes to refine. They also differ in spatial and temporal resolution, assumed correlation structures, and mathematical approach of the models (see references in Table A4 for details). Importantly, the systems use a variety of transport models, which was demonstrated to be a driving factor behind differences in atmospheric inversion-based flux estimates, and specifically their distribution across latitudinal bands (Gaubert et al., 2019; Schuh et al., 2019). Four inversion systems (CAMS-FT21r2, CMS-flux, GONGGA, THU) used satellite xCO<sub>2</sub> retrievals from GOSAT and/or OCO-2, scaled to the WMO 2019 calibration scale. One inversion this year (CMS-Flux) used these xCO<sub>2</sub> datasets in addition to the in-situ observational CO<sub>2</sub> mole fraction records.

The original products delivered by the inverse modellers were modified to facilitate the comparison to the other elements of the budget, specifically on two accounts: (1) global total fossil fuel emissions including cement carbonation CO<sub>2</sub> uptake, and (2) riverine CO<sub>2</sub> transport. Details are given below. We note that with these adjustments the inverse results no longer represent the net atmosphere-surface exchange over land/ocean areas as sensed by atmospheric observations. Instead, for land, they become the net uptake of CO<sub>2</sub> by vegetation and soils that is not exported by fluvial systems, similar to the DGVMs estimates. For oceans, they become the net uptake of anthropogenic CO<sub>2</sub>, similar to the GOBMs estimates.

The inversion systems prescribe global fossil fuel emissions based on the GCP's Gridded Fossil Emissions Dataset versions 2022.1 or 2022.2 (GCP-GridFED; Jones et al., 2022), which are updates to GCP-GridFEDv2021 presented by Jones et al. (2021). GCP-GridFEDv2022 scales gridded estimates of CO<sub>2</sub> emissions from EDGARv4.3.2 (Janssens-Maenhout et al., 2019) within national territories to match national emissions estimates provided by the GCB for the years 1959-2021, which were compiled following the methodology described in Section 2.1. Small differences between the systems due to for instance regridding to the transport model resolution, or use of different GridFED versions with different cement carbonation sinks (which were only present starting with GridFEDv2022.1), are adjusted in the latitudinal partitioning we present, to ensure agreement with the estimate of  $E_{FOS}$  in this budget. We also note that the ocean fluxes used as prior by 6 out of 9 inversions are part of the suite of the ocean process model or fCO<sub>2</sub> data products listed in Section 2.4. Although these fluxes are further adjusted by the atmospheric inversions, it makes the inversion estimates of the ocean fluxes not completely independent of  $S_{OCEAN}$  assessed here.

To facilitate comparisons to the independent  $S_{OCEAN}$  and  $S_{LAND}$ , we used the same corrections for transport and outgassing of carbon transported from land to ocean, as done for the observation-based estimates of  $S_{OCEAN}$  (see Appendix C.3).

The atmospheric inversions are evaluated using vertical profiles of atmospheric CO<sub>2</sub> concentrations (Figure B4). More than 30 aircraft programs over the globe, either regular programs or repeated surveys over at least 9 months (except for SH programs), have been used to assess system performance (with space-time observational coverage sparse in the SH and tropics, and denser in NH mid-latitudes; Table A6). The nine systems are compared to the independent aircraft CO<sub>2</sub> measurements between 2 and 7 km above sea level between 2001 and 2021. Results are shown in Figure B4 and discussed in Appendix C.5.2

With a relatively small ensemble ( $N=9$ ) of systems that moreover share some a-priori fluxes used with one another, or with the process-based models, it is difficult to justify using their mean and standard deviation as a metric for uncertainty across the ensemble. We therefore report their full range (min-max) without their mean. More details on the atmospheric inversions methodology can be found in Appendix C.5.

## 2.7 Processes not included in the global carbon budget

The contribution of anthropogenic CO and CH<sub>4</sub> to the global carbon budget is not fully accounted for in Eq. (1) and is described in Appendix D1. The contributions to CO<sub>2</sub> emissions of decomposition of carbonates not accounted for is described in Appendix D2. The contribution of anthropogenic changes in river fluxes is conceptually included in Eq. (1) in  $S_{OCEAN}$  and in  $S_{LAND}$ , but it is not represented in the process models used to quantify these fluxes. This effect is discussed in Appendix D3. Similarly, the loss of additional sink capacity from reduced forest cover is missing in the combination of approaches used here to estimate both land fluxes ( $E_{LUC}$  and  $S_{LAND}$ ) and its potential effect is discussed and quantified in Appendix D4.

## 3 Results

For each component of the global carbon budget, we present results for three different time periods: the full historical period, from 1850 to 2021, the six decades in which we have atmospheric concentration records from Mauna Loa (1960-2021), a specific focus on last year (2021), and the projection for the current year (2022). Subsequently, we assess the combined constraints from the budget components (often referred to as a bottom-up budget) against the top-down constraints from inverse modelling of atmospheric observations. We do this for the global balance of the last decade, as well as for a regional breakdown of land and ocean sinks by broad latitude bands.

### 3.1 Fossil CO<sub>2</sub> Emissions

#### 3.1.1 Historical period 1850-2021

Cumulative fossil CO<sub>2</sub> emissions for 1850-2021 were  $465 \pm 25$  GtC, including the cement carbonation sink (Figure 3, Table 8, all cumulative numbers are rounded to the nearest 5GtC).

In this period, 46% of fossil CO<sub>2</sub> emissions came from coal, 35% from oil, 15% from natural gas, 3% from decomposition of carbonates, and 1% from flaring.

In 1850, the UK stood for 62% of global fossil CO<sub>2</sub> emissions. In 1891 the combined cumulative emissions of the current members of the European Union reached and subsequently surpassed the level of the UK. Since 1917 US cumulative emissions have been the largest. Over the entire period 1850-2021, US cumulative emissions amounted to 115GtC (24% of world total), the EU's to 80 GtC (17%), and China's to 70 GtC (14%). In addition to the estimates of fossil CO<sub>2</sub> emissions that we provide here (see Methods), there are three additional global datasets with long time series that include all sources of fossil CO<sub>2</sub> emissions: CDIAC-FF (Gilfillan and Marland, 2021), CEDS version v\_2021\_04\_21 (Hoesly et al., 2018; O'Rourke et al., 2021) and PRIMAP-hist version 2.3.1 (Gütschow et al., 2016, 2021), although these datasets are not entirely independent from each other (Andrew, 2020a). CDIAC-FF has the lowest cumulative emissions over 1750-2018 at 437 GtC, GCP has 443 GtC, CEDS 445 GtC, PRIMAP-hist TP 453 GtC, and PRIMAP-hist CR 455 GtC. CDIAC-FF

excludes emissions from lime production, while neither CDIAC-FF nor GCP explicitly include emissions from international bunker fuels prior to 1950. CEDS has higher emissions from international shipping in recent years, while PRIMAP-hist has higher fugitive emissions than the other datasets. However, in general these four datasets are in relative agreement as to total historical global emissions of fossil CO<sub>2</sub>.

### **3.1.2 Recent period 1960-2021**

Global fossil CO<sub>2</sub> emissions, E<sub>FOS</sub> (including the cement carbonation sink), have increased every decade from an average of  $3.0 \pm 0.2$  GtC yr<sup>-1</sup> for the decade of the 1960s to an average of  $9.6 \pm 0.5$  GtC yr<sup>-1</sup> during 2012-2021 (Table 6, Figure 2 and Figure 5). The growth rate in these emissions decreased between the 1960s and the 1990s, from 4.3% yr<sup>-1</sup> in the 1960s (1960-1969), 3.2% yr<sup>-1</sup> in the 1970s (1970-1979), 1.6% yr<sup>-1</sup> in the 1980s (1980-1989), to 0.9% yr<sup>-1</sup> in the 1990s (1990-1999). After this period, the growth rate began increasing again in the 2000s at an average growth rate of 3.0% yr<sup>-1</sup>, decreasing to 0.5% yr<sup>-1</sup> for the last decade (2012-2021). China's emissions increased by +1.5% yr<sup>-1</sup> on average over the last 10 years dominating the global trend, and India's emissions increased by +3.8% yr<sup>-1</sup>, while emissions decreased in EU27 by -1.8% yr<sup>-1</sup>, and in the USA by -1.1% yr<sup>-1</sup>. Figure 6 illustrates the spatial distribution of fossil fuel emissions for the 2012-2021 period.

E<sub>FOS</sub> includes the uptake of CO<sub>2</sub> by cement via carbonation which has increased with increasing stocks of cement products, from an average of 20 MtC yr<sup>-1</sup> (0.02 GtC yr<sup>-1</sup>) in the 1960s to an average of 200 MtC yr<sup>-1</sup> (0.2 GtC yr<sup>-1</sup>) during 2012-2021 (Figure 5).

### **3.1.3 Final year 2021**

Global fossil CO<sub>2</sub> emissions were 5.1% higher in 2021 than in 2020, because of the global rebound from the worst of the COVID-19 pandemic, with an increase of 0.5 GtC to reach  $9.9 \pm 0.5$  GtC (including the cement carbonation sink) in 2021 (Figure 5), distributed among coal (41%), oil (32%), natural gas (22%), cement (5%) and others (1%). Compared to the previous year, 2021 emissions from coal, oil and gas increased by 5.7%, 5.8% and 4.8% respectively, while emissions from cement increased by 2.1%. All growth rates presented are adjusted for the leap year, unless stated otherwise.

In 2021, the largest absolute contributions to global fossil CO<sub>2</sub> emissions were from China (31%), the USA (14%), the EU27 (8%), and India (7%). These four regions account for 59% of global CO<sub>2</sub> emissions, while the rest of the world contributed 41%, including international aviation and marine bunker fuels (2.8% of the total). Growth rates for these countries from 2020 to 2021 were 3.5% (China), 6.2% (USA), 6.8% (EU27), and 11.1% (India), with +4.5% for the rest of the world. The per-capita fossil CO<sub>2</sub> emissions in 2021 were 1.3 tC person<sup>-1</sup> yr<sup>-1</sup> for the globe, and were 4.0 (USA), 2.2 (China), 1.7 (EU27) and 0.5 (India) tC person<sup>-1</sup> yr<sup>-1</sup> for the four highest emitting countries (Figure 5).

The post-COVID-19 rebound in emissions of 5.1% in 2021 is close to the projected increase of 4.8% published in Friedlingstein et al. (2021) (Table 7). Of the regions, the projection for the 'rest of world' region was least accurate (off by -1.3%), largely because of poorly projected emissions from international transport (bunker fuels), which were subject to very large changes during this period.

### **3.1.4 Year 2022 Projection**

Globally, we estimate that global fossil CO<sub>2</sub> emissions (including cement carbonation) will grow by 1.1% in 2022 (0.0% to 1.7%) to 10.0 GtC (36.5 GtCO<sub>2</sub>), exceeding their 2019 emission levels of 9.9 GtC (36.2 GtCO<sub>2</sub>). Global increase in 2022 emissions per fuel types are projected to be +0.8% (range 0.0% to 1.7%) for coal, +2.2% (range -0.7% to 2.9%) for oil, +1.1% (range 0.0% to 2.2%) for natural gas, and -2.8% (range -5.5% to -0.2%) for cement.

For China, projected fossil emissions in 2022 are expected to decline by 1.5% (range -3.0% to +0.1%) compared with 2021 emissions, bringing 2022 emissions for China around 3.0 GtC yr<sup>-1</sup> (11.1 GtCO<sub>2</sub> yr<sup>-1</sup>). Changes in fuel specific projections for China are -0.5% for coal, -2.3% for oil, -1.1% natural gas, and -9.2% for cement.

For the USA, the Energy Information Administration (EIA) emissions projection for 2022 combined with cement clinker data from USGS gives an increase of 1.6% (range -0.9% to +4.1%) compared to 2021, bringing USA 2022 emissions to around 1.4 GtC yr<sup>-1</sup> (5.1 GtCO<sub>2</sub> yr<sup>-1</sup>). This is based on separate projections for coal -2.8%, oil +1.9%, natural gas +4.1%, and cement +0.7%.

For the European Union, our projection for 2022 is for a decline of 1.0% (range -2.9% to +1.0%) over 2021, with 2022 emissions around 0.8 GtC yr<sup>-1</sup> (2.8 GtCO<sub>2</sub> yr<sup>-1</sup>). This is based on separate projections for coal of +7.5%, oil +0.6%, natural gas -11.0%, and cement unchanged.

For India, our projection for 2022 is an increase of 5.6% (range of 3.5% to 7.7%) over 2021, with 2022 emissions around 0.8 GtC yr<sup>-1</sup> (2.9 GtCO<sub>2</sub> yr<sup>-1</sup>). This is based on separate projections for coal of +5.0%, oil +8.0%, natural gas -3.0%, and cement +10.0%.

For the rest of the world, the expected growth rate for 2022 is 2.5% (range 0.1% to 2.3%). The fuel-specific projected 2022 growth rates for the rest of the world are: +1.4% (range -0.6% to +3.4%) for coal, +3.2% (1.6% to +4.9%) for oil, +2.6% (1.1% to 4.1%) for natural gas, +2.8% (+0.6% to +5.1%) for cement.

## **3.2 Emissions from Land Use Changes**

### **3.2.1 Historical period 1850-2021**

Cumulative CO<sub>2</sub> emissions from land-use changes (E<sub>LUC</sub>) for 1850-2021 were 205 ± 60 GtC (Table 8; Figure 3; Figure 14). The cumulative emissions from E<sub>LUC</sub> show a large spread among individual estimates of 140 GtC (updated H&N2017), 280 GtC (BLUE), and 190 GtC (OSCAR) for the three bookkeeping models and a similar wide estimate of 185 ± 60 GtC for the DGVMs (all cumulative numbers are rounded to the nearest 5GtC). These estimates are broadly consistent with indirect constraints from vegetation biomass observations, giving a cumulative source of 155 ± 50 GtC over the 1901-2012 period (Li et al., 2017). However, given the large spread, a best estimate is difficult to ascertain.

### **3.2.2 Recent period 1960-2021**

In contrast to growing fossil emissions, CO<sub>2</sub> emissions from land-use, land-use change, and forestry have remained relatively constant, over the 1960-1999 period, but showing a slight decrease of about 0.1 GtC per decade since the 1990s, reaching 1.2 ± 0.7 GtC yr<sup>-1</sup> for the 2012-2021 period (Table 6), but with large spread across estimates (Table 5, Figure 7). Different from the bookkeeping average, the DGVMs model average grows



slightly larger over the 1970-2021 period and shows no sign of decreasing emissions in the recent decades (Table 5, Figure 7). This is, however, expected as DGVM-based estimates include the loss of additional sink capacity, which grows with time, while the bookkeeping estimates do not (Appendix D4).

$E_{LUC}$  is a net term of various gross fluxes, which comprise emissions and removals. Gross emissions on average over the 1850-2021 period are two (BLUE, OSCAR) to three (updated H&N2017) times larger than the net  $E_{LUC}$  emissions. Gross emissions show a moderate increase from an average of  $3.2 \pm 0.9$  GtC yr<sup>-1</sup> for the decade of the 1960s to an average of  $3.8 \pm 0.7$  GtC yr<sup>-1</sup> during 2012-2021 (Figure 7). Increases in gross removals, from  $1.8 \pm 0.4$  GtC yr<sup>-1</sup> for the 1960s to  $2.6 \pm 0.4$  GtC yr<sup>-1</sup> for 2012-2021, were slightly larger than the increase in gross emissions. Since the processes behind gross removals, foremost forest regrowth and soil recovery, are all slow, while gross emissions include a large instantaneous component, short-term changes in land-use dynamics, such as a temporary decrease in deforestation, influences gross emissions dynamics more than gross removals dynamics. It is these relative changes to each other that explain the small decrease in net  $E_{LUC}$  emissions over the last two decades and the last few years. Gross fluxes often differ more across the three bookkeeping estimates than net fluxes, which is expected due to different process representation; in particular, treatment of shifting cultivation, which increases both gross emissions and removals, differs across models.

There is a smaller decrease in net CO<sub>2</sub> emissions from land-use change in the last few years (Figure 7) than in our last year's estimate (Friedlingstein et al., 2021), which places our updated estimates between last year's estimate and the estimate from the GCB2020 (Friedlingstein et al., 2020). This change is principally attributable to changes in  $E_{LUC}$  estimates from BLUE and OSCAR, which relate to improvements in the underlying land-use forcing (see Appendix C.2.2 for details). These changes address issues identified with last year's land-use forcing (see Friedlingstein et al., 2022) and remove/attenuate several emission peaks in Brazil and the Democratic Republic of the Congo and lead to higher net emissions in Brazil in the last decades compared to last year's global carbon budget (the emissions averaged over the three bookkeeping models for Brazil for the 2011-2020 period were 168 MtC yr<sup>-1</sup> in GCB2021 as compared to 289 MtC yr<sup>-1</sup> in GCB2022). A remaining caveat is that global land-use change data for model input does not capture forest degradation, which often occurs on small scale or without forest cover changes easily detectable from remote sensing and poses a growing threat to forest area and carbon stocks that may surpass deforestation effects (e.g., Matricardi et al., 2020, Qin et al., 2021). While independent pan-tropical or global estimates of vegetation cover dynamics or carbon stock changes based on satellite remote sensing have become available in recent years, a direct comparison to our estimates is not possible, most importantly because satellite-based estimates usually do not distinguish between anthropogenic drivers and natural forest cover losses (e.g. from drought or natural wildfires) (Pongratz et al., 2021).

We additionally separate the net  $E_{LUC}$  into four component fluxes to gain further insight into the drivers of emissions: deforestation, re/afforestation and wood harvest (i.e. all fluxes on forest lands), emissions from organic soils (i.e. peat drainage and peat fires), and fluxes associated with all other transitions (Figure 7; Sec. C.2.1). On average over the 2012-2021 period and over the three bookkeeping estimates, fluxes from deforestation amount to  $1.8 \pm 0.4$  GtC yr<sup>-1</sup> and from re/afforestation and wood harvest to  $-0.9 \pm 0.3$  GtC yr<sup>-1</sup> (Table 5). Emissions from organic soils ( $0.2 \pm 0.1$  GtC yr<sup>-1</sup>) and the net flux from other transitions ( $0.2 \pm 0.1$  GtC yr<sup>-1</sup>) are substantially less important globally. Deforestation is thus the main driver of global gross sources.

The relatively small deforestation flux ( $1.8 \pm 0.4 \text{ GtC yr}^{-1}$ ) in comparison to the gross emission estimate above ( $3.8 \pm 0.7 \text{ GtC yr}^{-1}$ ) is explained by the fact that emissions associated with wood harvesting do not count as deforestation as they do not change the land cover. This split into component fluxes clarifies the potentials for emission reduction and carbon dioxide removal: the emissions from deforestation could be halted (largely) without compromising carbon uptake by forests and would contribute to emissions reduction. By contrast, reducing wood harvesting would have limited potential to reduce emissions as it would be associated with less forest regrowth; sinks and sources cannot be decoupled here. Carbon dioxide removal in forests could instead be increased by re/afforestation.

Overall, highest land-use emissions occur in the tropical regions of all three continents. The top three emitters (both cumulatively 1959-2021 and on average over 2012-2021) are Brazil (in particular the Amazon Arc of Deforestation), Indonesia and the Democratic Republic of the Congo, with these 3 countries contributing  $0.7 \text{ GtC yr}^{-1}$  or 58% of the global total land-use emissions (average over 2012-2021) (Figure 6b). This is related to massive expansion of cropland, particularly in the last few decades in Latin America, Southeast Asia, and sub-Saharan Africa Emissions (Hong et al., 2021), to a substantial part for export of agricultural products (Pendrill et al., 2019). Emission intensity is high in many tropical countries, particularly of Southeast Asia, due to high rates of land conversion in regions of carbon-dense and often still pristine, undegraded natural forests (Hong et al., 2021). Emissions are further increased by peat fires in equatorial Asia (GFED4s, van der Werf et al., 2017). Uptake due to land-use change occurs, particularly in Europe, partly related to expanding forest area as a consequence of the forest transition in the 19<sup>th</sup> and 20<sup>th</sup> century and subsequent regrowth of forest (Figure 6b) (Mather 2001; McGrath et al., 2015).

While the mentioned patterns are supported by independent literature and robust, we acknowledge that model spread is substantially larger on regional than global level, as has been shown for bookkeeping models (Bastos et al., 2021) as well as DGVMs (Obermeier et al., 2021). Assessments for individual regions will be performed as part of REgional Carbon Cycle Assessment and Processes (RECCAP2; Ciais et al., 2020) or already exist for selected regions (e.g., for Europe by Petrescu et al., 2020, for Brazil by Rosan et al., 2021, for 8 selected countries/regions in comparison to inventory data by Schwingshackl et al., *subm.*).

National GHG inventory data (NGHGI) under the LULUCF sector or data submitted by countries to FAOSTAT differ from the global models' definition of  $E_{LUC}$  we adopt here in that in the NGHGI reporting, the natural fluxes ( $S_{LAND}$ ) are counted towards  $E_{LUC}$  when they occur on managed land (Grassi et al., 2018). In order to compare our results to the NGHGI approach, we perform a re-mapping of our  $E_{LUC}$  estimates by adding  $S_{LAND}$  in managed forest from the DGVMs simulations (following Grassi et al., 2021) to the bookkeeping  $E_{LUC}$  estimate (see Appendix C.2.3). For the 2012-2021 period, we estimate that  $1.8 \text{ GtC yr}^{-1}$  of  $S_{LAND}$  occurred in managed forests and is then reallocated to  $E_{LUC}$  here, as done in the NGHGI method. Doing so, our mean estimate of  $E_{LUC}$  is reduced from a source of  $1.2 \text{ GtC}$  to a sink of  $0.6 \text{ GtC}$ , very similar to the NGHGI estimate of a  $0.5 \text{ GtC}$  sink (Table 9). The re-mapping approach has been shown to be generally applicable also on country-level (Grassi et al., 2022b; Schwingshackl et al., *subm.*). Country-level analysis suggests, e.g., that the bookkeeping mean estimates higher deforestation emissions than the national report in Indonesia, but estimates less  $\text{CO}_2$  removal by afforestation than the national report in China. The fraction of the natural  $\text{CO}_2$  sinks that the NGHGI estimates include differs substantially across countries, related to varying proportions of managed vs all forest

areas (Schwingshackl et al., *subm.*). Comparing  $E_{LUC}$  and NGHGI on the basis of the four component fluxes (Grassi et al., 2022b) we find that NGHGI deforestation emissions are reported to be smaller than the bookkeeping estimate ( $1.1 \text{ GtC yr}^{-1}$  averaged over 2012-2021). A reason for this lies in the fact that country reports do not (fully) capture the carbon flux consequences of shifting cultivation. Conversely, carbon uptake in forests (re/afforestation and forestry) is substantially larger than the bookkeeping estimate ( $1.75 \text{ GtC yr}^{-1}$  averaged over 2012-2021), owing to the inclusion of natural  $\text{CO}_2$  fluxes on managed land in the NGHGI. Emissions from organic soils and the net flux from other transitions are similar to the estimates based on the bookkeeping approach and the external peat drainage and burning datasets. Though estimates between NGHGI, FAOSTAT, individual process-based models and the mapped budget estimates still differ in value and need further analysis, the approach taken here provides a possibility to relate the global models' and NGHGI approach to each other routinely and thus link the anthropogenic carbon budget estimates of land  $\text{CO}_2$  fluxes directly to the Global Stocktake, as part of UNFCCC Paris Agreement.

### 3.2.3 Final year 2021

The global  $\text{CO}_2$  emissions from land-use change are estimated as  $1.1 \pm 0.7 \text{ GtC}$  in 2021, similar to the 2020 estimate. However, confidence in the annual change remains low.

Land-use change and related emissions may have been affected by the COVID-19 pandemic (e.g. Poulter et al., 2021). During the period of the pandemic, environmental protection policies and their implementation may have been weakened in Brazil (Vale et al., 2021). In other countries, too, monitoring capacities and legal enforcement of measures to reduce tropical deforestation have been reduced due to budget restrictions of environmental agencies or impairments to ground-based monitoring that prevents land grabs and tenure conflicts (Brancalion et al., 2020, Amador-Jiménez et al., 2020). Effects of the pandemic on trends in fire activity or forest cover changes are hard to separate from those of general political developments and environmental changes and the long-term consequences of disruptions in agricultural and forestry economic activities (e.g., Gruère and Brooks, 2020; Golar et al., 2020; Beckman and Countryman, 2021) remain to be seen. Overall, there is limited evidence so far that COVID-19 was a key driver of changes in LULUCF emissions at global scale. Impacts vary across countries and deforestation-curbing and enhancing factors may partly compensate each other (Wunder et al., 2021).

### 3.2.4 Year 2022 Projection

In Indonesia, peat fire emissions are very low, potentially related to a relatively wet dry season (GFED4.1s, van der Werf et al., 2017). In South America, the trajectory of tropical deforestation and degradation fires resembles the long-term average; global emissions from tropical deforestation and degradation fires were estimated to be  $116 \text{ TgC}$  by August 23 (GFED4.1s, van der Werf et al., 2017). Our preliminary estimate of  $E_{LUC}$  for 2022 is substantially lower than the 2012-2021 average, which saw years of anomalously dry conditions in Indonesia and high deforestation fires in South America (Friedlingstein et al., 2022). Based on the fire emissions until August 23, we expect  $E_{LUC}$  emissions of around  $1.0 \text{ GtC}$  in 2022. Note that although our extrapolation is based on tropical deforestation and degradation fires, degradation attributable to selective logging, edge-effects or fragmentation will not be captured. Further, deforestation and fires in deforestation zones may become more disconnected, partly due changes in legislation in some regions. For example, Van Wees et al. (2021) found that

the contribution from fires to forest loss decreased in the Amazon and in Indonesia over the period of 2003-2018. More recent years, however, saw an uptick in the Amazon again (Tyukavina et al., 2022 with update) and more work is needed to understand fire-deforestation relations.

The fires in Mediterranean Europe in summer 2022 and in the U.S. in spring 2022, though above average for those regions, only contribute a small amount to global emissions. However, they were unrelated to land-use change and are thus not attributed to  $E_{LUC}$ , but would be part of the natural land sink.

Land use dynamics may be influenced by the disruption to the global food market associated with the war in Ukraine, but scientific evidence so far is very limited. High food prices, which preceded but were exacerbated by the war (Torero 2022), are generally linked to higher deforestation (Angelsen and Kaimowitz 1999), while high prices on agricultural inputs such as fertilizers and fuel, which are also under pressure from embargoes, may impair yields.

### **3.3 Total anthropogenic emissions**

Cumulative anthropogenic CO<sub>2</sub> emissions for 1850-2021 totalled  $670 \pm 65$  GtC ( $2455 \pm 240$  GtCO<sub>2</sub>), of which 70% (470 GtC) occurred since 1960 and 33% (220 GtC) since 2000 (Table 6 and 8). Total anthropogenic emissions more than doubled over the last 60 years, from  $4.5 \pm 0.7$  GtC yr<sup>-1</sup> for the decade of the 1960s to an average of  $10.8 \pm 0.8$  GtC yr<sup>-1</sup> during 2012-2021, and reaching  $10.9 \pm 0.9$  GtC ( $40.0 \pm 3.3$  GtCO<sub>2</sub>) in 2021. For 2022, we project global total anthropogenic CO<sub>2</sub> emissions from fossil and land use changes to be also around 10.9 GtC (40.1 GtCO<sub>2</sub>). All values here include the cement carbonation sink (currently about 0.2 GtC yr<sup>-1</sup>). During the historical period 1850-2021, 30% of historical emissions were from land use change and 70% from fossil emissions. However, fossil emissions have grown significantly since 1960 while land use changes have not, and consequently the contributions of land use change to total anthropogenic emissions were smaller during recent periods (18% during the period 1960-2021 and 11% during 2012-2021).

## **3.4 Atmospheric CO<sub>2</sub>**

### **3.4.1 Historical period 1850-2021**

Atmospheric CO<sub>2</sub> concentration was approximately 278 parts per million (ppm) in 1750, reaching 300 ppm in the 1910s, 350 ppm in the late 1980s, and reaching  $414.71 \pm 0.1$  ppm in 2021 (Dlugokencky and Tans, 2022); Figure 1). The mass of carbon in the atmosphere increased by 48% from 590 GtC in 1750 to 879 GtC in 2021. Current CO<sub>2</sub> concentrations in the atmosphere are unprecedented in the last 2 million years and the current rate of atmospheric CO<sub>2</sub> increase is at least 10 times faster than at any other time during the last 800,000 years (Canadell et al., 2021).

### **3.4.2 Recent period 1960-2021**

The growth rate in atmospheric CO<sub>2</sub> level increased from  $1.7 \pm 0.07$  GtC yr<sup>-1</sup> in the 1960s to  $5.2 \pm 0.02$  GtC yr<sup>-1</sup> during 2012-2022 with important decadal variations (Table 6, Figure 3 and Figure 4). During the last decade (2012-2021), the growth rate in atmospheric CO<sub>2</sub> concentration continued to increase, albeit with large interannual variability (Figure 4).

The airborne fraction (AF), defined as the ratio of atmospheric CO<sub>2</sub> growth rate to total anthropogenic emissions:

$$AF = G_{ATM} / (E_{FOS} + E_{LUC}) \quad (2)$$

provides a diagnostic of the relative strength of the land and ocean carbon sinks in removing part of the anthropogenic CO<sub>2</sub> perturbation. The evolution of AF over the last 60 years shows no significant trend, remaining at around 44%, albeit showing a large interannual and decadal variability driven by the year-to-year variability in G<sub>ATM</sub> (Figure 9). The observed stability of the airborne fraction over the 1960-2020 period indicates that the ocean and land CO<sub>2</sub> sinks have been removing on average about 55% of the anthropogenic emissions (see sections 3.5 and 3.6).

### 3.4.3 Final year 2021

The growth rate in atmospheric CO<sub>2</sub> concentration was  $5.2 \pm 0.2$  GtC ( $2.46 \pm 0.08$  ppm) in 2021 (Figure 4; Dlugokencky and Tans, 2022), slightly above the 2020 growth rate (5.0 GtC) but similar to the 2011-2020 average (5.2 GtC).

### 3.4.4 Year 2022 Projection

The 2022 growth in atmospheric CO<sub>2</sub> concentration (G<sub>ATM</sub>) is projected to be about 5.5 GtC (2.58 ppm) based on GLO observations until August 2022, bringing the atmospheric CO<sub>2</sub> concentration to an expected level of 417.3 ppm averaged over the year, 51% over the pre-industrial level.

## 3.5 Ocean Sink

### 3.5.1 Historical period 1850-2021

Cumulated since 1850, the ocean sink adds up to  $175 \pm 35$  GtC, with more than two thirds of this amount (120 GtC) being taken up by the global ocean since 1960. Over the historical period, the ocean sink increased in pace with the anthropogenic emissions exponential increase (Figure 3b). Since 1850, the ocean has removed 26% of total anthropogenic emissions.

### 3.5.2 Recent period 1960-2021

The ocean CO<sub>2</sub> sink increased from  $1.1 \pm 0.4$  GtC yr<sup>-1</sup> in the 1960s to  $2.9 \pm 0.4$  GtC yr<sup>-1</sup> during 2012-2021 (Table 6), with interannual variations of the order of a few tenths of GtC yr<sup>-1</sup> (Figure 10). The ocean-borne fraction (S<sub>OCEAN</sub>/(E<sub>FOS</sub>+E<sub>LUC</sub>)) has been remarkably constant around 25% on average (Figure 9). Variations around this mean illustrate decadal variability of the ocean carbon sink. So far, there is no indication of a decrease in the ocean-borne fraction from 1960 to 2021. The increase of the ocean sink is primarily driven by the increased atmospheric CO<sub>2</sub> concentration, with the strongest CO<sub>2</sub> induced signal in the North Atlantic and the Southern Ocean (Figure 11a). The effect of climate change is much weaker, reducing the ocean sink globally by  $0.11 \pm 0.09$  GtC yr<sup>-1</sup> (-4.2%) during 2012-2021 (nine models simulate a weakening of the ocean sink by climate change, range -3.2 to -8.9%, and only one model simulates a strengthening by 4.8%), and does not show clear spatial patterns across the GOBMs ensemble (Figure 11b). This is the combined effect of change and

variability in all atmospheric forcing fields, previously attributed to wind and temperature changes in one model (LeQuéré et al., 2010).

The global net air-sea CO<sub>2</sub> flux is a residual of large natural and anthropogenic CO<sub>2</sub> fluxes into and out of the ocean with distinct regional and seasonal variations (Figure 6 and B1). Natural fluxes dominate on regional scales, but largely cancel out when integrated globally (Gruber et al., 2009). Mid-latitudes in all basins and the high-latitude North Atlantic dominate the ocean CO<sub>2</sub> uptake where low temperatures and high wind speeds facilitate CO<sub>2</sub> uptake at the surface (Takahashi et al., 2009). In these regions, formation of mode, intermediate and deep-water masses transport anthropogenic carbon into the ocean interior, thus allowing for continued CO<sub>2</sub> uptake at the surface. Outgassing of natural CO<sub>2</sub> occurs mostly in the tropics, especially in the equatorial upwelling region, and to a lesser extent in the North Pacific and polar Southern Ocean, mirroring a well-established understanding of regional patterns of air-sea CO<sub>2</sub> exchange (e.g., Takahashi et al., 2009, Gruber et al., 2009). These patterns are also noticeable in the Surface Ocean CO<sub>2</sub> Atlas (SOCAT) dataset, where an ocean fCO<sub>2</sub> value above the atmospheric level indicates outgassing (Figure B1). This map further illustrates the data-sparsity in the Indian Ocean and the southern hemisphere in general.

Interannual variability of the ocean carbon sink is driven by climate variability with a first-order effect from a stronger ocean sink during large El Niño events (e.g., 1997-1998) (Figure 10; Rödenbeck et al., 2014, Hauck et al., 2020). The GOBMs show the same patterns of decadal variability as the mean of the fCO<sub>2</sub>-based data products, with a stagnation of the ocean sink in the 1990s and a strengthening since the early 2000s (Figure 10, Le Quéré et al., 2007; Landschützer et al., 2015, 2016; DeVries et al., 2017; Hauck et al., 2020; McKinley et al., 2020). Different explanations have been proposed for this decadal variability, ranging from the ocean's response to changes in atmospheric wind and pressure systems (e.g., Le Quéré et al., 2007, Keppler and Landschützer, 2019), including variations in upper ocean overturning circulation (DeVries et al., 2017) to the eruption of Mount Pinatubo and its effects on sea surface temperature and slowed atmospheric CO<sub>2</sub> growth rate in the 1990s (McKinley et al., 2020). The main origin of the decadal variability is a matter of debate with a number of studies initially pointing to the Southern Ocean (see review in Canadell et al., 2021), but also contributions from the North Atlantic and North Pacific (Landschützer et al., 2016, DeVries et al., 2019), or a global signal (McKinley et al., 2020) were proposed.

Although all individual GOBMs and data-products fall within the observational constraint, the ensemble means of GOBMs, and data-products adjusted for the riverine flux diverge over time with a mean offset increasing from 0.28 GtC yr<sup>-1</sup> in the 1990s to 0.61 GtC yr<sup>-1</sup> in the decade 2012-2021 and reaching 0.79 GtC yr<sup>-1</sup> in 2021. The SO<sub>CEAN</sub> positive trend over time diverges by a factor two since 2002 (GOBMs: 0.28 ± 0.07 GtC yr<sup>-1</sup> per decade, data-products: 0.61 ± 0.17 GtC yr<sup>-1</sup> per decade, SO<sub>CEAN</sub>: 0.45 GtC yr<sup>-1</sup> per decade) and by a factor of three since 2010 (GOBMs: 0.21 ± 0.14 GtC yr<sup>-1</sup> per decade, data-products: 0.66 ± 0.38 GtC yr<sup>-1</sup> per decade, SO<sub>CEAN</sub>: 0.44 GtC yr<sup>-1</sup> per decade). The GOBMs estimate is slightly higher (<0.1 GtC yr<sup>-1</sup>) than in the previous global carbon budget (Friedlingstein et al., 2022), because two new models are included (CESM2, MRI) and four models revised their estimates upwards (CESM-ETHZ, CNRM, FESOM2-REcoM, PlankTOM). The data-product estimate is higher by about 0.1 GtC yr<sup>-1</sup> compared to Friedlingstein et al. (2022) as a result of an upward correction in three products (Jena-MLS, MPI-SOMFFN, OS-ETHZ-Gracer), the submission of LDEO-HPD

which is above average, the non-availability of the CSIR product, and the small upward correction of the river flux adjustment.

The discrepancy between the two types of estimates stems mostly from a larger Southern Ocean sink in the data-products prior to 2001, and from a larger *SOCEAN* trend in the northern and southern extra-tropics since then (Figure 13). Note that the location of the mean offset (but not its trend) depends strongly on the choice of regional river flux adjustment and would occur in the tropics rather than in the Southern Ocean when using the dataset of Lacroix et al. (2020) instead of Aumont et al. (2001). Other possible explanations for the discrepancy in the Southern Ocean could be missing winter observations and data sparsity in general (Bushinsky et al., 2019, Gloege et al., 2021), or model biases (as indicated by the large model spread in the South, Figure 13, and the larger model-data mismatch, Figure B2).

In GCB releases until 2021, the ocean sink 1959-1989 was only estimated by GOBMs due to the absence of *fCO<sub>2</sub>* observations. Now, the first data-based estimates extending back to 1957/58 are becoming available (Jena-MLS, Rödenbeck et al., 2022, LDEO-HPD, Bennington et al., 2022; Gloege et al. 2022). These are based on a multi-linear regression of *pCO<sub>2</sub>* with environmental predictors (Rödenbeck et al., 2022, included here) or on model-data *pCO<sub>2</sub>* misfits and their relation to environmental predictors (Bennington et al., 2022). The Jena-MLS estimate falls well within the range of GOBM estimates and has a correlation of 0.98 with *SOCEAN* (1959-2021 as well as 1959-1989). It agrees well on the mean *SOCEAN* estimate since 1977 with a slightly higher amplitude of variability (Figure 10). Until 1976, Jena-MLS is 0.2-0.3 GtCyr<sup>-1</sup> below the central *SOCEAN* estimate. The agreement especially on phasing of variability is impressive, and the discrepancies in the mean flux 1959-1976 could be explained by an overestimated trend of Jena-MLS (Rödenbeck et al., 2022). Bennington et al. (2022) report a larger flux into the pre-1990 ocean than in Jena-MLS.

The reported *SOCEAN* estimate from GOBMs and data-products is  $2.1 \pm 0.4$  GtC yr<sup>-1</sup> over the period 1994 to 2007, which is in agreement with the ocean interior estimate of  $2.2 \pm 0.4$  GtC yr<sup>-1</sup> which accounts for the climate effect on the natural CO<sub>2</sub> flux of  $-0.4 \pm 0.24$  GtC yr<sup>-1</sup> (Gruber et al., 2019) to match the definition of *SOCEAN* used here (Hauck et al., 2020). This comparison depends critically on the estimate of the climate effect on the natural CO<sub>2</sub> flux, which is smaller from the GOBMs (-0.1 GtC yr<sup>-1</sup>) than in Gruber et al. (2019). Uncertainties of these two estimates would also overlap when using the GOBM estimate of the climate effect on the natural CO<sub>2</sub> flux.

During 2010-2016, the ocean CO<sub>2</sub> sink appears to have intensified in line with the expected increase from atmospheric CO<sub>2</sub> (McKinley et al., 2020). This effect is stronger in the *fCO<sub>2</sub>*-based data products (Figure 10, ocean sink 2016 minus 2010, GOBMs:  $+0.42 \pm 0.09$  GtC yr<sup>-1</sup>, data-products:  $+0.52 \pm 0.22$  GtC yr<sup>-1</sup>). The reduction of -0.09 GtC yr<sup>-1</sup> (range: -0.39 to +0.01 GtC yr<sup>-1</sup>) in the ocean CO<sub>2</sub> sink in 2017 is consistent with the return to normal conditions after the El Niño in 2015/16, which caused an enhanced sink in previous years. After 2017, the GOBMs ensemble mean suggests the ocean sink levelling off at about 2.6 GtC yr<sup>-1</sup>, whereas the data-products' estimate increases by  $0.24 \pm 0.17$  GtC yr<sup>-1</sup> over the same period.

### 3.5.3 Final year 2021

The estimated ocean CO<sub>2</sub> sink was  $2.9 \pm 0.4$  GtC in 2021. This is a decrease of 0.12 GtC compared to 2020, in line with the expected sink weakening from persistent La Niña conditions. GOBM and data-product estimates

consistently result in a stagnation of  $S_{OCEAN}$  (GOBMs:  $-0.09 \pm 0.15$  GtC, data-products:  $-0.15 \pm 0.24$  GtC). Seven models and six data products show a decrease in  $S_{OCEAN}$  (GOBMs down to  $-0.31$  GtC, data-products down to  $-0.58$  GtC), while three models and two data products show an increase in  $S_{OCEAN}$  (GOBMs up to  $0.15$  GtC, data-products up to  $0.12$  GtC; Figure 10). The data-products have a larger uncertainty at the tails of the reconstructed time series (e.g., Watson et al., 2020). Specifically, the data-products' estimate of the last year is regularly adjusted in the following release owing to the tail effect and an incrementally increasing data availability with 1-5 years lag (Figure 10 inset).

#### 3.5.4 Year 2022 Projection

Using a feed-forward neural network method (see section 2.4) we project an ocean sink of 2.9 GtC for 2022. This is similar to the year 2021 as the La Niña conditions persist in 2022.

#### 3.5.5 Model Evaluation

The additional simulation D allows to separate the anthropogenic carbon component (steady state and non-steady state,  $\text{sim D} - \text{sim A}$ ) and to compare the model flux and DIC inventory change directly to the interior ocean estimate of Gruber et al. (2019) without further assumptions. The GOBMs ensemble average of anthropogenic carbon inventory changes 1994-2007 amounts to  $2.2 \text{ GtC yr}^{-1}$  and is thus lower than the  $2.6 \pm 0.3 \text{ GtC yr}^{-1}$  estimated by Gruber et al (2019). Only four models with the highest sink estimate fall within the range reported by Gruber et al. (2019). This suggests that the majority of the GOBMs underestimate anthropogenic carbon uptake by 10-20%. Analysis of Earth System Models indicate that an underestimation by about 10% may be due to biases in ocean carbon transport and mixing from the surface mixed layer to the ocean interior (Goris et al., 2018, Terhaar et al., 2021, Bourgeois et al., 2022, Terhaar et al., 2022), biases in the chemical buffer capacity (Revelle factor) of the ocean (Vaithinada Ayar et al., 2022; Terhaar et al., 2022) and partly due to a late starting date of the simulations (mirrored in atmospheric  $\text{CO}_2$  chosen for the preindustrial control simulation, Table A2, Bronselaer et al., 2017, Terhaar et al., 2022). Interestingly, and in contrast to the uncertainties in the surface  $\text{CO}_2$  flux, we find the largest mismatch in interior ocean carbon accumulation in the tropics (93% of the mismatch), with minor contribution from the north (1%) and the south (6%). This highlights the role of interior ocean carbon redistribution for those inventories (Khaliwala et al., 2009).

The evaluation of the ocean estimates (Figure B2) shows an RMSE from annually detrended data of 0.4 to 2.6  $\mu\text{atm}$  for the seven  $f\text{CO}_2$ -based data products over the globe, relative to the  $f\text{CO}_2$  observations from the SOCAT v2022 dataset for the period 1990-2021. The GOBMs RMSEs are larger and range from 3.0 to 4.8  $\mu\text{atm}$ . The RMSEs are generally larger at high latitudes compared to the tropics, for both the data products and the GOBMs. The data products have RMSEs of 0.4 to 3.2  $\mu\text{atm}$  in the tropics, 0.8 to 2.8  $\mu\text{atm}$  in the north, and 0.8 to 3.6  $\mu\text{atm}$  in the south. Note that the data products are based on the SOCAT v2022 database, hence the SOCAT is not an independent dataset for the evaluation of the data products. The GOBMs RMSEs are more spread across regions, ranging from 2.5 to 3.9  $\mu\text{atm}$  in the tropics, 3.1 to 6.5  $\mu\text{atm}$  in the North, and 5.4 to 7.9  $\mu\text{atm}$  in the South. The higher RMSEs occur in regions with stronger climate variability, such as the northern and southern high latitudes (poleward of the subtropical gyres). The upper range of the model RMSEs have decreased somewhat relative to Friedlingstein et al. (2022).



## 3.6 Land Sink

### 3.6.1 Historical period 1850-2021

Cumulated since 1850, the terrestrial CO<sub>2</sub> sink amounts to  $210 \pm 45$  GtC, 31% of total anthropogenic emissions. Over the historical period, the sink increased in pace with the anthropogenic emissions exponential increase (Figure 3b).

### 3.6.2 Recent period 1960-2021

The terrestrial CO<sub>2</sub> sink increased from  $1.2 \pm 0.4$  GtC yr<sup>-1</sup> in the 1960s to  $3.1 \pm 0.6$  GtC yr<sup>-1</sup> during 2012-2021, with important interannual variations of up to 2 GtC yr<sup>-1</sup> generally showing a decreased land sink during El Niño events (Figure 8), responsible for the corresponding enhanced growth rate in atmospheric CO<sub>2</sub> concentration. The larger land CO<sub>2</sub> sink during 2012-2021 compared to the 1960s is reproduced by all the DGVMs in response to the increase in both atmospheric CO<sub>2</sub> and nitrogen deposition, and the changes in climate, and is consistent with constraints from the other budget terms (Table 5).

Over the period 1960 to present the increase in the global terrestrial CO<sub>2</sub> sink is largely attributed to the CO<sub>2</sub> fertilisation effect (Prentice et al., 2001, Piao et al., 2009), directly stimulating plant photosynthesis and increased plant water use in water limited systems, with a small negative contribution of climate change (Figure 11). There is a range of evidence to support a positive terrestrial carbon sink in response to increasing atmospheric CO<sub>2</sub>, albeit with uncertain magnitude (Walker et al., 2021). As expected from theory, the greatest CO<sub>2</sub> effect is simulated in the tropical forest regions, associated with warm temperatures and long growing seasons (Hickler et al., 2008) (Figure 11a). However, evidence from tropical intact forest plots indicate an overall decline in the land sink across Amazonia (1985-2011), attributed to enhanced mortality offsetting productivity gains (Brienen et al., 2005, Hubau et al., 2020). During 2012-2021 the land sink is positive in all regions (Figure 6) with the exception of eastern Brazil, Southwest USA, Southeast Europe and Central Asia, North and South Africa, and eastern Australia, where the negative effects of climate variability and change (i.e. reduced rainfall) counterbalance CO<sub>2</sub> effects. This is clearly visible on Figure 11 where the effects of CO<sub>2</sub> (Figure 11a) and climate (Figure 11b) as simulated by the DGVMs are isolated. The negative effect of climate is the strongest in most of South America, Central America, Southwest US, Central Europe, western Sahel, southern Africa, Southeast Asia and southern China, and eastern Australia (Figure 11b). Globally, climate change reduces the land sink by  $0.63 \pm 0.52$  GtC yr<sup>-1</sup> or 17% (2012-2021).

Since 2020 the globe has experienced La Niña conditions which would be expected to lead to an increased land carbon sink. A clear peak in the global land sink is not evident in S<sub>LAND</sub>, and we find that a La Niña- driven increase in tropical land sink is offset by a reduced high latitude extra-tropical land sink, which may be linked to the land response to recent climate extremes. In the past years several regions experienced record-setting fire events. While global burned area has declined over the past decades mostly due to declining fire activity in savannas (Andela et al., 2017), forest fire emissions are rising and have the potential to counter the negative fire trend in savannas (Zheng et al., 2021). Noteworthy events include the 2019-2020 Black Summer event in Australia (emissions of roughly 0.2 GtC; van der Velde et al., 2021) and Siberia in 2021 where emissions approached 0.4 GtC or three times the 1997-2020 average according to GFED4s. While other regions, including

Western US and Mediterranean Europe, also experienced intense fire seasons in 2021 their emissions are substantially lower.

Despite these regional negative effects of climate change on  $S_{\text{LAND}}$ , the efficiency of land to remove anthropogenic  $\text{CO}_2$  emissions has remained broadly constant over the last six decades, with a land-borne fraction ( $S_{\text{LAND}}/(E_{\text{FOS}}+E_{\text{LUC}})$ ) of  $\sim 30\%$  (Figure 9).

### 3.6.3 Final year 2021

The terrestrial  $\text{CO}_2$  sink from the DGVMs ensemble was  $3.5 \pm 0.9 \text{ GtC}$  in 2021, slightly above the decadal average of  $3.1 \pm 0.6 \text{ GtC yr}^{-1}$  (Figure 4, Table 6). We note that the DGVMs estimate for 2021 is larger, but within the uncertainty, than the  $2.8 \pm 0.9 \text{ GtC yr}^{-1}$  estimate from the residual sink from the global budget ( $E_{\text{FOS}}+E_{\text{LUC}}-G_{\text{ATM}}-S_{\text{OCEAN}}$ ) (Table 5).

### 3.6.4 Year 2022 Projection

Using a feed-forward neural network method we project a land sink of  $3.4 \text{ GtC}$  for 2022, very similar to the 2021 estimate. As for the ocean sink, we attribute this to the persistence of La Niña conditions in 2022.

### 3.6.5 Model Evaluation

The evaluation of the DGVMs (Figure B3) shows generally high skill scores across models for runoff, and to a lesser extent for vegetation biomass, GPP, and ecosystem respiration (Figure B3, left panel). Skill score was lowest for leaf area index and net ecosystem exchange, with a widest disparity among models for soil carbon. These conclusions are supported by a more comprehensive analysis of DGVM performance in comparison with benchmark data (Seiler et al., 2022). Furthermore, results show how DGVM differences are often of similar magnitude compared with the range across observational datasets.

## 3.7 Partitioning the carbon sinks

### 3.7.1 Global sinks and spread of estimates

In the period 2012-2021, the bottom-up view of total global carbon sinks provided by the GCB,  $S_{\text{OCEAN}}$  for the ocean and  $S_{\text{LAND}}-E_{\text{LUC}}$  for the land (to be comparable to inversions), agrees closely with the top-down global carbon sinks delivered by the atmospheric inversions. Figure 12 shows both total sink estimates of the last decade split by ocean and land (including  $E_{\text{LUC}}$ ), which match the difference between  $G_{\text{ATM}}$  and  $E_{\text{FOS}}$  to within  $0.01\text{-}0.12 \text{ GtC yr}^{-1}$  for inverse systems, and to  $0.34 \text{ GtC yr}^{-1}$  for the GCB mean. The latter represents the  $B_{\text{IM}}$  discussed in Section 3.8, which by design is minimal for the inverse systems.

The distributions based on the individual models and data products reveal substantial spread but converge near the decadal means quoted in Tables 5 and 6. Sink estimates for  $S_{\text{OCEAN}}$  and from inverse systems are mostly non-Gaussian, while the ensemble of DGVMs appears more normally distributed justifying the use of a multi-model mean and standard deviation for their errors in the budget. Noteworthy is that the tails of the distributions provided by the land and ocean bottom-up estimates would not agree with the global constraint provided by the fossil fuel emissions and the observed atmospheric  $\text{CO}_2$  growth rate ( $E_{\text{FOS}} - G_{\text{ATM}}$ ). This illustrates the power of the atmospheric joint constraint from  $G_{\text{ATM}}$  and the global  $\text{CO}_2$  observation network it derives from.

### 3.7.2 Total atmosphere-to-land fluxes

The total atmosphere-to-land fluxes ( $S_{\text{LAND}} - E_{\text{LUC}}$ ), calculated here as the difference between  $S_{\text{LAND}}$  from the DGVMs and  $E_{\text{LUC}}$  from the bookkeeping models, amounts to a  $1.9 \pm 0.9 \text{ GtC yr}^{-1}$  sink during 2012-2021 (Table 5). Estimates of total atmosphere-to-land fluxes ( $S_{\text{LAND}} - E_{\text{LUC}}$ ) from the DGVMs alone ( $1.5 \pm 0.5 \text{ GtC yr}^{-1}$ ) are consistent with this estimate and also with the global carbon budget constraint ( $E_{\text{FOS}} - G_{\text{ATM}} - S_{\text{OCEAN}}$ ,  $1.5 \pm 0.6 \text{ GtC yr}^{-1}$  Table 5). For the last decade (2012-2021), the inversions estimate the net atmosphere-to-land uptake to lie within a range of 1.1 to 1.7  $\text{GtC yr}^{-1}$ , consistent with the GCB and DGVMs estimates of  $S_{\text{LAND}} - E_{\text{LUC}}$  (Figure 13 top row).

### 3.7.3 Total atmosphere-to-ocean fluxes

For the 2012-2021 period, the GOBMs ( $2.6 \pm 0.5 \text{ GtC yr}^{-1}$ ) produce a lower estimate for the ocean sink than the  $f\text{CO}_2$ -based data products ( $3.2 \pm 0.6 \text{ GtC yr}^{-1}$ ), which shows up in Figure 12 as a separate peak in the distribution from the GOBMs (triangle symbols pointing right) and from the  $f\text{CO}_2$ -based products (triangle symbols pointing left). Atmospheric inversions ( $2.7$  to  $3.3 \text{ GtC yr}^{-1}$ ) also suggest higher ocean uptake in the recent decade (Figure 13 top row). In interpreting these differences, we caution that the riverine transport of carbon taken up on land and outgassing from the ocean is a substantial ( $0.65 \text{ GtC yr}^{-1}$ ) and uncertain term that separates the various methods. A recent estimate of decadal ocean uptake from observed  $\text{O}_2/\text{N}_2$  ratios (Tohjima et al., 2019) also points towards a larger ocean sink, albeit with large uncertainty (2012-2016:  $3.1 \pm 1.5 \text{ GtC yr}^{-1}$ ).

### 3.7.4 Regional breakdown and interannual variability

Figure 13 also shows the latitudinal partitioning of the total atmosphere-to-surface fluxes excluding fossil  $\text{CO}_2$  emissions ( $S_{\text{OCEAN}} + S_{\text{LAND}} - E_{\text{LUC}}$ ) according to the multi-model average estimates from GOBMs and ocean  $f\text{CO}_2$ -based products ( $S_{\text{OCEAN}}$ ) and DGVMs ( $S_{\text{LAND}} - E_{\text{LUC}}$ ), and from atmospheric inversions ( $S_{\text{OCEAN}}$  and  $S_{\text{LAND}} - E_{\text{LUC}}$ ).

#### 3.7.4.1 North

Despite being one of the most densely observed and studied regions of our globe, annual mean carbon sink estimates in the northern extra-tropics (north of  $30^\circ\text{N}$ ) continue to differ. The atmospheric inversions suggest an atmosphere-to-surface sink ( $S_{\text{OCEAN}} + S_{\text{LAND}} - E_{\text{LUC}}$ ) for 2012-2021 of 2.0 to 3.2  $\text{GtC yr}^{-1}$ , which is higher than the process models' estimate of  $2.2 \pm 0.4 \text{ GtC yr}^{-1}$  (Figure 13). The GOBMs ( $1.2 \pm 0.2 \text{ GtC yr}^{-1}$ ),  $f\text{CO}_2$ -based data products ( $1.4 \pm 0.1 \text{ GtC yr}^{-1}$ ), and inversion systems ( $0.9$  to  $1.4 \text{ GtC yr}^{-1}$ ) produce consistent estimates of the ocean sink. Thus, the difference mainly arises from the total land flux ( $S_{\text{LAND}} - E_{\text{LUC}}$ ) estimate, which is  $1.0 \pm 0.4 \text{ GtC yr}^{-1}$  in the DGVMs compared to 0.6 to 2.0  $\text{GtC yr}^{-1}$  in the atmospheric inversions (Figure 13, second row).

Discrepancies in the northern land fluxes conforms with persistent issues surrounding the quantification of the drivers of the global net land  $\text{CO}_2$  flux (Arneeth et al., 2017; Huntzinger et al., 2017; O'Sullivan et al., 2022) and the distribution of atmosphere-to-land fluxes between the tropics and high northern latitudes (Baccini et al., 2017; Schimel et al., 2015; Stephens et al., 2007; Ciais et al. 2019; Gaubert et al., 2019).

In the northern extratropics, the process models, inversions, and fCO<sub>2</sub>-based data products consistently suggest that most of the variability stems from the land (Figure 13). Inversions generally estimate similar interannual variations (IAV) over land to DGVMs (0.30 – 0.37 vs 0.17 – 0.69 GtC yr<sup>-1</sup>, averaged over 1990-2021), and they have higher IAV in ocean fluxes (0.05 – 0.09 GtC yr<sup>-1</sup>) relative to GOBMs (0.02 – 0.06 GtC yr<sup>-1</sup>, Figure B2), and fCO<sub>2</sub>-based data products (0.03 – 0.09 GtC yr<sup>-1</sup>).

#### 3.7.4.2 Tropics

In the tropics (30°S-30°N), both the atmospheric inversions and process models estimate a total carbon balance (SOCEAN+SLAND-ELUC) that is close to neutral over the past decade. The GOBMs (0.06 ± 0.34 GtC yr<sup>-1</sup>), fCO<sub>2</sub>-based data products (0.00 ± 0.06 GtC yr<sup>-1</sup>), and inversion systems (-0.2 to 0.5 GtC yr<sup>-1</sup>) all indicate an approximately neutral tropical ocean flux (see Figure B1 for spatial patterns). DGVMs indicate a net land sink (SLAND-ELUC) of 0.5 ± 0.3 GtC yr<sup>-1</sup>, whereas the inversion systems indicate a net land flux between -0.9 and 0.7 GtC yr<sup>-1</sup>, though with high uncertainty (Figure 13, third row).

The tropical lands are the origin of most of the atmospheric CO<sub>2</sub> interannual variability (Ahlström et al., 2015), consistently among the process models and inversions (Figure 13). The interannual variability in the tropics is similar among the ocean data products (0.07 – 0.16 GtC yr<sup>-1</sup>) and the GOBMs (0.07 – 0.16 GtC yr<sup>-1</sup>, Figure B2), which is the highest ocean sink variability of all regions. The DGVMs and inversions indicate that atmosphere-to-land CO<sub>2</sub> fluxes are more variable than atmosphere-to-ocean CO<sub>2</sub> fluxes in the tropics, with interannual variability of 0.5 to 1.1 and 0.8 to 1.0 GtC yr<sup>-1</sup> for DGVMs and inversions, respectively.

#### 3.7.4.3 South

In the southern extra-tropics (south of 30°S), the atmospheric inversions suggest a total atmosphere-to-surface sink (SOCEAN+SLAND-ELUC) for 2012-2021 of 1.6 to 1.9 GtC yr<sup>-1</sup>, slightly higher than the process models' estimate of 1.4 ± 0.3 GtC yr<sup>-1</sup> (Figure 13). An approximately neutral total land flux (SLAND-ELUC) for the southern extra-tropics is estimated by both the DGVMs (0.02 ± 0.06 GtC yr<sup>-1</sup>) and the inversion systems (sink of -0.2 to 0.2 GtC yr<sup>-1</sup>). This means nearly all carbon uptake is due to oceanic sinks south of 30°S. The Southern Ocean flux in the fCO<sub>2</sub>-based data products (1.8 ± 0.1 GtC yr<sup>-1</sup>) and inversion estimates (1.6 to 1.9 GtCyr-1) is higher than in the GOBMs (1.4 ± 0.3 GtC yr<sup>-1</sup>) (Figure 13, bottom row). This discrepancy in the mean flux is likely explained by the uncertainty in the regional distribution of the river flux adjustment (Aumont et al., 2001, Lacroix et al., 2020) applied to fCO<sub>2</sub>-based data products and inverse systems to isolate the anthropogenic SOCEAN flux. Other possibly contributing factors are that the data-products potentially underestimate the winter CO<sub>2</sub> outgassing south of the Polar Front (Bushinsky et al., 2019) and potential model biases. CO<sub>2</sub> fluxes from this region are more sparsely sampled by all methods, especially in wintertime (Figure B1). Dominant biases in Earth System Models are related to mode water formation, stratification, and the chemical buffer capacity (Terhaar et al., 2021, Bourgeois et al., 2022, Terhaar et al., 2022).

The interannual variability in the southern extra-tropics is low because of the dominance of ocean areas with low variability compared to land areas. The split between land (SLAND-ELUC) and ocean (SOCEAN) shows a substantial contribution to variability in the south coming from the land, with no consistency between the

DGVMs and the inversions or among inversions. This is expected due to the difficulty of separating exactly the land and oceanic fluxes when viewed from atmospheric observations alone. The  $\text{SoCEAN}$  interannual variability was found to be higher in the  $\text{fCO}_2$ -based data products ( $0.09$  to  $0.19 \text{ GtC yr}^{-1}$ ) compared to GOBMs ( $0.03$  to  $0.06 \text{ GtC yr}^{-1}$ ) in 1990-2021 (Figure B2). Model subsampling experiments recently illustrated that observation-based products may overestimate decadal variability in the Southern Ocean carbon sink by 30% due to data sparsity, based on one data product with the highest decadal variability (Gloege et al., 2021).

### 3.7.4.4 Tropical vs northern land uptake

A continuing conundrum is the partitioning of the global atmosphere-land flux between the northern hemisphere land and the tropical land (Stephens et al., 2017; Pan et al., 2011; Gaubert et al., 2019). It is of importance because each region has its own history of land-use change, climate drivers, and impact of increasing atmospheric  $\text{CO}_2$  and nitrogen deposition. Quantifying the magnitude of each sink is a prerequisite to understanding how each individual driver impacts the tropical and mid/high-latitude carbon balance.

We define the North-South (N-S) difference as net atmosphere-land flux north of  $30^\circ\text{N}$  minus the net atmosphere-land flux south of  $30^\circ\text{N}$ . For the inversions, the N-S difference ranges from  $0.1 \text{ GtC yr}^{-1}$  to  $2.9 \text{ GtC yr}^{-1}$  across this year's inversion ensemble with a preference across models for either a smaller Northern land sink with a near neutral tropical land flux (medium N-S difference), or a large Northern land sink and a tropical land source (large N-S difference).

In the ensemble of DGVMs the N-S difference is  $0.6 \pm 0.5 \text{ GtC yr}^{-1}$ , a much narrower range than the one from inversions. Only two DGVMs have a N-S difference larger than  $1.0 \text{ GtC yr}^{-1}$ . The larger agreement across DGVMs than across inversions is to be expected as there is no correlation between Northern and Tropical land sinks in the DGVMs as opposed to the inversions where the sum of the two regions being well-constrained leads to an anti-correlation between these two regions. The much smaller spread in the N-S difference between the DGVMs could help to scrutinise the inverse systems further. For example, a large northern land sink and a tropical land source in an inversion would suggest a large sensitivity to  $\text{CO}_2$  fertilisation (the dominant factor driving the land sinks) for Northern ecosystems, which would be not mirrored by tropical ecosystems. Such a combination could be hard to reconcile with the process understanding gained from the DGVMs ensembles and independent measurements (e.g. Free Air  $\text{CO}_2$  Enrichment experiments). Such investigations will be further pursued in the upcoming assessment from REgional Carbon Cycle Assessment and Processes (RECCAP2; Ciais et al., 2020).

## 3.8 Closing the Global Carbon Cycle

### 3.8.1 Partitioning of Cumulative Emissions and Sink Fluxes

The global carbon budget over the historical period (1850-2021) is shown in Figure 3.

Emissions during the period 1850-2021 amounted to  $670 \pm 65 \text{ GtC}$  and were partitioned among the atmosphere ( $275 \pm 5 \text{ GtC}$ ; 41%), ocean ( $175 \pm 35 \text{ GtC}$ ; 26%), and the land ( $210 \pm 45 \text{ GtC}$ ; 31%). The cumulative land sink is almost equal to the cumulative land-use emissions ( $200 \pm 60 \text{ GtC}$ ), making the global land nearly neutral over the whole 1850-2021 period.

The use of nearly independent estimates for the individual terms of the global carbon budget shows a cumulative budget imbalance of 15 GtC (2% of total emissions) during 1850-2021 (Figure 3, Table 8), which, if correct, suggests that emissions could be slightly too high by the same proportion (2%) or that the combined land and ocean sinks are slightly underestimated (by about 3%), although these are well within the uncertainty range of each component of the budget. Nevertheless, part of the imbalance could originate from the estimation of significant increase in  $E_{FOS}$  and  $E_{LUC}$  between the mid 1920s and the mid 1960s which is unmatched by a similar growth in atmospheric  $CO_2$  concentration as recorded in ice cores (Figure 3). However, the known loss of additional sink capacity of 30-40 GtC (over the 1850-2020 period) due to reduced forest cover has not been accounted for in our method and would exacerbate the budget imbalance (see Appendix D.4) .

For the more recent 1960-2021 period where direct atmospheric  $CO_2$  measurements are available, total emissions ( $E_{FOS} + E_{LUC}$ ) amounted to  $470 \pm 50$  GtC, of which  $385 \pm 20$  GtC (82%) were caused by fossil  $CO_2$  emissions, and  $85 \pm 45$  GtC (18%) by land-use change (Table 8). The total emissions were partitioned among the atmosphere ( $210 \pm 5$  GtC; 45%), ocean ( $120 \pm 25$  GtC; 26%), and the land ( $145 \pm 30$  GtC; 30%), with a near zero ( $-5$  GtC) unattributed budget imbalance. All components except land-use change emissions have significantly grown since 1960, with important interannual variability in the growth rate in atmospheric  $CO_2$  concentration and in the land  $CO_2$  sink (Figure 4), and some decadal variability in all terms (Table 6). Differences with previous budget releases are documented in Figure B5.

The global carbon budget averaged over the last decade (2012-2021) is shown in Figure 2, Figure 14 (right panel) and Table 6. For this period, 89% of the total emissions ( $E_{FOS} + E_{LUC}$ ) were from fossil  $CO_2$  emissions ( $E_{FOS}$ ), and 11% from land-use change ( $E_{LUC}$ ). The total emissions were partitioned among the atmosphere (48%), ocean (26%) and land (29%), with a near-zero unattributed budget imbalance ( $\sim 3\%$ ). For single years, the budget imbalance can be larger (Figure 4). For 2021, the combination of our estimated sources ( $10.9 \pm 0.9$  GtC  $yr^{-1}$ ) and sinks ( $11.6 \pm 1.0$  GtC  $yr^{-1}$ ) leads to a  $B_{IM}$  of  $-0.6$  GtC, suggesting a slight underestimation of the anthropogenic sources, and/or an overestimation of the combined land and ocean sinks

### **3.8.2 Carbon Budget Imbalance trend and variability**

The carbon budget imbalance ( $B_{IM}$ ; Eq. 1, Figure 4) quantifies the mismatch between the estimated total emissions and the estimated changes in the atmosphere, land, and ocean reservoirs. The mean budget imbalance from 1960 to 2021 is very small (4.6 GtC over the period, i.e. average of  $0.07$  GtC  $yr^{-1}$ ) and shows no trend over the full time series (Figure 4). The process models (GOBMs and DGVMs) and data-products have been selected to match observational constraints in the 1990s, but no further constraints have been applied to their representation of trend and variability. Therefore, the near-zero mean and trend in the budget imbalance is seen as evidence of a coherent community understanding of the emissions and their partitioning on those time scales (Figure 4). However, the budget imbalance shows substantial variability of the order of  $\pm 1$  GtC  $yr^{-1}$ , particularly over semi-decadal time scales, although most of the variability is within the uncertainty of the estimates. The positive carbon imbalance during the 1960s, and early 1990s, indicates that either the emissions were overestimated, or the sinks were underestimated during these periods. The reverse is true for the 1970s, and to a lower extent for the 1980s and 2012-2021 period (Figure 4, Table 6).

We cannot attribute the cause of the variability in the budget imbalance with our analysis, we only note that the budget imbalance is unlikely to be explained by errors or biases in the emissions alone because of its large semi-decadal variability component, a variability that is untypical of emissions and has not changed in the past 60 years despite a near tripling in emissions (Figure 4). Errors in  $S_{\text{LAND}}$  and  $S_{\text{OCEAN}}$  are more likely to be the main cause for the budget imbalance, especially on interannual to semi-decadal timescales. For example, underestimation of the  $S_{\text{LAND}}$  by DGVMs has been reported following the eruption of Mount Pinatubo in 1991 possibly due to missing responses to changes in diffuse radiation (Mercado et al., 2009). Although since GCB2021 we accounted for aerosol effects on solar radiation quantity and quality (diffuse vs direct), most DGVMs only used the former as input (i.e., total solar radiation) (Table A1). Thus, the ensemble mean may not capture the full effects of volcanic eruptions, i.e. associated with high light scattering sulphate aerosols, on the land carbon sink (O’Sullivan et al., 2021). DGVMs are suspected to overestimate the land sink in response to the wet decade of the 1970s (Sitch et al., 2008). Quasi-decadal variability in the ocean sink has also been reported, with all methods agreeing on a smaller than expected ocean  $\text{CO}_2$  sink in the 1990s and a larger than expected sink in the 2000s (Figure 10; Landschützer et al., 2016, DeVries et al., 2019, Hauck et al., 2020, McKinley et al., 2020). Errors in sink estimates could also be driven by errors in the climatic forcing data, particularly precipitation for  $S_{\text{LAND}}$  and wind for  $S_{\text{OCEAN}}$ . Also, the  $B_{\text{IM}}$  shows substantial departure from zero on yearly time scales (Figure 4e), highlighting unresolved variability of the carbon cycle, likely in the land sink ( $S_{\text{LAND}}$ ), given its large year to year variability (Figure 4d and 8).

Both the budget imbalance ( $B_{\text{IM}}$ , Table 6) and the residual land sink from the global budget ( $E_{\text{FOS}} + E_{\text{LUC}} - G_{\text{ATM}} - S_{\text{OCEAN}}$ , Table 5) include an error term due to the inconsistencies that arises from using  $E_{\text{LUC}}$  from bookkeeping models, and  $S_{\text{LAND}}$  from DGVMs, most notably the loss of additional sink capacity (see section 2.7 and Appendix D.4). Other differences include a better accounting of land use changes practices and processes in bookkeeping models than in DGVMs, or the bookkeeping models error of having present-day observed carbon densities fixed in the past. That the budget imbalance shows no clear trend towards larger values over time is an indication that these inconsistencies probably play a minor role compared to other errors in  $S_{\text{LAND}}$  or  $S_{\text{OCEAN}}$ . Although the budget imbalance is near zero for the recent decades, it could be due to compensation of errors. We cannot exclude an overestimation of  $\text{CO}_2$  emissions, particularly from land-use change, given their large uncertainty, as has been suggested elsewhere (Piao et al., 2018), combined with an underestimate of the sinks. A larger DGVM ( $S_{\text{LAND}} - E_{\text{LUC}}$ ) over the extra-tropics would reconcile model results with inversion estimates for fluxes in the total land during the past decade (Figure 13; Table 5). Likewise, a larger  $S_{\text{OCEAN}}$  is also possible given the higher estimates from the data-products (see section 3.1.2, Figure 10 and Figure 13), the underestimation of interior ocean anthropogenic carbon accumulation in the GOBMs (section 3.5.5), and the recently suggested upward adjustments of the ocean carbon sink in Earth System Models (Terhaar et al., 2022), and in data-products, here related to a potential temperature bias and skin effects (Watson et al., 2020, Dong et al., 2022, Figure 10). If  $S_{\text{OCEAN}}$  were to be based on data-products alone, with all data-products including this adjustment, this would result in a 2012-2021  $S_{\text{OCEAN}}$  of  $3.8 \text{ GtC yr}^{-1}$  (Dong et al., 2022) or  $>4 \text{ GtC yr}^{-1}$  (Watson et al., 2020), i.e., outside of the range supported by the atmospheric inversions and with an implied negative  $B_{\text{IM}}$  of more than  $-1 \text{ GtC yr}^{-1}$  indicating that a closure of the budget could only be achieved with either anthropogenic emissions being significantly larger and/or the net land sink being substantially smaller than estimated here.

More integrated use of observations in the Global Carbon Budget, either on their own or for further constraining model results, should help resolve some of the budget imbalance (Peters et al., 2017).

#### **4 Tracking progress towards mitigation targets**

The average growth in global fossil CO<sub>2</sub> emissions peaked at +3% per year during the 2000s, driven by the rapid growth in emissions in China. In the last decade, however, the global growth rate has slowly declined, reaching a low +0.5% per year over 2012-2021 (including the 2020 global decline and the 2021 emissions rebound).

While this slowdown in global fossil CO<sub>2</sub> emissions growth is welcome, it is far from the emission decrease needed to be consistent with the temperature goals of the Paris Agreement.

Since the 1990s, the average growth rate of fossil CO<sub>2</sub> emissions has continuously declined across the group of developed countries of the Organisation for Economic Co-operation and Development (OECD), with emissions peaking in around 2005 and now declining at around 1% yr<sup>-1</sup> (Le Quéré et al., 2021). In the decade 2012-2021, territorial fossil CO<sub>2</sub> emissions decreased significantly (at the 95% confidence level) in 24 countries whose economies grew significantly (also at the 95% confidence level): Belgium, Croatia, Czech Republic, Denmark, Estonia, Finland, France, Germany, Hong Kong, Israel, Italy, Japan, Luxembourg, Malta, Mexico, Netherlands, Norway, Singapore, Slovenia, Sweden, Switzerland, United Kingdom, USA, and Uruguay (updated from Le Quéré et al., 2019). Altogether, these 24 countries emitted 2.4 GtC yr<sup>-1</sup> (8.8 GtCO<sub>2</sub> yr<sup>-1</sup>) on average over the last decade, about one quarter of world CO<sub>2</sub> fossil emissions. Consumption-based emissions also fell significantly during the final decade for which estimates are available (2011-2020) in 15 of these countries: Belgium, Denmark, Estonia, Finland, France, Germany, Hong Kong, Israel, Japan, Luxembourg, Mexico, Netherlands, Singapore, Sweden, United Kingdom, and Uruguay. Figure 15 shows that the emission declines in the USA and the EU27 are primarily driven by increased decarbonisation (CO<sub>2</sub> emissions per unit energy) in the last decade compared to the previous, with smaller contributions in the EU27 from slightly weaker economic growth and slightly larger declines in energy per GDP. These countries have stable or declining energy use and so decarbonisation policies replace existing fossil fuel infrastructure (Le Quéré et al. 2019).

In contrast, fossil CO<sub>2</sub> emissions continue to grow in non-OECD countries, although the growth rate has slowed from almost 6% yr<sup>-1</sup> during the 2000s to less than 2% yr<sup>-1</sup> in the last decade. Representing 47% of non-OECD emissions in 2021, a large part of this slowdown is due to China, which has seen emissions growth decline from nearly 10% yr<sup>-1</sup> in the 2000s to 1.5% yr<sup>-1</sup> in the last decade. Excluding China, non-OECD emissions grew at 3.3% yr<sup>-1</sup> in the 2000s compared to 1.6% yr<sup>-1</sup> in the last decade. Figure 15 shows that, compared to the previous decade, China has had weaker economic growth in the last decade and a higher decarbonisation rate, with more rapid declines in energy per GDP that are now back to levels seen during the 1990s. India and the rest of the world have strong economic growth that is not offset by decarbonisation or declines in energy per GDP, driving up fossil CO<sub>2</sub> emissions. Despite the high deployment of renewables in some countries (e.g., India), fossil energy sources continue to grow to meet growing energy demand (Le Quéré et al. 2019).

Globally, fossil CO<sub>2</sub> emissions growth is slowing, and this is due to the emergence of climate policy (Eskander and Fankhauser 2020; Le Quere et al 2019) and technological change, which is leading to a shift from coal to gas and growth in renewable energies, and reduced expansion of coal capacity. At the aggregated global level,



decarbonisation shows a strong and growing signal in the last decade, with smaller contributions from lower economic growth and declines in energy per GDP. Despite the slowing growth in global fossil CO<sub>2</sub> emissions, emissions are still growing, far from the reductions needed to meet the ambitious climate goals of the UNFCCC Paris agreement.

We update the remaining carbon budget assessed by the IPCC AR6 (Canadell et al., 2021), accounting for the 2020 to 2022 estimated emissions from fossil fuel combustion ( $E_{FOS}$ ) and land use changes ( $E_{LUC}$ ). From January 2023, the remaining carbon (50% likelihood) for limiting global warming to 1.5°C, 1.7°C and 2°C is estimated to amount to 105, 200, and 335 GtC (380, 730, 1230 GtCO<sub>2</sub>). These numbers include an uncertainty based on model spread (as in IPCC AR6), which is reflected through the percent likelihood of exceeding the given temperature threshold. These remaining amounts correspond respectively to about 9, 18 and 30 years from the beginning of 2023, at the 2022 level of total CO<sub>2</sub> emissions. Reaching net zero CO<sub>2</sub> emissions by 2050 entails cutting total anthropogenic CO<sub>2</sub> emissions by about 0.4 GtC (1.4 GtCO<sub>2</sub>) each year on average, comparable to the decrease observed in 2020 during the COVID-19 pandemic.

## **5 Discussion**

Each year when the global carbon budget is published, each flux component is updated for all previous years to consider corrections that are the result of further scrutiny and verification of the underlying data in the primary input data sets. Annual estimates may be updated with improvements in data quality and timeliness (e.g., to eliminate the need for extrapolation of forcing data such as land-use). Of all terms in the global budget, only the fossil CO<sub>2</sub> emissions and the growth rate in atmospheric CO<sub>2</sub> concentration are based primarily on empirical inputs supporting annual estimates in this carbon budget. The carbon budget imbalance, yet an imperfect measure, provides a strong indication of the limitations in observations in understanding and representing processes in models, and/or in the integration of the carbon budget components.

The persistent unexplained variability in the carbon budget imbalance limits our ability to verify reported emissions (Peters et al., 2017) and suggests we do not yet have a complete understanding of the underlying carbon cycle dynamics on annual to decadal timescales. Resolving most of this unexplained variability should be possible through different and complementary approaches. First, as intended with our annual updates, the imbalance as an error term is reduced by improvements of individual components of the global carbon budget that follow from improving the underlying data and statistics and by improving the models through the resolution of some of the key uncertainties detailed in Table 10. Second, additional clues to the origin and processes responsible for the variability in the budget imbalance could be obtained through a closer scrutiny of carbon variability in light of other Earth system data (e.g., heat balance, water balance), and the use of a wider range of biogeochemical observations to better understand the land-ocean partitioning of the carbon imbalance (e.g. oxygen, carbon isotopes). Finally, additional information could also be obtained through higher resolution and process knowledge at the regional level, and through the introduction of inferred fluxes such as those based on satellite CO<sub>2</sub> retrievals. The limit of the resolution of the carbon budget imbalance is yet unclear, but most certainly not yet reached given the possibilities for improvements that lie ahead.

Estimates of global fossil CO<sub>2</sub> emissions from different datasets are in relatively good agreement when the different system boundaries of these datasets are considered (Andrew, 2020a). But while estimates of E<sub>FOS</sub> are derived from reported activity data requiring much fewer complex transformations than some other components of the budget, uncertainties remain, and one reason for the apparently low variation between datasets is precisely the reliance on the same underlying reported energy data. The budget excludes some sources of fossil CO<sub>2</sub> emissions, which available evidence suggests are relatively small (<1%). We have added emissions from lime production in China and the US, but these are still absent in most other non-Annex I countries, and before 1990 in other Annex I countries.

Estimates of E<sub>LUC</sub> suffer from a range of intertwined issues, including the poor quality of historical land-cover and land-use change maps, the rudimentary representation of management processes in most models, and the confusion in methodologies and boundary conditions used across methods (e.g., Arneeth et al., 2017; Pongratz et al., 2014, see also Appendix D.4 on the loss of sink capacity; Bastos et al., 2021). Uncertainties in current and historical carbon stocks in soils and vegetation also add uncertainty in the E<sub>LUC</sub> estimates. Unless a major effort to resolve these issues is made, little progress is expected in the resolution of E<sub>LUC</sub>. This is particularly concerning given the growing importance of E<sub>LUC</sub> for climate mitigation strategies, and the large issues in the quantification of the cumulative emissions over the historical period that arise from large uncertainties in E<sub>LUC</sub>.

By adding the DGVMs estimates of CO<sub>2</sub> fluxes due to environmental change from countries' managed forest areas (part of S<sub>LAND</sub> in this budget) to the budget E<sub>LUC</sub> estimate, we successfully reconciled the large gap between our E<sub>LUC</sub> estimate and the land use flux from NGHGs using the approach described in Grassi et al. (2021) for future scenario and in Grassi et al. (2022b) using data from the Global Carbon Budget 2021. The updated data presented here can be used as potential adjustment in the policy context, e.g., to help assessing the collective countries' progress towards the goal of the Paris Agreement and avoiding double-accounting for the sink in managed forests. In the absence of this adjustment, collective progress would hence appear better than it is (Grassi et al. 2021). The need of such adjustment whenever a comparison between LULUCF fluxes reported by countries and the global emission estimates of the IPCC is attempted is recommended also in the recent UNFCCC Synthesis report for the first Global Stocktake (UNFCCC, 2022). However, this adjustment should be seen as a short-term and pragmatic fix based on existing data, rather than a definitive solution to bridge the differences between global models and national inventories. Additional steps are needed to understand and reconcile the remaining differences, some of which are relevant at the country level (Grassi, et al. 2022b, Schwingshackl, et al., subm.).

The comparison of GOBMs, data products and inversions highlights substantial discrepancy in the Southern Ocean (Figure 13, Hauck et al., 2020). A large part of the uncertainty in the mean fluxes stems from the regional distribution of the river flux adjustment term. The current distribution (Aumont et al., 2001) is based on one model study yielding the largest riverine outgassing flux south of 20°S, whereas a recent study, also based on one model, simulates the largest share of the outgassing to occur in the tropics (Lacroix et al., 2020). The long-standing sparse data coverage of fCO<sub>2</sub> observations in the Southern compared to the Northern Hemisphere (e.g., Takahashi et al., 2009) continues to exist (Bakker et al., 2016, 2022, Figure B1) and to lead to substantially higher uncertainty in the S<sub>OCEAN</sub> estimate for the Southern Hemisphere (Watson et al., 2020, Gloege et al., 2021). This discrepancy, which also hampers model improvement, points to the need for increased high-quality

fCO<sub>2</sub> observations especially in the Southern Ocean. At the same time, model uncertainty is illustrated by the large spread of individual GOBM estimates (indicated by shading in Figure 13) and highlights the need for model improvement. The diverging trends in S<sub>ocean</sub> from different methods is a matter of concern, which is unresolved. The assessment of the net land-atmosphere exchange from DGVMs and atmospheric inversions also shows substantial discrepancy, particularly for the estimate of the total land flux over the northern extra-tropic. This discrepancy highlights the difficulty to quantify complex processes (CO<sub>2</sub> fertilisation, nitrogen deposition and fertilisers, climate change and variability, land management, etc.) that collectively determine the net land CO<sub>2</sub> flux. Resolving the differences in the Northern Hemisphere land sink will require the consideration and inclusion of larger volumes of observations.

We provide metrics for the evaluation of the ocean and land models and the atmospheric inversions (Figs. B2 to B4). These metrics expand the use of observations in the global carbon budget, helping 1) to support improvements in the ocean and land carbon models that produce the sink estimates, and 2) to constrain the representation of key underlying processes in the models and to allocate the regional partitioning of the CO<sub>2</sub> fluxes. However, GOBMs skills have changed little since the introduction of the ocean model evaluation. The additional simulation allows for direct comparison with interior ocean anthropogenic carbon estimates and suggests that the models underestimate anthropogenic carbon uptake and storage. This is an initial step towards the introduction of a broader range of observations that we hope will support continued improvements in the annual estimates of the global carbon budget.

We assessed before that a sustained decrease of –1% in global emissions could be detected at the 66% likelihood level after a decade only (Peters et al., 2017). Similarly, a change in behaviour of the land and/or ocean carbon sink would take as long to detect, and much longer if it emerges more slowly. To continue reducing the carbon imbalance on annual to decadal time scales, regionalising the carbon budget, and integrating multiple variables are powerful ways to shorten the detection limit and ensure the research community can rapidly identify issues of concern in the evolution of the global carbon cycle under the current rapid and unprecedented changing environmental conditions.

## 6 Conclusions

The estimation of global CO<sub>2</sub> emissions and sinks is a major effort by the carbon cycle research community that requires a careful compilation and synthesis of measurements, statistical estimates, and model results. The delivery of an annual carbon budget serves two purposes. First, there is a large demand for up-to-date information on the state of the anthropogenic perturbation of the climate system and its underpinning causes. A broad stakeholder community relies on the data sets associated with the annual carbon budget including scientists, policy makers, businesses, journalists, and non-governmental organisations engaged in adapting to and mitigating human-driven climate change. Second, over the last decades we have seen unprecedented changes in the human and biophysical environments (e.g., changes in the growth of fossil fuel emissions, impact of COVID-19 pandemic, Earth's warming, and strength of the carbon sinks), which call for frequent assessments of the state of the planet, a better quantification of the causes of changes in the contemporary global carbon cycle, and an improved capacity to anticipate its evolution in the future. Building this scientific

1468 understanding to meet the extraordinary climate mitigation challenge requires frequent, robust, transparent, and  
1469 traceable data sets and methods that can be scrutinised and replicated. This paper via ‘living data’ helps to keep  
1470 track of new budget updates.

1471

## 1472 7 Data availability

1473 The data presented here are made available in the belief that their wide dissemination will lead to greater  
1474 understanding and new scientific insights of how the carbon cycle works, how humans are altering it, and how  
1475 we can mitigate the resulting human-driven climate change. Full contact details and information on how to cite  
1476 the data shown here are given at the top of each page in the accompanying database and summarised in Table 2.

1477 The accompanying database includes three Excel files organised in the following spreadsheets:

1478 File [Global\\_Carbon\\_Budget\\_2022v0.1.xlsx](#) includes the following:

- 1479 1. Summary
- 1480 2. The global carbon budget (1959-2021);
- 1481 3. The historical global carbon budget (1750-2021);
- 1482 4. Global CO<sub>2</sub> emissions from fossil fuels and cement production by fuel type, and the per-capita emissions  
1483 (1850-2021);
- 1484 5. CO<sub>2</sub> emissions from land-use change from the individual bookkeeping models (1959-2021);
- 1485 6. Ocean CO<sub>2</sub> sink from the individual ocean models and fCO<sub>2</sub>-based products (1959-2021);
- 1486 7. Terrestrial CO<sub>2</sub> sink from the individual DGVMs (1959-2021);
- 1487 8. Cement carbonation CO<sub>2</sub> sink (1959-2021).

1488 File [National\\_Fossil\\_Carbon\\_Emissions\\_2022v0.1.xlsx](#) includes the following:

- 1489 1. Summary
- 1490 2. Territorial country CO<sub>2</sub> emissions from fossil fuels and cement production (1850-2021);
- 1491 3. Consumption country CO<sub>2</sub> emissions from fossil fuels and cement production and emissions transfer from  
1492 the international trade of goods and services (1990-2020) using CDIAC/UNFCCC data as reference;
- 1493 4. Emissions transfers (Consumption minus territorial emissions; 1990-2020);
- 1494 5. Country definitions.

1495 File [National\\_LandUseChange\\_Carbon\\_Emissions\\_2022v0.1.xlsx](#) includes the following:

- 1496 1. Summary
- 1497 2. Territorial country CO<sub>2</sub> emissions from Land Use Change (1850-2021) from three bookkeeping models;

1498

All three spreadsheets are published by the Integrated Carbon Observation System (ICOS) Carbon Portal and are available at <https://doi.org/10.18160/GCP-2022> (Friedlingstein et al., 2022b). National emissions data are also available from the Global Carbon Atlas (<http://www.globalcarbonatlas.org/>, last access: 25 September 2022) and from Our World in Data (<https://ourworldindata.org/co2-emissions>, last access: 25 September 2022).

## 8 Author contributions

PF, MOS, MWJ, RMA, LGr, JH, CLQ, ITL, AO, GPP, WP, JP, CIS, and SS designed the study, conducted the analysis, and wrote the paper with input from JGC, PC and RBJ. RMA, GPP and JIK produced the fossil fuel emissions and their uncertainties and analysed the emissions data. MH and GM provided fossil fuel emission data. JP, TGa, CIS and RAH provided the bookkeeping land-use change emissions with synthesis by JP and CIS. JH, LB, ÖG, NG, TI, KL, NMa, LR, JS, RS, HiT, and ReW provided an update of the global ocean biogeochemical models, MG, LGl, LGr, YI, AJ, ChR, JDS, and JZ provided an update of the ocean fCO<sub>2</sub> data products, with synthesis on both streams by JH, LGr and NMa. SRA, NRB, MB, HCB, MC, WE, RAF, TGk, KK, NL, NMe, NMM, DRM, SN, TO, DP, KP, ChR, IS, TS, AJS, CoS, ST, TT, BT, RiW, CW, AW provided ocean fCO<sub>2</sub> measurements for the year 2021, with synthesis by AO and KO. AA, VKA, SF, AKJ, EK, DK, JK, MJM, MOS, BP, QS, HaT, APW, WY, XY, and SZ provided an update of the Dynamic Global Vegetation Models, with synthesis by SS and MOS. WP, ITL, FC, JL, YN, PIP, ChR, XT, and BZ provided an updated atmospheric inversion, WP, FC, and ITL developed the protocol and produced the evaluation. RMA provided predictions of the 2022 emissions and atmospheric CO<sub>2</sub> growth rate. PL provided the predictions of the 2022 ocean and land sinks. LPC, GCH, KKG, TMR and GRvdW provided forcing data for land-use change. RA, GG, FT, and CY provided data for the land-use change NGHGI mapping. PPT provided key atmospheric CO<sub>2</sub> data. MWJ produced the model atmospheric CO<sub>2</sub> forcing and the atmospheric CO<sub>2</sub> growth rate. MOS and NB produced the aerosol diffuse radiative forcing for the DGVMs. IH provided the climate forcing data for the DGVMs. ER provided the evaluation of the DGVMs. MWJ provided the emissions prior for use in the inversion systems. ZL provided seasonal emissions data for most recent years for the emission prior. MWJ and MOS developed the new data management pipeline which automates many aspects of the data collation, analysis, plotting and synthesis. PF, MOS and MMJ coordinated the effort, revised all figures, tables, text and/or numbers to ensure the update was clear from the 2021 edition and in line with the [globalcarbonatlas.org](http://www.globalcarbonatlas.org).

**Competing interests.** The authors declare that they have no conflict of interest.

## 9 Acknowledgements

We thank all people and institutions who provided the data used in this global carbon budget 2022 and the Global Carbon Project members for their input throughout the development of this publication. We thank Nigel Hawtin for producing Figure 2 and Figure 14. We thank Thomas Hawes for technical support with the data management pipeline. We thank Ed Dlugokencky for providing atmospheric CO<sub>2</sub> measurements. We thank Ian G. C. Ashton, Fatemeh Cheginig, Trang T. Chau, Sam Ditkovsky, Christian Ethé, Amanda R. Fay, Lonneke Goddijn-Murphy, T. Holding, Fabrice Lacroix, Enhui Liao, Galen A. McKinley, Shijie Shu, Richard Sims, Jade Skye, Andrew J. Watson, David Willis, and David K. Woolf for their involvement in the development, use and analysis of the models and data-products used here. Daniel Kennedy thanks all the scientists, software engineers, and administrators who contributed to the development of CESM2. We thank Joe Salisbury, Doug Vandemark, Christopher W. Hunt, and Peter Landschützer who contributed to the provision of surface ocean CO<sub>2</sub> observations for the year 2021 (see Table A5). We also thank Benjamin Pfeil, Rocío Castaño-Primo, and Stephen D. Jones of the Ocean Thematic Centre of the EU Integrated Carbon Observation System (ICOS) Research Infrastructure, Eugene Burger of NOAA's Pacific Marine Environmental Laboratory and Alex Kozyr of NOAA's National Centers for Environmental Information, for their contribution to surface ocean CO<sub>2</sub> data and metadata management. This is PMEL contribution 5434. We thank the scientists, institutions, and funding agencies responsible for the collection and quality control of the data in SOCAT as well as the International Ocean Carbon Coordination Project (IOCCP), the Surface Ocean Lower Atmosphere Study (SOLAS) and the Integrated Marine Biosphere Research (IMBeR) program for their support. We thank data providers ObsPack GLOBALVIEWplus v7.0 and NRT v7.2 for atmospheric CO<sub>2</sub> observations. We thank the individuals and institutions that provided the databases used for the model evaluations used here. We thank Fortunat Joos, Samar Khatiwala and Timothy DeVries for providing historical data. Matthew J. McGrath thanks the whole ORCHIDEE group. Ian Harris thanks the Japan Meteorological Agency (JMA) for producing the Japanese 55-year Reanalysis (JRA-55). Anthony P. Walker thanks ORNL which is managed by UT-Battelle, LLC, for the DOE under contract DE-AC05-1008 00OR22725. Yosuke Niwa thanks CSIRO, EC, EMPA, FMI, IPEN, JMA, LSCE, NCAR, NIES, NILU, NIWA, NOAA, SIO, and TU/NIPR for providing data for NISMON-CO<sub>2</sub>. Xiangjun Tian thanks Zhe Jin, Yilong Wang, Tao Wang and Shilong Piao for their contributions to the GONGGA inversion system. Bo Zheng thanks the comments and suggestions from Philippe Ciais and Frédéric Chevallier. Frédéric Chevallier thanks Marine Remaud who maintained the atmospheric transport model for the CAMS inversion. Paul I. Palmer thanks Liang Feng and acknowledges ongoing support from the National Centre for Earth Observation. Junjie Liu thanks the

Jet Propulsion Laboratory, California Institute of Technology. Wiley Evans thanks the Tula Foundation for funding support. Australian ocean CO<sub>2</sub> data were sourced from Australia's Integrated Marine Observing System (IMOS); IMOS is enabled by the National Collaborative Research Infrastructure Strategy (NCRIS). Margot Cronin thanks Anthony English, Clynt Gregory and Gordon Furey (P&O Maritime Services) for their support. Nathalie Lefèvre thanks the crew of the Cap San Lorenzo and the US IMAGO of IRD Brest for technical support. Henry C. Bittig is grateful for the skillful technical support of M. Glockzin and B. Sadkowiak. Meike Becker and Are Olsen thank Sparebanken Vest/Agenda Vestlandet for their support for the observations on the Statsraad Lehmkuhl. Thanos Gkritzalis thanks the personnel and crew of Simon Stevin. Matthew W. Jones thanks Anthony J. De-Gol for his technical and conceptual assistance with the development of GCP-GridFED. FAOSTAT is funded by FAO member states through their contributions to the FAO Regular Programme, data contributions by national experts are greatly acknowledged. The views expressed in this paper are the authors' only and do not necessarily reflect those of FAO. Finally, we thank all funders who have supported the individual and joint contributions to this work (see Table A9), as well as the reviewers of this manuscript and previous versions, and the many researchers who have provided feedback.

## References

- Ahlström, A., Raupach, M. R., Schurgers, G., Smith, B., Arneeth, A., Jung, M., Reichstein, M., Canadell, J. G., Friedlingstein, P., Jain, A. K., Kato, E., Poulter, B., Sitch, S., Stocker, B. D., Viovy, N., Wang, Y. P., Wiltshire, A., Zaehle, S., and Zeng, N.: The dominant role of semi-arid ecosystems in the trend and variability of the land CO<sub>2</sub> sink, 348, 895–899, <https://doi.org/10.1126/science.aaa1668>, 2015.
- Amador-Jiménez, M., Millner, N., Palmer, C., Pennington, R. T., and Sileci, L.: The Unintended Impact of Colombia's Covid-19 Lockdown on Forest Fires, *Environ Resource Econ*, 76, 1081–1105, <https://doi.org/10.1007/s10640-020-00501-5>, 2020.
- Amante, C. and Eakins, B. W.: ETOPO1 Global Relief Model converted to PanMap layer format, <https://doi.org/10.1594/PANGAEA.769615>, 2009.
- Andela, N., Morton, D. C., Giglio, L., Chen, Y., van der Werf, G. R., Kasibhatla, P. S., DeFries, R. S., Collatz, G. J., Hantson, S., Kloster, S., Bachelet, D., Forrest, M., Lasslop, G., Li, F., Mangeon, S., Melton, J. R., Yue, C., and Randerson, J. T.: A human-driven decline in global burned area, *Science*, 356, 1356–1362, <https://doi.org/10.1126/science.aal4108>, 2017.
- Andres, R. J., Boden, T. A., Bréon, F.-M., Ciais, P., Davis, S., Erickson, D., Gregg, J. S., Jacobson, A., Marland, G., Miller, J., Oda, T., Olivier, J. G. J., Raupach, M. R., Rayner, P., and Treanton, K.: A synthesis of carbon dioxide emissions from fossil-fuel combustion, *Biogeosciences*, 9, 1845–1871, <https://doi.org/10.5194/bg-9->

1592 1845-2012, 2012.

1593 Andres, R. J., Boden, T. A., and Higdon, D.: A new evaluation of the uncertainty associated with CDIAC  
 1594 estimates of fossil fuel carbon dioxide emission, *Tellus B: Chemical and Physical Meteorology*, 66, 23616,  
 1595 <https://doi.org/10.3402/tellusb.v66.23616>, 2014.

1596 Andrew, R. M.: A comparison of estimates of global carbon dioxide emissions from fossil carbon sources, *Earth*  
 1597 *Syst. Sci. Data*, 12, 1437–1465, <https://doi.org/10.5194/essd-12-1437-2020>, 2020a.

1598 Andrew, R. M.: Timely estimates of India’s annual and monthly fossil CO<sub>2</sub> emissions, *Earth Syst. Sci. Data*, 12,  
 1599 2411–2421, <https://doi.org/10.5194/essd-12-2411-2020>, 2020b.

1600 Andrew, R. M.: Towards near real-time, monthly fossil CO<sub>2</sub> emissions estimates for the European Union with  
 1601 current-year projections, *Atmospheric Pollution Research*, 101229, <https://doi.org/10.1016/j.apr.2021.101229>,  
 1602 2021.

1603 Andrew, R. M. and Peters, G. P.: A multi-region input–output table based on the global trade analysis project  
 1604 database (GTAP-MRIO), *Economic Systems Research*, 25, 99–121,  
 1605 <https://doi.org/10.1080/09535314.2012.761953>, 2013.

1606 Andrew, R. M. and Peters, G. P.: The Global Carbon Project’s fossil CO<sub>2</sub> emissions dataset (2021v34),  
 1607 <https://doi.org/10.5281/ZENODO.5569235>, 2021.

1608 Angelsen, A. and Kaimowitz, D.: Rethinking the Causes of Deforestation: Lessons from Economic Models,  
 1609 *World Bank Res. Obs.*, 14, 73–98, <https://doi.org/10.1093/wbro/14.1.73>, 1999.

1610 Aragão, L. E. O. C., Anderson, L. O., Fonseca, M. G., Rosan, T. M., Vedovato, L. B., Wagner, F. H., Silva, C.  
 1611 V. J., Silva Junior, C. H. L., Arai, E., Aguiar, A. P., Barlow, J., Berenguer, E., Deeter, M. N., Domingues, L. G.,  
 1612 Gatti, L., Gloor, M., Malhi, Y., Marengo, J. A., Miller, J. B., Phillips, O. L., and Saatchi, S.: 21st Century  
 1613 drought-related fires counteract the decline of Amazon deforestation carbon emissions, *Nat Commun*, 9, 536,  
 1614 <https://doi.org/10.1038/s41467-017-02771-y>, 2018.

1615 Archer, D., Eby, M., Brovkin, V., Ridgwell, A., Cao, L., Mikolajewicz, U., Caldeira, K., Matsumoto, K.,  
 1616 Munhoven, G., Montenegro, A., and Tokos, K.: Atmospheric Lifetime of Fossil Fuel Carbon Dioxide, *Annu.*  
 1617 *Rev. Earth Planet. Sci.*, 37, 117–134, <https://doi.org/10.1146/annurev.earth.031208.100206>, 2009.

1618 Arneth, A., Sitch, S., Pongratz, J., Stocker, B. D., Ciais, P., Poulter, B., Bayer, A. D., Bondeau, A., Calle, L.,  
 1619 Chini, L. P., Gasser, T., Fader, M., Friedlingstein, P., Kato, E., Li, W., Lindeskog, M., Nabel, J. E. M. S., Pugh,  
 1620 T. A. M., Robertson, E., Viovy, N., Yue, C., and Zaehle, S.: Historical carbon dioxide emissions caused by  
 1621 land-use changes are possibly larger than assumed, *Nature Geosci*, 10, 79–84, <https://doi.org/10.1038/ngeo2882>,  
 1622 2017.

1623 Arora, V. K., Boer, G. J., Christian, J. R., Curry, C. L., Denman, K. L., Zahariev, K., Flato, G. M., Scinocca, J.  
 1624 F., Merryfield, W. J., and Lee, W. G.: The Effect of Terrestrial Photosynthesis Down Regulation on the  
 1625 Twentieth-Century Carbon Budget Simulated with the CCCma Earth System Model, 22, 6066–6088,



1626 <https://doi.org/10.1175/2009JCLI3037.1>, 2009.

1627 Asaadi, A., Arora, V. K., Melton, J. R., and Bartlett, P.: An improved parameterization of leaf area index (LAI)  
 1628 seasonality in the Canadian Land Surface Scheme (CLASS) and Canadian Terrestrial Ecosystem Model  
 1629 (CTEM) modelling framework, 15, 6885–6907, <https://doi.org/10.5194/bg-15-6885-2018>, 2018.

1630 Aumont, O., Orr, J. C., Monfray, P., Ludwig, W., Amiotte-Suchet, P., and Probst, J.-L.: Riverine-driven  
 1631 interhemispheric transport of carbon, *Global Biogeochem. Cycles*, 15, 393–405,  
 1632 <https://doi.org/10.1029/1999GB001238>, 2001.

1633 Aumont, O., Ethé, C., Tagliabue, A., Bopp, L., and Gehlen, M.: PISCES-v2: an ocean biogeochemical model  
 1634 for carbon and ecosystem studies, 8, 2465–2513, <https://doi.org/10.5194/gmd-8-2465-2015>, 2015.

1635 Avitabile, V., Herold, M., Heuvelink, G. B. M., Lewis, S. L., Phillips, O. L., Asner, G. P., Armston, J., Ashton,  
 1636 P. S., Banin, L., Bayol, N., Berry, N. J., Boeckx, P., de Jong, B. H. J., DeVries, B., Girardin, C. A. J., Kearsley,  
 1637 E., Lindsell, J. A., Lopez-Gonzalez, G., Lucas, R., Malhi, Y., Morel, A., Mitchard, E. T. A., Nagy, L., Qie, L.,  
 1638 Quinones, M. J., Ryan, C. M., Ferry, S. J. W., Sunderland, T., Laurin, G. V., Gatti, R. C., Valentini, R.,  
 1639 Verbeeck, H., Wijaya, A., and Willcock, S.: An integrated pan-tropical biomass map using multiple reference  
 1640 datasets, *Glob Change Biol*, 22, 1406–1420, <https://doi.org/10.1111/gcb.13139>, 2016.

1641 Baccini, A., Walker, W., Carvalho, L., Farina, M., Sulla-Menashe, D., and Houghton, R. A.: Tropical forests are  
 1642 a net carbon source based on aboveground measurements of gain and loss, *Science*, 358, 230–234,  
 1643 <https://doi.org/10.1126/science.aam5962>, 2017.

1644 Bakker, D. C. E., Pfeil, B., Landa, C. S., Metzl, N., O'Brien, K. M., Olsen, A., Smith, K., Cosca, C., Harasawa,  
 1645 S., Jones, S. D., Nakaoka, S., Nojiri, Y., Schuster, U., Steinhoff, T., Sweeney, C., Takahashi, T., Tilbrook, B.,  
 1646 Wada, C., Wanninkhof, R., Alin, S. R., Balestrini, C. F., Barbero, L., Bates, N. R., Bianchi, A. A., Bonou, F.,  
 1647 Boutin, J., Bozec, Y., Burger, E. F., Cai, W.-J., Castle, R. D., Chen, L., Chierici, M., Currie, K., Evans, W.,  
 1648 Featherstone, C., Feely, R. A., Fransson, A., Goyet, C., Greenwood, N., Gregor, L., Hankin, S., Hardman-  
 1649 Mountford, N. J., Harlay, J., Hauck, J., Hoppema, M., Humphreys, M. P., Hunt, C. W., Huss, B., Ibáñez, J. S.  
 1650 P., Johannessen, T., Keeling, R., Kitidis, V., Körtzinger, A., Kozyr, A., Krasakopoulou, E., Kuwata, A.,  
 1651 Landschützer, P., Lauvset, S. K., Lefèvre, N., Lo Monaco, C., Manke, A., Mathis, J. T., Merlivat, L., Millero, F.  
 1652 J., Monteiro, P. M. S., Munro, D. R., Murata, A., Newberger, T., Omar, A. M., Ono, T., Paterson, K., Pearce,  
 1653 D., Pierrot, D., Robbins, L. L., Saito, S., Salisbury, J., Schlitzer, R., Schneider, B., Schweitzer, R., Sieger, R.,  
 1654 Skjelvan, I., Sullivan, K. F., Sutherland, S. C., Sutton, A. J., Tadokoro, K., Telszewski, M., Tuma, M., van  
 1655 Heuven, S. M. A. C., Vandemark, D., Ward, B., Watson, A. J., and Xu, S.: A multi-decade record of high-  
 1656 quality CO<sub>2</sub> data in version 3 of the Surface Ocean CO<sub>2</sub> Atlas (SOCAT), *Earth Syst. Sci. Data*, 8, 383–413,  
 1657 <https://doi.org/10.5194/essd-8-383-2016>, 2016.

1658 Bakker, Dorothee C. E.; Alin, Simone R.; Becker, Meike; Bittig, Henry C.; Castaño-Primo, Rocío; Feely,  
 1659 Richard A.; Gkritzalis, Thanos; Kadono, Koji; Kozyr, Alex; Lauvset, Siv K.; Metzl, Nicolas; Munro, David R.;  
 1660 Nakaoka, Shin-ichiro; Nojiri, Yukihiro; O'Brien, Kevin M.; Olsen, Are; Pfeil, Benjamin; Pierrot, Denis;  
 1661 Steinhoff, Tobias; Sullivan, Kevin F.; Sutton, Adrienne J.; Sweeney, Colm; Tilbrook, Bronte; Wada, Chisato;

1662 Wanninkhof, Rik; Willstrand Wranne, Anna; Akl, John; Apelthun, Lisa B.; Bates, Nicholas; Beatty, Cory M.;  
 1663 Burger, Eugene F.; Cai, Wei-Jun; Cosca, Catherine E.; Corredor, Jorge E.; Cronin, Margot; Cross, Jessica N.;  
 1664 De Carlo, Eric H.; DeGrandpre, Michael D.; Emerson, Steven; Enright, Matt P.; Enyo, Kazutaka; Evans, Wiley;  
 1665 Frangoulis, Constantin; Fransson, Agneta; García-Ibáñez, Maribel I.; Gehrung, Martina; Giannoudi, Louisa;  
 1666 Glockzin, Michael; Hales, Burke; Howden, Stephan D.; Hunt, Christopher W.; Ibáñez, J. Severino P.; Jones,  
 1667 Steve D.; Kamb, Linus; Körtzinger, Arne; Landa, Camilla S.; Landschützer, Peter; Lefèvre, Nathalie; Lo  
 1668 Monaco, Claire; Macovei, Vlad A.; Maenner Jones, Stacy; Meinig, Christian; Millero, Frank J.; Monacci,  
 1669 Natalie M.; Mordy, Calvin; Morell, Julio M.; Murata, Akihiko; Musielewicz, Sylvia; Neill, Craig; Newberger,  
 1670 Tim; Nomura, Daiki; Ohman, Mark; Ono, Tsuneo; Passmore, Abe; Petersen, Wilhelm; Petihakis, George;  
 1671 Perivoliotis, Leonidas; Plueddemann, Albert J.; Rehder, Gregor; Reynaud, Thierry; Rodriguez, Carmen; Ross,  
 1672 Andrew; Rutgersson, Anna; Sabine, Christopher L.; Salisbury, Joseph E.; Schlitzer, Reiner; Send, Uwe;  
 1673 Skjelvan, Ingunn; Stamataki, Natalia; Sutherland, Stewart C.; Sweeney, Colm; Tadokoro, Kazuaki; Tanhua,  
 1674 Toste; Telszewski, Maciej; Trull, Tom; Vandemark, Douglas; van Ooijen, Erik; Voynova, Yoana G.; Wang,  
 1675 Hongjie; Weller, Robert A.; Whitehead, Chris; Wilson, Doug (2022). Surface Ocean CO<sub>2</sub> Atlas Database  
 1676 Version 2022 (SOCATv2022) (NCEI Accession 0253659). NOAA National Centers for Environmental  
 1677 Information. <https://doi.org/10.25921/1h9f-nb73>.  
  
 1678 Ballantyne, A. P., Alden, C. B., Miller, J. B., Tans, P. P., and White, J. W. C.: Increase in observed net carbon  
 1679 dioxide uptake by land and oceans during the past 50 years, *Nature*, 488, 70–72,  
 1680 <https://doi.org/10.1038/nature11299>, 2012.  
  
 1681 Ballantyne, A. P., Andres, R., Houghton, R., Stocker, B. D., Wanninkhof, R., Anderegg, W., Cooper, L. A.,  
 1682 DeGrandpre, M., Tans, P. P., Miller, J. B., Alden, C., and White, J. W. C.: Audit of the global carbon budget:  
 1683 estimate errors and their impact on uptake uncertainty, *Biogeosciences*, 12, 2565–2584,  
 1684 <https://doi.org/10.5194/bg-12-2565-2015>, 2015.  
  
 1685 Bastos, A., O’Sullivan, M., Ciais, P., Makowski, D., Sitch, S., Friedlingstein, P., Chevallier, F., Rödenbeck, C.,  
 1686 Pongratz, J., Luijkx, I. T., Patra, P. K., Peylin, P., Canadell, J. G., Lauerwald, R., Li, W., Smith, N. E., Peters,  
 1687 W., Goll, D. S., Jain, A. K., Kato, E., Lienert, S., Lombardozzi, D. L., Haverd, V., Nabel, J. E. M. S., Poulter,  
 1688 B., Tian, H., Walker, A. P., and Zaehle, S.: Sources of Uncertainty in Regional and Global Terrestrial CO<sub>2</sub>  
 1689 Exchange Estimates, *Global Biogeochem. Cycles*, 34, <https://doi.org/10.1029/2019GB006393>, 2020.  
  
 1690 Bastos, A., Hartung, K., Nützel, T. B., Nabel, J. E. M. S., Houghton, R. A., and Pongratz, J.: Comparison of  
 1691 uncertainties in land-use change fluxes from bookkeeping model parameterisation, 12, 745–762,  
 1692 <https://doi.org/10.5194/esd-12-745-2021>, 2021.  
  
 1693 Basu, S., Baker, D. F., Chevallier, F., Patra, P. K., Liu, J., and Miller, J. B.: The impact of transport model  
 1694 differences on CO<sub>2</sub> surface flux estimates from OCO-2 retrievals of column average CO<sub>2</sub>, *Atmos. Chem. Phys.*,  
 1695 18, 7189–7215, <https://doi.org/10.5194/acp-18-7189-2018>, 2018.  
  
 1696 Bauer, J. E., Cai, W.-J., Raymond, P. A., Bianchi, T. S., Hopkinson, C. S., and Regnier, P. A. G.: The changing  
 1697 carbon cycle of the coastal ocean, *Nature*, 504, 61–70, <https://doi.org/10.1038/nature12857>, 2013.

1698 Beckman, J. and Countryman, A. M.: The Importance of Agriculture in the Economy: Impacts from COVID-19,  
1699 103, 1595–1611, <https://doi.org/10.1111/ajae.12212>, 2021.

1700 Bellouin, N., Rae, J., Jones, A., Johnson, C., Haywood, J., and Boucher, O.: Aerosol forcing in the Climate  
1701 Model Intercomparison Project (CMIP5) simulations by HadGEM2-ES and the role of ammonium nitrate, 116,  
1702 <https://doi.org/10.1029/2011JD016074>, 2011.

1703 Bennington, V., Gloege, L., and McKinley, G. A.: Variability in the Global Ocean Carbon Sink From 1959 to  
1704 2020 by Correcting Models with Observations, *Geophys. Res. Lett.*, 49, e2022GL098632,  
1705 <https://doi.org/10.1029/2022GL098632>, 2022.

1706 Berthet, S., S  f  rian, R., Bricaud, C., Chevallier, M., Voldoire, A., and Eth  , C.: Evaluation of an Online Grid-  
1707 Coarsening Algorithm in a Global Eddy-Admitting Ocean Biogeochemical Model, 11, 1759–1783,  
1708 <https://doi.org/10.1029/2019MS001644>, 2019.

1709 Bourgeois, T., Goris, N., Schwinger, J., and Tjiputra, J. F.: Stratification constrains future heat and carbon  
1710 uptake in the Southern Ocean between 30  S and 55  S, *Nat. Commun.*, 13, 340, [https://doi.org/10.1038/s41467-](https://doi.org/10.1038/s41467-022-27979-5)  
1711 [022-27979-5](https://doi.org/10.1038/s41467-022-27979-5), 2022.

1712 Brancalion, P. H. S., Broadbent, E. N., de-Miguel, S., Cardil, A., Rosa, M. R., Almeida, C. T., Almeida, D. R.  
1713 A., Chakravarty, S., Zhou, M., Gamarra, J. G. P., Liang, J., Crouzeilles, R., H  rault, B., Arag  o, L. E. O. C.,  
1714 Silva, C. A., and Almeyda-Zambrano, A. M.: Emerging threats linking tropical deforestation and the COVID-19  
1715 pandemic, *Perspectives in Ecology and Conservation*, 18, 243–246,  
1716 <https://doi.org/10.1016/j.pecon.2020.09.006>, 2020.

1717 Brien  n, R. J. W., Phillips, O. L., Feldpausch, T. R., Gloor, E., Baker, T. R., Lloyd, J., Lopez-Gonzalez, G.,  
1718 Monteagudo-Mendoza, A., Malhi, Y., Lewis, S. L., V  squez Martinez, R., Alexiades, M.,   lvarez D  vila, E.,  
1719 Alvarez-Loayza, P., Andrade, A., Arag  o, L. E. O. C., Araujo-Murakami, A., Arets, E. J. M. M., Arroyo, L.,  
1720 Aymard C., G. A., B  nki, O. S., Baraloto, C., Barroso, J., Bonal, D., Boot, R. G. A., Camargo, J. L. C., Castilho,  
1721 C. V., Chama, V., Chao, K. J., Chave, J., Comiskey, J. A., Cornejo Valverde, F., da Costa, L., de Oliveira, E. A.,  
1722 Di Fiore, A., Erwin, T. L., Fauset, S., Forsthofer, M., Galbraith, D. R., Grahame, E. S., Groot, N., H  rault, B.,  
1723 Higuchi, N., Honorio Coronado, E. N., Keeling, H., Killeen, T. J., Laurance, W. F., Laurance, S., Licona, J.,  
1724 Magnussen, W. E., Marimon, B. S., Marimon-Junior, B. H., Mendoza, C., Neill, D. A., Nogueira, E. M., N    ez,  
1725 P., Pallqui Camacho, N. C., Parada, A., Pardo-Molina, G., Peacock, J., Pe    a-Claros, M., Pickavance, G. C.,  
1726 Pitman, N. C. A., Poorter, L., Prieto, A., Quesada, C. A., Ram  rez, F., Ram  rez-Angulo, H., Restrepo, Z.,  
1727 Roopsind, A., Rudas, A., Salom  o, R. P., Schwarz, M., Silva, N., Silva-Espejo, J. E., Silveira, M., Stropp, J.,  
1728 Talbot, J., ter Steege, H., Teran-Aguilar, J., Terborgh, J., Thomas-Caesar, R., Toledo, M., Torello-Raventos, M.,  
1729 Umetsu, R. K., van der Heijden, G. M. F., van der Hout, P., Guimar  es Vieira, I. C., Vieira, S. A., Vilanova, E.,  
1730 Vos, V. A., and Zagt, R. J.: Long-term decline of the Amazon carbon sink, 519, 344–348,  
1731 <https://doi.org/10.1038/nature14283>, 2015.

1732 Broecker, W. S.: Ocean chemistry during glacial time, *Geochimica et Cosmochimica Acta*, 46, 1689–1705,  
1733 [https://doi.org/10.1016/0016-7037\(82\)90110-7](https://doi.org/10.1016/0016-7037(82)90110-7), 1982.

1734 Bruno, M. and Joos, F.: Terrestrial carbon storage during the past 200 years: A Monte Carlo Analysis of CO<sub>2</sub>  
 1735 data from ice core and atmospheric measurements, *Global Biogeochem. Cycles*, 11, 111–124,  
 1736 <https://doi.org/10.1029/96GB03611>, 1997.

1737 Buitenhuis, E. T., Hashioka, T., and Quéré, C. L.: Combined constraints on global ocean primary production  
 1738 using observations and models: OCEAN PRIMARY PRODUCTION, *Global Biogeochem. Cycles*, 27, 847–  
 1739 858, <https://doi.org/10.1002/gbc.20074>, 2013.

1740 Burton, C., Betts, R., Cardoso, M., Feldpausch, T. R., Harper, A., Jones, C. D., Kelley, D. I., Robertson, E., and  
 1741 Wiltshire, A.: Representation of fire, land-use change and vegetation dynamics in the Joint UK Land  
 1742 Environment Simulator vn4.9 (JULES), *Geosci. Model Dev.*, 12, 179–193, [https://doi.org/10.5194/gmd-12-179-](https://doi.org/10.5194/gmd-12-179-2019)  
 1743 2019, 2019.

1744 Bushinsky, S. M., Landschützer, P., Rödenbeck, C., Gray, A. R., Baker, D., Mazloff, M. R., Resplandy, L.,  
 1745 Johnson, K. S., and Sarmiento, J. L.: Reassessing Southern Ocean Air-Sea CO<sub>2</sub> Flux Estimates With the  
 1746 Addition of Biogeochemical Float Observations, *Global Biogeochem. Cycles*, 33, 1370–1388,  
 1747 <https://doi.org/10.1029/2019GB006176>, 2019.

1748 Canadell, J. G., Le Quere, C., Raupach, M. R., Field, C. B., Buitenhuis, E. T., Ciais, P., Conway, T. J., Gillett,  
 1749 N. P., Houghton, R. A., and Marland, G.: Contributions to accelerating atmospheric CO<sub>2</sub> growth from economic  
 1750 activity, carbon intensity, and efficiency of natural sinks, *Proceedings of the National Academy of Sciences*,  
 1751 104, 18866–18870, <https://doi.org/10.1073/pnas.0702737104>, 2007.

1752 Canadell, J. G., Monteiro, P. M. S., Costa, M. H., Cotrim da Cunha, L., Cox, P. M., Eliseev, A. V., Henson, S.,  
 1753 Ishii, M., Jaccard, S., Koven, C., Lohila, A., Patra, P. K., Piao, S., Rogelj, J., Syampungani, S., Zaehle, S., and  
 1754 Zickfeld, K.: Global Carbon and other Biogeochemical Cycles and Feedbacks. In: *Climate Change 2021: The*  
 1755 *Physical Science Basis. Contribution of Working Group I to the Sixth Assessment Report of the*  
 1756 *Intergovernmental Panel on Climate Change* [Masson-Delmotte, V., P. Zhai, A. Pirani, S. L. Connors, C. Péan,  
 1757 S. Berger, N. Caud, Y. Chen, L. Goldfarb, M. I. Gomis, M. Huang, K. Leitzell, E. Lonnoy, J.B.R. Matthews, T.  
 1758 K. Maycock, T. Waterfield, O. Yelekçi, R. Yu and B. Zhou (eds.)]. Cambridge University Press, 2021.

1759 Cao, Z., Myers, R. J., Lupton, R. C., Duan, H., Sacchi, R., Zhou, N., Reed Miller, T., Cullen, J. M., Ge, Q., and  
 1760 Liu, G.: The sponge effect and carbon emission mitigation potentials of the global cement cycle, *Nat Commun*,  
 1761 11, 3777, <https://doi.org/10.1038/s41467-020-17583-w>, 2020.

1762 Carbon Monitor: CO<sub>2</sub> Emissions Variation, available at: <https://carbonmonitor.org/>, last access: 25 September  
 1763 2022., 2022.

1764 Chatfield, C.: The Holt-Winters Forecasting Procedure, 27, 264–279, <https://doi.org/10.2307/2347162>, 1978.

1765 Chau, T. T. T., Gehlen, M., and Chevallier, F.: QUALITY INFORMATION DOCUMENT for Global Ocean  
 1766 Surface Carbon Product MULTIOBS\_GLO\_BIO CARBON\_SURFACE\_REP\_015\_008, Le Laboratoire des  
 1767 Sciences du Climat et de l’Environnement, 2020.

1768 Chau, T. T. T., Gehlen, M., and Chevallier, F.: A seamless ensemble-based reconstruction of surface ocean  
1769  $p\text{CO}_2$  and air–sea  $\text{CO}_2$  fluxes over the global coastal and open oceans, *Biogeosciences*, 19, 1087–1109,  
1770 <https://doi.org/10.5194/bg-19-1087-2022>, 2022.

1771 Chevallier, F.: On the parallelization of atmospheric inversions of  $\text{CO}_2$  surface fluxes within a variational  
1772 framework, 6, 783–790, <https://doi.org/10.5194/gmd-6-783-2013>, 2013.

1773 Chevallier, F., Fisher, M., Peylin, P., Serrar, S., Bousquet, P., Bréon, F.-M., Chédin, A., and Ciais, P.: Inferring  
1774  $\text{CO}_2$  sources and sinks from satellite observations: Method and application to TOVS data, *J. Geophys. Res.*,  
1775 110, D24309, <https://doi.org/10.1029/2005JD006390>, 2005.

1776 Chevallier, F., Remaud, M., O'Dell, C. W., Baker, D., Peylin, P., and Cozic, A.: Objective evaluation of  
1777 surface- and satellite-driven carbon dioxide atmospheric inversions, *Atmos. Chem. Phys.*, 19, 14233–14251,  
1778 <https://doi.org/10.5194/acp-19-14233-2019>, 2019.

1779 Chini, L., Hurtt, G., Sahajpal, R., Frolking, S., Klein Goldewijk, K., Sitch, S., Ganzenmüller, R., Ma, L., Ott, L.,  
1780 Pongratz, J., and Poulter, B.: Land-use harmonization datasets for annual global carbon budgets, 13, 4175–4189,  
1781 <https://doi.org/10.5194/essd-13-4175-2021>, 2021.

1782 Ciais, P., Sabine, C., Bala, G., Bopp, L., Brovkin, V., Canadell, J. G., Chhabra, A., DeFries, R., Galloway, J.,  
1783 Heimann, M., Jones, C., Le Quéré, C., Myneni, R., Piao, S., Thornton, P., Willem, J., Friedlingstein, P., and  
1784 Munhoven, G.: Carbon and Other Biogeochemical Cycles, in *Climate Change 2013: The Physical Science*  
1785 *Basis, Contribution of Working Group I to the Fifth Assessment Report of the Intergovernmental Panel on*  
1786 *Climate Change*, edited by: Intergovernmental Panel on Climate Change, Cambridge University Press,  
1787 Cambridge, UK, 465–570, 2013.

1788 Ciais, P., Tan, J., Wang, X., Roedenbeck, C., Chevallier, F., Piao, S.-L., Moriarty, R., Broquet, G., Le Quéré, C.,  
1789 Canadell, J. G., Peng, S., Poulter, B., Liu, Z., and Tans, P.: Five decades of northern land carbon uptake  
1790 revealed by the interhemispheric  $\text{CO}_2$  gradient, *Nature*, 568, 221–225, [https://doi.org/10.1038/s41586-019-](https://doi.org/10.1038/s41586-019-1078-6)  
1791 1078-6, 2019.

1792 Ciais, P., Bastos, A., Chevallier, F., Lauerwald, R., Poulter, B., Canadell, P., Hugelius, G., Jackson, R. B., Jain,  
1793 A., Jones, M., Kondo, M., Luijkx, I. T., Patra, P. K., Peters, W., Pongratz, J., Petrescu, A. M. R., Piao, S., Qiu,  
1794 C., Von Randow, C., Regnier, P., Saunois, M., Scholes, R., Shvidenko, A., Tian, H., Yang, H., Wang, X., and  
1795 Zheng, B.: Definitions and methods to estimate regional land carbon fluxes for the second phase of the REgional  
1796 Carbon Cycle Assessment and Processes Project (RECCAP-2), *Geosci. Model Dev.*, 15, 1289–1316,  
1797 <https://doi.org/10.5194/gmd-15-1289-2022>, 2022.

1798 Collier, N., Hoffman, F. M., Lawrence, D. M., Keppel-Aleks, G., Koven, C. D., Riley, W. J., Mu, M., and  
1799 Randerson, J. T.: The International Land Model Benchmarking (ILAMB) System: Design, Theory, and  
1800 Implementation, *J. Adv. Model. Earth Syst.*, 10, 2731–2754, <https://doi.org/10.1029/2018MS001354>, 2018.

1801 Conchedda, G. and Tubiello, F. N.: Drainage of organic soils and GHG emissions: Validation with country data,  
1802 *Biosphere – Biogeosciences*, <https://doi.org/10.5194/essd-2020-202>, 2020.

1803 Cooper, D. J., Watson, A. J., and Ling, R. D.: Variation of pCO<sub>2</sub> along a North Atlantic shipping route (U.K. to  
1804 the Caribbean): A year of automated observations, *Marine Chemistry*, 60, 147–164,  
1805 [https://doi.org/10.1016/S0304-4203\(97\)00082-0](https://doi.org/10.1016/S0304-4203(97)00082-0), 1998.

1806 Cox, A., Vermeulen, A., Manning, A., Beyersdorf, A., Zahn, A., Manning, A., Watson, A., Karion, A., Hensen,  
1807 A., Arlyn Andrews, Frumau, A., Colomb, A., Scheeren, B., Law, B., Baier, B., Munger, B., Paplawsky, B.,  
1808 Viner, B., Stephens, B., Daube, B., Labuschagne, C., Myhre, C. L., Hanson, C., Miller, C. E., Plass-Duelmer,  
1809 C., Plass-Duelmer, C., Gerbig, C., Sloop, C. D., Sweeney, C., Kubistin, D., Goto, D., Jaffe, D., Say, D., Van  
1810 Dinter, D., Bowling, D., Lam, D. H. Y., Dickon Young, Worthy, D., Dlugokencky, E., Kozlova, E., Gloor, E.,  
1811 Cuevas, E., Reyes-Sanchez, E., Hintsa, E., Kort, E., Morgan, E., Obersteiner, F., Apadula, F., Francois Gheusi,  
1812 Meinhardt, F., Moore, F., Vitkova, G., Chen, G., Bentz, G., Manca, G., Brailsford, G., Forster, G., Boenisch, H.,  
1813 Riris, H., Meijer, H., Timas, H., Matsueda, H., Huilin Chen, Levin, I., Lehner, I., Mammarella, I., Bartyzel, J.,  
1814 Abshire, J. B., Elkins, J. W., Levula, J., Jaroslaw Necki, Pichon, J. M., Peischl, J., Müller-Williams, J., Turnbull,  
1815 J., Miller, J. B., Lee, J., Lin, J., Josep-Anton Morgui, DiGangi, J. P., Hatakka, J., Coletta, J. D., Worsey, J.,  
1816 Holst, J., Kominkova, K., McKain, K., Saito, K., Aikin, K., Davis, K., Thoning, K., Tørseth, K., Haszpra, L.,  
1817 Mitchell, L., Gatti, L. V., Emmenegger, L., Lukasz Chmura, Merchant, L., Sha, M. K., Delmotte, M., et al.:  
1818 Multi-laboratory compilation of atmospheric carbon dioxide data for the period 1957-2019;  
1819 `obspack_co2_1_GLOBALVIEWplus_v6.1_2021-03-01`, <https://doi.org/10.25925/20201204>, 2021.

1820 Cox, P. M., Pearson, D., Booth, B. B., Friedlingstein, P., Huntingford, C., Jones, C. D., and Luke, C. M.:  
1821 Sensitivity of tropical carbon to climate change constrained by carbon dioxide variability, *Nature*, 494, 341–344,  
1822 <https://doi.org/10.1038/nature11882>, 2013.

1823 Crippa, M., Janssens-Maenhout, G., Guizzardi, D., Van Dingenen, R., and Dentener, F.: Contribution and  
1824 uncertainty of sectorial and regional emissions to regional and global PM<sub>2.5</sub> health impacts, 19, 5165–5186,  
1825 <https://doi.org/10.5194/acp-19-5165-2019>, 2019.

1826 Dai, A. and Trenberth, K. E.: Estimates of Freshwater Discharge from Continents: Latitudinal and Seasonal  
1827 Variations, 3, 660–687, [https://doi.org/10.1175/1525-7541\(2002\)003<0660:EOFDFC>2.0.CO;2](https://doi.org/10.1175/1525-7541(2002)003<0660:EOFDFC>2.0.CO;2), 2002.

1828 Davis, S. J. and Caldeira, K.: Consumption-based accounting of CO<sub>2</sub> emissions, *Proceedings of the National*  
1829 *Academy of Sciences*, 107, 5687–5692, <https://doi.org/10.1073/pnas.0906974107>, 2010.

1830 De Kauwe, M. G., Disney, M. I., Quaife, T., Lewis, P., and Williams, M.: An assessment of the MODIS  
1831 collection 5 leaf area index product for a region of mixed coniferous forest, *Remote Sensing of Environment*,  
1832 115, 767–780, <https://doi.org/10.1016/j.rse.2010.11.004>, 2011.

1833 De Kauwe, M. G., Medlyn, B. E., Zaehle, S., Walker, A. P., Dietze, M. C., Wang, Y.-P., Luo, Y., Jain, A. K.,  
1834 El-Masri, B., Hickler, T., Wårlind, D., Weng, E., Parton, W. J., Thornton, P. E., Wang, S., Prentice, I. C., Asao,  
1835 S., Smith, B., McCarthy, H. R., Iversen, C. M., Hanson, P. J., Warren, J. M., Oren, R., and Norby, R. J.: Where  
1836 does the carbon go? A model–data intercomparison of vegetation carbon allocation and turnover processes at  
1837 two temperate forest free-air CO<sub>2</sub> enrichment sites, *New Phytol.*, 203, 883–899,  
1838 <https://doi.org/10.1111/nph.12847>, 2014.

1839 Decharme, B., Delire, C., Minvielle, M., Colin, J., Vergnes, J.-P., Alias, A., Saint-Martin, D., Séférian, R.,  
1840 Sénési, S., and Voldoire, A.: Recent Changes in the ISBA-CTrip Land Surface System for Use in the CNRM-  
1841 CM6 Climate Model and in Global Off-Line Hydrological Applications, 11, 1207–1252,  
1842 <https://doi.org/10.1029/2018MS001545>, 2019.

1843 Delire, C., Séférian, R., Decharme, B., Alkama, R., Calvet, J.-C., Carrer, D., Gibelin, A.-L., Joetzjer, E., Morel,  
1844 X., Rocher, M., and Tzanos, D.: The Global Land Carbon Cycle Simulated With ISBA-CTrip: Improvements  
1845 Over the Last Decade, 12, e2019MS001886, <https://doi.org/10.1029/2019MS001886>, 2020.

1846 Denman, K. L., Brasseur, G., Chidthaisong, A., Ciais, P., Cox, P. M., Dickinson, R. E., Hauglustaine, D.,  
1847 Heinze, C., Holland, E., Jacob, D., Lohmann, U., Ramachandran, S., Leite da Silva Dias, P., Wofsy, S. C., and  
1848 Zhang, X.: Couplings Between Changes in the Climate System and Biogeochemistry, in: Climate Change 2007:  
1849 The Physical Science Basis. Contribution of Working Group I to the Fourth Assessment Report of the  
1850 Intergovernmental Panel on Climate Change, edited by: Solomon, S., Qin, D., Manning, M., Marquis, M.,  
1851 Averyt, K., Tignor, M. M. B., Miller, H. L., and Chen, Z. L., Cambridge University Press, Cambridge, UK and  
1852 New York, USA, 499–587, 2007.

1853 Denning, A. S., Fung, I. Y., and Randall, D.: Latitudinal gradient of atmospheric CO<sub>2</sub> due to seasonal exchange  
1854 with land biota, *Nature*, 376, 240–243, <https://doi.org/10.1038/376240a0>, 1995.

1855 Denvil-Sommer, A., Gehlen, M., Vrac, M., and Mejia, C.: LSCE-FFNN-v1: a two-step neural network model  
1856 for the reconstruction of surface ocean pCO<sub>2</sub> over the global ocean, 12, 2091–2105,  
1857 <https://doi.org/10.5194/gmd-12-2091-2019>, 2019.

1858 DeVries, T.: The oceanic anthropogenic CO<sub>2</sub> sink: Storage, air-sea fluxes, and transports over the industrial  
1859 era, *Global Biogeochem. Cycles*, 28, 631–647, <https://doi.org/10.1002/2013GB004739>, 2014.

1860 DeVries, T., Holzer, M., and Primeau, F.: Recent increase in oceanic carbon uptake driven by weaker upper-  
1861 ocean overturning, *Nature*, 542, 215–218, <https://doi.org/10.1038/nature21068>, 2017.

1862 DeVries, T., Quéré, C. L., Andrews, O., Berthet, S., Hauck, J., Ilyina, T., Landschützer, P., Lenton, A., Lima, I.  
1863 D., Nowicki, M., Schwinger, J., and Séférian, R.: Decadal trends in the ocean carbon sink, *PNAS*, 116, 11646–  
1864 11651, <https://doi.org/10.1073/pnas.1900371116>, 2019.

1865 Di Sarra, A. G., Karion, A., Arlyn Andrews, Colomb, A., Scheeren, B., Viner, B., Myhre, C. L., Miller, C. E.,  
1866 Plass-Duelmer, C., Plass-Duelmer, C., Sloop, C. D., Sweeney, C., Kubistin, D., Jaffé, D., Dlugokencky, E.,  
1867 Vitkova, G., Manca, G., Huilin Chen, Lehner, I., Mammarella, I., Pichon, J. M., Müller-Williams, J., Miller, J.  
1868 B., Lee, J., Hatakka, J., Holst, J., Kominkova, K., McKain, K., Thoning, K., Tørseth, K., Emmenegger, L., Sha,  
1869 M. K., Delmotte, M., Fischer, M. L., Schumacher, M., Leuenberger, M., Steinbacher, M., De Mazière, M.,  
1870 Lindauer, M., Mölder, M., Heliasz, M., Marek, M. V., Ramonet, M., Lopez, M., Laurent, O., Hermanssen, O.,  
1871 Trisolino, P., Cristofanelli, P., Smith, P., Bakwin, P., Bergamaschi, P., Keronen, P., Tans, P., Piacentino, S.,  
1872 Biraud, S. C., Conil, S., De Wekker, S., Biermann, T., Laurila, T., Aalto, T., and Kazan, V.: Multi-laboratory  
1873 compilation of atmospheric carbon dioxide data for the years 2020-2021; obspack\_co2\_1\_NRT\_v6.1.1\_2021-  
1874 05-17, <https://doi.org/10.25925/20210517>, 2021.

1875 Dickson, A. G., Sabine, C. L., and Christian, J. R.: Guide to best practices for ocean CO<sub>2</sub> measurement. Sidney,  
 1876 British Columbia, North Pacific Marine Science Organization, 191pp. (PICES Special Publication 3; IOCCP  
 1877 Report 8). DOI: <https://doi.org/10.25607/OBP-1342>, 2007.

1878 Dlugokencky, E. and Tans, P.: Trends in atmospheric carbon dioxide, National Oceanic and Atmospheric  
 1879 Administration, Global Monitoring Laboratory (NOAA/GML), available at:  
 1880 <http://www.gml.noaa.gov/gmd/ccgg/trends/global.html>, accessed: 16 November 2020., 2020.

1881 Dlugokencky, E. and Tans, P.: Trends in atmospheric carbon dioxide, National Oceanic and Atmospheric  
 1882 Administration, Global Monitoring Laboratory (NOAA/GML), available at:  
 1883 <http://www.gml.noaa.gov/gmd/ccgg/trends/global.html>, last access: 25 September 2022., 2022.

1884 Doney, S. C., Lima, I., Feely, R. A., Glover, D. M., Lindsay, K., Mahowald, N., Moore, J. K., and Wanninkhof,  
 1885 R.: Mechanisms governing interannual variability in upper-ocean inorganic carbon system and air–sea CO<sub>2</sub>  
 1886 fluxes: Physical climate and atmospheric dust, Deep Sea Research Part II: Topical Studies in Oceanography, 56,  
 1887 640–655, <https://doi.org/10.1016/j.dsr2.2008.12.006>, 2009.

1888 Dong, Y., Bakker, D. C. E., Bell, T. G., Huang, B., Landschützer, P., Liss, P. S., and Yang, M.: Update on the  
 1889 Temperature Corrections of Global Air-Sea CO<sub>2</sub> Flux Estimates, Glob. Biogeochem. Cycles, 36,  
 1890 e2022GB007360, <https://doi.org/10.1029/2022GB007360>, 2022.

1891 Dou, X., Wang, Y., Ciais, P., Chevallier, F., Davis, S. J., Crippa, M., Janssens-Maenhout, G., Guizzardi, D.,  
 1892 Solazzo, E., Yan, F., Huo, D., Zheng, B., Zhu, B., Cui, D., Ke, P., Sun, T., Wang, H., Zhang, Q., Gentine, P.,  
 1893 Deng, Z., and Liu, Z.: Near-real-time global gridded daily CO<sub>2</sub> emissions, The Innovation, 3, 100182,  
 1894 <https://doi.org/10.1016/j.xinn.2021.100182>, 2022.

1895 Duce, R. A., LaRoche, J., Altieri, K., Arrigo, K. R., Baker, A. R., Capone, D. G., Cornell, S., Dentener, F.,  
 1896 Galloway, J., Ganeshram, R. S., Geider, R. J., Jickells, T., Kuypers, M. M., Langlois, R., Liss, P. S., Liu, S. M.,  
 1897 Middelburg, J. J., Moore, C. M., Nickovic, S., Oschlies, A., Pedersen, T., Prospero, J., Schlitzer, R., Seitzinger,  
 1898 S., Sorensen, L. L., Uematsu, M., Ulloa, O., Voss, M., Ward, B., and Zamora, L.: Impacts of Atmospheric  
 1899 Anthropogenic Nitrogen on the Open Ocean, Science, 320, 893–897, <https://doi.org/10.1126/science.1150369>,  
 1900 2008.

1901 Dufour, C. O., Sommer, J. L., Gehlen, M., Orr, J. C., Molines, J., Simeon, J., and Barnier, B.: Eddy  
 1902 compensation and controls of the enhanced sea-to-air CO<sub>2</sub> flux during positive phases of the Southern Annular  
 1903 Mode, Global Biogeochem. Cycles, 27, 950–961, <https://doi.org/10.1002/gbc.20090>, 2013.

1904 Eakins, B. W. and Sharman, G. F.: National Geophysical Data Center: Volumes of the World’s Oceans from  
 1905 ETOPO1, available at: [https://www.ngdc.noaa.gov/mgg/global/etopo1\\_ocean\\_volumes.html](https://www.ngdc.noaa.gov/mgg/global/etopo1_ocean_volumes.html), last access: 25  
 1906 September 2022, U.S. Department of Commerce, 2010.

1907 Eggleston, H. S., Buendia, L., Miwa, K., Ngara, T., and Tanabe, K.: Volume 4: Agriculture, forestry and land  
 1908 use. in: 2006 IPCC guidelines for national greenhouse gas inventories., 2006.

1909 EIA: U.S. Energy Information Administration: Short-Term Energy Outlook, available at:



- 1910 <http://www.eia.gov/forecasts/steo/outlook>, last access: 25 September 2022., 2022.
- 1911 Erb, K.-H., Kastner, T., Luyssaert, S., Houghton, R. A., Kuemmerle, T., Olofsson, P., and Haberl, H.: Bias in  
1912 the attribution of forest carbon sinks, *Nature Clim Change*, 3, 854–856, <https://doi.org/10.1038/nclimate2004>,  
1913 2013.
- 1914 Erb, K.-H., Kastner, T., Plutzer, C., Bais, A. L. S., Carvalhais, N., Fetzel, T., Gingrich, S., Haberl, H., Lauk, C.,  
1915 Niedertscheider, M., Pongratz, J., Thurner, M., and Luyssaert, S.: Unexpectedly large impact of forest  
1916 management and grazing on global vegetation biomass, *Nature*, 553, 73–76,  
1917 <https://doi.org/10.1038/nature25138>, 2018.
- 1918 Eskander, S. M. S. U. and Fankhauser, S.: Reduction in greenhouse gas emissions from national climate  
1919 legislation, *Nat. Clim. Chang.*, 10, 750–756, <https://doi.org/10.1038/s41558-020-0831-z>, 2020.
- 1920 Etheridge, D. M., Steele, L. P., Langenfelds, R. L., Francey, R. J., Barnola, J.-M., and Morgan, V. I.: Natural  
1921 and anthropogenic changes in atmospheric CO<sub>2</sub> over the last 1000 years from air in Antarctic ice and firn, *J.*  
1922 *Geophys. Res.*, 101, 4115–4128, <https://doi.org/10.1029/95JD03410>, 1996.
- 1923 Eyring, V., Bony, S., Meehl, G. A., Senior, C. A., Stevens, B., Stouffer, R. J., and Taylor, K. E.: Overview of  
1924 the Coupled Model Intercomparison Project Phase 6 (CMIP6) experimental design and organization, *Geosci.*  
1925 *Model Dev.*, 9, 1937–1958, <https://doi.org/10.5194/gmd-9-1937-2016>, 2016.
- 1926 FAO: Global Forest Resources Assessment 2020: Main report, FAO, Rome, Italy, 184 pp.,  
1927 <https://doi.org/10.4060/ca9825en>, 2020.
- 1928 FAO: FAOSTAT Statistical Database, domains Climate Change, available at:  
1929 <http://www.fao.org/faostat/en/#data/GT>, last access: 25 September 2022, 2021.
- 1930 FAOSTAT: FAOSTAT: Food and Agriculture Organization Statistics Division, available at:  
1931 <http://faostat.fao.org/>, last access: 25 September 2022), 2021.
- 1932 FAO/UNEP: Food and Agriculture Organisation / United Nations Environment Programme: The state of food  
1933 and agriculture 1981, available at: <https://www.fao.org/3/ap661e/ap661e.pdf>, last access: 25 September 2022,  
1934 1981.
- 1935 Fan, L., Wigneron, J.-P., Ciais, P., Chave, J., Brandt, M., Fensholt, R., Saatchi, S. S., Bastos, A., Al-Yaari, A.,  
1936 Hufkens, K., Qin, Y., Xiao, X., Chen, C., Myneni, R. B., Fernandez-Moran, R., Mialon, A., Rodriguez-  
1937 Fernandez, N. J., Kerr, Y., Tian, F., and Peñuelas, J.: Satellite-observed pantropical carbon dynamics, *Nat.*  
1938 *Plants*, 5, 944–951, <https://doi.org/10.1038/s41477-019-0478-9>, 2019.
- 1939 Fay, A. R. and McKinley, G. A.: Global open-ocean biomes: mean and temporal variability, 6, 273–284,  
1940 <https://doi.org/10.5194/essd-6-273-2014>, 2014.
- 1941 Fay, A. R., Gregor, L., Landschützer, P., McKinley, G. A., Gruber, N., Gehlen, M., Iida, Y., Laruelle, G. G.,  
1942 Rödenbeck, C., and Zeng, J.: Harmonization of global surface ocean pCO<sub>2</sub> mapped products and their flux

- 1943 calculations; an improved estimate of the ocean carbon sink, 1–32, <https://doi.org/10.5194/essd-2021-16>, 2021a.
- 1944 Fay, A. R., Gregor, L., Landschützer, P., McKinley, G. A., Gruber, N., Gehlen, M., Iida, Y., Laruelle, G. G.,
- 1945 Rödenbeck, C., Roobaert, A., and Zeng, J.: SeaFlux: harmonization of air–sea CO<sub>2</sub> fluxes from surface pCO<sub>2</sub>
- 1946 data products using a standardized approach, 13, 4693–4710, <https://doi.org/10.5194/essd-13-4693-2021>, 2021b.
- 1947 Feng, L., Palmer, P. I., Bosch, H., and Dance, S.: Estimating surface CO<sub>2</sub> fluxes from space-borne CO<sub>2</sub> dry air
- 1948 mole fraction observations using an ensemble Kalman Filter, 15, 2009.
- 1949 Feng, L., Palmer, P. I., Parker, R. J., Deutscher, N. M., Feist, D. G., Kivi, R., Morino, I., and Sussmann, R.:
- 1950 Estimates of European uptake of CO<sub>2</sub> inferred from GOSAT XCO<sub>2</sub> retrievals: sensitivity to measurement bias
- 1951 inside and outside Europe, *Atmos. Chem. Phys.*, 16, 1289–1302, <https://doi.org/10.5194/acp-16-1289-2016>,
- 1952 2016.
- 1953 Feng, Y., Zeng, Z., Searchinger, T. D., Ziegler, A. D., Wu, J., Wang, D., He, X., Elsen, P. R., Ciais, P., Xu, R.,
- 1954 Guo, Z., Peng, L., Tao, Y., Spracklen, D. V., Holden, J., Liu, X., Zheng, Y., Xu, P., Chen, J., Jiang, X., Song,
- 1955 X.-P., Lakshmi, V., Wood, E. F., and Zheng, C.: Doubling of annual forest carbon loss over the tropics during
- 1956 the early twenty-first century, *Nat. Sustain.*, 1–8, <https://doi.org/10.1038/s41893-022-00854-3>, 2022.
- 1957 Friedlingstein, P., Houghton, R. A., Marland, G., Hackler, J., Boden, T. A., Conway, T. J., Canadell, J. G.,
- 1958 Raupach, M. R., Ciais, P., and Le Quéré, C.: Update on CO<sub>2</sub> emissions, *Nature Geosci.*, 3, 811–812,
- 1959 <https://doi.org/10.1038/ngeo1022>, 2010.
- 1960 Friedlingstein, P., Andrew, R. M., Rogelj, J., Peters, G. P., Canadell, J. G., Knutti, R., Luderer, G., Raupach, M.
- 1961 R., Schaeffer, M., van Vuuren, D. P., and Le Quéré, C.: Persistent growth of CO<sub>2</sub> emissions and implications
- 1962 for reaching climate targets, *Nature Geosci.*, 7, 709–715, <https://doi.org/10.1038/ngeo2248>, 2014.
- 1963 Friedlingstein, P., Jones, M. W., O’Sullivan, M., Andrew, R. M., Hauck, J., Peters, G. P., Peters, W., Pongratz,
- 1964 J., Sitch, S., Le Quéré, C., Bakker, D. C. E., Canadell, J. G., Ciais, P., Jackson, R. B., Anthoni, P., Barbero, L.,
- 1965 Bastos, A., Bastrikov, V., Becker, M., Bopp, L., Buitenhuis, E., Chandra, N., Chevallier, F., Chini, L. P., Currie,
- 1966 K. I., Feely, R. A., Gehlen, M., Gilfillan, D., Gkritzalis, T., Goll, D. S., Gruber, N., Gutekunst, S., Harris, I.,
- 1967 Haverd, V., Houghton, R. A., Hurtt, G., Ilyina, T., Jain, A. K., Joetzjer, E., Kaplan, J. O., Kato, E., Klein
- 1968 Goldewijk, K., Korsbakken, J. I., Landschützer, P., Lauvset, S. K., Lefèvre, N., Lenton, A., Lienert, S.,
- 1969 Lombardozzi, D., Marland, G., McGuire, P. C., Melton, J. R., Metzl, N., Munro, D. R., Nabel, J. E. M. S.,
- 1970 Nakaoka, S.-I., Neill, C., Omar, A. M., Ono, T., Peregón, A., Pierrot, D., Poulter, B., Rehder, G., Resplandy, L.,
- 1971 Robertson, E., Rödenbeck, C., Séférian, R., Schwinger, J., Smith, N., Tans, P. P., Tian, H., Tilbrook, B.,
- 1972 Tubiello, F. N., van der Werf, G. R., Wiltshire, A. J., and Zaehele, S.: Global Carbon Budget 2019, *Earth Syst.*
- 1973 *Sci. Data*, 11, 1783–1838, <https://doi.org/10.5194/essd-11-1783-2019>, 2019.
- 1974 Friedlingstein, P., O’Sullivan, M., Jones, M. W., Andrew, R. M., Hauck, J., Olsen, A., Peters, G. P., Peters, W.,
- 1975 Pongratz, J., Sitch, S., Le Quéré, C., Canadell, J. G., Ciais, P., Jackson, R. B., Alin, S., Aragão, L. E. O. C.,
- 1976 Arneth, A., Arora, V., Bates, N. R., Becker, M., Benoit-Cattin, A., Bittig, H. C., Bopp, L., Bultan, S., Chandra,
- 1977 N., Chevallier, F., Chini, L. P., Evans, W., Florentie, L., Forster, P. M., Gasser, T., Gehlen, M., Gilfillan, D.,
- 1978 Gkritzalis, T., Gregor, L., Gruber, N., Harris, I., Hartung, K., Haverd, V., Houghton, R. A., Ilyina, T., Jain, A.

- 1979 K., Joetzjer, E., Kadono, K., Kato, E., Kitidis, V., Korsbakken, J. I., Landschützer, P., Lefèvre, N., Lenton, A.,  
1980 Lienert, S., Liu, Z., Lombardozi, D., Marland, G., Metzl, N., Munro, D. R., Nabel, J. E. M. S., Nakaoka, S.-I.,  
1981 Niwa, Y., O'Brien, K., Ono, T., Palmer, P. I., Pierrot, D., Poulter, B., Resplandy, L., Robertson, E., Rödenbeck,  
1982 C., Schwinger, J., Séférian, R., Skjelvan, I., Smith, A. J. P., Sutton, A. J., Tanhua, T., Tans, P. P., Tian, H.,  
1983 Tilbrook, B., van der Werf, G., Vuichard, N., Walker, A. P., Wanninkhof, R., Watson, A. J., Willis, D.,  
1984 Wiltshire, A. J., Yuan, W., Yue, X., and Zaehle, S.: Global Carbon Budget 2020, *Earth Syst. Sci. Data*, 12,  
1985 3269–3340, <https://doi.org/10.5194/essd-12-3269-2020>, 2020.
- 1986 Friedlingstein, P., Jones, M. W., O'Sullivan, M., Andrew, R. M., Bakker, D. C. E., Hauck, J., Le Quéré, C.,  
1987 Peters, G. P., Peters, W., Pongratz, J., Sitch, S., Canadell, J. G., Ciais, P., Jackson, R. B., Alin, S. R., Anthoni,  
1988 P., Bates, N. R., Becker, M., Bellouin, N., Bopp, L., Chau, T. T. T., Chevallier, F., Chini, L. P., Cronin, M.,  
1989 Currie, K. I., Decharme, B., Djeutchouang, L. M., Dou, X., Evans, W., Feely, R. A., Feng, L., Gasser, T.,  
1990 Gilfillan, D., Gkritzalis, T., Grassi, G., Gregor, L., Gruber, N., Gürses, Ö., Harris, I., Houghton, R. A., Hurtt, G.  
1991 C., Iida, Y., Ilyina, T., Luijkx, I. T., Jain, A., Jones, S. D., Kato, E., Kennedy, D., Klein Goldewijk, K., Knauer,  
1992 J., Korsbakken, J. I., Körtzinger, A., Landschützer, P., Lauvset, S. K., Lefèvre, N., Lienert, S., Liu, J., Marland,  
1993 G., McGuire, P. C., Melton, J. R., Munro, D. R., Nabel, J. E. M. S., Nakaoka, S.-I., Niwa, Y., Ono, T., Pierrot,  
1994 D., Poulter, B., Rehder, G., Resplandy, L., Robertson, E., Rödenbeck, C., Rosan, T. M., Schwinger, J.,  
1995 Schwingshackl, C., Séférian, R., Sutton, A. J., Sweeney, C., Tanhua, T., Tans, P. P., Tian, H., Tilbrook, B.,  
1996 Tubiello, F., van der Werf, G. R., Vuichard, N., Wada, C., Wanninkhof, R., Watson, A. J., Willis, D., Wiltshire,  
1997 A. J., Yuan, W., Yue, C., Yue, X., Zaehle, S., and Zeng, J.: Global Carbon Budget 2021, *Earth Syst. Sci. Data*,  
1998 14, 1917–2005, <https://doi.org/10.5194/essd-14-1917-2022>, 2022a.
- 1999 Friedlingstein, P., O'Sullivan, M., Jones, M. W., Andrew, R. M., Gregor, L., Hauck, L., Le Quéré, C., Luijkx, I.  
2000 T., Olsen, A., Peters, G. P., Peters, W., Pongratz, J., Schwingshackl, C., Sitch, S., Canadell, J. G., Ciais, P.,  
2001 Jackson, R. B., Alin, S., Alkama, R., Arneeth, A., Arora, V. K., Bates, N. R., Becker, M., Bellouin, N., Bittig, H.  
2002 C., Bopp, L., Chevallier, F., Chini, L. P., Cronin, M., Evans, W., Falk, S., Feely, R. A., Gasser, T., Gehlen, M.,  
2003 Gkritzalis, T., Gloege, L., Grassi, G., Gruber, N., Gürses, Ö., Harris, I., Hefner, M., Houghton, R. A., Hurtt, G.  
2004 C., Iida, Y., Ilyina, T., Jain, A. T., Jersild, A., Kadono, K., Kato, E., Kennedy, D., Klein Goldewijk, K., Knauer,  
2005 J., Korsbakken, J. I., Landschützer, P., Lefèvre, N., Lindsay, Keith., Liu, J., Marland, G., Mayot, N., McGrath,  
2006 M. J., Metzl, N., Monacci, N. M., Munro, D. R., Nakaoka, S.-I., Niwa, Y., O'Brien, K., Ono, T., Palmer, P. I.,  
2007 Pan, N., Pierrot, D., Pocock, K., Poulter, B., Resplandy, L., Robertson, E., Rödenbeck, C., Rodriguez, C.,  
2008 Rosan, T. M., Schwinger, J., Séférian, R., Shutler, J. D., Skjelvan, I., Steinhoff, T., Sun, Q., Sutton, A. J.,  
2009 Sweeney, C., Takao, S., Tanhua, T., Tans, P. P., Tian, X., Tian, H., Tilbrook, B., Tsujino, H., Tubiello, F., van  
2010 der Werf, G. R., Walker, A. P., Wanninkhof, R., Whitehead, C., Wranne, A., Wright, R. M., Yuan, W., Yue, C.,  
2011 Yue, X., Zaehle, S., Zeng, J., Zheng, B. and Zhu, L.: Supplemental data of the Global Carbon Budget 2022,  
2012 ICOS-ERIC Carbon Portal, <https://doi.org/10.18160/GCP-2022>, 2022b.
- 2013 Ganzenmüller, R., Bultan, S., Winkler, K., Fuchs, R., Zabel, F., and Pongratz, J.: Land-use change emissions  
2014 based on high-resolution activity data substantially lower than previously estimated, *Environ. Res. Lett.*, 17,  
2015 064050, <https://doi.org/10.1088/1748-9326/ac70d8>, 2022.
- 2016 Gasser, T. and Ciais, P.: A theoretical framework for the net land-to-atmosphere CO<sub>2</sub> flux and its implications

2017 in the definition of "emissions from land-use change", *Earth Syst. Dynam.*, 4, 171–186,  
2018 <https://doi.org/10.5194/esd-4-171-2013>, 2013.

2019 Gasser, T., Crepin, L., Quilcaille, Y., Houghton, R. A., Ciais, P., and Obersteiner, M.: Historical CO<sub>2</sub> emissions  
2020 from land use and land cover change and their uncertainty, *Biogeosciences*, 17, 4075–4101,  
2021 <https://doi.org/10.5194/bg-17-4075-2020>, 2020.

2022 Gaubert, B., Stephens, B. B., Basu, S., Chevallier, F., Deng, F., Kort, E. A., Patra, P. K., Peters, W., Rödenbeck,  
2023 C., Saeki, T., Schimel, D., Van der Laan-Luijkx, I., Wofsy, S., and Yin, Y.: Global atmospheric CO<sub>2</sub> inverse  
2024 models converging on neutral tropical land exchange, but disagreeing on fossil fuel and atmospheric growth  
2025 rate, *Biogeosciences*, 16, 117–134, <https://doi.org/10.5194/bg-16-117-2019>, 2019.

2026 Gaubert, B., Emmons, L. K., Raeder, K., Tilmes, S., Miyazaki, K., Arellano Jr., A. F., Elguindi, N., Granier, C.,  
2027 Tang, W., Barré, J., Worden, H. M., Buchholz, R. R., Edwards, D. P., Franke, P., Anderson, J. L., Saunio, M.,  
2028 Schroeder, J., Woo, J.-H., Simpson, I. J., Blake, D. R., Meinardi, S., Wennberg, P. O., Crounse, J., Teng, A.,  
2029 Kim, M., Dickerson, R. R., He, H., Ren, X., Pusede, S. E., and Diskin, G. S.: Correcting model biases of CO in  
2030 East Asia: impact on oxidant distributions during KORUS-AQ, 20, 14617–14647, [https://doi.org/10.5194/acp-](https://doi.org/10.5194/acp-20-14617-2020)  
2031 [20-14617-2020](https://doi.org/10.5194/acp-20-14617-2020), 2020.

2032 GCCA, 2021. Concrete Future: The GCCA 2050 Cement and Concrete Industry Roadmap for Net Zero  
2033 Concrete, available at: <https://gccassociation.org/concretetofuture/> , last access: 2 August 2022.

2034 Giglio, L., Schroeder, W., and Justice, C. O.: The collection 6 MODIS active fire detection algorithm and fire  
2035 products, *Remote Sensing of Environment*, 178, 31–41, <https://doi.org/10.1016/j.rse.2016.02.054>, 2016.

2036 Gilfillan, D. and Marland, G.: CDIAC-FF: global and national CO<sub>2</sub> emissions from fossil fuel combustion and  
2037 cement manufacture: 1751–2017, 13, 1667–1680, <https://doi.org/10.5194/essd-13-1667-2021>, 2021.

2038 Gloege, L., McKinley, G. A., Landschützer, P., Fay, A. R., Frölicher, T. L., Fyfe, J. C., Ilyina, T., Jones, S.,  
2039 Lovenduski, N. S., Rodgers, K. B., Schlunegger, S., and Takano, Y.: Quantifying Errors in Observationally  
2040 Based Estimates of Ocean Carbon Sink Variability, 35, e2020GB006788,  
2041 <https://doi.org/10.1029/2020GB006788>, 2021.

2042 Gloege, L., Yan, M., Zheng, T., and McKinley, G. A.: Improved Quantification of Ocean Carbon Uptake by  
2043 Using Machine Learning to Merge Global Models and pCO<sub>2</sub> Data, *J. Adv. Model. Earth Syst.*, 14,  
2044 e2021MS002620, <https://doi.org/10.1029/2021MS002620>, 2022.

2045 Goddijn-Murphy, L. M., Woolf, D. K., Land, P. E., Shutler, J. D., and Donlon, C.: The OceanFlux Greenhouse  
2046 Gases methodology for deriving a sea surface climatology of CO<sub>2</sub> fugacity in support of air–sea gas flux  
2047 studies, 11, 519–541, <https://doi.org/10.5194/os-11-519-2015>, 2015.

2048 Golar, G., Malik, A., Muis, H., Herman, A., Nurudin, N., and Lukman, L.: The social-economic impact of  
2049 COVID-19 pandemic: implications for potential forest degradation, *Heliyon*, 6, e05354,  
2050 <https://doi.org/10.1016/j.heliyon.2020.e05354>, 2020.

2051 Goris, N., Tjiputra, J. F., Olsen, A., Schwinger, J., Lauvset, S. K., and Jeansson, E.: Constraining Projection-  
 2052 Based Estimates of the Future North Atlantic Carbon Uptake, *J. Clim.*, 31, 3959–3978,  
 2053 <https://doi.org/10.1175/JCLI-D-17-0564.1>, 2018.

2054 Grassi, G., House, J., Kurz, W. A., Cescatti, A., Houghton, R. A., Peters, G. P., Sanz, M. J., Viñas, R. A.,  
 2055 Alkama, R., Arneth, A., Bondeau, A., Dentener, F., Fader, M., Federici, S., Friedlingstein, P., Jain, A. K., Kato,  
 2056 E., Koven, C. D., Lee, D., Nabel, J. E. M. S., Nassikas, A. A., Perugini, L., Rossi, S., Sitch, S., Viovy, N.,  
 2057 Wiltshire, A., and Zaehle, S.: Reconciling global-model estimates and country reporting of anthropogenic forest  
 2058 CO<sub>2</sub> sinks, *Nature Clim Change*, 8, 914–920, <https://doi.org/10.1038/s41558-018-0283-x>, 2018.

2059 Grassi, G., Stehfest, E., Rogelj, J., van Vuuren, D., Cescatti, A., House, J., Nabuurs, G.-J., Rossi, S., Alkama,  
 2060 R., Viñas, R. A., Calvin, K., Ceccherini, G., Federici, S., Fujimori, S., Gusti, M., Hasegawa, T., Havlik, P.,  
 2061 Humpenöder, F., Korosuo, A., Perugini, L., Tubiello, F. N., and Popp, A.: Critical adjustment of land mitigation  
 2062 pathways for assessing countries’ climate progress, *Nat. Clim. Chang.*, 11, 425–434,  
 2063 <https://doi.org/10.1038/s41558-021-01033-6>, 2021.

2064 Grassi, G., Conchedda, G., Federici, S., Abad Viñas, R., Korosuo, A., Melo, J., Rossi, S., Sandker, M.,  
 2065 Somogyi, Z., and Tubiello, F. N.: Carbon fluxes from land 2000–2020: bringing clarity on countries’ reporting,  
 2066 *Biogeosciences and biodiversity*, <https://doi.org/10.5194/essd-2022-104>, 2022a.

2067 Grassi, G., Schwingshackl, C., Gasser, T., Houghton, R. A., Sitch, S., Canadell, J. G., Cescatti, A., Ciais, P.,  
 2068 Federici, S., Friedlingstein, P., Kurz, W. A., Sanz Sanchez, M. J., Abad Viñas, R., Alkama, R., Ceccherini, G.,  
 2069 Kato, E., Kennedy, D., Knauer, J., Korosuo, A., McGrath, M. J., Nabel, J., Poulter, B., Rossi, S., Walker, A. P.,  
 2070 Yuan, W., Yue, X., and Pongratz, J.: Mapping land-use fluxes for 2001–2020 from global models to national  
 2071 inventories, *ESSD – Land/Land Cover and Land Use*, <https://doi.org/10.5194/essd-2022-245>, 2022b.

2072 Gregg, J. S., Andres, R. J., and Marland, G.: China: Emissions pattern of the world leader in CO<sub>2</sub> emissions  
 2073 from fossil fuel consumption and cement production, *Geophys. Res. Lett.*, 35, L08806,  
 2074 <https://doi.org/10.1029/2007GL032887>, 2008.

2075 Gregor, L. and Gruber, N.: OceanSODA-ETHZ: a global gridded data set of the surface ocean carbonate system  
 2076 for seasonal to decadal studies of ocean acidification, 13, 777–808, <https://doi.org/10.5194/essd-13-777-2021>,  
 2077 2021.

2078 Gregor, L., Lebehot, A. D., Kok, S., and Scheel Monteiro, P. M.: A comparative assessment of the uncertainties  
 2079 of global surface ocean CO<sub>2</sub> estimates using a machine-learning ensemble (CSIR-ML6 version 2019a) – have  
 2080 we hit the wall?, 12, 5113–5136, <https://doi.org/10.5194/gmd-12-5113-2019>, 2019.

2081 Gruber, N., Gloor, M., Mikaloff Fletcher, S. E., Doney, S. C., Dutkiewicz, S., Follows, M. J., Gerber, M.,  
 2082 Jacobson, A. R., Joos, F., Lindsay, K., Menemenlis, D., Mouchet, A., Müller, S. A., Sarmiento, J. L., and  
 2083 Takahashi, T.: Oceanic sources, sinks, and transport of atmospheric CO<sub>2</sub>, 23,  
 2084 <https://doi.org/10.1029/2008GB003349>, 2009.

2085 Gruber, N., Clement, D., Carter, B. R., Feely, R. A., van Heuven, S., Hoppema, M., Ishii, M., Key, R. M.,

2086 Kozyr, A., Lauvset, S. K., Lo Monaco, C., Mathis, J. T., Murata, A., Olsen, A., Perez, F. F., Sabine, C. L.,  
2087 Tanhua, T., and Wanninkhof, R.: The oceanic sink for anthropogenic CO<sub>2</sub> from 1994 to 2007, 363, 1193–1199,  
2088 <https://doi.org/10.1126/science.aau5153>, 2019.

2089 Gruère, G. and Brooks, J.: Viewpoint: Characterising early agricultural and food policy responses to the  
2090 outbreak of COVID-19, *Food Policy*, 100, 102017, <https://doi.org/10.1016/j.foodpol.2020.102017>, 2021.

2091 Guan, D., Liu, Z., Geng, Y., Lindner, S., and Hubacek, K.: The gigatonne gap in China's carbon dioxide  
2092 inventories, *Nature Clim Change*, 2, 672–675, <https://doi.org/10.1038/nclimate1560>, 2012.

2093 Gulev, S. K., Thorne, P. W., Ahn, J., Dentener, F. J., Domingues, C. M., Gerland, S., Gong, D. S., Kaufman, S.,  
2094 Nnamchi, H. C., Quaas, J., Rivera, J. A., Sathyendranath, S., Smith, S. L., Trewin, B., von Shuckmann, K., and  
2095 Vose, R. S.: Changing State of the Climate System. In: *Climate Change 2021: The Physical Science Basis*.  
2096 Contribution of Working Group I to the Sixth Assessment Report of the Intergovernmental Panel on Climate  
2097 Change [Masson-Delmotte, V., Zhai, P., Pirani, A., Connors, S. L., Péan, C., Berger, S., Caud, N., Chen, Y.,  
2098 Goldfarb, L., Gomis, M. I., Huang, M., Leitzell, K., Lonnoy, E., Matthews, J.B.R., Maycock, T.K., Waterfield,  
2099 T., Yelekçi, O., Yu, R. and Zhou, B. (eds.)]. Cambridge University Press, Cambridge, United Kingdom and  
2100 New York, NY, USA, pp. 287–422, doi:10.1017/9781009157896.004, 2021.

2101 Guo, R., Wang, J., Bing, L., Tong, D., Ciais, P., Davis, S. J., Andrew, R. M., Xi, F., and Liu, Z.: Global CO<sub>2</sub>  
2102 uptake by cement from 1930 to 2019, 13, 1791–1805, <https://doi.org/10.5194/essd-13-1791-2021>, 2021.

2103 Gütschow, J., Jeffery, M. L., Gieseke, R., Gebel, R., Stevens, D., Krapp, M., and Rocha, M.: The PRIMAP-hist  
2104 national historical emissions time series, 8, 571–603, <https://doi.org/10.5194/essd-8-571-2016>, 2016.

2105 Gütschow, J., Günther, A., and Pflüger, M.: The PRIMAP-hist national historical emissions time series (1750-  
2106 2019) v2.3.1, <https://doi.org/10.5281/zenodo.5494497>, 2021.

2107 Hall, B. D., Crotwell, A. M., Kitzis, D. R., Mefford, T., Miller, B. R., Schibig, M. F., and Tans, P. P.: Revision  
2108 of the World Meteorological Organization Global Atmosphere Watch (WMO/GAW) CO<sub>2</sub> calibration scale, 14,  
2109 3015–3032, <https://doi.org/10.5194/amt-14-3015-2021>, 2021.

2110 Hansen, M. C., Potapov, P. V., Moore, R., Hancher, M., Turubanova, S. A., Tyukavina, A., Thau, D., Stehman,  
2111 S. V., Goetz, S. J., Loveland, T. R., Kommareddy, A., Egorov, A., Chini, L., Justice, C. O., and Townshend, J.  
2112 R. G.: High-Resolution Global Maps of 21st-Century Forest Cover Change, *Science*, 342, 850–853,  
2113 <https://doi.org/10.1126/science.1244693>, 2013.

2114 Hansis, E., Davis, S. J., and Pongratz, J.: Relevance of methodological choices for accounting of land use  
2115 change carbon fluxes, *Global Biogeochem. Cycles*, 29, 1230–1246, <https://doi.org/10.1002/2014GB004997>,  
2116 2015.

2117 Harris, I., Jones, P. D., Osborn, T. J., and Lister, D. H.: Updated high-resolution grids of monthly climatic  
2118 observations - the CRU TS3.10 Dataset, *Int. J. Climatol.*, 34, 623–642, <https://doi.org/10.1002/joc.3711>, 2014.

2119 Harris, I., Osborn, T. J., Jones, P., and Lister, D.: Version 4 of the CRU TS monthly high-resolution gridded

2120 multivariate climate dataset, *Sci Data*, 7, 109, <https://doi.org/10.1038/s41597-020-0453-3>, 2020.

2121 Hauck, J., Zeising, M., Le Quéré, C., Gruber, N., Bakker, D. C. E., Bopp, L., Chau, T. T. T., Gürses, Ö., Ilyina,  
 2122 T., Landschützer, P., Lenton, A., Resplandy, L., Rödenbeck, C., Schwinger, J., and Séférian, R.: Consistency  
 2123 and Challenges in the Ocean Carbon Sink Estimate for the Global Carbon Budget, *Front. Mar. Sci.*, 7, 571720,  
 2124 <https://doi.org/10.3389/fmars.2020.571720>, 2020.

2125 Haverd, V., Smith, B., Nieradzik, L., Briggs, P. R., Woodgate, W., Trudinger, C. M., Canadell, J. G., and Cuntz,  
 2126 M.: A new version of the CABLE land surface model (Subversion revision r4601) incorporating land use and  
 2127 land cover change, woody vegetation demography, and a novel optimisation-based approach to plant  
 2128 coordination of photosynthesis, *Geosci. Model Dev.*, 11, 2995–3026, [https://doi.org/10.5194/gmd-11-2995-](https://doi.org/10.5194/gmd-11-2995-2018)  
 2129 2018, 2018.

2130 Heinimann, A., Mertz, O., Frohling, S., Christensen, A. E., Hurni, K., Sedano, F., Chini, L. P., Sahajpal, R.,  
 2131 Hansen, M., and Hurr, G.: A global view of shifting cultivation: Recent, current, and future extent, *PLOS ONE*,  
 2132 12, e0184479, <https://doi.org/10.1371/journal.pone.0184479>, 2017.

2133 Hertwich, E. G. and Peters, G. P.: Carbon Footprint of Nations: A Global, Trade-Linked Analysis, *Environ. Sci.*  
 2134 *Technol.*, 43, 6414–6420, <https://doi.org/10.1021/es803496a>, 2009.

2135 Hickler, T., Smith, B., Prentice, I. C., Mjöfors, K., Miller, P., Arneth, A., and Sykes, M. T.: CO<sub>2</sub> fertilization in  
 2136 temperate FACE experiments not representative of boreal and tropical forests, 14, 1531–1542,  
 2137 <https://doi.org/10.1111/j.1365-2486.2008.01598.x>, 2008.

2138 Ho, D. T., Wanninkhof, R., Schlosser, P., Ullman, D. S., Hebert, D., and Sullivan, K. F.: Toward a universal  
 2139 relationship between wind speed and gas exchange: Gas transfer velocities measured with <sup>3</sup>He/SF<sub>6</sub> during the  
 2140 Southern Ocean Gas Exchange Experiment, 116, <https://doi.org/10.1029/2010JC006854>, 2011.

2141 Hoesly, R. M., Smith, S. J., Feng, L., Klimont, Z., Janssens-Maenhout, G., Pitkanen, T., Seibert, J. J., Vu, L.,  
 2142 Andres, R. J., Bolt, R. M., Bond, T. C., Dawidowski, L., Kholod, N., Kurokawa, J., Li, M., Liu, L., Lu, Z.,  
 2143 Moura, M. C. P., O'Rourke, P. R., and Zhang, Q.: Historical (1750–2014) anthropogenic emissions of reactive  
 2144 gases and aerosols from the Community Emissions Data System (CEDS), *Geosci. Model Dev.*, 11, 369–408,  
 2145 <https://doi.org/10.5194/gmd-11-369-2018>, 2018.

2146 Hong, C., Burney, J. A., Pongratz, J., Nabel, J. E. M. S., Mueller, N. D., Jackson, R. B., and Davis, S. J.: Global  
 2147 and regional drivers of land-use emissions in 1961–2017, 589, 554–561, [https://doi.org/10.1038/s41586-020-](https://doi.org/10.1038/s41586-020-03138-y)  
 2148 03138-y, 2021.

2149 Hooijer, A., Page, S., Canadell, J. G., Silvius, M., Kwadijk, J., Wösten, H., and Jauhiainen, J.: Current and  
 2150 future CO<sub>2</sub> emissions from drained peatlands in Southeast Asia, *Biogeosciences*, 7, 1505–1514,  
 2151 <https://doi.org/10.5194/bg-7-1505-2010>, 2010.

2152 Houghton, R. A.: Why are estimates of the terrestrial carbon balance so different?, 9, 500–509,  
 2153 <https://doi.org/10.1046/j.1365-2486.2003.00620.x>, 2003.

2154 Houghton, R. A. and Nassikas, A. A.: Global and regional fluxes of carbon from land use and land cover change  
 2155 1850-2015: Carbon Emissions From Land Use, *Global Biogeochem. Cycles*, 31, 456–472,  
 2156 <https://doi.org/10.1002/2016GB005546>, 2017.

2157 Houghton, R. A., House, J. I., Pongratz, J., van der Werf, G. R., DeFries, R. S., Hansen, M. C., Le Quéré, C.,  
 2158 and Ramankutty, N.: Carbon emissions from land use and land-cover change, *Biogeosciences*, 9, 5125–5142,  
 2159 <https://doi.org/10.5194/bg-9-5125-2012>, 2012.

2160 Hubau, W., Lewis, S. L., Phillips, O. L., Affum-Baffoe, K., Beeckman, H., Cuní-Sanchez, A., Daniels, A. K.,  
 2161 Ewango, C. E. N., Fauset, S., Mukinzi, J. M., Sheil, D., Sonké, B., Sullivan, M. J. P., Sunderland, T. C. H.,  
 2162 Taedoumg, H., Thomas, S. C., White, L. J. T., Abernethy, K. A., Adu-Bredu, S., Amani, C. A., Baker, T. R.,  
 2163 Banin, L. F., Baya, F., Begne, S. K., Bennett, A. C., Benedet, F., Bitariho, R., Bocko, Y. E., Boeckx, P.,  
 2164 Boundja, P., Brienens, R. J. W., Brncic, T., Chezeaux, E., Chuyong, G. B., Clark, C. J., Collins, M., Comiskey, J.  
 2165 A., Coomes, D. A., Dargie, G. C., de Haulleville, T., Kamdem, M. N. D., Doucet, J.-L., Esquivel-Muelbert, A.,  
 2166 Feldpausch, T. R., Fofanah, A., Foli, E. G., Gilpin, M., Gloor, E., Gonmadje, C., Gourlet-Fleury, S., Hall, J. S.,  
 2167 Hamilton, A. C., Harris, D. J., Hart, T. B., Hockemba, M. B. N., Hladik, A., Ifo, S. A., Jeffery, K. J., Jucker, T.,  
 2168 Yakusu, E. K., Kearsley, E., Kenfack, D., Koch, A., Leal, M. E., Levesley, A., Lindsell, J. A., Lisingo, J.,  
 2169 Lopez-Gonzalez, G., Lovett, J. C., Makana, J.-R., Malhi, Y., Marshall, A. R., Martin, J., Martin, E. H., Mbayu,  
 2170 F. M., Medjibe, V. P., Mihindou, V., Mitchard, E. T. A., Moore, S., Munishi, P. K. T., Bengone, N. N., Ojo, L.,  
 2171 Ondo, F. E., Peh, K. S.-H., Pickavance, G. C., Poulsen, A. D., Poulsen, J. R., Qie, L., Reitsma, J., Rovero, F.,  
 2172 Swaine, M. D., Talbot, J., Taplin, J., Taylor, D. M., Thomas, D. W., Toirambe, B., Mukendi, J. T., Tuagben, D.,  
 2173 Umunay, P. M., et al.: Asynchronous carbon sink saturation in African and Amazonian tropical forests, 579, 80–  
 2174 87, <https://doi.org/10.1038/s41586-020-2035-0>, 2020.

2175 Hugelius, G., Bockheim, J. G., Camill, P., Elberling, B., Grosse, G., Harden, J. W., Johnson, K., Jorgenson, T.,  
 2176 Koven, C. D., Kuhry, P., Michaelson, G., Mishra, U., Palmtag, J., Ping, C.-L., O'Donnell, J., Schirrmeister, L.,  
 2177 Schuur, E. A. G., Sheng, Y., Smith, L. C., Strauss, J., and Yu, Z.: A new data set for estimating organic carbon  
 2178 storage to 3 m depth in soils of the northern circumpolar permafrost region, *Earth Syst. Sci. Data*, 5, 393–402,  
 2179 <https://doi.org/10.5194/essd-5-393-2013>, 2013.

2180 Humphrey, V., Zscheischler, J., Ciais, P., Gudmundsson, L., Sitch, S., and Seneviratne, S. I.: Sensitivity of  
 2181 atmospheric CO<sub>2</sub> growth rate to observed changes in terrestrial water storage, 560, 628–631,  
 2182 <https://doi.org/10.1038/s41586-018-0424-4>, 2018.

2183 Humphrey, V., Berg, A., Ciais, P., Gentine, P., Jung, M., Reichstein, M., Seneviratne, S. I., and Frankenberg,  
 2184 C.: Soil moisture–atmosphere feedback dominates land carbon uptake variability, 592, 65–69,  
 2185 <https://doi.org/10.1038/s41586-021-03325-5>, 2021.

2186 Huntzinger, D. N., Michalak, A. M., Schwalm, C., Ciais, P., King, A. W., Fang, Y., Schaefer, K., Wei, Y.,  
 2187 Cook, R. B., Fisher, J. B., Hayes, D., Huang, M., Ito, A., Jain, A. K., Lei, H., Lu, C., Maignan, F., Mao, J.,  
 2188 Parazoo, N., Peng, S., Poulter, B., Ricciuto, D., Shi, X., Tian, H., Wang, W., Zeng, N., and Zhao, F.:  
 2189 Uncertainty in the response of terrestrial carbon sink to environmental drivers undermines carbon-climate  
 2190 feedback predictions, *Sci Rep*, 7, 4765, <https://doi.org/10.1038/s41598-017-03818-2>, 2017.



- 2191 Hurtt, G., Chini, L., Sahajpal, R., Frolking, S., Bodirsky, B. L., Calvin, K., Doelman, J., Fisk, J., Fujimori, S.,  
 2192 Klein Goldewijk, K., Hasegawa, T., Havlik, P., Heinemann, A., Humpenöder, F., Jungclaus, J., Kaplan, J.,  
 2193 Krisztin, T., Lawrence, D., Lawrence, P., Mertz, O., Pongratz, J., Popp, A., Riahi, K., Shevliakova, E., Stehfest,  
 2194 E., Thornton, P., van Vuuren, D., and Zhang, X.: input4MIPs.CMIP6.CMIP.UofMD.UofMD-landState-2-1-h,  
 2195 <https://doi.org/10.22033/ESGF/input4MIPs.1127>, 2017.
- 2196 Hurtt, G. C., Chini, L. P., Frolking, S., Betts, R. A., Feddema, J., Fischer, G., Fisk, J. P., Hibbard, K., Houghton,  
 2197 R. A., Janetos, A., Jones, C. D., Kindermann, G., Kinoshita, T., Klein Goldewijk, K., Riahi, K., Shevliakova, E.,  
 2198 Smith, S., Stehfest, E., Thomson, A., Thornton, P., van Vuuren, D. P., and Wang, Y. P.: Harmonization of land-  
 2199 use scenarios for the period 1500–2100: 600 years of global gridded annual land-use transitions, wood harvest,  
 2200 and resulting secondary lands, *Climatic Change*, 109, 117–161, <https://doi.org/10.1007/s10584-011-0153-2>,  
 2201 2011.
- 2202 Hurtt, G. C., Chini, L., Sahajpal, R., Frolking, S., Bodirsky, B. L., Calvin, K., Doelman, J. C., Fisk, J., Fujimori,  
 2203 S., Klein Goldewijk, K., Hasegawa, T., Havlik, P., Heinemann, A., Humpenöder, F., Jungclaus, J., Kaplan, J. O.,  
 2204 Kennedy, J., Krisztin, T., Lawrence, D., Lawrence, P., Ma, L., Mertz, O., Pongratz, J., Popp, A., Poulter, B.,  
 2205 Riahi, K., Shevliakova, E., Stehfest, E., Thornton, P., Tubiello, F. N., van Vuuren, D. P., and Zhang, X.:  
 2206 Harmonization of global land use change and management for the period 850–2100 (LUH2) for CMIP6, *Geosci.*  
 2207 *Model Dev.*, 13, 5425–5464, <https://doi.org/10.5194/gmd-13-5425-2020>, 2020.
- 2208 IEA: International Energy Agency: Global Energy Review, available at: [https://www.iea.org/reports/global-](https://www.iea.org/reports/global-energy-review-2021)  
 2209 [energy-review-2021](https://www.iea.org/reports/global-energy-review-2021), last access: 25 September 2022, 2021a.
- 2210 IEA: International Energy Agency: World Energy Outlook, available at: [https://www.iea.org/reports/world-](https://www.iea.org/reports/world-energy-outlook-2021)  
 2211 [energy-outlook-2021](https://www.iea.org/reports/world-energy-outlook-2021), last access: 25 September 2022, 2021b.
- 2212 IEA/OECD: International Energy Agency/Organisation for Economic Cooperation and Development: CO2  
 2213 emissions from fuel combustion, available at: [https://webstore.iea.org/co2-emissions-from-fuel-combustion-](https://webstore.iea.org/co2-emissions-from-fuel-combustion-2019-highlights)  
 2214 [2019-highlights](https://webstore.iea.org/co2-emissions-from-fuel-combustion-2019-highlights), last access: 25 September 2022, 2019.
- 2215 Iida, Y., Kojima, A., Takatani, Y., Nakano, T., Sugimoto, H., Midorikawa, T., and Ishii, M.: Trends in pCO2  
 2216 and sea–air CO2 flux over the global open oceans for the last two decades, *J Oceanogr*, 71, 637–661,  
 2217 <https://doi.org/10.1007/s10872-015-0306-4>, 2015.
- 2218 Iida, Y., Takatani, Y., Kojima, A., and Ishii, M.: Global trends of ocean CO2 sink and ocean acidification: an  
 2219 observation-based reconstruction of surface ocean inorganic carbon variables, *J Oceanogr*, 77, 323–358,  
 2220 <https://doi.org/10.1007/s10872-020-00571-5>, 2021.
- 2221 Ilyina, T., Six, K. D., Segschneider, J., Maier-Reimer, E., Li, H., and Núñez-Riboni, I.: Global ocean  
 2222 biogeochemistry model HAMOCC: Model architecture and performance as component of the MPI-Earth system  
 2223 model in different CMIP5 experimental realizations: The Model Hamocc within Mpi-Esm in Cmp5, *J. Adv.*  
 2224 *Model. Earth Syst.*, 5, 287–315, <https://doi.org/10.1029/2012MS000178>, 2013.
- 2225 IMF: International Monetary Fund: World Economic Outlook, available at: <http://www.imf.org>, last access: 25

- 2226 September 2022, 2022.
- 2227 Inness, A., Ades, M., Agustí-Panareda, A., Barré, J., Benedictow, A., Blechschmidt, A.-M., Dominguez, J. J.,  
 2228 Engelen, R., Eskes, H., Flemming, J., Huijnen, V., Jones, L., Kipling, Z., Massart, S., Parrington, M., Peuch, V.-  
 2229 H., Razinger, M., Remy, S., Schulz, M., and Suttie, M.: The CAMS reanalysis of atmospheric composition, 19,  
 2230 3515–3556, <https://doi.org/10.5194/acp-19-3515-2019>, 2019.
- 2231 IPCC: Summary for Policymakers. In: Climate Change 2021: The Physical Science Basis. Contribution of  
 2232 Working Group I to the Sixth Assessment Report of the Intergovernmental Panel on Climate Change [Masson-  
 2233 Delmotte, V., P. Zhai, A. Pirani, S.L. Connors, C. Péan, S. Berger, N. Caud, Y. Chen, L. Goldfarb, M.I. Gomis,  
 2234 M. Huang, K. Leitzell, E. Lonnoy, J.B.R. Matthews, T.K. Maycock, T. Waterfield, O. Yelekçi, R. Yu, and B.  
 2235 Zhou (eds.)]. Cambridge University Press, 2021.
- 2236 Ito, A. and Inatomi, M.: Use of a process-based model for assessing the methane budgets of global terrestrial  
 2237 ecosystems and evaluation of uncertainty, 9, 759–773, <https://doi.org/10.5194/bg-9-759-2012>, 2012.
- 2238 Jackson, R. B., Canadell, J. G., Le Quéré, C., Andrew, R. M., Korsbakken, J. I., Peters, G. P., and Nakicenovic,  
 2239 N.: Reaching peak emissions, *Nature Clim Change*, 6, 7–10, <https://doi.org/10.1038/nclimate2892>, 2016.
- 2240 Jackson, R. B., Le Quéré, C., Andrew, R. M., Canadell, J. G., Korsbakken, J. I., Liu, Z., Peters, G. P., and  
 2241 Zheng, B.: Global energy growth is outpacing decarbonization, *Environ. Res. Lett.*, 13, 120401,  
 2242 <https://doi.org/10.1088/1748-9326/aaf303>, 2018.
- 2243 Jackson, R. B., Friedlingstein, P., Andrew, R. M., Canadell, J. G., Le Quéré, C., and Peters, G. P.: Persistent  
 2244 fossil fuel growth threatens the Paris Agreement and planetary health, *Environ. Res. Lett.*, 14, 121001,  
 2245 <https://doi.org/10.1088/1748-9326/ab57b3>, 2019.
- 2246 Jackson, R. B., Friedlingstein, P., Quéré, C. L., Abernethy, S., Andrew, R. M., Canadell, J. G., Ciais, P., Davis,  
 2247 S. J., Deng, Z., Liu, Z., Korsbakken, J. I., and Peters, G. P.: Global fossil carbon emissions rebound near pre-  
 2248 COVID-19 levels, *Environ. Res. Lett.*, 17, 031001, <https://doi.org/10.1088/1748-9326/ac55b6>, 2022.
- 2249 Jacobson, A. R., Mikaloff Fletcher, S. E., Gruber, N., Sarmiento, J. L., and Gloor, M.: A joint atmosphere-ocean  
 2250 inversion for surface fluxes of carbon dioxide: 1. Methods and global-scale fluxes: JOINT INVERSION-  
 2251 METHODS AND GLOBAL FLUXES, *Global Biogeochem. Cycles*, 21,  
 2252 <https://doi.org/10.1029/2005GB002556>, 2007.
- 2253 Jähne, B.: Air-Sea Gas Exchange, in: *Encyclopedia of Ocean Sciences*, Elsevier, 1–13,  
 2254 <https://doi.org/10.1016/B978-0-12-409548-9.11613-6>, 2019.
- 2255 Jähne, B. and Haußecker, H.: Air-water gas exchange, *Annu. Rev. Fluid Mech.*, 30, 443–468,  
 2256 <https://doi.org/10.1146/annurev.fluid.30.1.443>, 1998.
- 2257 Jain, A. K., Meiyappan, P., Song, Y., and House, J. I.: CO<sub>2</sub> emissions from land-use change affected more by  
 2258 nitrogen cycle, than by the choice of land-cover data, 19, 2893–2906, <https://doi.org/10.1111/gcb.12207>, 2013.

- 2259 Janssens-Maenhout, G., Crippa, M., Guizzardi, D., Muntean, M., Schaaf, E., Dentener, F., Bergamaschi, P.,  
2260 Pagliari, V., Olivier, J. G. J., Peters, J. A. H. W., van Aardenne, J. A., Monni, S., Doering, U., Petrescu, A. M.  
2261 R., Solazzo, E., and Oreggioni, G. D.: EDGAR v4.3.2 Global Atlas of the three major greenhouse gas emissions  
2262 for the period 1970–2012, *Earth Syst. Sci. Data*, 11, 959–1002, <https://doi.org/10.5194/essd-11-959-2019>, 2019.
- 2263 Jin, Z., Wang, T., Zhang, H., Wang, Y., Ding, J., and Tian, X.: Constraint of satellite CO<sub>2</sub> retrieval on the global  
2264 carbon cycle from a Chinese atmospheric inversion system, under review, *Sci. China Earth Sci.*, 2022.
- 2265 JODI: Joint Organisations Data Initiative, available at: <https://www.jodidata.org>, last access: 25 September  
2266 2022, 2022.
- 2267 Jones, M. W., Andrew, R. M., Peters, G. P., Janssens-Maenhout, G., De-Gol, A. J., Ciais, P., Patra, P. K.,  
2268 Chevallier, F., and Le Quéré, C.: Gridded fossil CO<sub>2</sub> emissions and related O<sub>2</sub> combustion consistent with  
2269 national inventories 1959–2018, *Sci Data*, 8, 2, <https://doi.org/10.1038/s41597-020-00779-6>, 2021.
- 2270 Jones, M. W., Andrew, R. M., Peters, G. P., Janssens-Maenhout, G., De-Gol, A. J., Dou, X., Liu, Z., Pickers, P.,  
2271 Ciais, P., Patra, P. K., Chevallier, F., and Le Quéré, C.: Gridded fossil CO<sub>2</sub> emissions and related O<sub>2</sub>  
2272 combustion consistent with national inventories 1959–2021, <https://doi.org/10.5281/zenodo.4277266>, 2022.
- 2273 Joos, F. and Spahni, R.: Rates of change in natural and anthropogenic radiative forcing over the past 20,000  
2274 years, *Proceedings of the National Academy of Sciences*, 105, 1425–1430,  
2275 <https://doi.org/10.1073/pnas.0707386105>, 2008.
- 2276 Joos, F., Spahni, R., Stocker, B. D., Lienert, S., Müller, J., Fischer, H., Schmitt, J., Prentice, I. C., Otto-Bliesner,  
2277 B., and Liu, Z.: N<sub>2</sub>O changes from the Last Glacial Maximum to the preindustrial – Part 2: terrestrial N<sub>2</sub>O  
2278 emissions and carbon–nitrogen cycle interactions, *Biogeosciences*, 17, 3511–3543, [https://doi.org/10.5194/bg-](https://doi.org/10.5194/bg-17-3511-2020)  
2279 17-3511-2020, 2020.
- 2280 Jung, M., Reichstein, M., Ciais, P., Seneviratne, S. I., Sheffield, J., Goulden, M. L., Bonan, G., Cescatti, A.,  
2281 Chen, J., de Jeu, R., Dolman, A. J., Eugster, W., Gerten, D., Gianelle, D., Gobron, N., Heinke, J., Kimball, J.,  
2282 Law, B. E., Montagnani, L., Mu, Q., Mueller, B., Oleson, K., Papale, D., Richardson, A. D., Rouspard, O.,  
2283 Running, S., Tomelleri, E., Viovy, N., Weber, U., Williams, C., Wood, E., Zaehle, S., and Zhang, K.: Recent  
2284 decline in the global land evapotranspiration trend due to limited moisture supply, *Nature*, 467, 951–954,  
2285 <https://doi.org/10.1038/nature09396>, 2010.
- 2286 Jung, M., Reichstein, M., Schwalm, C. R., Huntingford, C., Sitch, S., Ahlström, A., Arneeth, A., Camps-Valls,  
2287 G., Ciais, P., Friedlingstein, P., Gans, F., Ichii, K., Jain, A. K., Kato, E., Papale, D., Poulter, B., Raduly, B.,  
2288 Rödenbeck, C., Tramontana, G., Viovy, N., Wang, Y.-P., Weber, U., Zaehle, S., and Zeng, N.: Compensatory  
2289 water effects link yearly global land CO<sub>2</sub> sink changes to temperature, *Nature*, 541, 516–520,  
2290 <https://doi.org/10.1038/nature20780>, 2017.
- 2291 Kalnay, E., Kanamitsu, M., Kistler, R., Collins, W., Deaven, D., Gandin, L., Iredell, M., Saha, S., White, G.,  
2292 Woollen, J., Zhu, Y., Chelliah, M., Ebisuzaki, W., Higgins, W., Janowiak, J., Mo, K. C., Ropelewski, C., Wang,  
2293 J., Leetmaa, A., Reynolds, R., Jenne, R., and Joseph, D.: The NCEP/NCAR 40-Year Reanalysis Project, 77,

- 2294 437–472, [https://doi.org/10.1175/1520-0477\(1996\)077<0437:TNYRP>2.0.CO;2](https://doi.org/10.1175/1520-0477(1996)077<0437:TNYRP>2.0.CO;2), 1996.
- 2295 Kato, E., Kinoshita, T., Ito, A., Kawamiya, M., and Yamagata, Y.: Evaluation of spatially explicit emission  
2296 scenario of land-use change and biomass burning using a process-based biogeochemical model, 8, 104–122,  
2297 <https://doi.org/10.1080/1747423X.2011.628705>, 2013.
- 2298 Keeling, C. D., Bacastow, R. B., Bainbridge, A. E., Ekdahl, C. A., Guenther, P. R., Waterman, L. S., and Chin,  
2299 J. F. S.: Atmospheric carbon dioxide variations at Mauna Loa Observatory, Hawaii, 28, 538–551,  
2300 <https://doi.org/10.1111/j.2153-3490.1976.tb00701.x>, 1976.
- 2301 Keeling, R. F. and Manning, A. C.: 5.15 - Studies of Recent Changes in Atmospheric O<sub>2</sub> Content, in: *Treatise*  
2302 *on Geochemistry (Second Edition)*, edited by: Holland, H. D. and Turekian, K. K., Elsevier, Oxford, 385–404,  
2303 <https://doi.org/10.1016/B978-0-08-095975-7.00420-4>, 2014.
- 2304 Keppler, L. and Landschützer, P.: Regional Wind Variability Modulates the Southern Ocean Carbon Sink, *Sci*  
2305 *Rep*, 9, 7384, <https://doi.org/10.1038/s41598-019-43826-y>, 2019.
- 2306 Khatiwala, S., Primeau, F., and Hall, T.: Reconstruction of the history of anthropogenic CO<sub>2</sub> concentrations in  
2307 the ocean, *Nature*, 462, 346–349, <https://doi.org/10.1038/nature08526>, 2009.
- 2308 Khatiwala, S., Tanhua, T., Mikaloff Fletcher, S., Gerber, M., Doney, S. C., Graven, H. D., Gruber, N.,  
2309 McKinley, G. A., Murata, A., Ríos, A. F., and Sabine, C. L.: Global ocean storage of anthropogenic carbon,  
2310 *Biogeosciences*, 10, 2169–2191, <https://doi.org/10.5194/bg-10-2169-2013>, 2013.
- 2311 Klein Goldewijk, K., Beusen, A., Doelman, J., and Stehfest, E.: Anthropogenic land use estimates for the  
2312 Holocene – HYDE 3.2, *Earth Syst. Sci. Data*, 9, 927–953, <https://doi.org/10.5194/essd-9-927-2017>, 2017a.
- 2313 Klein Goldewijk, K., Dekker, S. C., and van Zanden, J. L.: Per-capita estimations of long-term historical land  
2314 use and the consequences for global change research, *Journal of Land Use Science*, 1747423X.2017.1354938,  
2315 <https://doi.org/10.1080/1747423X.2017.1354938>, 2017b.
- 2316 Kobayashi, S., Ota, Y., Harada, Y., Ebata, A., Moriya, M., Onoda, H., Onogi, K., Kamahori, H., Kobayashi, C.,  
2317 Endo, H., Miyaoka, K., and Takahashi, K.: The JRA-55 Reanalysis: General Specifications and Basic  
2318 Characteristics, *Journal of the Meteorological Society of Japan*, 93, 5–48, <https://doi.org/10.2151/jmsj.2015-001>, 2015.
- 2320 Kong, Y., Zheng, B., Zhang, Q., and He, K.: Global and regional carbon budget for 2015–2020 inferred from  
2321 OCO-2 based on an ensemble Kalman filter coupled with GEOS-Chem, *Atmospheric Chem. Phys.*, 22, 10769–  
2322 10788, <https://doi.org/10.5194/acp-22-10769-2022>, 2022.
- 2323 Korsbakken, J. I., Peters, G. P., and Andrew, R. M.: Uncertainties around reductions in China’s coal use and  
2324 CO<sub>2</sub> emissions, *Nature Clim Change*, 6, 687–690, <https://doi.org/10.1038/nclimate2963>, 2016.
- 2325 Krinner, G., Viovy, N., de Noblet-Ducoudré, N., Ogée, J., Polcher, J., Friedlingstein, P., Ciais, P., Sitch, S., and  
2326 Prentice, I. C.: A dynamic global vegetation model for studies of the coupled atmosphere-biosphere system:

- 2327 DVGM for coupled climate studies, *Global Biogeochem. Cycles*, 19, <https://doi.org/10.1029/2003GB002199>,  
2328 2005.
- 2329 Lacroix, F., Ilyina, T., and Hartmann, J.: Oceanic CO<sub>2</sub> outgassing and biological production hotspots induced  
2330 by pre-industrial river loads of nutrients and carbon in a global modeling approach, *Biogeosciences*, 17, 55–88,  
2331 <https://doi.org/10.5194/bg-17-55-2020>, 2020.
- 2332 Lacroix, F., Ilyina, T., Mathis, M., Laruelle, G. G., and Regnier, P.: Historical increases in land-derived nutrient  
2333 inputs may alleviate effects of a changing physical climate on the oceanic carbon cycle, *Glob Change Biol*, 27,  
2334 5491–5513, <https://doi.org/10.1111/gcb.15822>, 2021.
- 2335 Landschützer, P., Gruber, N., Bakker, D. C. E., Schuster, U., Nakaoka, S., Payne, M. R., Sasse, T. P., and Zeng,  
2336 J.: A neural network-based estimate of the seasonal to inter-annual variability of the Atlantic Ocean carbon sink,  
2337 *Biogeosciences*, 10, 7793–7815, <https://doi.org/10.5194/bg-10-7793-2013>, 2013.
- 2338 Landschützer, P., Gruber, N., Bakker, D. C. E., and Schuster, U.: Recent variability of the global ocean carbon  
2339 sink, *Global Biogeochem. Cycles*, 28, 927–949, <https://doi.org/10.1002/2014GB004853>, 2014.
- 2340 Landschützer, P., Gruber, N., Haumann, F. A., Rödenbeck, C., Bakker, D. C. E., van Heuven, S., Hoppema, M.,  
2341 Metzl, N., Sweeney, C., Takahashi, T., Tilbrook, B., and Wanninkhof, R.: The reinvigoration of the Southern  
2342 Ocean carbon sink, *Science*, 349, 1221–1224, <https://doi.org/10.1126/science.aab2620>, 2015.
- 2343 Landschützer, P., Gruber, N., and Bakker, D. C. E.: Decadal variations and trends of the global ocean carbon  
2344 sink: decadal air-sea CO<sub>2</sub> flux variability, *Global Biogeochem. Cycles*, 30, 1396–1417,  
2345 <https://doi.org/10.1002/2015GB005359>, 2016.
- 2346 Landschützer, P., Laruelle, G. G., Roobaert, A., and Regnier, P.: A uniform pCO<sub>2</sub> climatology combining open  
2347 and coastal oceans, 12, 2537–2553, <https://doi.org/10.5194/essd-12-2537-2020>, 2020.
- 2348 Lang, F., Ackermann, L., Huang, Y., Truong, S. C. H., Siems, S. T., and Manton, M. J.: A climatology of open  
2349 and closed mesoscale cellular convection over the Southern Ocean derived from Himawari-8 observations, 1–  
2350 27, <https://doi.org/10.5194/acp-2021-681>, 2021.
- 2351 Lasslop, G., Reichstein, M., Papale, D., Richardson, A. D., Arneeth, A., Barr, A., Stoy, P., and Wohlfahrt, G.:  
2352 Separation of net ecosystem exchange into assimilation and respiration using a light response curve approach:  
2353 critical issues and global evaluation: Separation of NEE into GPP and RECO, 16, 187–208,  
2354 <https://doi.org/10.1111/j.1365-2486.2009.02041.x>, 2010.
- 2355 Lawrence, D. M., Fisher, R. A., Koven, C. D., Oleson, K. W., Swenson, S. C., Bonan, G., Collier, N., Ghimire,  
2356 B., van Kampenhout, L., Kennedy, D., Kluzek, E., Lawrence, P. J., Li, F., Li, H., Lombardozzi, D., Riley, W. J.,  
2357 Sacks, W. J., Shi, M., Vertenstein, M., Wieder, W. R., Xu, C., Ali, A. A., Badger, A. M., Bisht, G., van den  
2358 Broeke, M., Brunke, M. A., Burns, S. P., Buzan, J., Clark, M., Craig, A., Dahlin, K., Drewniak, B., Fisher, J. B.,  
2359 Flanner, M., Fox, A. M., Gentine, P., Hoffman, F., Keppel-Aleks, G., Knox, R., Kumar, S., Lenaerts, J., Leung,  
2360 L. R., Lipscomb, W. H., Lu, Y., Pandey, A., Pelletier, J. D., Perket, J., Randerson, J. T., Ricciuto, D. M.,

2361 Sanderson, B. M., Slater, A., Subin, Z. M., Tang, J., Thomas, R. Q., Val Martin, M., and Zeng, X.: The  
 2362 Community Land Model Version 5: Description of New Features, Benchmarking, and Impact of Forcing  
 2363 Uncertainty, 11, 4245–4287, <https://doi.org/10.1029/2018MS001583>, 2019.

2364 Le Quéré, C., Rödenbeck, C., Buitenhuis, E. T., Conway, T. J., Langenfelds, R., Gomez, A., Labuschagne, C.,  
 2365 Ramonet, M., Nakazawa, T., Metzl, N., Gillett, N., and Heimann, M.: Saturation of the Southern Ocean CO<sub>2</sub>  
 2366 Sink Due to Recent Climate Change, 316, 1735–1738, <https://doi.org/10.1126/science.1136188>, 2007.

2367 Le Quéré, C., Raupach, M. R., Canadell, J. G., Marland, G., Bopp, L., Ciais, P., Conway, T. J., Doney, S. C.,  
 2368 Feely, R. A., Foster, P., Friedlingstein, P., Gurney, K., Houghton, R. A., House, J. I., Huntingford, C., Levy, P.  
 2369 E., Lomas, M. R., Majkut, J., Metzl, N., Ometto, J. P., Peters, G. P., Prentice, I. C., Randerson, J. T., Running,  
 2370 S. W., Sarmiento, J. L., Schuster, U., Sitch, S., Takahashi, T., Viovy, N., van der Werf, G. R., and Woodward,  
 2371 F. I.: Trends in the sources and sinks of carbon dioxide, *Nature Geosci*, 2, 831–836,  
 2372 <https://doi.org/10.1038/ngeo689>, 2009.

2373 Le Quéré, C., Andres, R. J., Boden, T., Conway, T., Houghton, R. A., House, J. I., Marland, G., Peters, G. P.,  
 2374 van der Werf, G. R., Ahlström, A., Andrew, R. M., Bopp, L., Canadell, J. G., Ciais, P., Doney, S. C., Enright,  
 2375 C., Friedlingstein, P., Huntingford, C., Jain, A. K., Jourdain, C., Kato, E., Keeling, R. F., Klein Goldewijk, K.,  
 2376 Levis, S., Levy, P., Lomas, M., Poulter, B., Raupach, M. R., Schwinger, J., Sitch, S., Stocker, B. D., Viovy, N.,  
 2377 Zaehle, S., and Zeng, N.: The global carbon budget 1959–2011, *Earth Syst. Sci. Data*, 5, 165–185,  
 2378 <https://doi.org/10.5194/essd-5-165-2013>, 2013.

2379 Le Quéré, C., Peters, G. P., Andres, R. J., Andrew, R. M., Boden, T. A., Ciais, P., Friedlingstein, P., Houghton,  
 2380 R. A., Marland, G., Moriarty, R., Sitch, S., Tans, P., Arneeth, A., Arvanitis, A., Bakker, D. C. E., Bopp, L.,  
 2381 Canadell, J. G., Chini, L. P., Doney, S. C., Harper, A., Harris, I., House, J. I., Jain, A. K., Jones, S. D., Kato, E.,  
 2382 Keeling, R. F., Klein Goldewijk, K., Körtzinger, A., Koven, C., Lefèvre, N., Maignan, F., Omar, A., Ono, T.,  
 2383 Park, G.-H., Pfeil, B., Poulter, B., Raupach, M. R., Regnier, P., Rödenbeck, C., Saito, S., Schwinger, J.,  
 2384 Segschneider, J., Stocker, B. D., Takahashi, T., Tilbrook, B., van Heuven, S., Viovy, N., Wanninkhof, R.,  
 2385 Wiltshire, A., and Zaehle, S.: Global carbon budget 2013, *Earth Syst. Sci. Data*, 6, 235–263,  
 2386 <https://doi.org/10.5194/essd-6-235-2014>, 2014.

2387 Le Quéré, C., Moriarty, R., Andrew, R. M., Peters, G. P., Ciais, P., Friedlingstein, P., Jones, S. D., Sitch, S.,  
 2388 Tans, P., Arneeth, A., Boden, T. A., Bopp, L., Bozec, Y., Canadell, J. G., Chini, L. P., Chevallier, F., Cosca, C.  
 2389 E., Harris, I., Hoppema, M., Houghton, R. A., House, J. I., Jain, A. K., Johannessen, T., Kato, E., Keeling, R. F.,  
 2390 Kitidis, V., Klein Goldewijk, K., Koven, C., Landa, C. S., Landschützer, P., Lenton, A., Lima, I. D., Marland,  
 2391 G., Mathis, J. T., Metzl, N., Nojiri, Y., Olsen, A., Ono, T., Peng, S., Peters, W., Pfeil, B., Poulter, B., Raupach,  
 2392 M. R., Regnier, P., Rödenbeck, C., Saito, S., Salisbury, J. E., Schuster, U., Schwinger, J., Séférian, R.,  
 2393 Segschneider, J., Steinhoff, T., Stocker, B. D., Sutton, A. J., Takahashi, T., Tilbrook, B., van der Werf, G. R.,  
 2394 Viovy, N., Wang, Y.-P., Wanninkhof, R., Wiltshire, A., and Zeng, N.: Global carbon budget 2014, *Earth Syst.*  
 2395 *Sci. Data*, 7, 47–85, <https://doi.org/10.5194/essd-7-47-2015>, 2015a.

2396 Le Quéré, C., Moriarty, R., Andrew, R. M., Canadell, J. G., Sitch, S., Korsbakken, J. I., Friedlingstein, P.,  
 2397 Peters, G. P., Andres, R. J., Boden, T. A., Houghton, R. A., House, J. I., Keeling, R. F., Tans, P., Arneeth, A.,

2398 Bakker, D. C. E., Barbero, L., Bopp, L., Chang, J., Chevallier, F., Chini, L. P., Ciais, P., Fader, M., Feely, R. A.,  
 2399 Gkritzalis, T., Harris, I., Hauck, J., Ilyina, T., Jain, A. K., Kato, E., Kitidis, V., Klein Goldewijk, K., Koven, C.,  
 2400 Landschützer, P., Lauvset, S. K., Lefèvre, N., Lenton, A., Lima, I. D., Metzl, N., Millero, F., Munro, D. R.,  
 2401 Murata, A., Nabel, J. E. M. S., Nakaoka, S., Nojiri, Y., O'Brien, K., Olsen, A., Ono, T., Pérez, F. F., Pfeil, B.,  
 2402 Pierrot, D., Poulter, B., Rehder, G., Rödenbeck, C., Saito, S., Schuster, U., Schwinger, J., Séférian, R.,  
 2403 Steinhoff, T., Stocker, B. D., Sutton, A. J., Takahashi, T., Tilbrook, B., van der Laan-Luijkx, I. T., van der Werf,  
 2404 G. R., van Heuven, S., Vandemark, D., Viovy, N., Wiltshire, A., Zaehle, S., and Zeng, N.: Global Carbon  
 2405 Budget 2015, *Earth Syst. Sci. Data*, 7, 349–396, <https://doi.org/10.5194/essd-7-349-2015>, 2015b.

2406 Le Quéré, C., Andrew, R. M., Canadell, J. G., Sitch, S., Korsbakken, J. I., Peters, G. P., Manning, A. C., Boden,  
 2407 T. A., Tans, P. P., Houghton, R. A., Keeling, R. F., Alin, S., Andrews, O. D., Anthoni, P., Barbero, L., Bopp, L.,  
 2408 Chevallier, F., Chini, L. P., Ciais, P., Currie, K., Delire, C., Doney, S. C., Friedlingstein, P., Gkritzalis, T.,  
 2409 Harris, I., Hauck, J., Haverd, V., Hoppema, M., Klein Goldewijk, K., Jain, A. K., Kato, E., Körtzinger, A.,  
 2410 Landschützer, P., Lefèvre, N., Lenton, A., Lienert, S., Lombardozzi, D., Melton, J. R., Metzl, N., Millero, F.,  
 2411 Monteiro, P. M. S., Munro, D. R., Nabel, J. E. M. S., Nakaoka, S., O'Brien, K., Olsen, A., Omar, A. M., Ono,  
 2412 T., Pierrot, D., Poulter, B., Rödenbeck, C., Salisbury, J., Schuster, U., Schwinger, J., Séférian, R., Skjelvan, I.,  
 2413 Stocker, B. D., Sutton, A. J., Takahashi, T., Tian, H., Tilbrook, B., van der Laan-Luijkx, I. T., van der Werf, G.  
 2414 R., Viovy, N., Walker, A. P., Wiltshire, A. J., and Zaehle, S.: Global Carbon Budget 2016, *Earth Syst. Sci. Data*,  
 2415 8, 605–649, <https://doi.org/10.5194/essd-8-605-2016>, 2016.

2416 Le Quéré, C., Andrew, R. M., Friedlingstein, P., Sitch, S., Pongratz, J., Manning, A. C., Korsbakken, J. I.,  
 2417 Peters, G. P., Canadell, J. G., Jackson, R. B., Boden, T. A., Tans, P. P., Andrews, O. D., Arora, V. K., Bakker,  
 2418 D. C. E., Barbero, L., Becker, M., Betts, R. A., Bopp, L., Chevallier, F., Chini, L. P., Ciais, P., Cosca, C. E.,  
 2419 Cross, J., Currie, K., Gasser, T., Harris, I., Hauck, J., Haverd, V., Houghton, R. A., Hunt, C. W., Hurtt, G.,  
 2420 Ilyina, T., Jain, A. K., Kato, E., Kautz, M., Keeling, R. F., Klein Goldewijk, K., Körtzinger, A., Landschützer,  
 2421 P., Lefèvre, N., Lenton, A., Lienert, S., Lima, I., Lombardozzi, D., Metzl, N., Millero, F., Monteiro, P. M. S.,  
 2422 Munro, D. R., Nabel, J. E. M. S., Nakaoka, S., Nojiri, Y., Padin, X. A., Peregon, A., Pfeil, B., Pierrot, D.,  
 2423 Poulter, B., Rehder, G., Reimer, J., Rödenbeck, C., Schwinger, J., Séférian, R., Skjelvan, I., Stocker, B. D.,  
 2424 Tian, H., Tilbrook, B., Tubiello, F. N., van der Laan-Luijkx, I. T., van der Werf, G. R., van Heuven, S., Viovy,  
 2425 N., Vuichard, N., Walker, A. P., Watson, A. J., Wiltshire, A. J., Zaehle, S., and Zhu, D.: Global Carbon Budget  
 2426 2017, *Earth Syst. Sci. Data*, 10, 405–448, <https://doi.org/10.5194/essd-10-405-2018>, 2018a.

2427 Le Quéré, C., Andrew, R. M., Friedlingstein, P., Sitch, S., Hauck, J., Pongratz, J., Pickers, P. A., Korsbakken, J.  
 2428 I., Peters, G. P., Canadell, J. G., Arneeth, A., Arora, V. K., Barbero, L., Bastos, A., Bopp, L., Chevallier, F.,  
 2429 Chini, L. P., Ciais, P., Doney, S. C., Gkritzalis, T., Goll, D. S., Harris, I., Haverd, V., Hoffman, F. M.,  
 2430 Hoppema, M., Houghton, R. A., Hurtt, G., Ilyina, T., Jain, A. K., Johannessen, T., Jones, C. D., Kato, E.,  
 2431 Keeling, R. F., Klein Goldewijk, K., Landschützer, P., Lefèvre, N., Lienert, S., Liu, Z., Lombardozzi, D., Metzl,  
 2432 N., Munro, D. R., Nabel, J. E. M. S., Nakaoka, S., Neill, C., Olsen, A., Ono, T., Patra, P., Peregon, A., Peters,  
 2433 W., Peylin, P., Pfeil, B., Pierrot, D., Poulter, B., Rehder, G., Resplandy, L., Robertson, E., Rocher, M.,  
 2434 Rödenbeck, C., Schuster, U., Schwinger, J., Séférian, R., Skjelvan, I., Steinhoff, T., Sutton, A., Tans, P. P.,  
 2435 Tian, H., Tilbrook, B., Tubiello, F. N., van der Laan-Luijkx, I. T., van der Werf, G. R., Viovy, N., Walker, A.  
 2436 P., Wiltshire, A. J., Wright, R., Zaehle, S., and Zheng, B.: Global Carbon Budget 2018, *Earth Syst. Sci. Data*,

2437 10, 2141–2194, <https://doi.org/10.5194/essd-10-2141-2018>, 2018b.

2438 Le Quéré, C., Korsbakken, J. I., Wilson, C., Tosun, J., Andrew, R., Andres, R. J., Canadell, J. G., Jordan, A.,  
2439 Peters, G. P., and van Vuuren, D. P.: Drivers of declining CO<sub>2</sub> emissions in 18 developed economies, *Nat.*  
2440 *Clim. Chang.*, 9, 213–217, <https://doi.org/10.1038/s41558-019-0419-7>, 2019.

2441 Le Quéré, C., Peters, G. P., Friedlingstein, P., Andrew, R. M., Canadell, J. G., Davis, S. J., Jackson, R. B., and  
2442 Jones, M. W.: Fossil CO<sub>2</sub> emissions in the post-COVID-19 era, *Nat. Clim. Chang.*, 11, 197–199,  
2443 <https://doi.org/10.1038/s41558-021-01001-0>, 2021.

2444 Li, H. and Ilyina, T.: Current and Future Decadal Trends in the Oceanic Carbon Uptake Are Dominated by  
2445 Internal Variability, *Geophys. Res. Lett.*, 45, 916–925, <https://doi.org/10.1002/2017GL075370>, 2018.

2446 Li, W., Ciais, P., Peng, S., Yue, C., Wang, Y., Thurner, M., Saatchi, S. S., Arneeth, A., Avitabile, V., Carvalhais,  
2447 N., Harper, A. B., Kato, E., Koven, C., Liu, Y. Y., Nabel, J. E. M. S., Pan, Y., Pongratz, J., Poulter, B., Pugh, T.  
2448 A. M., Santoro, M., Sitch, S., Stocker, B. D., Viovy, N., Wiltshire, A., Yousefpour, R., and Zaehle, S.: Land-use  
2449 and land-cover change carbon emissions between 1901 and 2012 constrained by biomass observations,  
2450 *Biogeosciences*, 14, 5053–5067, <https://doi.org/10.5194/bg-14-5053-2017>, 2017.

2451 Liao, E., Resplandy, L., Liu, J., and Bowman, K. W.: Amplification of the Ocean Carbon Sink During El Niños:  
2452 Role of Poleward Ekman Transport and Influence on Atmospheric CO<sub>2</sub>, 34, e2020GB006574,  
2453 <https://doi.org/10.1029/2020GB006574>, 2020.

2454 Lienert, S. and Joos, F.: A Bayesian ensemble data assimilation to constrain model parameters and land-use  
2455 carbon emissions, *Biogeosciences*, 15, 2909–2930, <https://doi.org/10.5194/bg-15-2909-2018>, 2018.

2456 Liu, J., Baskaran, L., Bowman, K., Schimel, D., Bloom, A. A., Parazoo, N. C., Oda, T., Carroll, D.,  
2457 Menemenlis, D., Joiner, J., Commane, R., Daube, B., Gatti, L. V., McKain, K., Miller, J., Stephens, B. B.,  
2458 Sweeney, C., and Wofsy, S.: Carbon Monitoring System Flux Net Biosphere Exchange 2020 (CMS-Flux NBE  
2459 2020), 13, 299–330, <https://doi.org/10.5194/essd-13-299-2021>, 2021.

2460 Liu, Z., Guan, D., Wei, W., Davis, S. J., Ciais, P., Bai, J., Peng, S., Zhang, Q., Hubacek, K., Marland, G.,  
2461 Andres, R. J., Crawford-Brown, D., Lin, J., Zhao, H., Hong, C., Boden, T. A., Feng, K., Peters, G. P., Xi, F.,  
2462 Liu, J., Li, Y., Zhao, Y., Zeng, N., and He, K.: Reduced carbon emission estimates from fossil fuel combustion  
2463 and cement production in China, *Nature*, 524, 335–338, <https://doi.org/10.1038/nature14677>, 2015.

2464 Liu, Z., Ciais, P., Deng, Z., Davis, S. J., Zheng, B., Wang, Y., Cui, D., Zhu, B., Dou, X., Ke, P., Sun, T., Guo,  
2465 R., Zhong, H., Boucher, O., Bréon, F.-M., Lu, C., Guo, R., Xue, J., Boucher, E., Tanaka, K., and Chevallier, F.:  
2466 Carbon Monitor, a near-real-time daily dataset of global CO<sub>2</sub> emission from fossil fuel and cement production,  
2467 *Sci Data*, 7, 392, <https://doi.org/10.1038/s41597-020-00708-7>, 2020a.

2468 Liu, Z., Ciais, P., Deng, Z., Lei, R., Davis, S. J., Feng, S., Zheng, B., Cui, D., Dou, X., Zhu, B., Guo, R., Ke, P.,  
2469 Sun, T., Lu, C., He, P., Wang, Y., Yue, X., Wang, Y., Lei, Y., Zhou, H., Cai, Z., Wu, Y., Guo, R., Han, T., Xue,  
2470 J., Boucher, O., Boucher, E., Chevallier, F., Tanaka, K., Wei, Y., Zhong, H., Kang, C., Zhang, N., Chen, B., Xi,



2471 F., Liu, M., Bréon, F.-M., Lu, Y., Zhang, Q., Guan, D., Gong, P., Kammen, D. M., He, K., and Schellnhuber, H.  
2472 J.: Near-real-time monitoring of global CO<sub>2</sub> emissions reveals the effects of the COVID-19 pandemic, *Nat*  
2473 *Commun*, 11, 5172, <https://doi.org/10.1038/s41467-020-18922-7>, 2020b.

2474 Long, M. C., Moore, J. K., Lindsay, K., Levy, M., Doney, S. C., Luo, J. Y., et al., 2021. Simulations with the  
2475 Marine Biogeochemistry Library (MARBL). *Journal of Advances in Modeling Earth Systems*, 13,  
2476 e2021MS002647, <https://doi.org/10.1029/2021MS002647>.

2477 Ma, L., Hurtt, G. C., Chini, L. P., Sahajpal, R., Pongratz, J., Frohling, S., Stehfest, E., Klein Goldewijk, K.,  
2478 O’Leary, D., and Doelman, J. C.: Global rules for translating land-use change (LUH2) to land-cover change for  
2479 CMIP6 using GLM2, *Geosci. Model Dev.*, 13, 3203–3220, <https://doi.org/10.5194/gmd-13-3203-2020>, 2020.

2480 Maki, T., Ikegami, M., Fujita, T., Hirahara, T., Yamada, K., Mori, K., Takeuchi, A., Tsutsumi, Y., Suda, K., and  
2481 Conway, T. J.: New technique to analyse global distributions of CO<sub>2</sub> concentrations and fluxes from non-  
2482 processed observational data, 62, 797–809, <https://doi.org/10.1111/j.1600-0889.2010.00488.x>, 2010.

2483 MapBiomass: MapBiomass Collection 6, available at: <https://plataforma.brasil.mapbiomas.org/>, last access: 25  
2484 September 2022, 2022.

2485 Marland, G.: Uncertainties in Accounting for CO<sub>2</sub> From Fossil Fuels, 12, 136–139,  
2486 <https://doi.org/10.1111/j.1530-9290.2008.00014.x>, 2008.

2487 Marland, G., Hamal, K., and Jonas, M.: How Uncertain Are Estimates of CO<sub>2</sub> Emissions?, 13, 4–7,  
2488 <https://doi.org/10.1111/j.1530-9290.2009.00108.x>, 2009.

2489 Masarie, K. A. and Tans, P. P.: Extension and integration of atmospheric carbon dioxide data into a globally  
2490 consistent measurement record, *J. Geophys. Res.*, 100, 11593, <https://doi.org/10.1029/95JD00859>, 1995.

2491 Mather, A.: The transition from deforestation to reforestation in Europe., 35–52, 2001.

2492 Matricardi, E. A. T., Skole, D. L., Costa, O. B., Pedlowski, M. A., Samek, J. H., and Miguel, E. P.: Long-term  
2493 forest degradation surpasses deforestation in the Brazilian Amazon, 369, 1378–1382,  
2494 <https://doi.org/10.1126/science.abb3021>, 2020.

2495 Mauritsen, T., Bader, J., Becker, T., Behrens, J., Bittner, M., Brokopf, R., Brovkin, V., Claussen, M., Crueger,  
2496 T., Esch, M., Fast, I., Fiedler, S., Fläschner, D., Gayler, V., Giorgetta, M., Goll, D. S., Haak, H., Hagemann, S.,  
2497 Hedemann, C., Hohenegger, C., Ilyina, T., Jahns, T., Jimenéz-de-la-Cuesta, D., Jungclaus, J., Kleinen, T.,  
2498 Kloster, S., Kracher, D., Kinne, S., Kleberg, D., Lasslop, G., Kornblueh, L., Marotzke, J., Matei, D., Meraner,  
2499 K., Mikolajewicz, U., Modali, K., Möbis, B., Müller, W. A., Nabel, J. E. M. S., Nam, C. C. W., Notz, D.,  
2500 Nyawira, S.-S., Paulsen, H., Peters, K., Pincus, R., Pohlmann, H., Pongratz, J., Popp, M., Raddatz, T. J., Rast,  
2501 S., Redler, R., Reick, C. H., Rohrschneider, T., Schemann, V., Schmidt, H., Schnur, R., Schulzweida, U., Six,  
2502 K. D., Stein, L., Stemmler, I., Stevens, B., von Storch, J.-S., Tian, F., Voigt, A., Vrese, P., Wieners, K.-H.,  
2503 Wilkenskjaeld, S., Winkler, A., and Roeckner, E.: Developments in the MPI-M Earth System Model version 1.2  
2504 (MPI-ESM1.2) and Its Response to Increasing CO<sub>2</sub>, 11, 998–1038, <https://doi.org/10.1029/2018MS001400>,

2505 2019.

2506 McGrath, M. J., Luyssaert, S., Meyfroidt, P., Kaplan, J. O., Bürgi, M., Chen, Y., Erb, K., Gimmi, U.,  
 2507 McInerney, D., Naudts, K., Otto, J., Pasztor, F., Ryder, J., Schelhaas, M.-J., and Valade, A.: Reconstructing  
 2508 European forest management from 1600 to 2010, 12, 4291–4316, <https://doi.org/10.5194/bg-12-4291-2015>,  
 2509 2015.

2510 McKinley, G. A., Pilcher, D. J., Fay, A. R., Lindsay, K., Long, M. C., and Lovenduski, N. S.: Timescales for  
 2511 detection of trends in the ocean carbon sink, *Nature*, 530, 469–472, <https://doi.org/10.1038/nature16958>, 2016.

2512 McKinley, G. A., Fay, A. R., Eddebbar, Y. A., Gloege, L., and Lovenduski, N. S.: External Forcing Explains  
 2513 Recent Decadal Variability of the Ocean Carbon Sink, *AGU Advances*, 1,  
 2514 <https://doi.org/10.1029/2019AV000149>, 2020.

2515 McNeil, B. I.: Anthropogenic CO<sub>2</sub> Uptake by the Ocean Based on the Global Chlorofluorocarbon Data Set, 299,  
 2516 235–239, <https://doi.org/10.1126/science.1077429>, 2003.

2517 Meiyappan, P., Jain, A. K., and House, J. I.: Increased influence of nitrogen limitation on CO<sub>2</sub> emissions from  
 2518 future land use and land use change, *Global Biogeochem. Cycles*, 29, 1524–1548,  
 2519 <https://doi.org/10.1002/2015GB005086>, 2015.

2520 Melton, J. R., Arora, V. K., Wisernig-Cojoc, E., Seiler, C., Fortier, M., Chan, E., and Teckentrup, L.: CLASSIC  
 2521 v1.0: the open-source community successor to the Canadian Land Surface Scheme (CLASS) and the Canadian  
 2522 Terrestrial Ecosystem Model (CTEM) – Part 1: Model framework and site-level performance, *Geosci. Model*  
 2523 *Dev.*, 13, 2825–2850, <https://doi.org/10.5194/gmd-13-2825-2020>, 2020.

2524 Mercado, L. M., Bellouin, N., Sitch, S., Boucher, O., Huntingford, C., Wild, M., and Cox, P. M.: Impact of  
 2525 changes in diffuse radiation on the global land carbon sink, *Nature*, 458, 1014–1017,  
 2526 <https://doi.org/10.1038/nature07949>, 2009.

2527 Merchant, C. J., Embury, O., Bulgin, C. E., Block, T., Corlett, G. K., Fiedler, E., Good, S. A., Mittaz, J.,  
 2528 Rayner, N. A., Berry, D., Eastwood, S., Taylor, M., Tsushima, Y., Waterfall, A., Wilson, R., and Donlon, C.:  
 2529 Satellite-based time-series of sea-surface temperature since 1981 for climate applications, *Sci. Data*, 6, 223,  
 2530 <https://doi.org/10.1038/s41597-019-0236-x>, 2019.

2531 Mikaloff Fletcher, S. E., Gruber, N., Jacobson, A. R., Doney, S. C., Dutkiewicz, S., Gerber, M., Follows, M.,  
 2532 Joos, F., Lindsay, K., Menemenlis, D., Mouchet, A., Müller, S. A., and Sarmiento, J. L.: Inverse estimates of  
 2533 anthropogenic CO<sub>2</sub> uptake, transport, and storage by the ocean: air-sea exchange of anthropogenic carbon,  
 2534 *Global Biogeochem. Cycles*, 20, <https://doi.org/10.1029/2005GB002530>, 2006.

2535 Müller, J. and Joos, F.: Committed and projected future changes in global peatlands – continued transient model  
 2536 simulations since the Last Glacial Maximum, *Biogeosciences*, 18, 3657–3687, [https://doi.org/10.5194/bg-18-](https://doi.org/10.5194/bg-18-3657-2021)  
 2537 3657-2021, 2021.

2538 Myneni, R. B., Ramakrishna, R., Nemani, R., and Running, S. W.: Estimation of global leaf area index and

2539 absorbed par using radiative transfer models, *IEEE Trans. Geosci. Remote Sensing*, 35, 1380–1393,  
 2540 <https://doi.org/10.1109/36.649788>, 1997.

2541 Naegler, T.: Reconciliation of excess  $^{14}\text{C}$ -constrained global  $\text{CO}_2$  piston velocity estimates, 61, 372–384,  
 2542 <https://doi.org/10.1111/j.1600-0889.2008.00408.x>, 2009.

2543 Nakamura, T., Yamazaki, K., Iwamoto, K., Honda, M., Miyoshi, Y., Ogawa, Y., and Ukita, J.: A negative phase  
 2544 shift of the winter AO/NAO due to the recent Arctic sea-ice reduction in late autumn, 120, 3209–3227,  
 2545 <https://doi.org/10.1002/2014JD022848>, 2015.

2546 Nakano, H., Tsujino, H., Hirabara, M., Yasuda, T., Motoi, T., Ishii, M., and Yamanaka, G.: Uptake mechanism  
 2547 of anthropogenic  $\text{CO}_2$  in the Kuroshio Extension region in an ocean general circulation model, *J. Oceanogr.*, 67,  
 2548 765–783, <https://doi.org/10.1007/s10872-011-0075-7>, 2011.

2549 Narayanan, B., Aguiar, A., and McDougall, R.: Global Trade, Assistance, and Production: The GTAP 9 Data  
 2550 Base, Cent. Glob. Trade Anal. Purdue Univ., available at: [https://](https://www.gtap.agecon.purdue.edu/databases/v9/default.asp)  
 2551 [www.gtap.agecon.purdue.edu/databases/v9/default.asp](https://www.gtap.agecon.purdue.edu/databases/v9/default.asp), last access: 25 September 2022, 2015.

2552 NBS: National Bureau of Statistics of China: Statistical Communiqué of the People’s Republic of China on the  
 2553 2021 National Economic and Social Development, available at:  
 2554 [http://www.stats.gov.cn/english/PressRelease/202202/t20220227\\_1827963.html](http://www.stats.gov.cn/english/PressRelease/202202/t20220227_1827963.html), last access: 25 September  
 2555 2022, 2022.

2556 NCEP: National Centers for Environmental Prediction. ONI Index. Cold & Warm Episodes by Season, available  
 2557 at: [https://origin.cpc.ncep.noaa.gov/products/analysis\\_monitoring/ensostuff/ONI\\_v5.php](https://origin.cpc.ncep.noaa.gov/products/analysis_monitoring/ensostuff/ONI_v5.php), last access: 25  
 2558 September 2022, 2022.

2559 Nightingale, P. D., Liss, P. S., and Schlosser, P.: Measurements of air-sea gas transfer during an open ocean  
 2560 algal bloom, 27, 2117–2120, <https://doi.org/10.1029/2000GL011541>, 2000.

2561 Niwa, Y., Ishijima, K., Ito, A., and Iida, Y.: Toward a long-term atmospheric  $\text{CO}_2$  inversion for elucidating  
 2562 natural carbon fluxes: technical notes of NISMON- $\text{CO}_2$  v2021.1, *Prog. Earth Planet Sci.*, 9, 42,  
 2563 <https://doi.org/10.1186/s40645-022-00502-6>, 2022.

2564 Niwa, Y., Langenfelds, R., Krummel, P., Loh, Zoe, Worthy, Doug, Hatakka, Juha, Aalto, Tuula, Ramonet,  
 2565 Michel, Delmotte, Marc, Schmidt, Martina, Gheusi, Francois, Mihalopoulos, N., Morgui, J.A., Andrews, Arlyn,  
 2566 Dlugokencky, Ed, Lee, John, Sweeney, Colm, Thoning, Kirk, Tans, Pieter, De Wekker, Stephan, Fischer, Marc  
 2567 L., Jaffe, Dan, McKain, Kathryn, Viner, Brian, Miller, John B., Karion, Anna, Miller, Charles, Sloop,  
 2568 Christopher D., Saito, Kazuyuki, Aoki, Shuji, Morimoto, Shinji, Goto, Daisuke, Steinbacher, Martin, Myhre,  
 2569 Cathrine Lund, Hermanssen, Ove, Stephens, Britton, Keeling, Ralph, Afshar, Sara, Paplawsky, Bill, Cox, Adam,  
 2570 Walker, Stephen, Schuldt, Kenneth, Mukai, Hitoshi, Machida, Toshinobu, Sasakawa, Motoki, Nomura, Shohei,  
 2571 Ito, Akihiko, Iida, Yosuke, and Jones, Matthew W.: Long-term global  $\text{CO}_2$  fluxes estimated by NICAM-based  
 2572 Inverse Simulation for Monitoring  $\text{CO}_2$  (NISMON- $\text{CO}_2$ ) (ver.2022.1), <https://doi.org/10.17595/20201127.001>,  
 2573 2020.

2574 Obermeier, W. A., Nabel, J. E. M. S., Loughran, T., Hartung, K., Bastos, A., Havermann, F., Anthoni, P.,  
 2575 Arneth, A., Goll, D. S., Lienert, S., Lombardozzi, D., Luyssaert, S., McGuire, P. C., Melton, J. R., Poulter, B.,  
 2576 Sitch, S., Sullivan, M. O., Tian, H., Walker, A. P., Wiltshire, A. J., Zaehle, S., and Pongratz, J.: Modelled land  
 2577 use and land cover change emissions – a spatio-temporal comparison of different approaches, 12, 635–670,  
 2578 <https://doi.org/10.5194/esd-12-635-2021>, 2021.

2579 O’Rourke, P. R., Smith, S. J., Mott, A., Ahsan, H., McDuffie, E. E., Crippa, M., Klimont, Z., McDonald, B.,  
 2580 Wang, S., Nicholson, M. B., Feng, L., and Hoesly, R. M.: CEDS v\_2021\_04\_21 Release Emission Data,  
 2581 <https://doi.org/10.5281/zenodo.4741285>, 2021.

2582 Orr, J. C., Najjar, R. G., Aumont, O., Bopp, L., Bullister, J. L., Danabasoglu, G., Doney, S. C., Dunne, J. P.,  
 2583 Dutay, J.-C., Graven, H., Griffies, S. M., John, J. G., Joos, F., Levin, I., Lindsay, K., Matear, R. J., McKinley,  
 2584 G. A., Mouchet, A., Oschlies, A., Romanou, A., Schlitzer, R., Tagliabue, A., Tanhua, T., and Yool, A.:  
 2585 Biogeochemical protocols and diagnostics for the CMIP6 Ocean Model Intercomparison Project (OMIP), 10,  
 2586 2169–2199, <https://doi.org/10.5194/gmd-10-2169-2017>, 2017.

2587 O’Sullivan, M., Zhang, Y., Bellouin, N., Harris, I., Mercado, L. M., Sitch, S., Ciais, P., and Friedlingstein, P.:  
 2588 Aerosol–light interactions reduce the carbon budget imbalance, *Environ. Res. Lett.*, 16, 124072,  
 2589 <https://doi.org/10.1088/1748-9326/ac3b77>, 2021.

2590 O’Sullivan, M., Friedlingstein, P., Sitch, S., Anthoni, P., Arneth, A., Arora, V. K., Bastrikov, V., Delire, C.,  
 2591 Goll, D. S., Jain, A., Kato, E., Kennedy, D., Knauer, J., Lienert, S., Lombardozzi, D., McGuire, P. C., Melton, J.  
 2592 R., Nabel, J. E. M. S., Pongratz, J., Poulter, B., Séférian, R., Tian, H., Vuichard, N., Walker, A. P., Yuan, W.,  
 2593 Yue, X., and Zaehle, S.: Process-oriented analysis of dominant sources of uncertainty in the land carbon sink,  
 2594 *Nat. Commun.*, 13, 4781, <https://doi.org/10.1038/s41467-022-32416-8>, 2022.

2595 Palmer, P. I., Feng, L., Baker, D., Chevallier, F., Bösch, H., and Somkuti, P.: Net carbon emissions from  
 2596 African biosphere dominate pan-tropical atmospheric CO<sub>2</sub> signal, *Nat Commun*, 10, 3344,  
 2597 <https://doi.org/10.1038/s41467-019-11097-w>, 2019.

2598 Pan, Y., Birdsey, R. A., Fang, J., Houghton, R., Kauppi, P. E., Kurz, W. A., Phillips, O. L., Shvidenko, A.,  
 2599 Lewis, S. L., Canadell, J. G., Ciais, P., Jackson, R. B., Pacala, S. W., McGuire, A. D., Piao, S., Rautiainen, A.,  
 2600 Sitch, S., and Hayes, D.: A Large and Persistent Carbon Sink in the World’s Forests, *Science*, 333, 988–993,  
 2601 <https://doi.org/10.1126/science.1201609>, 2011.

2602 Patra, P. K., Takigawa, M., Watanabe, S., Chandra, N., Ishijima, K., and Yamashita, Y.: Improved Chemical  
 2603 Tracer Simulation by MIROC4.0-based Atmospheric Chemistry-Transport Model (MIROC4-ACTM), *SOLA*,  
 2604 14, 91–96, <https://doi.org/10.2151/sola.2018-016>, 2018.

2605 Pendrill, F., Persson, U. M., Godar, J., Kastner, T., Moran, D., Schmidt, S., and Wood, R.: Agricultural and  
 2606 forestry trade drives large share of tropical deforestation emissions, *Global Environmental Change*, 56, 1–10,  
 2607 <https://doi.org/10.1016/j.gloenvcha.2019.03.002>, 2019.

2608 Peters, G. P., Andrew, R., and Lennox, J.: Constructing an environmentally-extended multi-regional input–

2609 output table using the GTAP database, *Economic Systems Research*, 23, 131–152,  
2610 <https://doi.org/10.1080/09535314.2011.563234>, 2011a.

2611 Peters, G. P., Minx, J. C., Weber, C. L., and Edenhofer, O.: Growth in emission transfers via international trade  
2612 from 1990 to 2008, *Proceedings of the National Academy of Sciences*, 108, 8903–8908,  
2613 <https://doi.org/10.1073/pnas.1006388108>, 2011b.

2614 Peters, G. P., Davis, S. J., and Andrew, R.: A synthesis of carbon in international trade, *Biogeosciences*, 9,  
2615 3247–3276, <https://doi.org/10.5194/bg-9-3247-2012>, 2012a.

2616 Peters, G. P., Marland, G., Le Quéré, C., Boden, T., Canadell, J. G., and Raupach, M. R.: Rapid growth in CO<sub>2</sub>  
2617 emissions after the 2008–2009 global financial crisis, *Nature Clim Change*, 2, 2–4,  
2618 <https://doi.org/10.1038/nclimate1332>, 2012b.

2619 Peters, G. P., Andrew, R. M., Boden, T., Canadell, J. G., Ciais, P., Le Quéré, C., Marland, G., Raupach, M. R.,  
2620 and Wilson, C.: The challenge to keep global warming below 2 °C, *Nature Clim Change*, 3, 4–6,  
2621 <https://doi.org/10.1038/nclimate1783>, 2013.

2622 Peters, G. P., Le Quéré, C., Andrew, R. M., Canadell, J. G., Friedlingstein, P., Ilyina, T., Jackson, R. B., Joos,  
2623 F., Korsbakken, J. I., McKinley, G. A., Sitch, S., and Tans, P.: Towards real-time verification of CO<sub>2</sub> emissions,  
2624 *Nature Clim Change*, 7, 848–850, <https://doi.org/10.1038/s41558-017-0013-9>, 2017.

2625 Peters, G. P., Andrew, R. M., Canadell, J. G., Friedlingstein, P., Jackson, R. B., Korsbakken, J. I., Le Quéré, C.,  
2626 and Peregon, A.: Carbon dioxide emissions continue to grow amidst slowly emerging climate policies, *Nat.*  
2627 *Clim. Chang.*, 10, 3–6, <https://doi.org/10.1038/s41558-019-0659-6>, 2020.

2628 Petrescu, A. M. R., Peters, G. P., Janssens-Maenhout, G., Ciais, P., Tubiello, F. N., Grassi, G., Nabuurs, G.-J.,  
2629 Leip, A., Carmona-Garcia, G., Winiwarter, W., Höglund-Isaksson, L., Günther, D., Solazzo, E., Kiesow, A.,  
2630 Bastos, A., Pongratz, J., Nabel, J. E. M. S., Conchedda, G., Pilli, R., Andrew, R. M., Schelhaas, M.-J., and  
2631 Dolman, A. J.: European anthropogenic AFOLU greenhouse gas emissions: a review and benchmark data, *Earth*  
2632 *Syst. Sci. Data*, 12, 961–1001, <https://doi.org/10.5194/essd-12-961-2020>, 2020.

2633 Pfeil, B., Olsen, A., Bakker, D. C. E., Hankin, S., Koyuk, H., Kozyr, A., Malczyk, J., Manke, A., Metzl, N.,  
2634 Sabine, C. L., Akl, J., Alin, S. R., Bates, N., Bellerby, R. G. J., Borges, A., Boutin, J., Brown, P. J., Cai, W.-J.,  
2635 Chavez, F. P., Chen, A., Cosca, C., Fassbender, A. J., Feely, R. A., González-Dávila, M., Goyet, C., Hales, B.,  
2636 Hardman-Mountford, N., Heinze, C., Hood, M., Hoppema, M., Hunt, C. W., Hydes, D., Ishii, M., Johannessen,  
2637 T., Jones, S. D., Key, R. M., Körtzinger, A., Landschützer, P., Lauvset, S. K., Lefèvre, N., Lenton, A.,  
2638 Laurantou, A., Merlivat, L., Midorikawa, T., Mintrop, L., Miyazaki, C., Murata, A., Nakadate, A., Nakano, Y.,  
2639 Nakaoka, S., Nojiri, Y., Omar, A. M., Padin, X. A., Park, G.-H., Paterson, K., Perez, F. F., Pierrot, D., Poisson,  
2640 A., Ríos, A. F., Santana-Casiano, J. M., Salisbury, J., Sarma, V. V. S. S., Schlitzer, R., Schneider, B., Schuster,  
2641 U., Sieger, R., Skjelvan, I., Steinhoff, T., Suzuki, T., Takahashi, T., Tedesco, K., Telszewski, M., Thomas, H.,  
2642 Tilbrook, B., Tjiputra, J., Vandemark, D., Veness, T., Wanninkhof, R., Watson, A. J., Weiss, R., Wong, C. S.,  
2643 and Yoshikawa-Inoue, H.: A uniform, quality controlled Surface Ocean CO<sub>2</sub> Atlas (SOCAT), *Earth Syst. Sci.*  
2644 *Data*, 5, 125–143, <https://doi.org/10.5194/essd-5-125-2013>, 2013.

2645 Piao, S., Ciais, P., Friedlingstein, P., de Noblet-Ducoudré, N., Cadule, P., Viovy, N., and Wang, T.:  
 2646 Spatiotemporal patterns of terrestrial carbon cycle during the 20th century, 23,  
 2647 <https://doi.org/10.1029/2008GB003339>, 2009.

2648 Piao, S., Huang, M., Liu, Z., Wang, X., Ciais, P., Canadell, J. G., Wang, K., Bastos, A., Friedlingstein, P.,  
 2649 Houghton, R. A., Le Quéré, C., Liu, Y., Myneni, R. B., Peng, S., Pongratz, J., Sitch, S., Yan, T., Wang, Y., Zhu,  
 2650 Z., Wu, D., and Wang, T.: Lower land-use emissions responsible for increased net land carbon sink during the  
 2651 slow warming period, *Nature Geosci*, 11, 739–743, <https://doi.org/10.1038/s41561-018-0204-7>, 2018.

2652 Pongratz, J., Reick, C. H., Houghton, R. A., and House, J. I.: Terminology as a key uncertainty in net land use  
 2653 and land cover change carbon flux estimates, *Earth Syst. Dynam.*, 5, 177–195, [https://doi.org/10.5194/esd-5-](https://doi.org/10.5194/esd-5-177-2014)  
 2654 177-2014, 2014.

2655 Potapov, P., Hansen, M. C., Laestadius, L., Turubanova, S., Yaroshenko, A., Thies, C., Smith, W., Zhuravleva,  
 2656 I., Komarova, A., Minnemeyer, S., and Esipova, E.: The last frontiers of wilderness: Tracking loss of intact  
 2657 forest landscapes from 2000 to 2013, 3, e1600821, <https://doi.org/10.1126/sciadv.1600821>, 2017.

2658 Poulter, B., Frank, D. C., Hodson, E. L., and Zimmermann, N. E.: Impacts of land cover and climate data  
 2659 selection on understanding terrestrial carbon dynamics and the CO<sub>2</sub> airborne fraction, *Biogeosciences*, 8, 2027–  
 2660 2036, <https://doi.org/10.5194/bg-8-2027-2011>, 2011.

2661 Poulter, B., Freeborn, P. H., Jolly, W. M., and Varner, J. M.: COVID-19 lockdowns drive decline in active fires  
 2662 in southeastern United States, *PNAS*, 118, <https://doi.org/10.1073/pnas.2105666118>, 2021.

2663 Prather, M.: Interactive comment on “Carbon dioxide and climate impulse response functions for the  
 2664 computation of greenhouse gas metrics: a multi-model analysis” by F. Joos et al., 6, 2012.

2665 Prentice, I. C., Farquhar, G. D., Fasham, M. J. R., Goulden, M. L., Heimann, M., Jaramillo, V. J., Kheshgi, H.  
 2666 S., Le Quéré, C., Scholes, R. J., and Wallace, D. W. R.: The Carbon Cycle and Atmospheric Carbon Dioxide, in  
 2667 *Climate Change 2001: The Scientific Basis. Contribution of Working Group I to the Third Assessment Report*  
 2668 *of the Intergovernmental Panel on Climate Change*, edited by: Houghton, J. T., Ding, Y., Griggs, D. J., Noguer,  
 2669 M., van der Linden, P. J., Dai, X., Maskell, K., and Johnson, C. A., Cambridge University Press, Cambridge,  
 2670 United Kingdom and New York, NY, USA, 183–237, 2001.

2671 Price, J. T. and Warren, R.: Literature Review of the Potential of “Blue Carbon” Activities to Reduce Emissions,  
 2672 available at: [https://avoid-net-uk.cc.ic.ac.uk/wp-content/uploads/delightful-downloads/2016/03/Literature-](https://avoid-net-uk.cc.ic.ac.uk/wp-content/uploads/delightful-downloads/2016/03/Literature-review-of-the-potential-of-blue-carbon-activities-to-reduce-emissions-AVOID2-WPE2.pdf)  
 2673 [review-of-the-potential-of-blue-carbon-activities-to-reduce-emissions-AVOID2-WPE2.pdf](https://avoid-net-uk.cc.ic.ac.uk/wp-content/uploads/delightful-downloads/2016/03/Literature-review-of-the-potential-of-blue-carbon-activities-to-reduce-emissions-AVOID2-WPE2.pdf), last access: 25  
 2674 September 2022, 2016.

2675 Qin, Y., Xiao, X., Wigneron, J.-P., Ciais, P., Brandt, M., Fan, L., Li, X., Crowell, S., Wu, X., Doughty, R.,  
 2676 Zhang, Y., Liu, F., Sitch, S., and Moore, B.: Carbon loss from forest degradation exceeds that from  
 2677 deforestation in the Brazilian Amazon, *Nat. Clim. Chang.*, 11, 442–448, [https://doi.org/10.1038/s41558-021-](https://doi.org/10.1038/s41558-021-01026-5)  
 2678 01026-5, 2021.

2679 Qiu, C., Ciais, P., Zhu, D., Guenet, B., Peng, S., Petrescu, A. M. R., Lauerwald, R., Makowski, D., Gallego-  
2680 Sala, A. V., Charman, D. J., and Brewer, S. C.: Large historical carbon emissions from cultivated northern  
2681 peatlands, 7, eabf1332, <https://doi.org/10.1126/sciadv.abf1332>, 2021.

2682 Raupach, M. R., Marland, G., Ciais, P., Le Quere, C., Canadell, J. G., Klepper, G., and Field, C. B.: Global and  
2683 regional drivers of accelerating CO<sub>2</sub> emissions, *Proceedings of the National Academy of Sciences*, 104, 10288–  
2684 10293, <https://doi.org/10.1073/pnas.0700609104>, 2007.

2685 Regnier, P., Friedlingstein, P., Ciais, P., Mackenzie, F. T., Gruber, N., Janssens, I. A., Laruelle, G. G.,  
2686 Lauerwald, R., Luyssaert, S., Andersson, A. J., Arndt, S., Arnosti, C., Borges, A. V., Dale, A. W., Gallego-Sala,  
2687 A., Godd  ris, Y., Goossens, N., Hartmann, J., Heinze, C., Ilyina, T., Joos, F., LaRowe, D. E., Leifeld, J.,  
2688 Meysman, F. J. R., Munhoven, G., Raymond, P. A., Spahni, R., Suntharalingam, P., and Thullner, M.:  
2689 Anthropogenic perturbation of the carbon fluxes from land to ocean, *Nature Geosci*, 6, 597–607,  
2690 <https://doi.org/10.1038/ngeo1830>, 2013.

2691 Regnier, P., Resplandy, L., Najjar, R. G., and Ciais, P.: The land-to-ocean loops of the global carbon cycle,  
2692 *Nature*, 603, 401–410, <https://doi.org/10.1038/s41586-021-04339-9>, 2022.

2693 Reick, C. H., Gayler, V., Goll, D., Hagemann, S., Heidkamp, M., Nabel, J. E. M. S., Raddatz, T., Roeckner, E.,  
2694 Schnur, R., and Wilkenskield, S.: JSBACH 3 - The land component of the MPI Earth System Model:  
2695 documentation of version 3.2, <https://doi.org/10.17617/2.3279802>, 2021.

2696 Remaud, M., Chevallier, F., Cozic, A., Lin, X., and Bousquet, P.: On the impact of recent developments of the  
2697 LMDz atmospheric general circulation model on the simulation of CO<sub>2</sub> transport, 11, 4489,  
2698 <https://doi.org/10.5194/gmd-11-4489-2018>, 2018.

2699 Resplandy, L., Keeling, R. F., R  denbeck, C., Stephens, B. B., Khatiwala, S., Rodgers, K. B., Long, M. C.,  
2700 Bopp, L., and Tans, P. P.: Revision of global carbon fluxes based on a reassessment of oceanic and riverine  
2701 carbon transport, *Nature Geosci*, 11, 504–509, <https://doi.org/10.1038/s41561-018-0151-3>, 2018.

2702 Reynolds, R. W., Rayner, N. A., Smith, T. M., Stokes, D. C., and Wang, W.: An Improved In Situ and Satellite  
2703 SST Analysis for Climate, *J. Clim.*, 15, 1609–1625, [https://doi.org/10.1175/1520-0442\(2002\)015<1609:AIISAS>2.0.CO;2](https://doi.org/10.1175/1520-0442(2002)015<1609:AIISAS>2.0.CO;2), 2002.

2705 Rhein, M., Rintoul, S. R., Aoki, S., Campos, E., Chambers, D., Feely, R. A., Gulev, S., Johnson, G. C., Josey, S.  
2706 A., Kostianoy, A., Mauritzen, C., Roemmich, D., and Talley, L. D.: *Observations: Ocean*, edited by: Stocker, T.  
2707 F., Qin, D., Plattner, G.-K., Tignor, M., Allen, S. K., Boschung, J., Nauels, A., Xia, Y., Bex, V., and Midgley, P.  
2708 M., Cambridge University Press, 255–316, 2013.

2709 R  denbeck, C., Houweling, S., Gloor, M., and Heimann, M.: CO<sub>2</sub> flux history 1982–2001 inferred from  
2710 atmospheric data using a global inversion of atmospheric transport, 46, 2003.

2711 R  denbeck, C., Keeling, R. F., Bakker, D. C. E., Metzl, N., Olsen, A., Sabine, C., and Heimann, M.: Global  
2712 surface-ocean pCO<sub>2</sub> and sea–air CO<sub>2</sub> flux variability from an observation-driven ocean mixed-layer scheme, 9,

2713 193–216, <https://doi.org/10.5194/os-9-193-2013>, 2013.

2714 Rödenbeck, C., Bakker, D. C. E., Metzl, N., Olsen, A., Sabine, C., Cassar, N., Reum, F., Keeling, R. F., and  
2715 Heimann, M.: Interannual sea–air CO<sub>2</sub> flux variability from an observation-driven ocean mixed-layer scheme,  
2716 11, 4599–4613, <https://doi.org/10.5194/bg-11-4599-2014>, 2014.

2717 Rödenbeck, C., Bakker, D. C. E., Gruber, N., Iida, Y., Jacobson, A. R., Jones, S., Landschützer, P., Metzl, N.,  
2718 Nakaoka, S., Olsen, A., Park, G.-H., Peylin, P., Rodgers, K. B., Sasse, T. P., Schuster, U., Shutler, J. D.,  
2719 Valsala, V., Wanninkhof, R., and Zeng, J.: Data-based estimates of the ocean carbon sink variability – first  
2720 results of the Surface Ocean CO<sub>2</sub> Mapping intercomparison (SOCOM), *Biogeosciences*, 12, 7251–7278,  
2721 <https://doi.org/10.5194/bg-12-7251-2015>, 2015.

2722 Rödenbeck, C., Zaehle, S., Keeling, R., and Heimann, M.: History of El Niño impacts on the global carbon  
2723 cycle 1957–2017: a quantification from atmospheric CO<sub>2</sub> data, 373, 20170303,  
2724 <https://doi.org/10.1098/rstb.2017.0303>, 2018.

2725 Rödenbeck, C., DeVries, T., Hauck, J., Le Quéré, C., and Keeling, R. F.: Data-based estimates of interannual  
2726 sea–air CO<sub>2</sub> flux variations 1957–2020 and their relation to environmental drivers, *Biogeosciences*, 19, 2627–  
2727 2652, <https://doi.org/10.5194/bg-19-2627-2022>, 2022.

2728 Roobaert, A., Laruelle, G. G., Landschützer, P., and Regnier, P.: Uncertainty in the global oceanic CO<sub>2</sub> uptake  
2729 induced by wind forcing: quantification and spatial analysis, 15, 1701–1720, [https://doi.org/10.5194/bg-15-](https://doi.org/10.5194/bg-15-1701-2018)  
2730 1701-2018, 2018.

2731 Rosan, T. M., Klein Goldewijk, K., Ganzenmüller, R., O’Sullivan, M., Pongratz, J., Mercado, L. M., Aragao, L.  
2732 E. O. C., Heinrich, V., Randow, C. V., Wiltshire, A., Tubiello, F. N., Bastos, A., Friedlingstein, P., and Sitch,  
2733 S.: A multi-data assessment of land use and land cover emissions from Brazil during 2000–2019, *Environ. Res.*  
2734 *Lett.*, 16, 074004, <https://doi.org/10.1088/1748-9326/ac08c3>, 2021.

2735 Rypdal, K., Paciorek, N., Eggleston, S., Goodwin, J., Irving, W., Penman, J., and Woodfield, M.: Volume 1:  
2736 Introduction to the 2006 Guidelines in: 2006 IPCC guidelines for national greenhouse gas inventories., 2006.

2737 Saatchi, S. S., Harris, N. L., Brown, S., Lefsky, M., Mitchard, E. T. A., Salas, W., Zutta, B. R., Buermann, W.,  
2738 Lewis, S. L., Hagen, S., Petrova, S., White, L., Silman, M., and Morel, A.: Benchmark map of forest carbon  
2739 stocks in tropical regions across three continents, *Proceedings of the National Academy of Sciences*, 108, 9899–  
2740 9904, <https://doi.org/10.1073/pnas.1019576108>, 2011.

2741 Sabine, C. L., Feely, R. A., Gruber, N., Key, R. M., Lee, K., Bullister, J. L., Wanninkhof, R., Wong, C. S.,  
2742 Wallace, D. W. R., Tilbrook, B., Millero, F. J., Peng, T.-H., Kozyr, A., Ono, T., and Rios, A. F.: The Oceanic  
2743 Sink for Anthropogenic CO<sub>2</sub>, 305, 367–371, <https://doi.org/10.1126/science.1097403>, 2004.

2744 Sarmiento, J. L., Orr, J. C., and Siegenthaler, U.: A perturbation simulation of CO<sub>2</sub> uptake in an ocean general  
2745 circulation model, 97, 3621–3645, <https://doi.org/10.1029/91JC02849>, 1992.

2746 Sato, M., Hansen, J. E., McCormick, M. P., and Pollack, J. B.: Stratospheric aerosol optical depths, 1850–1990,



2747 98, 22987–22994, <https://doi.org/10.1029/93JD02553>, 1993.

2748 Saunio, M., Stavert, A. R., Poulter, B., Bousquet, P., Canadell, J. G., Jackson, R. B., Raymond, P. A.,  
2749 Dlugokencky, E. J., Houweling, S., Patra, P. K., Ciais, P., Arora, V. K., Bastviken, D., Bergamaschi, P., Blake,  
2750 D. R., Brailsford, G., Bruhwiler, L., Carlson, K. M., Carrol, M., Castaldi, S., Chandra, N., Crevoisier, C., Crill,  
2751 P. M., Covey, K., Curry, C. L., Etiope, G., Frankenberg, C., Gedney, N., Hegglin, M. I., Höglund-Isaksson, L.,  
2752 Hugelius, G., Ishizawa, M., Ito, A., Janssens-Maenhout, G., Jensen, K. M., Joos, F., Kleinen, T., Krummel, P.  
2753 B., Langenfelds, R. L., Laruelle, G. G., Liu, L., Machida, T., Maksyutov, S., McDonald, K. C., McNorton, J.,  
2754 Miller, P. A., Melton, J. R., Morino, I., Müller, J., Murguía-Flores, F., Naik, V., Niwa, Y., Noce, S., O'Doherty,  
2755 S., Parker, R. J., Peng, C., Peng, S., Peters, G. P., Prigent, C., Prinn, R., Ramonet, M., Regnier, P., Riley, W. J.,  
2756 Rosentreter, J. A., Segers, A., Simpson, I. J., Shi, H., Smith, S. J., Steele, L. P., Thornton, B. F., Tian, H.,  
2757 Tohjima, Y., Tubiello, F. N., Tsuruta, A., Viovy, N., Voulgarakis, A., Weber, T. S., van Weele, M., van der  
2758 Werf, G. R., Weiss, R. F., Worthy, D., Wunch, D., Yin, Y., Yoshida, Y., Zhang, W., Zhang, Z., Zhao, Y.,  
2759 Zheng, B., Zhu, Q., Zhu, Q., and Zhuang, Q.: The Global Methane Budget 2000–2017, *Earth Syst. Sci. Data*, 12,  
2760 1561–1623, <https://doi.org/10.5194/essd-12-1561-2020>, 2020.

2761 Schimel, D., Alves, D., Enting, I. G., Heimann, M., Joos, F., Raynaud, D., Wigley, T., Prater, M., Derwent, R.,  
2762 Ehrlert, D., Fraser, P., Sanhueza, E., Zhou, X., Jonas, P., Charlson, R., Rodhe, H., Sadasivan, S., Shine, K. P.,  
2763 Fouquart, Y., Ramaswamy, V., Solomon, S., Srinivasan, J., Albritton, D., Derwent, R., Isaksen, I., Lal, M., and  
2764 Wuebbles, D.: Radiative Forcing of Climate Change, in: *Climate Change 1995 The Science of Climate Change*,  
2765 Contribution of Working Group I to the Second Assessment Report of the Intergovernmental Panel on Climate  
2766 Change, edited by: Houghton, J. T., Meira Filho, L. G., Callander, B. A., Harris, N., Kattenberg, A., and  
2767 Maskell, K., Cambridge University Press, Cambridge, United Kingdom and New York, NY, USA, 1995.

2768 Schimel, D., Stephens, B. B., and Fisher, J. B.: Effect of increasing CO<sub>2</sub> on the terrestrial carbon cycle, *Proc*  
2769 *Natl Acad Sci USA*, 112, 436–441, <https://doi.org/10.1073/pnas.1407302112>, 2015.

2770 Schourup-Kristensen, V., Sidorenko, D., Wolf-Gladrow, D. A., and Völker, C.: A skill assessment of the  
2771 biogeochemical model REcoM2 coupled to the Finite Element Sea Ice–Ocean Model (FESOM 1.3), *Geosci.*  
2772 *Model Dev.*, 7, 2769–2802, <https://doi.org/10.5194/gmd-7-2769-2014>, 2014.

2773 Schuh, A. E., Jacobson, A. R., Basu, S., Weir, B., Baker, D., Bowman, K., Chevallier, F., Crowell, S., Davis, K.  
2774 J., Deng, F., Denning, S., Feng, L., Jones, D., Liu, J., and Palmer, P. I.: Quantifying the Impact of Atmospheric  
2775 Transport Uncertainty on CO<sub>2</sub> Surface Flux Estimates, *Global Biogeochem. Cycles*, 33, 484–500,  
2776 <https://doi.org/10.1029/2018GB006086>, 2019.

2777 Schuldt et al. Multi-laboratory compilation of atmospheric carbon dioxide data for the period 1957–2020.  
2778 <https://doi.org/10.25925/20210801>

2779 Schuldt et al. Multi-laboratory compilation of atmospheric carbon dioxide data for the period 2021–2022.  
2780 <http://doi.org/10.25925/20220624>

2781 Schwinger, J., Goris, N., Tjiputra, J. F., Kriest, I., Bentsen, M., Bethke, I., Ilicak, M., Assmann, K. M., and  
2782 Heinze, C.: Evaluation of NorESM-OC (versions 1 and 1.2), the ocean carbon-cycle stand-alone configuration

2783 of the Norwegian Earth System Model (NorESM1), *Geosci. Model Dev.*, 9, 2589–2622,  
2784 <https://doi.org/10.5194/gmd-9-2589-2016>, 2016.

2785 Schwingshackl, C., Obermeier, W., Bultan, S., Grassi, G., Canadell, J. G., Friedlingstein, P., Gasser, T.,  
2786 Houghton, R. A., Kurz, W. A., Sitch, S., and Pongratz, J.: Separating natural and land-use CO<sub>2</sub> fluxes at  
2787 country-level to reconcile land-based mitigation estimates, submitted, *One Earth*, 2022.

2788 Séférian, R., Nabat, P., Michou, M., Saint-Martin, D., Voldoire, A., Colin, J., Decharme, B., Delire, C., Berthet,  
2789 S., Chevallier, M., Sénési, S., Franchisteguy, L., Vial, J., Mallet, M., Joetzjer, E., Geoffroy, O., Guérémy, J.-F.,  
2790 Moine, M.-P., Msadek, R., Ribes, A., Rocher, M., Roehrig, R., Salas-y-Mélia, D., Sanchez, E., Terray, L.,  
2791 Valcke, S., Waldman, R., Aumont, O., Bopp, L., Deshayes, J., Éthé, C., and Madec, G.: Evaluation of CNRM  
2792 Earth System Model, CNRM-ESM2-1: Role of Earth System Processes in Present-Day and Future Climate,  
2793 *Journal of Advances in Modeling Earth Systems*, 11, 4182–4227, <https://doi.org/10.1029/2019MS001791>, 2019.

2794 Seiler, C., Melton, J. R., Arora, V. K., Sitch, S., Friedlingstein, P., Anthoni, P., Goll, D., Jain, A. K., Joetzjer, E.,  
2795 Lienert, S., Lombardozzi, D., Luyssaert, S., Nabel, J. E. M. S., Tian, H., Vuichard, N., Walker, A. P., Yuan, W.,  
2796 and Zaehle, S.: Are Terrestrial Biosphere Models Fit for Simulating the Global Land Carbon Sink?, *J. Adv.*  
2797 *Model. Earth Syst.*, 14, e2021MS002946, <https://doi.org/10.1029/2021MS002946>, 2022.

2798 Sellar, A. A., Jones, C. G., Mulcahy, J. P., Tang, Y., Yool, A., Wiltshire, A., O'Connor, F. M., Stringer, M.,  
2799 Hill, R., Palmieri, J., Woodward, S., Mora, L., Kuhlbrodt, T., Rumbold, S. T., Kelley, D. I., Ellis, R., Johnson,  
2800 C. E., Walton, J., Abraham, N. L., Andrews, M. B., Andrews, T., Archibald, A. T., Berthou, S., Burke, E.,  
2801 Blockley, E., Carslaw, K., Dalvi, M., Edwards, J., Folberth, G. A., Gedney, N., Griffiths, P. T., Harper, A. B.,  
2802 Hendry, M. A., Hewitt, A. J., Johnson, B., Jones, A., Jones, C. D., Keeble, J., Liddicoat, S., Morgenstern, O.,  
2803 Parker, R. J., Predoi, V., Robertson, E., Siahaan, A., Smith, R. S., Swaminathan, R., Woodhouse, M. T., Zeng,  
2804 G., and Zerroukat, M.: UKESM1: Description and Evaluation of the U.K. Earth System Model, *J. Adv. Model.*  
2805 *Earth Syst.*, 11, 4513–4558, <https://doi.org/10.1029/2019MS001739>, 2019.

2806 Shu, S., Jain, A. K., Koven, C. D., and Mishra, U.: Estimation of Permafrost SOC Stock and Turnover Time  
2807 Using a Land Surface Model With Vertical Heterogeneity of Permafrost Soils, 34, e2020GB006585,  
2808 <https://doi.org/10.1029/2020GB006585>, 2020.

2809 Sitch, S., Huntingford, C., Gedney, N., Levy, P. E., Lomas, M., Piao, S. L., Betts, R., Ciais, P., Cox, P.,  
2810 Friedlingstein, P., Jones, C. D., Prentice, I. C., and Woodward, F. I.: Evaluation of the terrestrial carbon cycle,  
2811 future plant geography and climate-carbon cycle feedbacks using five Dynamic Global Vegetation Models  
2812 (DGVMs): Uncertainty In Land Carbon Cycle Feedbacks, 14, 2015–2039, [https://doi.org/10.1111/j.1365-](https://doi.org/10.1111/j.1365-2486.2008.01626.x)  
2813 [2486.2008.01626.x](https://doi.org/10.1111/j.1365-2486.2008.01626.x), 2008.

2814 Smith, B., Wårlind, D., Arneth, A., Hickler, T., Leadley, P., Siltberg, J., and Zaehle, S.: Implications of  
2815 incorporating N cycling and N limitations on primary production in an individual-based dynamic vegetation  
2816 model, *Biogeosciences*, 11, 2027–2054, <https://doi.org/10.5194/bg-11-2027-2014>, 2014.

2817 Stephens, B. B., Gurney, K. R., Tans, P. P., Sweeney, C., Peters, W., Bruhwiler, L., Ciais, P., Ramonet, M.,  
2818 Bousquet, P., Nakazawa, T., Aoki, S., Machida, T., Inoue, G., Vinnichenko, N., Lloyd, J., Jordan, A., Heimann,

2819 M., Shibistova, O., Langenfelds, R. L., Steele, L. P., Francey, R. J., and Denning, A. S.: Weak Northern and  
 2820 Strong Tropical Land Carbon Uptake from Vertical Profiles of Atmospheric CO<sub>2</sub>, *Science*, 316, 1732–1735,  
 2821 <https://doi.org/10.1126/science.1137004>, 2007.

2822 Stocker, T., Qin, D., and Plattner, G.-K.: *Climate Change 2013: The Physical Science Basis. Contribution of*  
 2823 *Working Group I to the Fifth Assessment Report of the Intergovernmental Panel on Climate Change*, edited by:  
 2824 Intergovernmental Panel on Climate Change, Cambridge University Press, Cambridge, 2013.

2825 Sweeney, C., Gloor, E., Jacobson, A. R., Key, R. M., McKinley, G., Sarmiento, J. L., and Wanninkhof, R.:  
 2826 Constraining global air-sea gas exchange for CO<sub>2</sub> with recent bomb 14C measurements, 21,  
 2827 <https://doi.org/10.1029/2006GB002784>, 2007.

2828 SX Coal: Monthly coal consumption estimates, <http://www.sxcoal.com/> (last access: 25 September 2022), 2022.

2829 Takahashi, T., Sutherland, S. C., Wanninkhof, R., Sweeney, C., Feely, R. A., Chipman, D. W., Hales, B.,  
 2830 Friederich, G., Chavez, F., Sabine, C., Watson, A., Bakker, D. C. E., Schuster, U., Metzl, N., Yoshikawa-Inoue,  
 2831 H., Ishii, M., Midorikawa, T., Nojiri, Y., Körtzinger, A., Steinhoff, T., Hoppema, M., Olafsson, J., Arnarson, T.  
 2832 S., Tilbrook, B., Johannessen, T., Olsen, A., Bellerby, R., Wong, C. S., Delille, B., Bates, N. R., and de Baar, H.  
 2833 J. W.: Climatological mean and decadal change in surface ocean pCO<sub>2</sub>, and net sea–air CO<sub>2</sub> flux over the  
 2834 global oceans, *Deep Sea Research Part II: Topical Studies in Oceanography*, 56, 554–577,  
 2835 <https://doi.org/10.1016/j.dsr2.2008.12.009>, 2009.

2836 Terhaar, J., Frölicher, T. L., and Joos, F.: Southern Ocean anthropogenic carbon sink constrained by sea surface  
 2837 salinity, *Sci. Adv.*, 7, eabd5964, <https://doi.org/10.1126/sciadv.abd5964>, 2021.

2838 Terhaar, J., Frölicher, T. L., and Joos, F.: Observation-constrained estimates of the global ocean carbon sink  
 2839 from Earth system models, *Biogeosciences*, 19, 4431–4457, <https://doi.org/10.5194/bg-19-4431-2022>, 2022.

2840 Thomason, L. W., Ernest, N., Millán, L., Rieger, L., Bourassa, A., Vernier, J.-P., Manney, G., Luo, B.,  
 2841 Arfeuille, F., and Peter, T.: A global space-based stratospheric aerosol climatology: 1979–2016, 10, 469–492,  
 2842 <https://doi.org/10.5194/essd-10-469-2018>, 2018.

2843 Tian, H., Xu, X., Lu, C., Liu, M., Ren, W., Chen, G., Melillo, J., and Liu, J.: Net exchanges of CO<sub>2</sub>, CH<sub>4</sub>, and  
 2844 N<sub>2</sub>O between China’s terrestrial ecosystems and the atmosphere and their contributions to global climate  
 2845 warming, 116, <https://doi.org/10.1029/2010JG001393>, 2011.

2846 Tian, H., Chen, G., Lu, C., Xu, X., Hayes, D. J., Ren, W., Pan, S., Huntzinger, D. N., and Wofsy, S. C.: North  
 2847 American terrestrial CO<sub>2</sub> uptake largely offset by CH<sub>4</sub> and N<sub>2</sub>O emissions: toward a full accounting of the  
 2848 greenhouse gas budget, *Climatic Change*, 129, 413–426, <https://doi.org/10.1007/s10584-014-1072-9>, 2015.

2849 Todd-Brown, K. E. O., Randerson, J. T., Post, W. M., Hoffman, F. M., Tarnocai, C., Schuur, E. A. G., and  
 2850 Allison, S. D.: Causes of variation in soil carbon simulations from CMIP5 Earth system models and comparison  
 2851 with observations, *Biogeosciences*, 10, 1717–1736, <https://doi.org/10.5194/bg-10-1717-2013>, 2013.

2852 Tohjima, Y., Mukai, H., Machida, T., Hoshina, Y., and Nakaoka, S.-I.: Global carbon

2853 budgets estimated from atmospheric O<sub>2</sub>/N<sub>2</sub> and CO<sub>2</sub> observations in the western  
 2854 Pacific region over a 15-year period, 19, 9269–9285, [https://doi.org/10.5194/acp-](https://doi.org/10.5194/acp-19-9269-2019)  
 2855 19–9269–2019, 2019.

2856 Torero, M. and FAO: Impact of the Ukraine-Russia conflict on global food security and related matters under  
 2857 the mandate of the Food and Agriculture Organization of the United Nations (FAO), available at:  
 2858 <https://www.fao.org/3/nj164en/nj164en.pdf>, last access: 25 Sept 2022, 2022.

2859 Tubiello, F. N., Conchedda, G., Wanner, N., Federici, S., Rossi, S., and Grassi, G.: Carbon emissions and  
 2860 removals from forests: new estimates, 1990–2020, *Earth Syst. Sci. Data*, 13, 1681–1691,  
 2861 <https://doi.org/10.5194/essd-13-1681-2021>, 2021.

2862 Tyukavina, A., Potapov, P., Hansen, M. C., Pickens, A. H., Stehman, S. V., Turubanova, S., Parker, D., Zalles,  
 2863 V., Lima, A., Kommareddy, I., Song, X.-P., Wang, L., and Harris, N.: Global Trends of Forest Loss Due to Fire  
 2864 From 2001 to 2019, *Front. Remote Sens.*, 3, 2022.

2865 UN: United Nations Statistics Division: National Accounts Main Aggregates Database, available at:  
 2866 <http://unstats.un.org/unsd/snaama/Introduction.asp>, last access: 25 September 2022, 2021.

2867 UNFCCC: Synthesis report for the technical assessment component of the first global stocktake, available at:  
 2868 <https://unfccc.int/documents/461466>, last access: 25 September 2022, 2022

2869 Urakawa, L. S., Tsujino, H., Nakano, H., Sakamoto, K., Yamanaka, G., and Toyoda, T.: The sensitivity of a  
 2870 depth-coordinate model to diapycnal mixing induced by practical implementations of the isopycnal tracer  
 2871 diffusion scheme, *Ocean Model.*, 154, 101693, <https://doi.org/10.1016/j.ocemod.2020.101693>, 2020.

2872 Vale, M. M., Berenguer, E., Argollo de Menezes, M., Viveiros de Castro, E. B., Pugliese de Siqueira, L., and  
 2873 Portela, R. de C. Q.: The COVID-19 pandemic as an opportunity to weaken environmental protection in Brazil,  
 2874 *Biological Conservation*, 255, 108994, <https://doi.org/10.1016/j.biocon.2021.108994>, 2021.

2875 van der Laan-Luijkx, I. T., van der Velde, I. R., van der Veen, E., Tsuruta, A., Stanislawska, K.,  
 2876 Babenhauserheide, A., Zhang, H. F., Liu, Y., He, W., Chen, H., Masarie, K. A., Krol, M. C., and Peters, W.:  
 2877 The CarbonTracker Data Assimilation Shell (CTDAS) v1.0: implementation and global carbon balance 2001–  
 2878 2015, *Geosci. Model Dev.*, 10, 2785–2800, <https://doi.org/10.5194/gmd-10-2785-2017>, 2017.

2879 van der Velde, I. R., Miller, J. B., Schaefer, K., van der Werf, G. R., Krol, M. C., and Peters, W.: Terrestrial  
 2880 cycling of 13CO<sub>2</sub> by photosynthesis, respiration, and biomass burning in SiBCASA, 11, 6553–6571,  
 2881 <https://doi.org/10.5194/bg-11-6553-2014>, 2014.

2882 van der Velde, I. R., van der Werf, G. R., Houweling, S., Maasakkers, J. D., Borsdorff, T., Landgraf, J., Tol, P.,  
 2883 van Kempen, T. A., van Hees, R., Hoogeveen, R., Veeffkind, J. P., and Aben, I.: Vast CO<sub>2</sub> release from  
 2884 Australian fires in 2019–2020 constrained by satellite, 597, 366–369, [https://doi.org/10.1038/s41586-021-](https://doi.org/10.1038/s41586-021-03712-y)  
 2885 03712-y, 2021.

2886 van der Werf, G. R., Randerson, J. T., Giglio, L., Collatz, G. J., Mu, M., Kasibhatla, P. S., Morton, D. C.,

2887 DeFries, R. S., Jin, Y., and van Leeuwen, T. T.: Global fire emissions and the contribution of deforestation,  
 2888 savanna, forest, agricultural, and peat fires (1997–2009), *Atmos. Chem. Phys.*, 10, 11707–11735,  
 2889 <https://doi.org/10.5194/acp-10-11707-2010>, 2010.

2890 van der Werf, G. R., Randerson, J. T., Giglio, L., van Leeuwen, T. T., Chen, Y., Rogers, B. M., Mu, M., van  
 2891 Marle, M. J. E., Morton, D. C., Collatz, G. J., Yokelson, R. J., and Kasibhatla, P. S.: Global fire emissions  
 2892 estimates during 1997–2016, *Earth Syst. Sci. Data*, 9, 697–720, <https://doi.org/10.5194/essd-9-697-2017>, 2017.

2893 van Wees, D., van der Werf, G. R., Randerson, J. T., Andela, N., Chen, Y., and Morton, D. C.: The role of fire  
 2894 in global forest loss dynamics, *Glob. Change Biol.*, 27, 2377–2391, <https://doi.org/10.1111/gcb.15591>, 2021.

2895 Vaittinada Ayar, P., Bopp, L., Christian, J. R., Ilyina, T., Krasting, J. P., Séférian, R., Tsujino, H., Watanabe,  
 2896 M., Yool, A., and Tjiputra, J.: Contrasting projections of the ENSO-driven CO<sub>2</sub> flux variability in the equatorial  
 2897 Pacific under high-warming scenario, *Earth Syst. Dynam.*, 13, 1097–1118, [https://doi.org/10.5194/esd-13-1097-](https://doi.org/10.5194/esd-13-1097-2022)  
 2898 2022, 2022.

2899 Viovy, N.: CRUNCEP data set, available at:  
 2900 [ftp://nacp.ornl.gov/synthesis/2009/frescati/temp/land\\_use\\_change/original/readme.htm](ftp://nacp.ornl.gov/synthesis/2009/frescati/temp/land_use_change/original/readme.htm), last access: 25  
 2901 September 2022, 2016.

2902 Vuichard, N., Messina, P., Luyssaert, S., Guenet, B., Zaehle, S., Ghattas, J., Bastrikov, V., and Peylin, P.:  
 2903 Accounting for carbon and nitrogen interactions in the global terrestrial ecosystem model ORCHIDEE (trunk  
 2904 version, rev 4999): multi-scale evaluation of gross primary production, *Geosci. Model Dev.*, 12, 4751–4779,  
 2905 <https://doi.org/10.5194/gmd-12-4751-2019>, 2019.

2906 Walker, A. P., Quaife, T., Bodegom, P. M., De Kauwe, M. G., Keenan, T. F., Joiner, J., Lomas, M. R.,  
 2907 MacBean, N., Xu, C., Yang, X., and Woodward, F. I.: The impact of alternative trait-scaling hypotheses for the  
 2908 maximum photosynthetic carboxylation rate (  $V_{cmax}$  ) on global gross primary production, *New Phytol.*, 215,  
 2909 1370–1386, <https://doi.org/10.1111/nph.14623>, 2017.

2910 Walker, A. P., De Kauwe, M. G., Bastos, A., Belmecheri, S., Georgiou, K., Keeling, R. F., McMahon, S. M.,  
 2911 Medlyn, B. E., Moore, D. J. P., Norby, R. J., Zaehle, S., Anderson-Teixeira, K. J., Battipaglia, G., Brien, R. J.  
 2912 W., Cabugao, K. G., Cailleret, M., Campbell, E., Canadell, J. G., Ciais, P., Craig, M. E., Ellsworth, D. S.,  
 2913 Farquhar, G. D., Fatichi, S., Fisher, J. B., Frank, D. C., Graven, H., Gu, L., Haverd, V., Heilman, K., Heimann,  
 2914 M., Hungate, B. A., Iversen, C. M., Joos, F., Jiang, M., Keenan, T. F., Knauer, J., Körner, C., Leshyk, V. O.,  
 2915 Leuzinger, S., Liu, Y., MacBean, N., Malhi, Y., McVicar, T. R., Penuelas, J., Pongratz, J., Powell, A. S., Riutta,  
 2916 T., Sabot, M. E. B., Schleucher, J., Sitch, S., Smith, W. K., Sulman, B., Taylor, B., Terrer, C., Torn, M. S.,  
 2917 Treseder, K. K., Trugman, A. T., Trumbore, S. E., van Mantgem, P. J., Voelker, S. L., Whelan, M. E., and  
 2918 Zuidema, P. A.: Integrating the evidence for a terrestrial carbon sink caused by increasing atmospheric CO<sub>2</sub>,  
 2919 229, 2413–2445, <https://doi.org/10.1111/nph.16866>, 2021.

2920 Wanninkhof, R.: Relationship between wind speed and gas exchange over the ocean, 97, 7373–7382,  
 2921 <https://doi.org/10.1029/92JC00188>, 1992.

2922 Wanninkhof, R.: Relationship between wind speed and gas exchange over the ocean revisited, 12, 351–362,  
 2923 <https://doi.org/10.4319/lom.2014.12.351>, 2014.

2924 Wanninkhof, R., Park, G.-H., Takahashi, T., Sweeney, C., Feely, R., Nojiri, Y., Gruber, N., Doney, S. C.,  
 2925 McKinley, G. A., Lenton, A., Le Quéré, C., Heinze, C., Schwinger, J., Graven, H., and Khatiwala, S.: Global  
 2926 ocean carbon uptake: magnitude, variability and trends, *Biogeosciences*, 10, 1983–2000,  
 2927 <https://doi.org/10.5194/bg-10-1983-2013>, 2013.

2928 Watson, A. J., Schuster, U., Shutler, J. D., Holding, T., Ashton, I. G. C., Landschützer, P., Woolf, D. K., and  
 2929 Goddijn-Murphy, L.: Revised estimates of ocean-atmosphere CO<sub>2</sub> flux are consistent with ocean carbon  
 2930 inventory, *Nat Commun*, 11, 4422, <https://doi.org/10.1038/s41467-020-18203-3>, 2020.

2931 Watson, R. T., Rohde, H., Oeschger, H., and Siegenthaler, U.: Greenhouse Gases and Aerosols, in: *Climate*  
 2932 *Change: The IPCC Scientific Assessment*. Intergovernmental Panel on Climate Change (IPCC), edited by:  
 2933 Houghton, J. T., Jenkins, G. J., and Ephraums, J. J., Cambridge University Press, Cambridge, 140, 1990.

2934 Weiss, R. F. and Price, B. A.: Nitrous oxide solubility in water and seawater, *Marine Chemistry*, 8, 347–359,  
 2935 [https://doi.org/10.1016/0304-4203\(80\)90024-9](https://doi.org/10.1016/0304-4203(80)90024-9), 1980.

2936 Wenzel, S., Cox, P. M., Eyring, V., and Friedlingstein, P.: Projected land photosynthesis constrained by changes  
 2937 in the seasonal cycle of atmospheric CO<sub>2</sub>, *Nature*, 538, 499–501, <https://doi.org/10.1038/nature19772>, 2016.

2938 Wilkenskjaeld, S., Kloster, S., Pongratz, J., Raddatz, T., and Reick, C. H.: Comparing the influence of net and  
 2939 gross anthropogenic land-use and land-cover changes on the carbon cycle in the MPI-ESM, *Biogeosciences*, 11,  
 2940 4817–4828, <https://doi.org/10.5194/bg-11-4817-2014>, 2014.

2941 Wiltshire, A. J., Burke, E. J., Chadburn, S. E., Jones, C. D., Cox, P. M., Davies-Barnard, T., Friedlingstein, P.,  
 2942 Harper, A. B., Liddicoat, S., Sitch, S., and Zaehle, S.: JULES-CN: a coupled terrestrial carbon–nitrogen scheme  
 2943 (JULES vn5.1), 14, 2161–2186, <https://doi.org/10.5194/gmd-14-2161-2021>, 2021.

2944 Woodward, F. I. and Lomas, M. R.: Vegetation dynamics – simulating responses to climatic change, *Biol. Rev.*,  
 2945 79, 643–670, <https://doi.org/10.1017/S1464793103006419>, 2004.

2946 Wright, R. M., Le Quéré, C., Buitenhuis, E., Pitois, S., and Gibbons, M. J.: Role of jellyfish in the plankton  
 2947 ecosystem revealed using a global ocean biogeochemical model, 18, 1291–1320, <https://doi.org/10.5194/bg-18-1291-2021>, 2021.

2949 Wunder, S., Kaimowitz, D., Jensen, S., and Feder, S.: Coronavirus, macroeconomy, and forests: What likely  
 2950 impacts?, *For. Policy Econ.*, 131, 102536, <https://doi.org/10.1016/j.forpol.2021.102536>, 2021.

2951 Xi, F., Davis, S. J., Ciais, P., Crawford-Brown, D., Guan, D., Pade, C., Shi, T., Syddall, M., Lv, J., Ji, L., Bing,  
 2952 L., Wang, J., Wei, W., Yang, K.-H., Lagerblad, B., Galan, I., Andrade, C., Zhang, Y., and Liu, Z.: Substantial  
 2953 global carbon uptake by cement carbonation, *Nature Geosci*, 9, 880–883, <https://doi.org/10.1038/ngeo2840>,  
 2954 2016.

2955 Xia, J., Chen, Y., Liang, S., Liu, D., and Yuan, W.: Global simulations of carbon allocation coefficients for  
 2956 deciduous vegetation types, 67, 28016, <https://doi.org/10.3402/tellusb.v67.28016>, 2015.

2957 Yeager, S. G., Rosenbloom, N., Glanville, A. A., Wu, X., Simpson, I., Li, H., Molina, M. J., Krumhardt, K.,  
 2958 Mogen, S., Lindsay, K., Lombardozzi, D., Wieder, W., Kim, W. M., Richter, J. H., Long, M., Danabasoglu, G.,  
 2959 Bailey, D., Holland, M., Lovenduski, N., Strand, W. G., and King, T.: The Seasonal-to-Multiyear Large  
 2960 Ensemble (SMYLE) prediction system using the Community Earth System Model version 2, *Geoscientific*  
 2961 *Model Development*, 15, 6451–6493, <https://doi.org/10.5194/gmd-15-6451-2022>, 2022.

2962 Yin, X.: Responses of leaf nitrogen concentration and specific leaf area to atmospheric CO<sub>2</sub> enrichment: a  
 2963 retrospective synthesis across 62 species: Leaf response to atmospheric CO<sub>2</sub> enrichment, 8, 631–642,  
 2964 <https://doi.org/10.1046/j.1365-2486.2002.00497.x>, 2002.

2965 Yu, Z., Ciais, P., Piao, S., Houghton, R. A., Lu, C., Tian, H., Agathokleous, E., Kattel, G. R., Sitch, S., Goll, D.,  
 2966 Yue, X., Walker, A., Friedlingstein, P., Jain, A. K., Liu, S., and Zhou, G.: Forest expansion dominates China's  
 2967 land carbon sink since 1980, *Nat. Commun.*, 13, 5374, <https://doi.org/10.1038/s41467-022-32961-2>, 2022.

2968 Yuan, W., Liu, D., Dong, W., Liu, S., Zhou, G., Yu, G., Zhao, T., Feng, J., Ma, Z., Chen, J., Chen, Y., Chen, S.,  
 2969 Han, S., Huang, J., Li, L., Liu, H., Liu, S., Ma, M., Wang, Y., Xia, J., Xu, W., Zhang, Q., Zhao, X., and Zhao,  
 2970 L.: Multiyear precipitation reduction strongly decreases carbon uptake over northern China, 119, 881–896,  
 2971 <https://doi.org/10.1002/2014JG002608>, 2014.

2972 Yue, C., Ciais, P., Luyssaert, S., Li, W., McGrath, M. J., Chang, J., and Peng, S.: Representing anthropogenic  
 2973 gross land use change, wood harvest, and forest age dynamics in a global vegetation model ORCHIDEE-MICT  
 2974 v8.4.2, 11, 409–428, <https://doi.org/10.5194/gmd-11-409-2018>, 2018.

2975 Yue, X. and Unger, N.: The Yale Interactive terrestrial Biosphere model version 1.0: description, evaluation and  
 2976 implementation into NASA GISS ModelE2, *Geosci. Model Dev.*, 8, 2399–2417, [https://doi.org/10.5194/gmd-8-](https://doi.org/10.5194/gmd-8-2399-2015)  
 2977 2399-2015, 2015.

2978 Zaehle, S. and Friend, A. D.: Carbon and nitrogen cycle dynamics in the O-CN land surface model: 1. Model  
 2979 description, site-scale evaluation, and sensitivity to parameter estimates: Site-scale evaluation of a C-N model,  
 2980 *Global Biogeochem. Cycles*, 24, <https://doi.org/10.1029/2009GB003521>, 2010.

2981 Zaehle, S., Ciais, P., Friend, A. D., and Prieur, V.: Carbon benefits of anthropogenic reactive nitrogen offset by  
 2982 nitrous oxide emissions, *Nature Geosci.*, 4, 601–605, <https://doi.org/10.1038/ngeo1207>, 2011.

2983 Zaehle, S., Medlyn, B. E., De Kauwe, M. G., Walker, A. P., Dietze, M. C., Hickler, T., Luo, Y., Wang, Y.-P., El-Masri,  
 2984 B., Thornton, P., Jain, A., Wang, S., Warlind, D., Weng, E., Parton, W., Iversen, C. M., Gallet-Budynek, A.,  
 2985 McCarthy, H., Finzi, A., Hanson, P. J., Prentice, I. C., Oren, R., and Norby, R. J.: Evaluation of 11 terrestrial  
 2986 carbon–nitrogen cycle models against observations from two temperate Free-Air CO<sub>2</sub> Enrichment studies,  
 2987 *New Phytol.*, 202, 803–822, <https://doi.org/10.1111/nph.12697>, 2014.

2988 Zeng, J., Nojiri, Y., Landschützer, P., Telszewski, M., and Nakaoka, S.: A Global Surface Ocean fCO<sub>2</sub> Climatology  
 2989 Based on a Feed-Forward Neural Network, 31, 1838–1849, <https://doi.org/10.1175/JTECH-D-13-00137.1>,  
 2990 2014.

2991 Zheng, B., Chevallier, F., Yin, Y., Ciais, P., Fortems-Cheiney, A., Deeter, M. N., Parker, R. J., Wang, Y., Worden, H.  
 2992 M., and Zhao, Y.: Global atmospheric carbon monoxide budget 2000–2017 inferred from multi-species  
 2993 atmospheric inversions, 26, 2019.

2994 Zheng, B., Ciais, P., Chevallier, F., Chuvieco, E., Chen, Y., and Yang, H.: Increasing forest fire emissions despite  
 2995 the decline in global burned area, 7, eabh2646, <https://doi.org/10.1126/sciadv.abh2646>, 2021.

2996 Zscheischler, J., Mahecha, M. D., Avitabile, V., Calle, L., Carvalhais, N., Ciais, P., Gans, F., Gruber, N.,  
 2997 Hartmann, J., Herold, M., Ichii, K., Jung, M., Landschützer, P., Laruelle, G. G., Lauerwald, R., Papale, D.,  
 2998 Peylin, P., Poulter, B., Ray, D., Regnier, P., Rödenbeck, C., Roman-Cuesta, R. M., Schwalm, C., Tramontana,  
 2999 G., Tyukavina, A., Valentini, R., van der Werf, G., West, T. O., Wolf, J. E., and Reichstein, M.: Reviews and  
 3000 syntheses: An empirical spatiotemporal description of the global surface–atmosphere carbon fluxes:  
 3001 opportunities and data limitations, Biogeosciences, 14, 3685–3703, <https://doi.org/10.5194/bg-14-3685-2017>,  
 3002 2017.

3003

3004

3005

3006

3007

3008



3009 **Tables**

3010

<b>Table 1. Factors used to convert carbon in various units (by convention, Unit 1 = Unit 2 × conversion).</b>			
Unit 1	Unit 2	Conversion	Source
GtC (gigatonnes of carbon)	ppm (parts per million) (a)	2.124 (b)	Ballantyne et al. (2012)
GtC (gigatonnes of carbon)	PgC (petagrams of carbon)	1	SI unit conversion
GtCO <sub>2</sub> (gigatonnes of carbon dioxide)	GtC (gigatonnes of carbon)	3.664	44.01/12.011 in mass equivalent
GtC (gigatonnes of carbon)	MtC (megatonnes of carbon)	1000	SI unit conversion
(a) Measurements of atmospheric CO <sub>2</sub> concentration have units of dry-air mole fraction. 'ppm' is an abbreviation for micromole/mol, dry air.			
(b) The use of a factor of 2.124 assumes that all the atmosphere is well mixed within one year. In reality, only the troposphere is well mixed and the growth rate of CO <sub>2</sub> concentration in the less well-mixed stratosphere is not measured by sites from the NOAA network. Using a factor of 2.124 makes the approximation that the growth rate of CO <sub>2</sub> concentration in the stratosphere equals that of the troposphere on a yearly basis.			

3011

3012

3013

<b>Table 2.</b> How to cite the individual components of the global carbon budget presented here.	
<b>Component</b>	<b>Primary reference</b>
Global fossil CO <sub>2</sub> emissions (EFOS), total and by fuel type	Updated from Andrew and Peters (2021)
National territorial fossil CO <sub>2</sub> emissions (EFOS)	Gilfillan and Marland (2022), UNFCCC (2022)
National consumption-based fossil CO <sub>2</sub> emissions (EFOS) by country (consumption)	Peters et al. (2011b) updated as described in this paper
Net land-use change flux (ELUC)	This paper (see Table 4 for individual model references).
Growth rate in atmospheric CO <sub>2</sub> concentration (GATM)	Dlugokencky and Tans (2022)
Ocean and land CO <sub>2</sub> sinks (SOCEAN and SLAND)	This paper (see Table 4 for individual model and data products references).

3014

**Table 3.** Main methodological changes in the global carbon budget since 2018. Methodological changes introduced in one year are kept for the following years unless noted. Empty cells mean there were no methodological changes introduced that year. Table A7 lists methodological changes from the first global carbon budget publication up to 2017.

Publication year	Fossil fuel emissions		LUC emissions	Reservoirs			Uncertainty & other changes
	Global	Country (territorial)		Atmosphere	Ocean	Land	
2018	Revision in cement emissions; Projection includes EU-specific data	Aggregation of overseas territories into governing nations for total of 213 countries a	Average of two bookkeeping models; use of 16 DGVMs	Use of four atmospheric inversions	Based on seven models	Based on 16 models; revised atmospheric forcing from CRUNCEP to CRUJRA	Introduction of metrics for evaluation of individual models using observations
Le Quéré et al. (2018b) GCB2018							
2019	Global emissions calculated as sum of all countries plus bunkers, rather than taken directly from CDIAC.		Average of two bookkeeping models; use of 15 DGVMs	Use of three atmospheric inversions	Based on nine models	Based on 16 models	
Friedlingstein et al. (2019) GCB2019							
2020	Cement carbonation now included in the EFOS estimate, reducing EFOS by about 0.2GtC yr <sup>-1</sup> for the last decade	India's emissions from Andrew (2020: India); Corrections to Netherland Antilles and Aruba and Soviet emissions before 1950 as per Andrew (2020: CO <sub>2</sub> ); China's coal emissions in 2019 derived from official statistics, emissions now shown for EU27 instead of EU28. Projection for 2020 based on assessment of four approaches.	Average of three bookkeeping models; use of 17 DGVMs. Estimate of gross land use sources and sinks provided	Use of six atmospheric inversions	Based on nine models. River flux revised and partitioned NH, Tropics, SH	Based on 17 models	
Friedlingstein et al. (2020) GCB2020							

2021	Projections are no longer an assessment of four approaches.	Official data included for a number of additional countries, new estimates for South Korea, added emissions from lime production in China.	ELUC estimate compared to the estimates adopted in national GHG inventories (NGHGI)		Average of means of eight models and means of seven data-products. Current year prediction of SOCEAN using a feed-forward neural network method	Current year prediction of SLAND using a feed-forward neural network method	
Friedlingstein et al. (2022a) GCB2021							
2022			ELUC provided at country level. Decomposition into fluxes from deforestation, organic soils, re/afforestation and wood harvest, and other transitions. Change in the methodology to derive LUC maps for Brazil to capture recent upturn in deforestation. Inclusion of two new datasets for peat drainage.	Use of nine atmospheric inversions	Average of means of ten models and means of seven data-products	Based on 16 models. Change in the methodology to derive LUC maps for Brazil to capture recent upturn in deforestation	
This study							

3016  
3017

**Table 4. References for the process models, bookkeeping models, ocean data products, and atmospheric inversions. All models and products are updated with new data to the end of year 2021, and the atmospheric forcing for the DGVMs has been updated as described in Appendix C.2.2.**

Model/data name	Reference	Change from Global Carbon Budget 2021 (Friedlingstein et al., 2022a)
<i>Bookkeeping models for land-use change emissions</i>		
BLUE	Hansis et al. (2015)	No change to model, but simulations performed with updated LUH2 forcing. Update in added peat drainage emissions (based on three spatially explicit datasets).
updated H&N2017	Houghton and Nassikas (2017)	Minor bug fix in the fuel harvest estimates, that was causing an overestimation of fuel sink. Update in added peat drainage emissions (based on three spatially explicit datasets).
OSCAR	Gasser et al. (2020)	No change to model, but land use forcing changed to LUH2-GCB2022 and FRA2020 (as used by H&N and extrapolated to 2021), both prescribed at higher spatial resolution (210 instead of 96 regions/countries). Constraining based on last year's budget data for SLAND over 1960-2021. Update in added peat drainage emissions (based on three spatially explicit datasets).
<i>Dynamic global vegetation models</i>		
CABLE-POP	Haverd et al. (2018)	changes in parameterisation. Diffuse fraction of incoming radiation read in as forcing.
CLASSIC	Melton et al. (2020) (a)	Minor bug fixes.
CLM5.0	Lawrence et al. (2019)	No change.
DLEM	Tian et al. (2015) (b)	No change.
IBIS	Yuan et al. (2014) (c)	No change.
ISAM	Meiyappan et al. (2015) (d)	No change.
JSBACH	Reick et al. (2021) (e)	No change.
JULES-ES	Wiltshire et al. (2021) (f)	Minor bug fixes. (Using JULES v6.3, suite u-co002)
LPJ-GUESS	Smith et al. (2014) (g)	No change.
LPJ	Poulter et al. (2011) (h)	No change.
LPX-Bern	Lienert and Joos (2018)	Following the results of Joos et al. (2018), we use modified parameter values which yield a more reasonable (lower) BNF, termed LPX v1.5. This parameter version has increased N immobilization and a stronger N limitation, than the previous version. The N <sub>2</sub> O Emissions were adjusted accordingly. The parameters

		were obtained by running an ensemble simulation and imposing various observational constraints and subsequently adjusting N immobilization. For the methodology see Lienert et. al. (2018).
OCN	Zaehle and Friend (2010) (i)	No change (uses r294).
ORCHIDEEv3	Vuichard et al. (2019) (j)	No change (ORCHIDEE - V3; revision 7267)
SDGVM	Walker et al. (2017) (k)	No change.
VISIT	Kato et al. (2013) (l)	No change.
YIBs	Yue and Unger (2015)	No change.
<i>Global ocean biogeochemistry models</i>		
NEMO-PlankTOM12	Wright et al. (2021)	Minor bug fixes
MICOM-HAMOCC (NorESM-OCv1.2)	Schwinger et al. (2016)	No change.
MPIOM-HAMOCC6	Lacroix et al. (2021)	No change.
NEMO3.6-PISCESv2-gas (CNRM)	Berthet et al. (2019) (m)	No change.
FESOM-2.1-REcoM2	Hauck et al. (2020) (n)	Extended spin-up, minor bug fixes
MOM6-COBALT (Princeton)	Liao et al. (2020)	No change
CESM-ETHZ	Doney et al. (2009)	Changed salinity restoring in the surface ocean from 700 days to 300 days, except for the Southern Ocean south of 45S, where the restoring timescale was set to 60 days.
NEMO-PISCES (IPSL)	Aumont et al. (2015)	No change.
MRI-ESM2-1	Nakano et al. (2011), Urakawa et al. (2020)	New this year.
CESM2	Long et al. (2021) (o)	New this year.
<i>ocean data products</i>		
MPI-SOMFFN	Landschützer et al. (2016)	update to SOCATv2022 measurements and timeperiod 1982-2021; The estimate now covers the full ocean domain as well as the Arctic Ocean extension described in: Landschützer, P., Laruelle, G. G., Roobaert, A., and Regnier, P.: A uniform pCO <sub>2</sub>

		climatology combining open and coastal oceans, Earth Syst. Sci. Data, 12, 2537–2553, <a href="https://doi.org/10.5194/essd-12-2537-2020">https://doi.org/10.5194/essd-12-2537-2020</a> , 2020.
Jena-MLS	Rödenbeck et al. (2022)	update to SOCATv2022 measurements, time period extended to 1957-2021
CMEMS-LSCE-FFNNv2	Chau et al. (2022)	Update to SOCATv2022 measurements and time period 1985-2021. The CMEMS-LSCE-FFNNv2 product now covers both the open ocean and coastal regions.
LDEO-HPD	Gloege et al. (2022) (p)	New this year
UOEx-Watson	Watson et al. (2020)	Updated to SOCAT v2022 and OISSTv2.1, as recalculated by Holding et al.
NIES-NN	Zeng et al. (2014)	Updated to SOCAT v2022. Small changes in method (gas-exchange coefficient $a = 0.271$ ; trend calculation 1990-2020, predictors include lon and lat)
JMA-MLR	Iida et al. (2021)	Updated to SOCATv2022 SST fields (MGDSST) updated
OS-ETHZ-GRaCER	Gregor and Gruber (2021)	No change
<i>Atmospheric inversions</i>		
CAMS	Chevallier et al. (2005) (q)	Updated to WMOX2019 scale. Extension to year 2021, revision of the station list, update of the prior fluxes
CarbonTracker Europe (CTE)	van der Laan-Luijkx et al. (2017)	Updated to WMOX2019 scale. Biosphere prior fluxes from the SiB4 model instead of SiBCASA model. Extension to 2021.
Jena CarboScope	Rödenbeck et al. (2018) (r)	Updated to WMOX2019 scale. Extension to 2021.
UoE in-situ	Feng et al., (2016) (s)	Updated to WMOX2019 scale. Updated station list, and refined land-ocean map. Extension to 2021.
NISMON-CO2	Niwa et al., (2022) (t)	Updated to WMOX2019 scale. Positive definite flux parameters and updated station list. Extension to 2021.
CMS-Flux	Liu et al., (2021)	Updated to WMOX2019 scale. Extension to 2021.
GONGGA	Jin et al. (2022 in review) (u)	New this year.
THU	Kong et al. (2022)	New this year.
CAMS-Satellite	Chevallier et al. (2005) (r)	New this year.
(a) see also Asaadi et al. (2018).		
(b) see also Tian et al. (2011)		
(c) the dynamic carbon allocation scheme was presented by Xia et al. (2015)		
(d) see also Jain et al. (2013). Soil biogeochemistry is updated based on Shu et al. (2020)		

(e) see also Mauritsen et al. (2019)
(f) see also Sellar et al. (2019) and Burton et al., (2019). JULES-ES is the Earth System configuration of the Joint UK Land Environment Simulator as used in the UK Earth System Model (UKESM).
(g) to account for the differences between the derivation of shortwave radiation from CRU cloudiness and DSWRF from CRUJRA, the photosynthesis scaling parameter $\alpha$ was modified (-15%) to yield similar results.
(h) compared to published version, decreased LPJ wood harvest efficiency so that 50 % of biomass was removed off-site compared to 85 % used in the 2012 budget. Residue management of managed grasslands increased so that 100 % of harvested grass enters the litter pool.
(i) see also Zaehle et al. (2011).
(j) see also Zaehle and Friend (2010) and Krinner et al. (2005)
(k) see also Woodward and Lomas (2004)
(l) see also Ito and Inatomi (2012).
(m) see also Séférian et al. (2019)
(n) see also Schourup-Kristensen et al (2014)
(o) see also Yeager et al. (2022)
(p) see also Bennington et al. (2022)
(q) see also Remaud (2018)
(r) see also Rödenbeck et al. (2003)
(r) see also Feng et al. (2009) and Palmer et al. (2019)
(t) see also Niwa et al. (2020)
(u) see also Tian et al. (2014)



**Table 5. Comparison of results from the bookkeeping method and budget residuals with results from the DGVMs and inverse estimates for different periods, the last decade, and the last year available. All values are in GtCyr<sup>-1</sup>. See Fig. 7 for explanation of the bookkeeping component fluxes. The DGVM uncertainties represent  $\pm 1\sigma$  of the decadal or annual (for 2021) estimates from the individual DGVMs: for the inverse systems the range of available results is given. All values are rounded to the nearest 0.1 GtC and therefore columns do not necessarily add to zero.**

		<i>Mean (GtC/yr)</i>						
		1960s	1970s	1980s	1990s	2000s	2012-2021	2021
Land-use change emissions (ELUC)	Bookkeeping (BK) Net flux (1a)	1.5 $\pm$ 0.7	1.2 $\pm$ 0.7	1.3 $\pm$ 0.7	1.5 $\pm$ 0.7	1.4 $\pm$ 0.7	1.2 $\pm$ 0.7	1.1 $\pm$ 0.7
	BK - deforestation	1.6 $\pm$ 0.4	1.5 $\pm$ 0.4	1.6 $\pm$ 0.4	1.8 $\pm$ 0.3	1.9 $\pm$ 0.4	1.8 $\pm$ 0.4	1.8 $\pm$ 0.4
	BK - organic soils	0.1 $\pm$ 0.1	0.1 $\pm$ 0.1	0.2 $\pm$ 0.1	0.2 $\pm$ 0.1	0.2 $\pm$ 0.1	0.2 $\pm$ 0.1	0.2 $\pm$ 0.1
	BK - re/afforestation and wood harvest	-	-	-	-	-	-	-
	BK - other transitions	0.6 $\pm$ 0.1	0.6 $\pm$ 0.1	0.6 $\pm$ 0.2	0.7 $\pm$ 0.1	0.8 $\pm$ 0.2	0.9 $\pm$ 0.3	1.0 $\pm$ 0.3
	DGVMs-net flux (1b)	0.4 $\pm$ 0.1	0.2 $\pm$ 0.1	0.2 $\pm$ 0.1	0.1 $\pm$ 0.1	0.1 $\pm$ 0.1	0.2 $\pm$ 0.1	0.1 $\pm$ 0.2
Terrestrial sink (SLAND)	Residual sink from global budget (EFOS+ELUC(1a)-GATM-SOCEAN) (2a)	1.4 $\pm$ 0.5	1.3 $\pm$ 0.5	1.5 $\pm$ 0.5	1.5 $\pm$ 0.6	1.6 $\pm$ 0.6	1.6 $\pm$ 0.5	1.6 $\pm$ 0.5
	DGVMs (2b)	1.7 $\pm$ 0.8	1.8 $\pm$ 0.8	1.6 $\pm$ 0.9	2.6 $\pm$ 0.9	2.8 $\pm$ 0.9	2.8 $\pm$ 0.9	2.8 $\pm$ 1
Total land fluxes (SLAND-ELUC)	GCB2022 Budget (2b-1a)	1.2 $\pm$ 0.4	2.2 $\pm$ 0.5	1.9 $\pm$ 0.7	2.5 $\pm$ 0.4	2.7 $\pm$ 0.5	3.1 $\pm$ 0.6	3.5 $\pm$ 0.9
	Budget constraint (2a-1a)	-	-	-	-	-	-	-
	DGVMs-net (2b-1b)	0.2 $\pm$ 0.4	0.6 $\pm$ 0.5	0.3 $\pm$ 0.5	1.1 $\pm$ 0.5	1.5 $\pm$ 0.6	1.5 $\pm$ 0.6	1.7 $\pm$ 0.7
	Inversions*	0.1 $\pm$ 0.4	0.9 $\pm$ 0.5	0.4 $\pm$ 0.5	0.9 $\pm$ 0.4	1.2 $\pm$ 0.3	1.5 $\pm$ 0.5	1.9 $\pm$ 0.7
		---	---	0.3-0.6 (2)	0.7-1.1 (3)	1.2-1.6 (3)	1.1-1.7 (7)	1.5-2.1 (9)

\*Estimates are adjusted for the pre-industrial influence of river fluxes, for the cement carbonation sink, and adjusted to common EFOS (Sect. 2.6). The ranges given include varying numbers (in parentheses) of inversions in each decade (Table A4)

**Table 6. Decadal mean in the five components of the anthropogenic CO<sub>2</sub> budget for different periods, and last year available. All values are in GtC yr<sup>-1</sup>, and uncertainties are reported as  $\pm 1\sigma$ . Fossil CO<sub>2</sub> emissions include cement carbonation. The table also shows the budget imbalance ( $B_{IM}$ ), which provides a measure of the discrepancies among the nearly independent estimates. A positive imbalance means the emissions are overestimated and/or the sinks are too small. All values are rounded to the nearest 0.1 GtC and therefore columns do not necessarily add to zero.**

		<i>Mean (GtC/yr)</i>							
		1960s	1970s	1980s	1990s	2000s	2012-2021	2021	2022 (Projection)
Total emissions (EFOS + ELUC)	Fossil CO <sub>2</sub> emissions (EFOS)*	3 $\pm$ 0.2	4.7 $\pm$ 0.2	5.5 $\pm$ 0.3	6.3 $\pm$ 0.3	7.7 $\pm$ 0.4	9.6 $\pm$ 0.5	9.9 $\pm$ 0.5	10 $\pm$ 0.5
	Land-use change emissions (ELUC)	1.5 $\pm$ 0.7	1.2 $\pm$ 0.7	1.3 $\pm$ 0.7	1.5 $\pm$ 0.7	1.4 $\pm$ 0.7	1.2 $\pm$ 0.7	1.1 $\pm$ 0.7	1 $\pm$ 0.7
	Total emissions	4.5 $\pm$ 0.7	5.9 $\pm$ 0.7	6.8 $\pm$ 0.8	7.8 $\pm$ 0.8	9.1 $\pm$ 0.8	10.8 $\pm$ 0.8	10.9 $\pm$ 0.9	10.9 $\pm$ 0.9
Partitioning	Growth rate in atmospheric CO <sub>2</sub> (GATM)	1.7 $\pm$ 0.07	2.8 $\pm$ 0.07	3.4 $\pm$ 0.02	3.1 $\pm$ 0.02	4 $\pm$ 0.02	5.2 $\pm$ 0.02	5.2 $\pm$ 0.2	5.5 $\pm$ 0.4
	Ocean sink (SOCEAN)	1.1 $\pm$ 0.4	1.4 $\pm$ 0.4	1.8 $\pm$ 0.4	2.1 $\pm$ 0.4	2.3 $\pm$ 0.4	2.9 $\pm$ 0.4	2.9 $\pm$ 0.4	2.9 $\pm$ 0.4
	Terrestrial sink (SLAND)	1.2 $\pm$ 0.4	2.2 $\pm$ 0.5	1.9 $\pm$ 0.7	2.5 $\pm$ 0.4	2.7 $\pm$ 0.5	3.1 $\pm$ 0.6	3.5 $\pm$ 0.9	3.4 $\pm$ 0.9

		1960s	1970s	1980s	1990s	2000s	2012-2021	2021	2022 (Projection)
Budget Imbalance	BIM=E FOS+E LUC- (GATM +SOCE AN+SL AND)	0.4	-0.4	-0.3	0.1	0.1	-0.3	-0.6	-0.9

\*Fossil emissions excluding the cement carbonation sink amount to  $3.1 \pm 0.2$  GtC/yr,  $4.7 \pm 0.2$  GtC/yr,  $5.5 \pm 0.3$  GtC/yr,  $6.4 \pm 0.3$  GtC/yr,  $7.9 \pm 0.4$  GtC/yr, and  $9.8 \pm 0.5$  GtC/yr for the decades 1960s to 2010s respectively and to  $10.1 \pm 0.5$  GtC/yr for 2021, and  $10.2 \pm 0.5$  GtC/yr for 2022.

3050

051

**Table 7.** Comparison of the projection with realised fossil CO2 emissions (EFOS). The ‘Actual’ values are first the estimate available using actual data, and the ‘Projected’ values refers to estimates made before the end of the year for each publication. Projections based on a different method from that described here during 2008-2014 are available in Le Quéré et al., (2016). All values are adjusted for leap years.

	World		China		USA		EU28 / EU27 (i)		India		Rest of World	
	Project ed	Actual	Proje cted	Actual	Proje cted	Actual	Proje cted	Actual	Proje cted	Actual	Proje cted	Actual
2015 (a)	-0.6%	0.06%	-3.9%	-0.7%	-1.5%	-2.5%	-	-	-	-	1.2%	1.2%
	(-1.6 to 0.5)		(-4.6 to -1.1)		(-5.5 to 0.3)						(-0.2 to 2.6)	
2016 (b)	-0.2%	0.20%	-0.5%	-0.3%	-1.7%	-2.1%	-	-	-	-	1.0%	1.3%
	(-1.0 to +1.8)		(-3.8 to +1.3)		(-4.0 to +0.6)						(-0.4 to +2.5)	
2017 (c)	2.0%	1.6%	3.5%	1.5%	-0.4%	-0.5%	-	-	2.00%	3.9%	1.6%	1.9%
	(+0.8 to +3.0)		(+0.7 to +5.4)		(-2.7 to +1.0)				(+0.2 to +3.8)		(0.0 to +3.2)	
2018 (d)	2.7%	2.1%	4.7%	2.3%	2.5%	2.8%	-0.7%	-2.1%	6.3%	8.0%	1.8%	1.7%
	(+1.8 to +3.7)		(+2.0 to +7.4)		(+0.5 to +4.5)		(-2.6 to +1.3)		(+4.3 to +8.3)		(+0.5 to +3.0)	
2019 (e)	0.5%	0.1%	2.6%	2.2%	-2.4%	-2.6%	-1.7%	-4.3%	1.8%	1.0%	0.5%	0.5%
	(-0.3 to +1.4)		(+0.7 to +4.4)		(-4.7 to -0.1)		(-5.1 to +1.8%)		(-0.7 to +3.7)		(-0.8 to +1.8)	
2020 (f)	-6.7%	-5.4%	-1.7%	1.4%	-12.2%	-10.6%	-11.3% (EU27)	-10.9%	-9.1%	-7.3%	-7.4%	-7.0%
2021 (g)	4.8%	5.1%	4.3%	3.5%	6.8%	6.2%	6.3%	6.8%	11.2%	11.1%	3.2%	4.5%
	(4.2 to 5.4%)		(3.0 to 5.4%)		(6.6 to 7.0%)		(4.3 to 8.3%)		(10.7 to 11.7%)		(2.0 to 4.3%)	
2022 (h)	1.1%		-1.5%		1.6%		-1.0%		5.6%		2.5%	
	(0% to 1.7%)		(-3.0 to 0.1%)		(-0.9 to 4.1%)		(-2.9 to 1.0%)		(3.5 to 7.7%)		(0.1 to 2.3%)	

(a) Jackson et al. (2016) and Le Quéré et al. (2015a). (b) Le Quéré et al. (2016). (c) Le Quéré et al. (2018a). (d) Le Quéré et al. (2018b). (e) Friedlingstein et al., (2019), (f) Friedlingstein et al., (2020), (g) Friedlingstein et al., (2022a), (h) This study

(i) EU28 until 2019, EU27 from 2020

052

053

054

055  
056  
057  
058  
059  
060  
061  
062  
063

**Table 8. Cumulative CO<sub>2</sub> for different time periods in gigatonnes of carbon (GtC). Fossil CO<sub>2</sub> emissions include cement carbonation. The budget imbalance (B<sub>IM</sub>) provides a measure of the discrepancies among the nearly independent estimates. All values are rounded to the nearest 5 GtC and therefore columns do not necessarily add to zero. Uncertainties are reported as follows: E<sub>FOS</sub> is 5% of cumulative emissions; E<sub>LUC</sub> prior to 1959 is 1σ spread from the DGVMs, E<sub>LUC</sub> post-1959 is 0.7\*number of years (where 0.7 GtC/yr is the uncertainty on the annual ELUC flux estimate); G<sub>ATM</sub> uncertainty is held constant at 5 GtC for all time periods; S<sub>OCEAN</sub> uncertainty is 20% of the cumulative sink (20% relates to the annual uncertainty of 0.4 GtC/yr, which is ~20% of the current ocean sink); and S<sub>LAND</sub> is the 1σ spread from the DGVMs estimates.**

		1750-2021	1850-2014	1850-2021	1960-2021	1850-2022
Emissions	Fossil CO2 emissions (EFOS)	470±25	400±20	465±25	385±20	475±25
	Land-use change emissions (ELUC)	235±70	195±60	205±60	85±45	205±60
	Total emissions	700±75	595±60	670±65	470±50	680±65
Partitioning	Growth rate in atmos CO2 (GATM)	295±5	235±5	275±5	210±5	280±5
	Ocean sink (SOCEAN)	185±35	155±30	175±35	120±25	180±35
	Terrestrial sink (SLAND)	230±50	185±40	210±45	145±30	210±45
Budget imbalance	BIM=EFOS+ELUC-(GATM+SOCEAN+SLAND)	-5	15	15	-5	10

064  
065  
066  
067

068  
069

Table 9: Mapping of global carbon cycle models' land flux definitions to the definition of the LULUCF net flux used in national Greenhouse Gas Inventories reported to UNFCCC. See Sec. C.2.3 and Tab. A8 for detail on methodology and comparison to other datasets.		
	2002-2011	2012-2021
ELUC from bookkeeping estimates (from Table 5)	1.4	1.2
SLAND on non-intact forest from DGVMs	-1.7	-1.8
ELUC plus SLAND on non-intact forests	-0.3	-0.6
National Greenhouse Gas Inventories	-0.4	-0.5

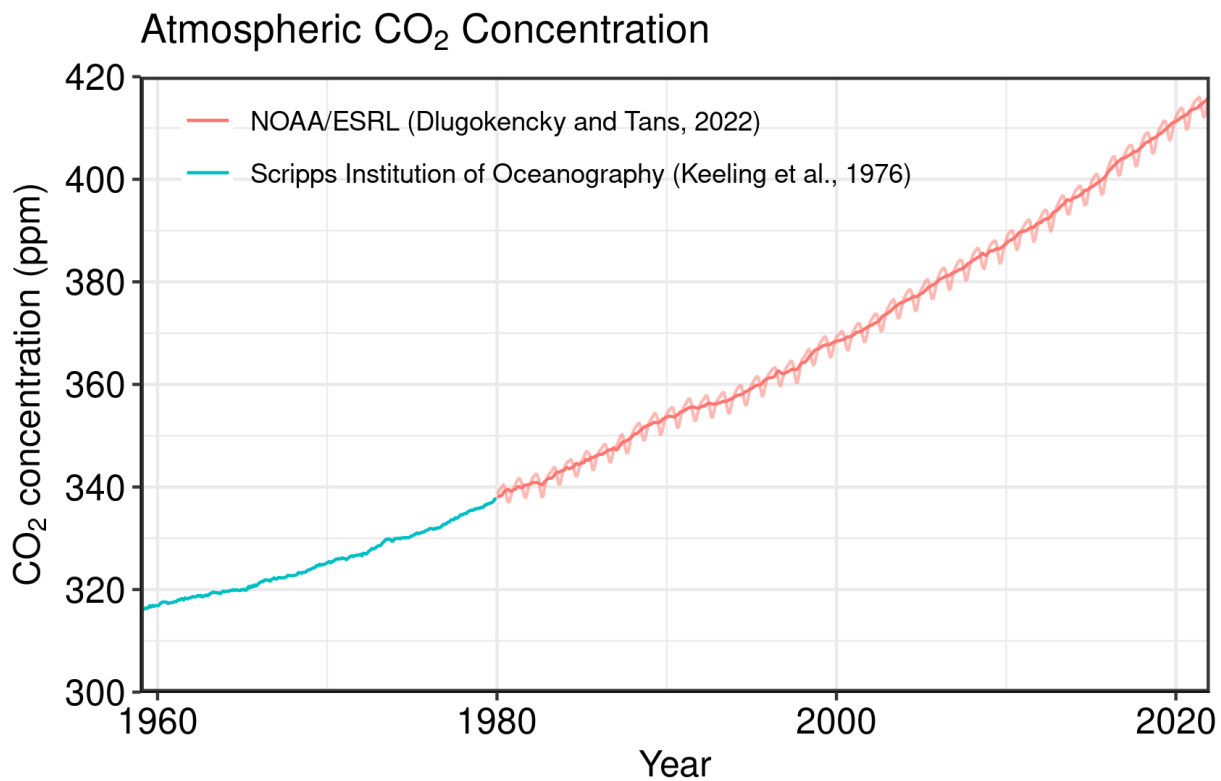
070  
071

**Table 10.** Major known sources of uncertainties in each component of the Global Carbon Budget, defined as input data or processes that have a demonstrated effect of at least  $\pm 0.3$  GtC yr<sup>-1</sup>.

Source of uncertainty	Time scale (years)	Location	Status	Evidence
Fossil CO2 emissions (EFOS; Section 2.1)				
energy statistics	annual to decadal	global, but mainly China & major developing countries	see Sect. 2.1	(Korsbakken et al., 2016, Guan et al., 2012)
carbon content of coal	annual to decadal	global, but mainly China & major developing countries	see Sect. 2.1	(Liu et al., 2015)
system boundary	annual to decadal	all countries	see Sect. 2.1	(Andrew, 2020)
Net land-use change flux (ELUC; section 2.2)				
land-cover and land-use change statistics	continuous	global; in particular tropics	see Sect. 2.4	(Houghton et al., 2012, Gasser et al., 2020, Ganzenmüller et al., 2022, Yu et al. 2022)
sub-grid-scale transitions	annual to decadal	global	see Sect. 2.4, Table A1	(Wilkenskjeld et al., 2014)
vegetation biomass	annual to decadal	global; in particular tropics	see Sect. 2.4	(Houghton et al., 2012, Bastos et al., 2021)
forest degradation (fire, selective logging)	annual to decadal	tropics	see Sec. 3.2.2, Table A1	(Aragão et al., 2018, Qin et al., 2020)
wood and crop harvest	annual to decadal	global; SE Asia	see Table A1	(Arneth et al., 2017, Erb et al., 2018)
peat burning (a)	multi-decadal trend	global	see Table A1	(van der Werf et al., 2010, 2017)
loss of additional sink capacity	multi-decadal trend	global	not included; see Appendix D4	(Pongratz et al, 2014, Gasser et al, 2020; Obermeier et al., 2021)
Atmospheric growth rate (GATM; section 2.3) no demonstrated uncertainties larger than $\pm 0.3$ GtC yr <sup>-1</sup> (b)				
Ocean sink (SOCEAN; section 2.4)				
sparsity in surface fCO2 observations	mean, decadal variability and trend	global, in particular southern hemisphere	see Sect 3.5.2	(Gloege et al., 2021, Denvil-Sommer et al., 2021, Bushinsky et al., 2019)
riverine carbon outgassing and its anthropogenic perturbation	annual to decadal	global, in particular partitioning between Tropics and South	see Sect. 2.4 (anthropogenic perturbations not included)	(Aumont et al., 2001, Resplandy et al., 2018, Lacroix et al., 2020)
Models underestimate interior ocean	annual to decadal	global	see Sect 3.5.5	(Friedlingstein et al., 2021, this study, see also Terhaar et al., 2022)

anthropogenic carbon storage				
near-surface temperature and salinity gradients	mean on all time-scales	global	see Sect. 3.8.2	(Watson et al., 2020, Dong et al., 2022)
Land sink (SLAND; section 2.5)				
strength of CO <sub>2</sub> fertilisation	multi-decadal trend	global	see Sect. 2.5	(Wenzel et al., 2016; Walker et al., 2021)
response to variability in temperature and rainfall	annual to decadal	global; in particular tropics	see Sect. 2.5	(Cox et al., 2013; Jung et al., 2017; Humphrey et al., 2018; 2021)
nutrient limitation and supply	annual to decadal	global		(Zaehle et al., 2014)
carbon allocation and tissue turnover rates	annual to decadal	global		(De Kauwe et al., 2014; O'Sullivan et al., 2022)
tree mortality	annual	global in particular tropics	see Sect. 2.5	(Hubau et al., 2021; Brien et al., 2020)
response to diffuse radiation	annual	global	see Sect. 2.5	(Mercado et al., 2009; O'Sullivan et al., 2021)
(a) As result of interactions between land-use and climate				
(b) The uncertainties in GATM have been estimated as $\pm 0.2$ GtC yr <sup>-1</sup> , although the conversion of the growth rate into a global annual flux assuming instantaneous mixing throughout the atmosphere introduces additional errors that have not yet been quantified.				





074

075

076

077

078

079

080

081

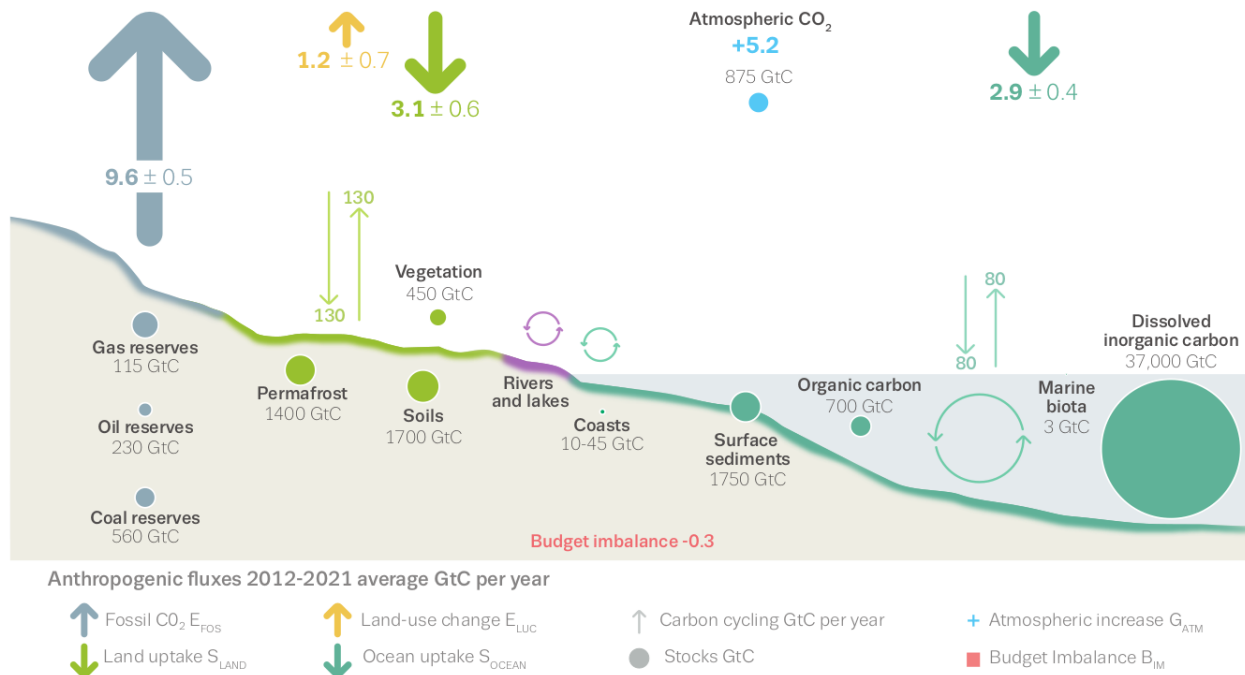
082

083

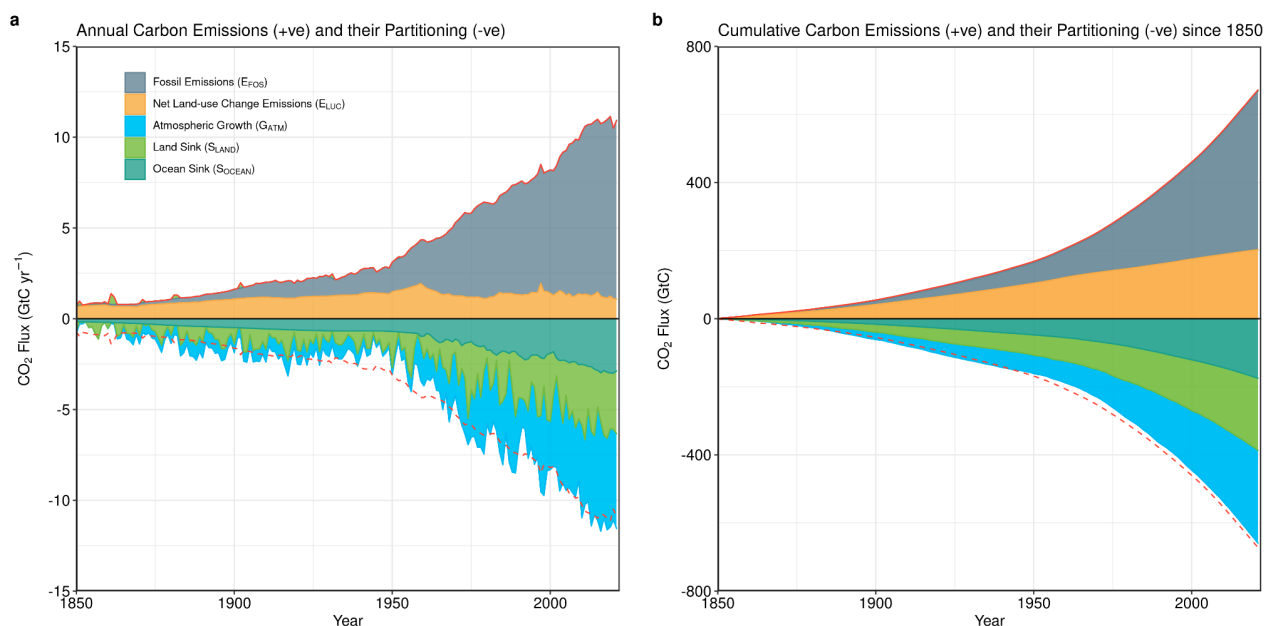
084

Figure 1. Surface average atmospheric CO<sub>2</sub> concentration (ppm). Since 1980, monthly data are from NOAA/GML (Dlugokencky and Tans, 2022) and are based on an average of direct atmospheric CO<sub>2</sub> measurements from multiple stations in the marine boundary layer (Masarie and Tans, 1995). The 1958-1979 monthly data are from the Scripps Institution of Oceanography, based on an average of direct atmospheric CO<sub>2</sub> measurements from the Mauna Loa and South Pole stations (Keeling et al., 1976). To account for the difference of mean CO<sub>2</sub> and seasonality between the NOAA/GML and the Scripps station networks used here, the Scripps surface average (from two stations) was de-seasonalised and adjusted to match the NOAA/GML surface average (from multiple stations) by adding the mean difference of 0.667 ppm, calculated here from overlapping data during 1980-2012.

# The global carbon cycle



**Figure 2.** Schematic representation of the overall perturbation of the global carbon cycle caused by anthropogenic activities, averaged globally for the decade 2012-2021. See legends for the corresponding arrows and units. The uncertainty in the atmospheric CO<sub>2</sub> growth rate is very small ( $\pm 0.02$  GtC yr<sup>-1</sup>) and is neglected for the figure. The anthropogenic perturbation occurs on top of an active carbon cycle, with fluxes and stocks represented in the background and taken from Canadell et al. (2021) for all numbers, except for the carbon stocks in coasts which is from a literature review of coastal marine sediments (Price and Warren, 2016).



**Figure 3. Combined components of the global carbon budget illustrated in Figure 2 as a function of time, for fossil  $\text{CO}_2$  emissions ( $E_{\text{FOS}}$ , including a small sink from cement carbonation; grey) and emissions from land-use change ( $E_{\text{LUC}}$ ; brown), as well as their partitioning among the atmosphere ( $G_{\text{ATM}}$ ; cyan), ocean ( $S_{\text{OCEAN}}$ ; blue), and land ( $S_{\text{LAND}}$ ; green). Panel (a) shows annual estimates of each flux and panel (b) the cumulative flux (the sum of all prior annual fluxes) since the year 1850. The partitioning is based on nearly independent estimates from observations (for  $G_{\text{ATM}}$ ) and from process model ensembles constrained by data (for  $S_{\text{OCEAN}}$  and  $S_{\text{LAND}}$ ) and does not exactly add up to the sum of the emissions, resulting in a budget imbalance ( $\text{BI}_M$ ) which is represented by the difference between the bottom red line (mirroring total emissions) and the sum of carbon fluxes in the ocean, land, and atmosphere reservoirs. All data are in  $\text{GtC yr}^{-1}$  (panel a) and  $\text{GtC}$  (panel b). The  $E_{\text{FOS}}$  estimate is based on a mosaic of different datasets, and has an uncertainty of  $\pm 5\%$  ( $\pm 1\sigma$ ). The  $E_{\text{LUC}}$  estimate is from three bookkeeping models (Table 4) with uncertainty of  $\pm 0.7 \text{ GtC yr}^{-1}$ . The  $G_{\text{ATM}}$  estimates prior to 1959 are from Joos and Spahni (2008) with uncertainties equivalent to about  $\pm 0.1\text{--}0.15 \text{ GtC yr}^{-1}$  and from Dlugokencky and Tans (2022) since 1959 with uncertainties of about  $\pm 0.07 \text{ GtC yr}^{-1}$  during 1959–1979 and  $\pm 0.02 \text{ GtC yr}^{-1}$  since 1980. The  $S_{\text{OCEAN}}$  estimate is the average from Khatiwala et al. (2013) and DeVries (2014) with uncertainty of about  $\pm 30\%$  prior to 1959, and the average of an ensemble of models and an ensemble of  $\text{fCO}_2$  data products (Table 4) with uncertainties of about  $\pm 0.4 \text{ GtC yr}^{-1}$  since 1959. The  $S_{\text{LAND}}$  estimate is the average of an ensemble of models (Table 4) with uncertainties of about  $\pm 1 \text{ GtC yr}^{-1}$ . See the text for more details of each component and their uncertainties.**

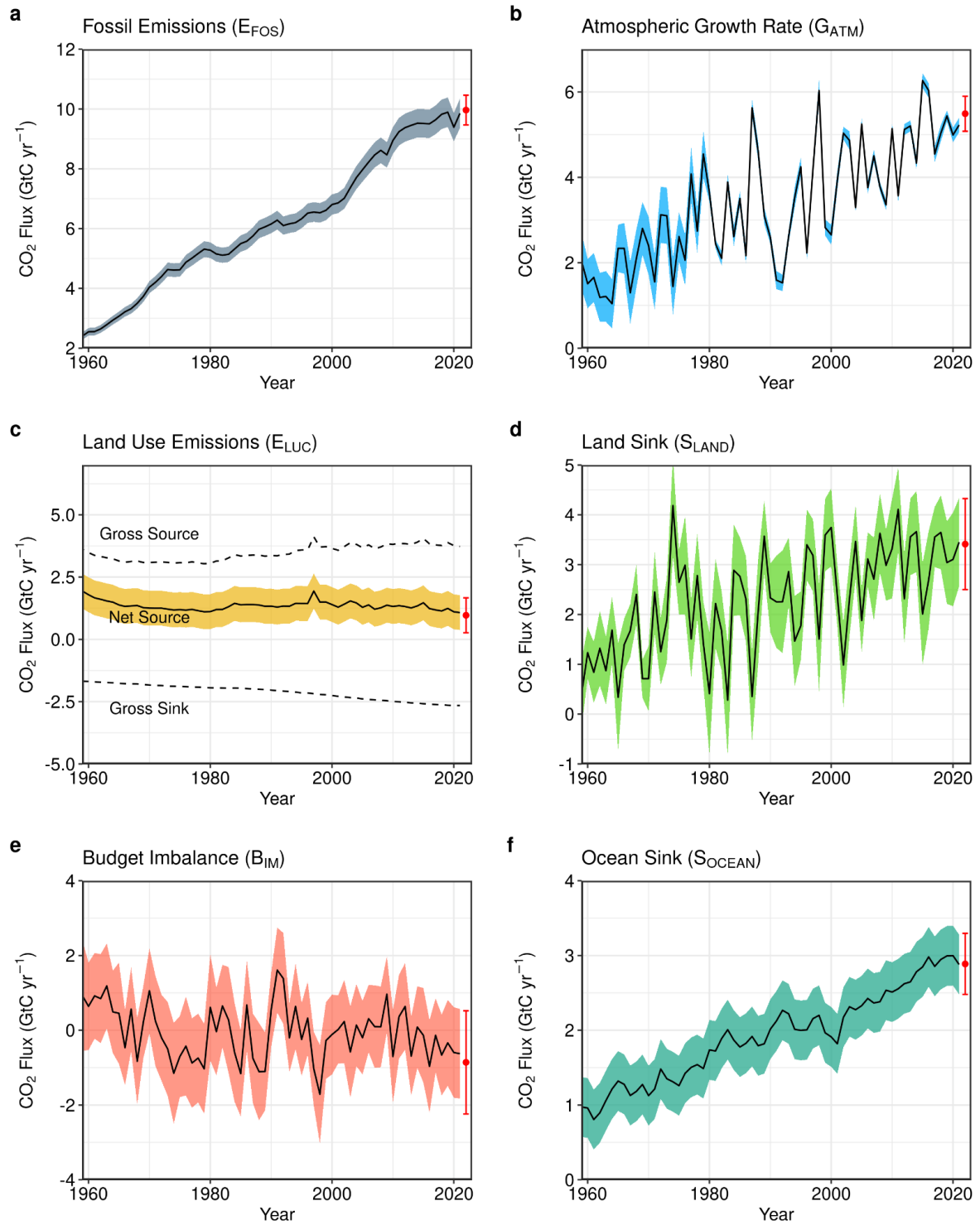


**Figure 4. Components of the global carbon budget and their uncertainties as a function of time, presented individually for (a) fossil CO<sub>2</sub> and cement carbonation emissions ( $E_{FOS}$ ), (b) growth rate in atmospheric CO<sub>2</sub> concentration ( $G_{ATM}$ ), (c) emissions from land-use change ( $E_{LUC}$ ), (d) the land CO<sub>2</sub> sink ( $S_{LAND}$ ), (e) the ocean CO<sub>2</sub> sink ( $S_{OCEAN}$ ), (f) the budget imbalance that is not accounted for by the other terms. Positive values of  $S_{LAND}$  and  $S_{OCEAN}$  represent a flux from the atmosphere to land or the ocean. All data are in GtC yr<sup>-1</sup> with the uncertainty bounds representing  $\pm 1$  standard deviation in shaded colour. Data sources are as in Figure 3. The red dots indicate our projections for the year 2022 and the red error bars the uncertainty in the projections (see methods).**

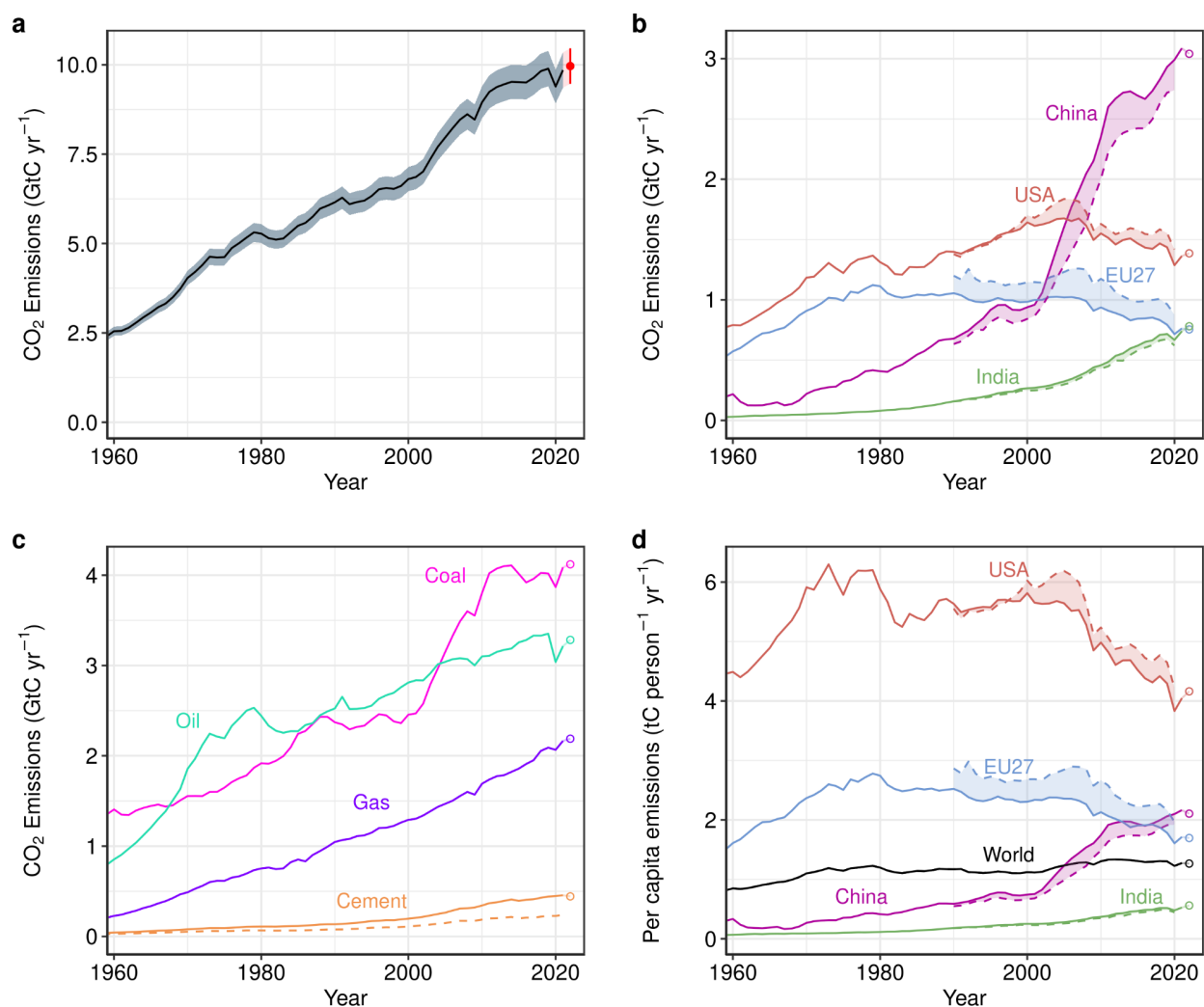


Figure 5. Fossil CO<sub>2</sub> emissions for (a) the globe, including an uncertainty of  $\pm 5\%$  (grey shading) and a projection through the year 2022 (red dot and uncertainty range), (b) territorial (solid lines) and consumption (dashed lines) emissions for the top three country emitters (USA, China, India) and for the European Union (EU27), (c) global emissions by fuel type, including coal, oil, gas, and cement, and cement minus cement carbonation (dashed), and (d) per-capita emissions the world and for the large emitters as in panel (b). Territorial emissions are primarily from a draft update of Gilfillan and Marland (2021) except for national data for Annex I countries for 1990-2020, which are reported to the UNFCCC as detailed in the text, as well as some improvements in individual countries, and extrapolated forward to 2021 using BP Energy Statistics. Consumption-based emissions are updated from Peters et al. (2011b). See Section 2.1 and Appendix C.1 for details of the calculations and data sources.

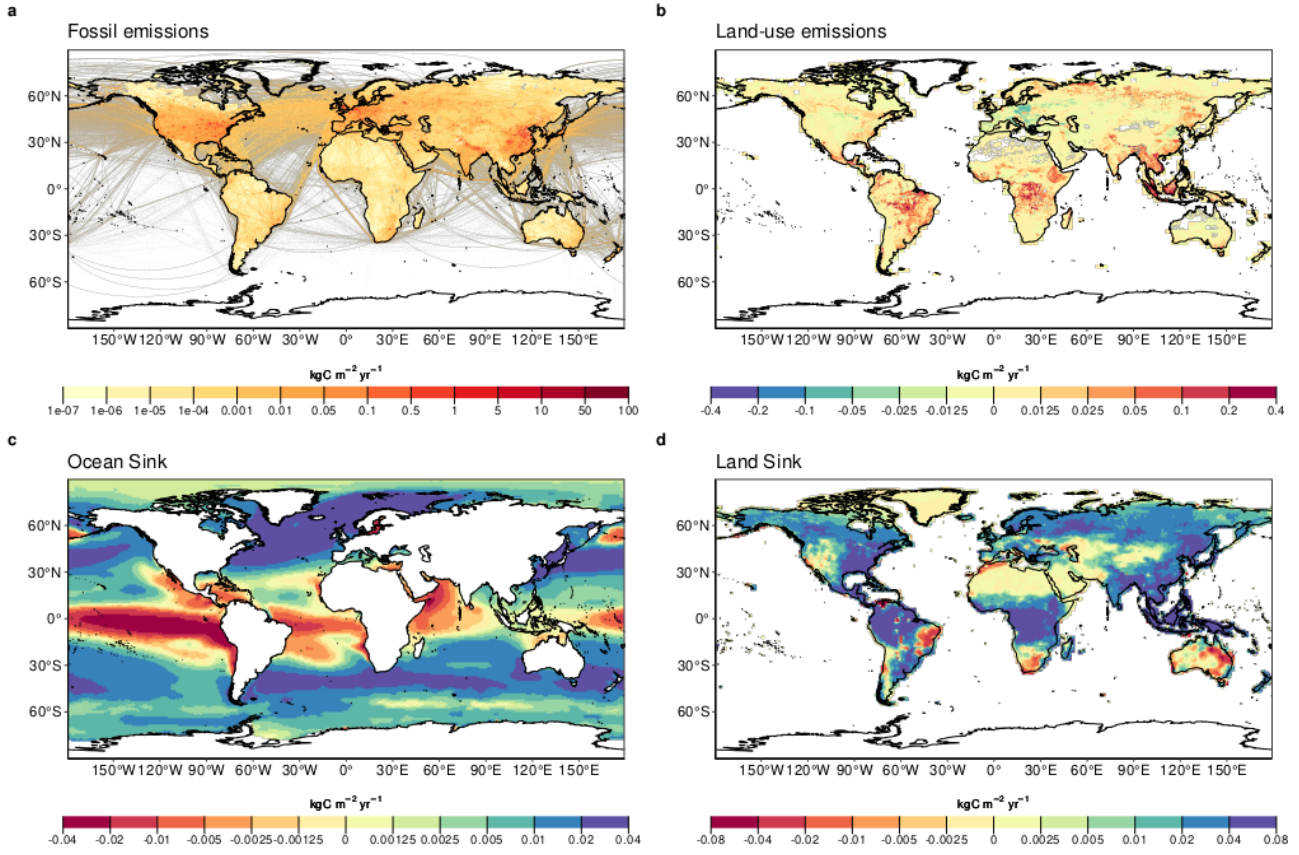
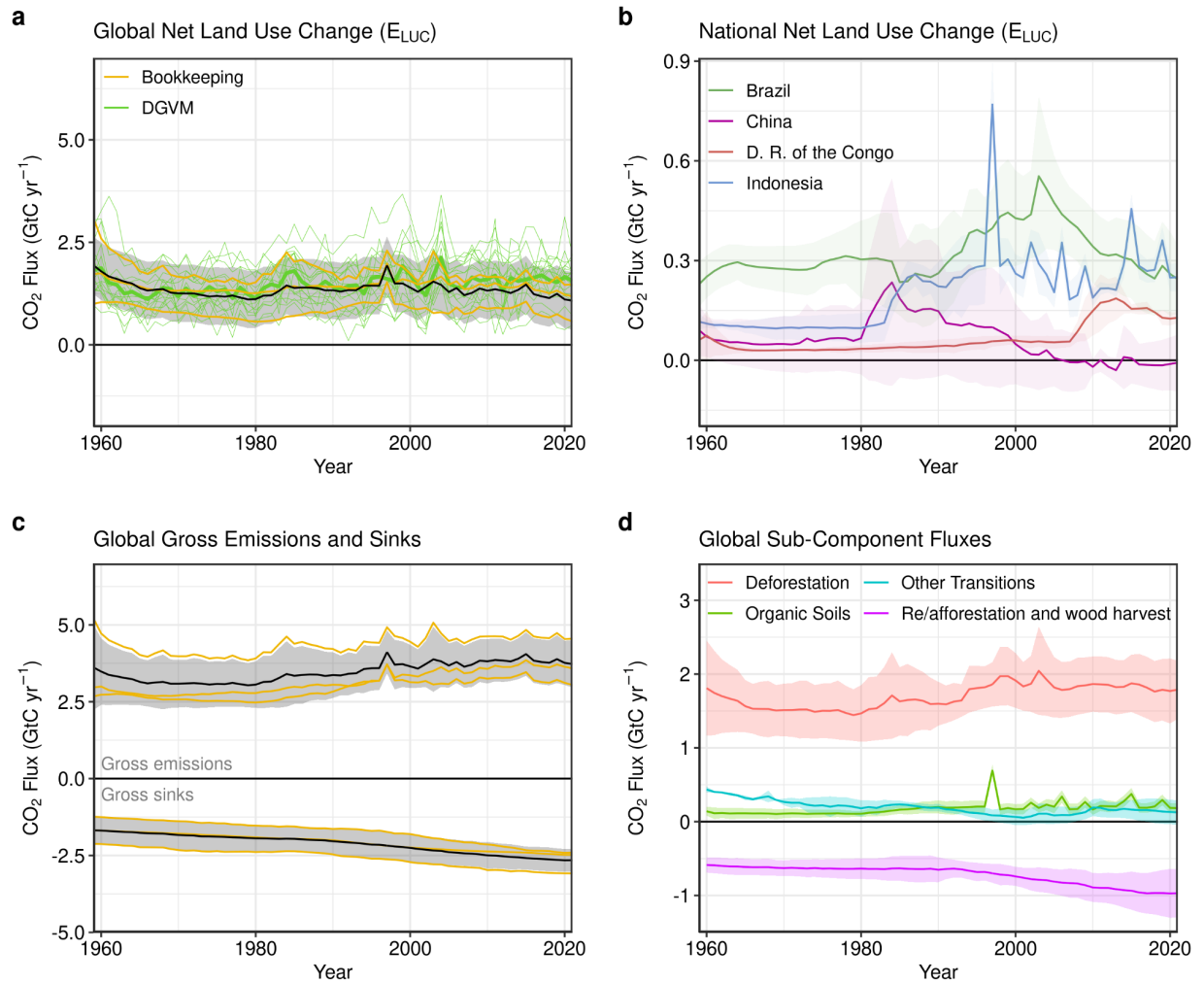
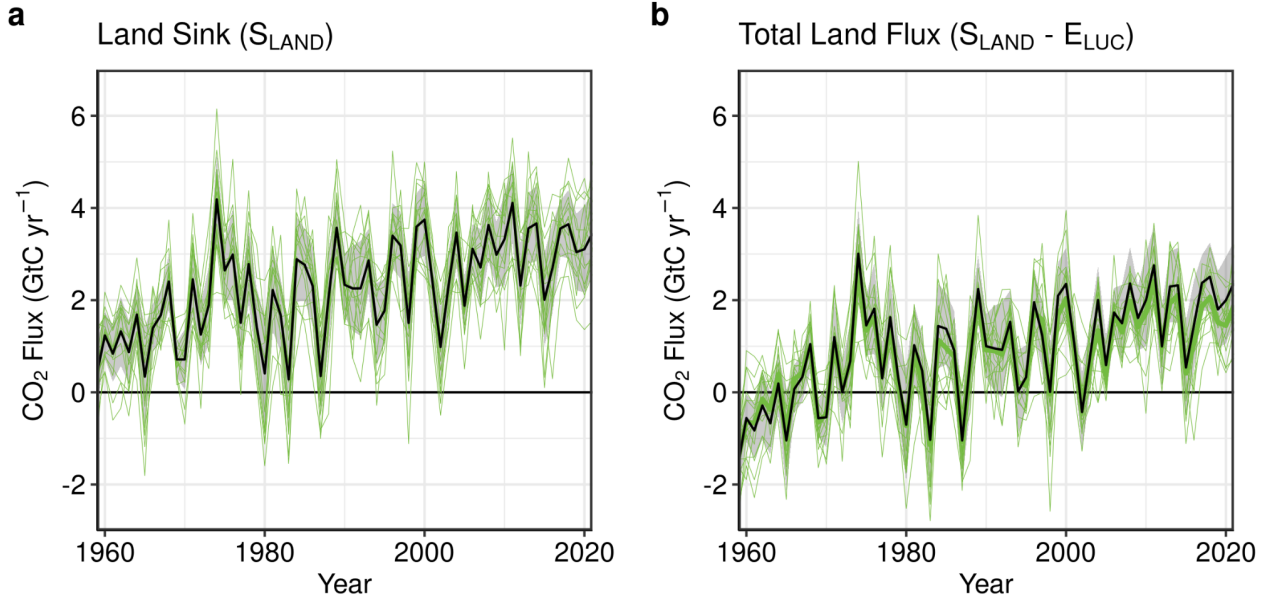


Figure 6. The 2012-2021 decadal mean components of the global carbon budget, presented for (a) fossil CO<sub>2</sub> emissions ( $E_{\text{FOS}}$ ), (b) land-use change emissions ( $E_{\text{LUC}}$ ), (c) the ocean CO<sub>2</sub> sink ( $S_{\text{OCEAN}}$ ), and (d) the land CO<sub>2</sub> sink ( $S_{\text{LAND}}$ ). Positive values for  $E_{\text{FOS}}$  and  $E_{\text{LUC}}$  represent a flux to the atmosphere, whereas positive values of  $S_{\text{OCEAN}}$  and  $S_{\text{LAND}}$  represent a flux from the atmosphere to the ocean or the land. In all panels, yellow/red (green/blue) colours represent a flux from (into) the land/ocean to (from) the atmosphere. All units are in  $\text{kgC m}^{-2} \text{yr}^{-1}$ . Note the different scales in each panel.  $E_{\text{FOS}}$  data shown is from GCP-GridFEDv2022.2.  $E_{\text{LUC}}$  data shown is only from BLUE as the updated H&N2017 and OSCAR do not resolve gridded fluxes.  $S_{\text{OCEAN}}$  data shown is the average of GOBMs and data-products means, using GOBMs simulation A, no adjustment for bias and drift applied to the gridded fields (see Section 2.4).  $S_{\text{LAND}}$  data shown is the average of DGVMs for simulation S2 (see Section 2.5).



**Figure 7. Net CO<sub>2</sub> exchanges between the atmosphere and the terrestrial biosphere related to land use change.** (a) Net CO<sub>2</sub> emissions from land-use change ( $E_{LUC}$ ) with estimates from the three bookkeeping models (yellow lines) and the budget estimate (black with  $\pm 1\sigma$  uncertainty), which is the average of the three bookkeeping models. Estimates from individual DGVMs (narrow green lines) and the DGVM ensemble mean (thick green line) are also shown. (b) Net CO<sub>2</sub> emissions from land-use change from the four countries with largest cumulative emissions since 1959. Values shown are the average of the three bookkeeping models, with shaded regions as  $\pm 1\sigma$  uncertainty. (c) CO<sub>2</sub> gross sinks (negative, from regrowth after agricultural abandonment and wood harvesting) and gross sources (positive, from decaying material left dead on site, products after clearing of natural vegetation for agricultural purposes, wood harvesting, and, for BLUE, degradation from primary to secondary land through usage of natural vegetation as rangeland, and also from emissions from peat drainage and peat burning). Values are shown for the three bookkeeping models (yellow lines) and for their average (black with  $\pm 1\sigma$  uncertainty). The sum of the gross sinks and sources is  $E_{LUC}$  shown in panel (a). (d) Sources and sinks aggregated into four components that contribute to the net fluxes of CO<sub>2</sub>, including: (i) gross sources from deforestation; (ii) re/afforestation and wood harvest (i.e., the net flux on forest lands comprising slash and product decay following wood harvest; sinks due to regrowth after wood harvest or after abandonment, including reforestation and abandonment as parts of shifting cultivation cycles; afforestation), (iii) emissions from organic soils (peat drainage and peat fire, and (iv) sources and sinks related to other land use transitions. The scale of the fluxes shown is smaller than in panel (c) because the substantial gross sources and sinks from wood harvesting are accounted for as net flux under (ii). The sum of the component fluxes is  $E_{LUC}$  shown in panel (a).





**Figure 8: (a) The land CO<sub>2</sub> sink ( $S_{\text{LAND}}$ ) estimated by individual DGVMs estimates (green), as well as the budget estimate (black with  $\pm 1\sigma$  uncertainty), which is the average of all DGVMs. (b) Total atmosphere-land CO<sub>2</sub> fluxes ( $S_{\text{LAND}} - E_{\text{LUC}}$ ). The budget estimate of the total land flux (black with  $\pm 1\sigma$  uncertainty) combines the DGVM estimate of  $S_{\text{LAND}}$  from panel (a) with the bookkeeping estimate of  $E_{\text{LUC}}$  from Figure 7(a). Uncertainties are similarly propagated in quadrature from the budget estimates of  $S_{\text{LAND}}$  from panel (a) and  $E_{\text{LUC}}$  from Figure 7(a). DGVMs also provide estimates of  $E_{\text{LUC}}$  (see Figure 7(a)), which can be combined with their own estimates of the land sink. Hence panel (b) also includes an estimate for the total land flux for individual DGVMs (thin green lines) and their multi-model mean (thick green line).**



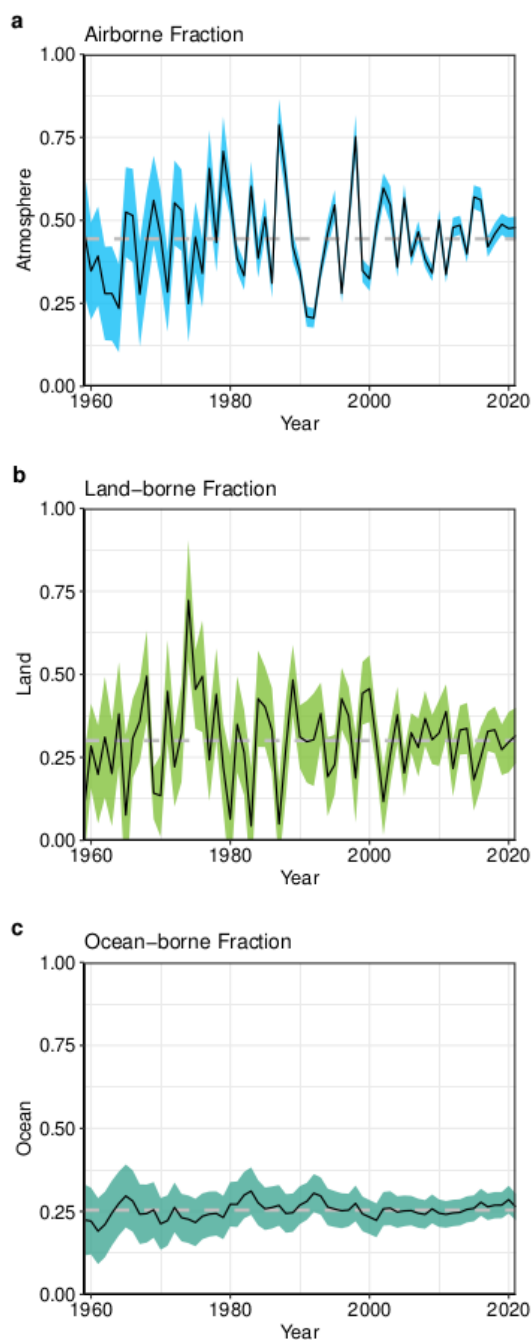


**Figure 9. The partitioning of total anthropogenic CO<sub>2</sub> emissions ( $E_{FOS} + E_{LUC}$ ) across (a) the atmosphere (airborne fraction), (b) land (land-borne fraction), and (c) ocean (ocean-borne fraction). Black lines represent the central estimate, and the coloured shading represents the uncertainty. The grey dashed lines represent the long-term average of the airborne (44%), land-borne (30%) and ocean-borne (25%) fractions during 1960-2021.**

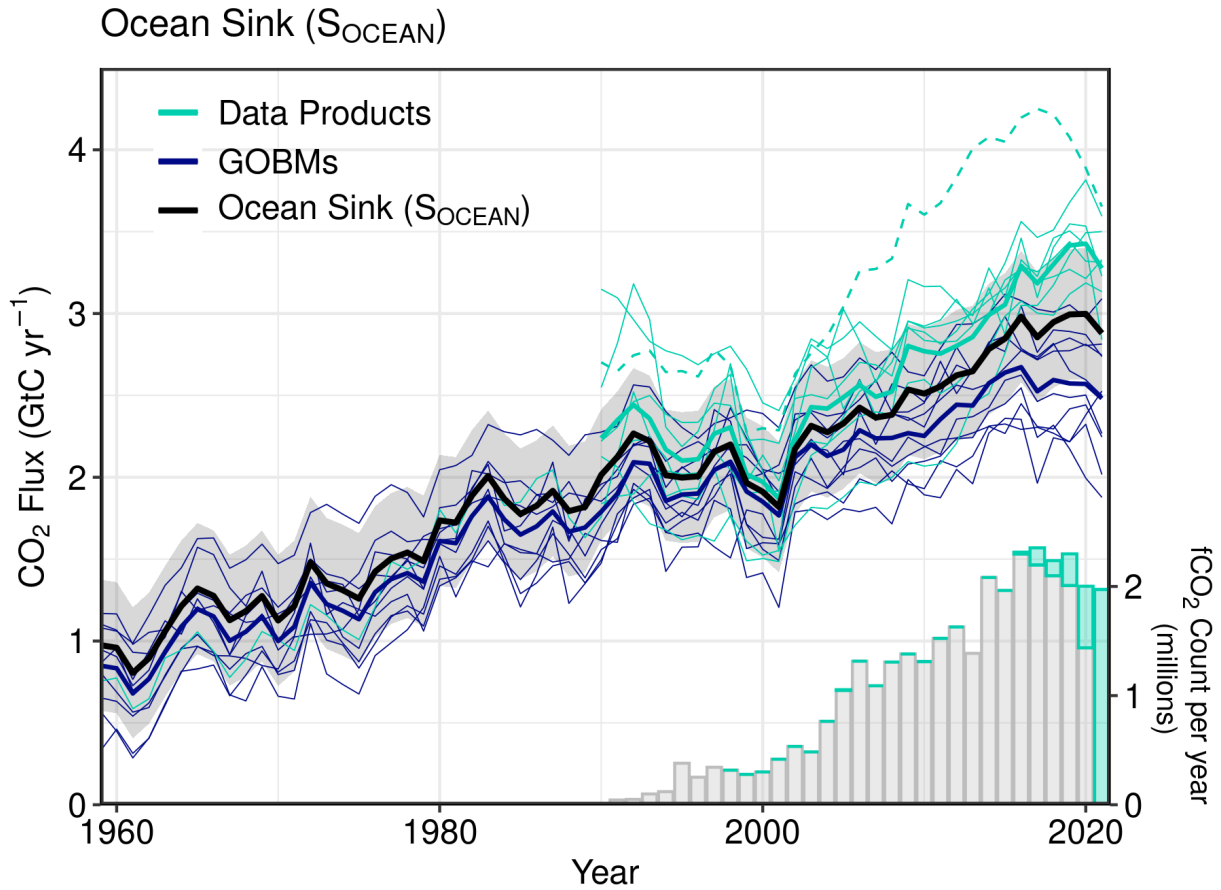


Figure 10. Comparison of the anthropogenic atmosphere-ocean  $\text{CO}_2$  flux showing the budget values of  $S_{\text{OCEAN}}$  (black; with the uncertainty in grey shading), individual ocean models (royal blue), and the ocean  $\text{fCO}_2$ -based data products (cyan; with Watson et al. (2020) in dashed line as not used for ensemble mean). Only one data product (Jena-MLS) extends back to 1959 (Rödenbeck et al., 2022). The  $\text{fCO}_2$ -based data products were adjusted for the pre-industrial ocean source of  $\text{CO}_2$  from river input to the ocean, by subtracting a source of  $0.65 \text{ GtC yr}^{-1}$  to make them comparable to  $S_{\text{OCEAN}}$  (see Section 2.4). Bar-plot in the lower right illustrates the number of  $\text{fCO}_2$  observations in the SOCAT v2022 database (Bakker et al., 2022). Grey bars indicate the number of data points in SOCAT v2021, and coloured bars the newly added observations in v2022.

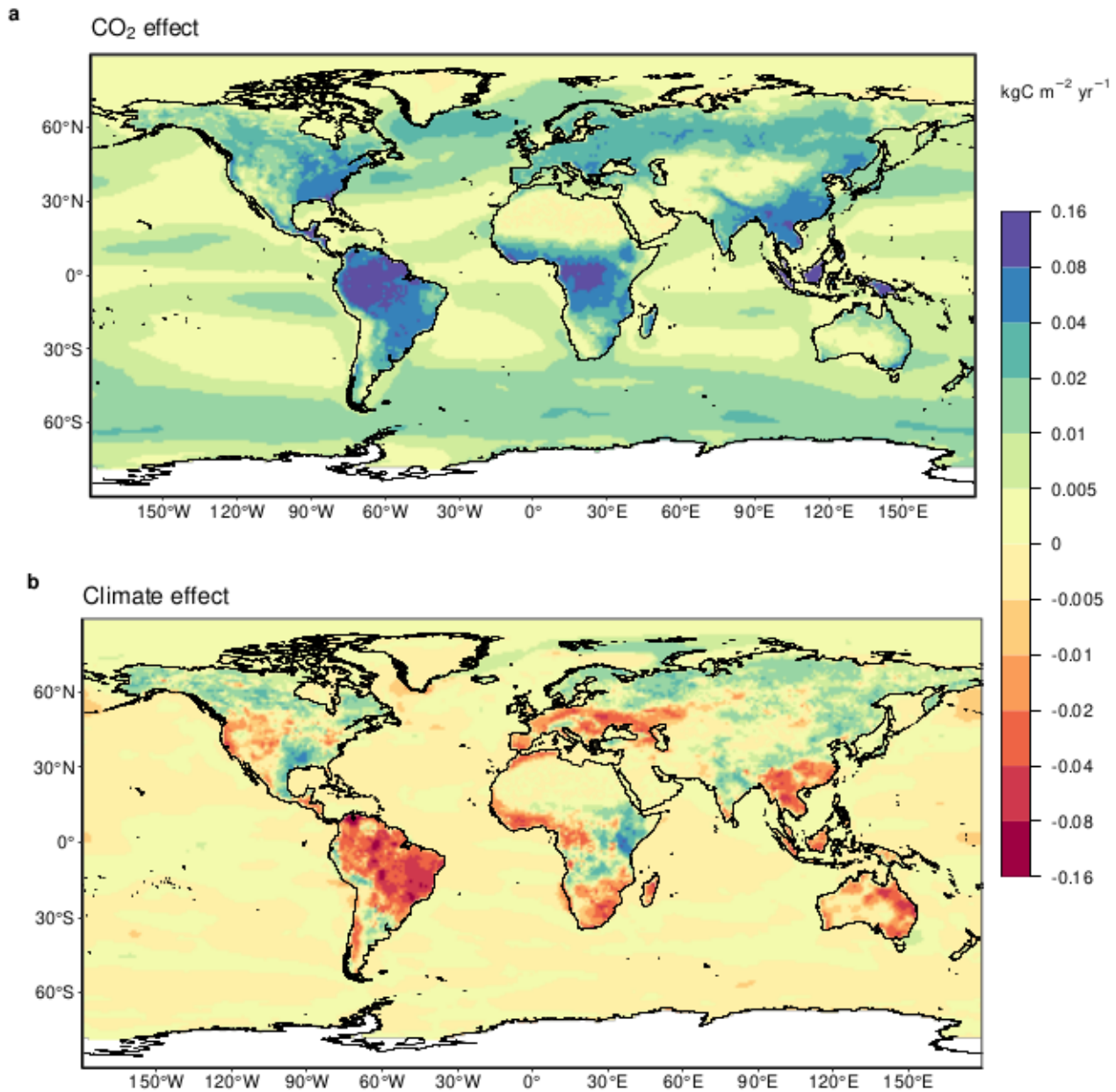


Figure 11. Attribution of the atmosphere-ocean ( $S_{\text{OCEAN}}$ ) and atmosphere-land ( $S_{\text{LAND}}$ ) CO<sub>2</sub> fluxes to (a) increasing atmospheric CO<sub>2</sub> concentrations and (b) changes in climate, averaged over the previous decade 2012-2021. All data shown is from the processed-based GOBMs and DGVMs. The sum of ocean CO<sub>2</sub> and climate effects will not equal the ocean sink shown in Figure 6 which includes the fCO<sub>2</sub>-based data products. See Appendix C.3.2 and C.4.1 for attribution methodology. Units are in kgC m<sup>-2</sup> yr<sup>-1</sup> (note the non-linear colour scale).

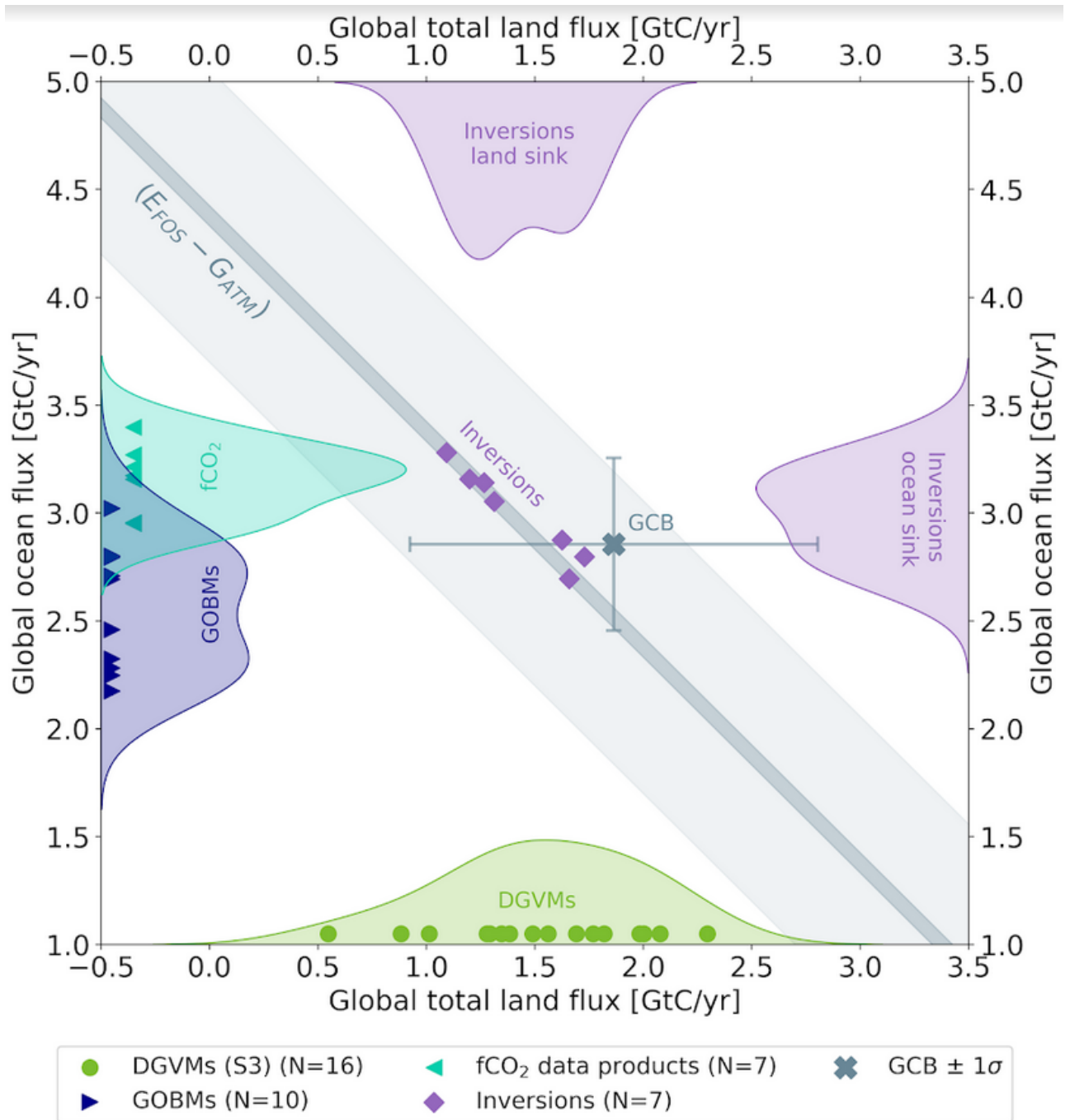


Figure 12. The 2012-2021 decadal mean net atmosphere-ocean and atmosphere-land fluxes derived from the ocean models and  $f\text{CO}_2$  products (y-axis, right and left pointing blue triangles respectively), and from the DGVMs (x-axis, green symbols), and the same fluxes estimated from the inversions (purple symbols on secondary x- and y-axis). The grey central point is the mean ( $\pm 1\sigma$ ) of  $S_{\text{OCEAN}}$  and  $(S_{\text{LAND}} - E_{\text{LUC}})$  as assessed in this budget. The shaded distributions show the density of the ensemble of individual estimates. The grey diagonal band represents the fossil fuel emissions minus the atmospheric growth rate from this budget ( $E_{\text{FOS}} - G_{\text{ATM}}$ ). Note that positive values are  $\text{CO}_2$  sinks.

Annual Carbon Fluxes to (-ve) or from (+ve) the Atmosphere

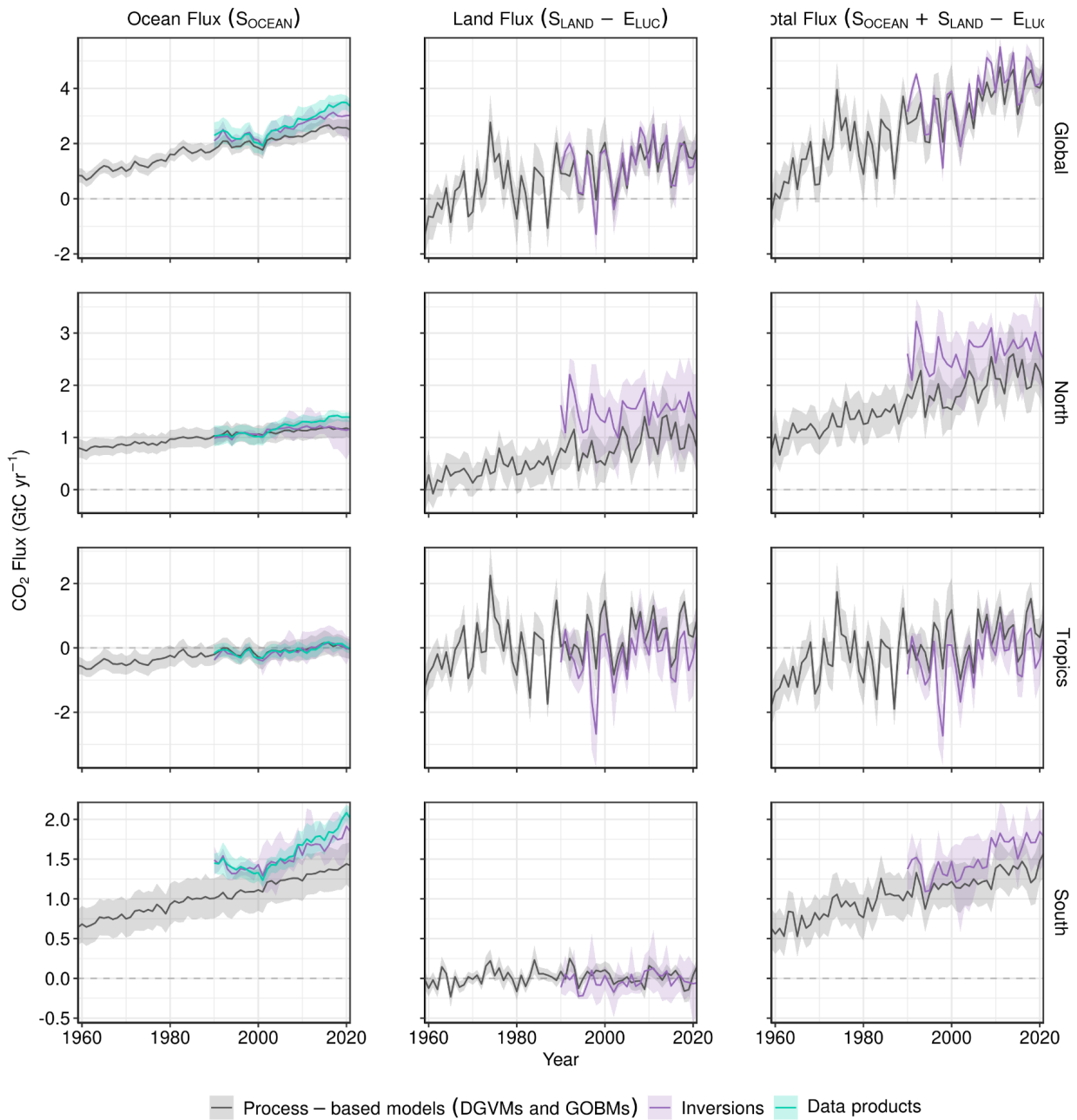


Figure 13. CO<sub>2</sub> fluxes between the atmosphere and the Earth's surface separated between land and oceans, globally and in three latitude bands. The ocean flux is  $S_{\text{OCEAN}}$  and the land flux is the net atmosphere-land fluxes from the DGVMs. The latitude bands are (top row) global, (2<sup>nd</sup> row) north (>30°N), (3<sup>rd</sup> row) tropics (30°S-30°N), and (bottom row) south (<30°S), and over ocean (left column), land (middle column), and total (right column). Estimates are shown for: process-based models (DGVMs for land, GOBMs for oceans); inversion systems (land and ocean); and fCO<sub>2</sub>-based data products (ocean only). Positive values indicate a flux from the atmosphere to the land or the ocean. Mean estimates from the combination of the process models for the land and oceans are shown (black line) with  $\pm 1$  standard deviation ( $1\sigma$ ) of the model ensemble (grey shading). For the total uncertainty in the process-based estimate of the total sink, uncertainties are summed in quadrature. Mean estimates from the atmospheric inversions are shown (purple lines) with their full spread (purple shading). Mean estimates from the fCO<sub>2</sub>-based data products are shown for the ocean domain (light blue lines) with their  $\pm 1\sigma$  spread (light blue shading). The global  $S_{\text{OCEAN}}$  (upper left) and the sum of  $S_{\text{OCEAN}}$  in all three regions represents the anthropogenic atmosphere-to-ocean flux based on the assumption that the preindustrial ocean sink was 0 GtC yr<sup>-1</sup> when riverine fluxes are not considered. This assumption does not hold at the regional level, where preindustrial fluxes can be significantly different from zero. Hence, the regional panels for  $S_{\text{OCEAN}}$  represent a combination of natural and anthropogenic fluxes. Bias-correction and area-weighting were only applied to global  $S_{\text{OCEAN}}$ ; hence the sum of the regions is slightly different from the global estimate (<0.05 GtC yr<sup>-1</sup>).

# Anthropogenic carbon flows

Cumulative changes 1850-2021  
GtC

Mean fluxes 2012-2021  
GtC per year

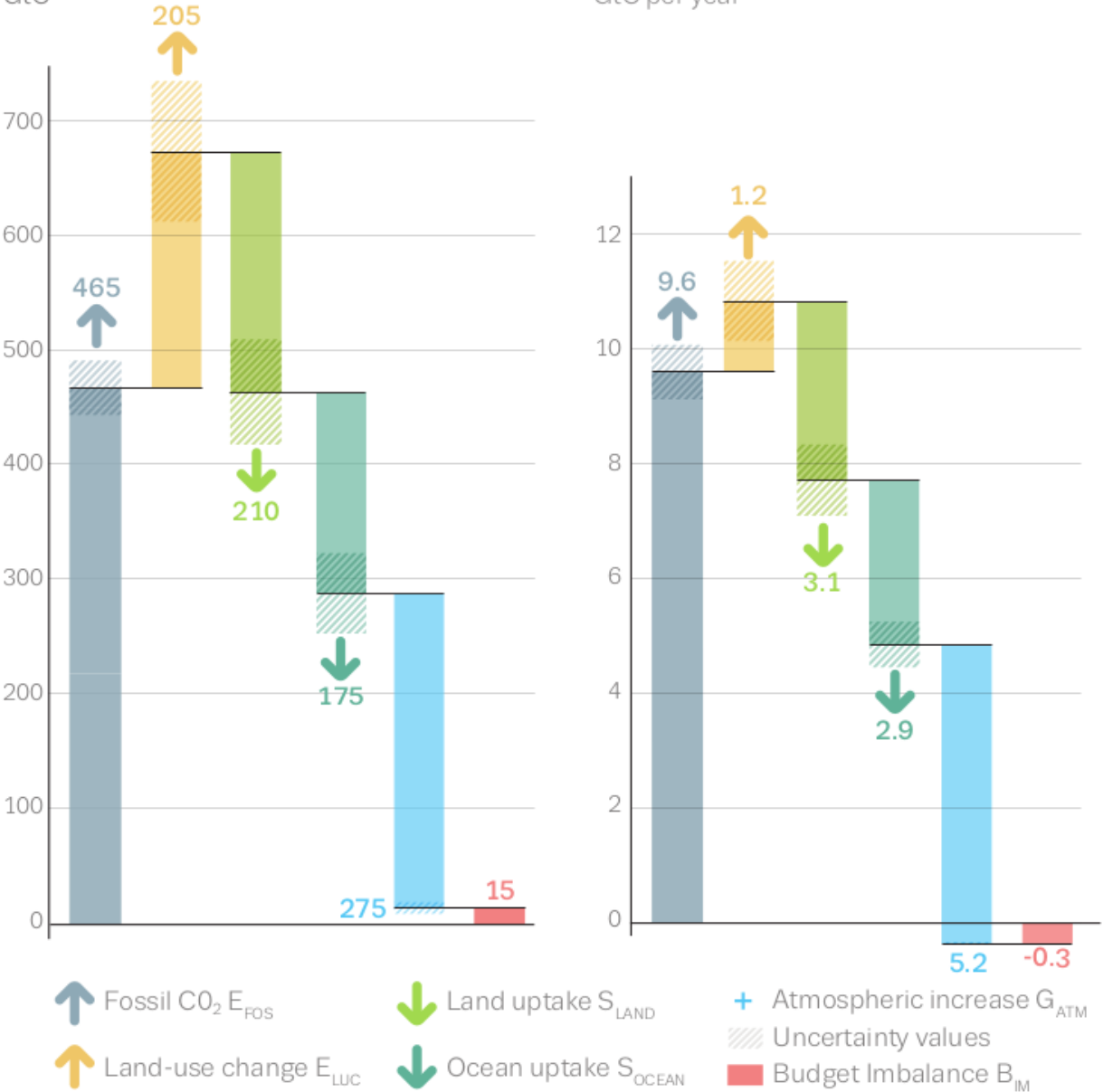


Figure 14. Cumulative changes over the 1850-2021 period (left) and average fluxes over the 2012-2021 period (right) for the anthropogenic perturbation of the global carbon cycle. See the caption of Figure 3 for key information and the methods in text for full details.



241  
242

243

244

245

246

247

248

249

250

251

**Figure 15. Kaya decomposition of the main drivers of fossil CO<sub>2</sub> emissions, considering population, GDP per person, Energy per GDP, and CO<sub>2</sub> emissions per energy, for China (top left), USA (top right), EU27 (middle left), India (middle right), Rest of the World (bottom left), and World (bottom right). Black dots are the annual fossil CO<sub>2</sub> emissions growth rate, coloured bars are the contributions from the different drivers. A general trend is that population and GDP growth put upward pressure on emissions, while energy per GDP and more recently CO<sub>2</sub> emissions per energy put downward pressure on emissions. Both the COVID-19 induced changes during 2020 and the recovery in 2021 led to a stark contrast to previous years, with different drivers in each region.**



252

253

Appendix A. Supplementary Tables

Table A1. Comparison of the processes included in the bookkeeping method and DGVMs in their estimates of ELUC and SLAND. See Table 4 for model references. All models include deforestation and forest regrowth after abandonment of agriculture (or from afforestation activities on agricultural land). Processes relevant for ELUC are only described for the DGVMs used with land-cover change in this study. Here we use the term “DGVM” in the broadest sense in terms of global vegetation models which are able to dynamically adjust to imposed LULCC.																			
	Bookkeeping Models			DGVMs															
	H&N	BLUE	OSCAR	CABLE-POP	CLASSIC	CLM5.0	DLEM	IBIS	ISAM	JSBACH	JULES-ES	LPJ-GUESS	LPJ	LPX-Bern	OCNv2	ORCHIDEEv3	SDGVM	VISIT	YIBs
<b>Processes relevant for ELUC</b>																			
Wood harvest and forest degradation (a)	yes	yes	yes	yes	no	yes	yes	yes	yes	yes	no	yes	yes	no (d)	yes	yes	no	yes	no
Shifting cultivation / Subgrid scale transitions	yes (b)	yes	yes	yes	no	yes	no	yes	no	yes	no	yes	yes	no (d)	no	no	no	yes	no
Cropland harvest (removed, R, or added to litter, L)	yes (R) (j)	yes (R) (j)	yes (R)	yes (R)	yes (L)	yes (R)	yes	yes (R)	yes	yes (R+L)	yes (R)	yes (R)	yes (L)	yes (R)	yes (R+L)	yes (R)	yes (R)	yes (R)	yes (L)
Peat fires	yes	yes	yes	no	no	yes	no	no	no	no	no	no	no	no	no	no	no	no	no
fire as a management tool	yes (j)	yes (j)	yes (h)	no	no	no	no	no	no	no	no	no	no	no	no	no	no	no	no
N fertilisation	yes (j)	yes (j)	yes (h)	no	no	yes	yes	no	yes	no	yes (i)	yes	no	yes	yes	yes	no	no	no
tillage	yes (j)	yes (j)	yes (h)	no	yes (g)	no	no	no	no	no	no	yes	no	no	no	yes (g)	no	no	no
irrigation	yes (j)	yes (j)	yes (h)	no	no	yes	yes	no	yes	no	no	yes	no	no	no	no	no	no	no
wetland drainage	yes (j)	yes (j)	yes (h)	no	no	no	no	no	yes	no	no	no	no	no	no	no	no	no	no
erosion	yes (j)	yes (j)	yes (h)	no	no	no	yes	no	no	no	no	no	no	no	no	no	no	yes	no
peat drainage	yes	yes	yes	no	no	no	no	no	no	no	no	no	no	no	no	no	no	no	no
Grazing and mowing Harvest (removed, r, or added to litter, l)	yes (r) (j)	yes (r) (j)	yes (r)	yes (r)	no	no	no	no	yes (r, l)	yes (l)	no	yes (r)	yes (l)	no	yes (r+l)	no	no	no	no
<b>Processes also relevant for SLAND (in addition to CO2 fertilisation and climate)</b>																			
Fire simulation and/or suppression	N.A.	N.A.	N.A.	no	yes	yes	no	yes	no	yes	yes	yes	yes	yes	no	no	yes	yes	no
Carbon-nitrogen interactions, including N deposition	N.A.	N.A.	N.A.	yes	no (f)	yes	yes	no	yes	yes	yes	yes	no	yes	yes	yes	yes (c)	no	no (f)
Separate treatment of direct and diffuse solar radiation	N.A.	N.A.	N.A.	yes	no	yes	no	no	no	no	yes	no	no	no	no	no	no	no	yes
(a) Refers to the routine harvest of established managed forests rather than pools of harvested products.																			
(b) No back- and forth-transitions between vegetation types at the country-level, but if forest loss based on FRA exceeded agricultural expansion based on FAO, then this amount of area was cleared for cropland and the same amount of area of old croplands abandoned.																			
(c) Limited. Nitrogen uptake is simulated as a function of soil C, and Vcmax is an empirical function of canopy N. Does not consider N deposition.																			
(d) Available but not active.																			
(e) Simple parameterization of nitrogen limitation based on Yin (2002; assessed on FACE experiments)																			
(f) Although C-N cycle interactions are not represented, the model includes a parameterization of down-regulation of photosynthesis as CO2 increases to emulate nutrient constraints (Arora et al., 2009)																			
(g) Tillage is represented over croplands by increased soil carbon decomposition rate and reduced humification of litter to soil carbon.																			
(h) as far as the DGVMs that OSCAR is calibrated to include it																			
(i) perfect fertilisation assumed, i.e. crops are not nitrogen limited and the implied fertiliser diagnosed																			
(j) Process captured implicitly by use of observed carbon densities.																			

254

255

256

Table A2. Comparison of the processes and model set up for the Global Ocean Biogeochemistry Models for their estimates of SOCEAN. See Table 4 for model references.										
	NEMO-PlankTOM 12	NEMO-PISCES (IPSL)	MICOM-HAMOC (NorESM1-OCv1.2)	MPIOM-HAMOC 6	FESOM-2.1-REcoM2	NEMO3.6-PISCESv2-gas (CNRM)	MOM6-COBALT (Princeton)	CESM-ETHZ	MRI-ESM2-1	CESM2
<b>Model specifics</b>										
Physical ocean model	NEMOv3.6-ORCA2	NEMOv3.6-eORCA1L75	MICOM (NorESM1-OCv1.2)	MPIOM	FESOM-2.1	NEMOv3.6-GELATOv6-eORCA1L75	MOM6-SIS2	CESMv1.3 (ocean model based on POP2)	MRI.CO Mv4	CESM2-POP2
Biogeochemistry model	PlankTOM 12	PISCESv2	HAMOC (NorESM1-OCv1.2)	HAMOC 6	REcoM-2-M	PISCESv2-gas	COBALTv2	BEC (modified & extended)	NPZD	MARBL
Horizontal resolution	2° lon, 0.3 to 1.5° lat	1° lon, 0.3 to 1° lat	1° lon, 0.17 to 0.25 lat	1.5°	unstructured mesh, 20-120 km resolution (CORE mesh)	1° lon, 0.3 to 1° lat	0.5° lon, 0.25 to 0.5° lat	1.125° lon, 0.53° to 0.27° lat	1° lon, 0.3 to 0.5° lat	1.125° lon, 0.53° to 0.27° lat
Vertical resolution	31 levels	75 levels, 1m at the surface	51 isopycnal layers + 2 layers representing a bulk mixed layer	40 levels	46 levels, 10 m spacing in the top 100 m	75 levels, 1m at surface	75 levels hybrid coordinates, 2m at surface	60 levels	60 levels with 1-level bottom boundary layer	60 levels
Total ocean area on native grid (km <sup>2</sup> )	3.6080E+08	3.6270E+08	3.6006E+08	3.6598E+08	3.6435E+08	3.6270E+08	3.6111E+08	3.5926E+08	3.6141E+08	3.61E+08
Gas-exchange parameterization	Wanninkhof et al. 1992	Orr et al., 2017	Orr et al., 2017, but with a=0.337	Orr et al., 2017	Orr et al., 2017	Orr et al., 2017	Orr et al., 2017	Wanninkhof (1992, coefficient a scaled down to 0.31)	Orr et al., 2017	Orr et al., 2017
CO <sub>2</sub> chemistry routines	Following Broecker et al. (1982)	mocsy	Following Dickson et al. 2007	Ilyina et al. (2013) adapted to comply with OMIP protocol (Orr et al., 2017)	mocsy	mocsy	mocsy	OCMIP2 (Orr et al.)	mocsy	OCMIP2 (Orr et al., 2017)
River input (PgC/yr) (organic/inorganic DIC)	0.723 / -	0.61 / -	0	0.77 / -	0 / 0	~0.611 / -	~0.07 / ~0.15	0.33 / -	0 / 0	0.173/0.263
Net flux to sediment (PgC/yr) (organic/other)	0.723 / -	0.59 / -	around 0.54 / -	- / 0.44	0 / 0	~0.656 / -	~0.11 / ~0.07 (CaCO <sub>3</sub> )	0.21 / -	0 / 0	0.345/0.110 (CaCO <sub>3</sub> )
<b>SPIN-UP procedure</b>										
Initialisation of carbon chemistry	GLODAPv1 (preindustrial DIC)	GLODAPv2 (preindustrial DIC)	GLODAPv1 (preindustrial DIC)	initialization from previous simulation	GLODAPv2 (preindustrial DIC)	GLODAPv2	GLODAPv2 (Alkalinity, DIC). DIC	GLODAPv2 (preindustrial DIC)	GLODAPv2 (preindustrial)	GLODAPv2 (preindustrial)

							corrected to 1959 level (simulation A and C) and to pre-industrial level (simulation B and D) using Khatiwala et al 2009		DIC)	DIC)
Preindustrial spin-up prior to 1850	spin-up 1750-1947	spin-up starting in 1836 with 3 loops of JRA55	1000 year spin up	~2000 years	189 years	long spin-up (> 1000 years)	Other bgc tracers initialized from a GFDL-ESM2M spin-up (> 1000 years)	spinup 1655-1849	1661 years with xCO2 = 284.32	spinup 1653-1850, xCO2= 278

#### Atmospheric forcing fields and CO2

Atmospheric forcing for (i) pre-industrial spin-up, (ii) spin-up 1850-1958 for simulation B, (iii) simulation B	looping NCEP year 1990 (i, ii, iii)	looping full JRA55 reanalysis	CORE-I (normal year) forcing (i, ii, iii)	OMIP climatology (i), NCEP year 1957 (ii,iii)	JRA55-do v.1.5.0 repeated year 1961 (i, ii, iii)	JRA55-do-v1.5.0 full reanalysis (i) cycling year 1958 (ii,iii)	GFDL-ESM2M internal forcing (i), JRA55-do-v1.5.0 repeat year 1959 (ii,iii)	COREv2 until 1835, from 1835-1850: JRA (i), normal year forcing created from JRA55-do version 1.3 (ii,iii)	JRA55-do v1.5.0 repeat year 1990/91 (i, ii, iii)	(i) repeating JRA 1958-2018 for spinup for A & D, repeating JRA 1990/1991 repeat year forcing for spinup for B & C, (ii) & (iii) JRA 1990/1991 repeat year forcing
Atmospheric CO2 for control spin-up 1850-1958 for simulation B, and for simulation B	constant 278ppm; converted to pCO2 temperature formulation (Sarmiento et al., 1992)	xCO2 of 286.46ppm, converted to pCO2 with constant sea-level pressure and water vapour pressure	xCO2 of 278ppm, converted to pCO2 with sea-level pressure and water vapour pressure	xCO2 of 278ppm, no conversion to pCO2	xCO2 of 278ppm, converted to pCO2 with sea-level pressure and water vapour pressure	xCO2 of 286.46ppm, converted to pCO2 with constant sea-level pressure and water vapour pressure	xCO2 of 278ppm, converted to pCO2 with sea-level pressure and water vapour pressure	xCO2 = 287.4ppm, converted to pCO2 with atmospheric pressure, and water vapour pressure	xCO2 of 284.32ppm (CMIP6 piControl), converted to pCO2 with water vapour and sea-level pressure (JRA55-	xCO2= 278

									do repeat year 1990/91)	
Atmospheric forcing for historical spin-up 1850-1958 for simulation A (i) and for simulation A (ii)	1750-1947: looping NCEP year 1990; 1948-2021: NCEP	1836-1958 : looping full JRA55 reanalysis (i), JRA55-do-v1.4 then 1.5 for 2020-21 (ii)	CORE-I (normal year) forcing; from 1948 onwards NCEP-R1 with CORE-II corrections	NCEP 6 hourly cyclic forcing (10 years starting from 1948, i), 1948-2021: transient NCEP forcing	JRA55-do-v1.5.0 repeated year 1961 (i), transient JRA55-do-v1.5.0 (ii)	JRA55-do cycling year 1958 (i), JRA55-do-v1.5.0 (ii)	JRA55-do-v1.5 repeat year 1959 (i), v1.5.0 (1959-2019, v1.5.0.1b (2020), v1.5.0.1 (2021; ii)	JRA55 version 1.3, repeat cycle between 1958-2018 (i), v1.3 (1959-2018), v.1.5.0.1 (2020-2021)	1653-1957: repeated cycle JRA55-do v1.5.0 1958-2018 (i), v1.5.0 (1958-2018), v1.5.0.1 (2019-2021; ii)	(i) repeating JRA 1958-2018, (ii) JRA 1958-2021
Atmospheric CO2 for historical spin-up 1850-1958 for simulation A (i) and simulation A (ii)	xCO2 provided by the GCB; converted to pCO2 temperature formulation (Sarmiento et al., 1992), monthly resolution (i, ii)	xCO2 as provided by the GCB, global mean, annual resolution, converted to pCO2 with sea-level pressure and water vapour pressure (i, ii)	xCO2 as provided by the GCB, converted to pCO2 with sea level pressure (taken from the atmospheric forcing) and water vapor correction (i, ii)	transient monthly xCO2 provided by GCB, no conversion (i, ii)	xCO2 as provided by the GCB, converted to pCO2 with sea-level pressure and water vapour pressure, global mean, monthly resolution (i, ii)	xCO2 as provided by the GCB, converted to pCO2 with constant sea-level pressure and water vapour pressure, global mean, yearly resolution (i, ii)	xCO2 at year 1959 level (315 ppm, i) and as provided by GCB (ii), both converted to pCO2 with sea-level pressure and water vapour pressure, global mean, yearly resolution	xCO2 as provided by the GCB, converted to pCO2 with locally determined atm. pressure, and water vapour pressure (i, ii)	xCO2 as provided for CMIP6 historical simulations, annual resolution (i), and as provided by GCB (ii), both converted to pCO2 with water vapour and sea-level pressure	annual global xCO2 provided by GCB, converted to equilibrium CO2* using atmospheric pressure and Weiss and Price (1980)

Table A3: Description of ocean data-products used for assessment of SOCEAN. See Table 4 for references.								
	Jena-MLS	MPI-SOMFFN	CMEMS-LSCE-FFNN	Watson et al	NIES-NN	JMA-MLR	OS-ETHZ-GRaCER	LDEO HPD
Method	Spatio-temporal interpolation (version oc_v2022). Spatio-temporal field of ocean-internal carbon sources/sinks is fit to the SOCATv2022 pCO2 data. Includes a multi-linear regression against environmental drivers to bridge data gaps,	A feed-forward neural network (FFN) determines non-linear relationship between SOCAT pCO2 measurements and environmental predictor data for 16 biogeochemical provinces (defined through a self-organizing map, SOM) and is used to fill the existing data gaps.	An ensemble of neural network models trained on 100 subsampled datasets from SOCAT and environmental predictors. The models are used to reconstruct sea surface fugacity of CO2 and convert to air-sea CO2 fluxes	Modified MPI-SOMFFN with SOCATv2022 pCO2 database. Corrected to the subskin temperature of the ocean as measured by satellite (Goddijn-Murphy et al, 2015). Flux calculation corrected for the cool and salty surface skin. Monthly climatology for skin temperature correction derived from ESA CCI product for the period 2003 to 2011 (Merchant et al, 2019).	A feed forward neural network model trained on SOCAT 2021 fCO2 and environmental predictor data. The fCO2 was normalized to the reference year 2000 by a global fCO2 trend: We fitted the dependence of fCO2 on year by linear regression. We subtracted the trend from fCO2 and used the neural network to model the nonlinear dependence of the residual on predictors. The trend was added to model predictions to reconstruct fCO2.	Fields of total alkalinity (TA) were estimated by using a multiple linear regressions (MLR) method based on GLODAPv2.2021 and satellite observation data. SOCATv2022 fCO2 data were converted to dissolved inorganic carbon (DIC) with the TA. Fields of DIC were estimated by using a MLR method based on the DIC and satellite observation data	Geospatial Random Cluster Ensemble Regression is a two-step cluster-regression approach, where multiple clustering instances with slight variations are run to create an ensemble of estimates. We use K-means clustering and a combination of Gradient boosted trees and Feed-forward neural-networks to estimate SOCAT v2022 fCO2.	Based on fCO2-misfit between observed fCO2 and eight of the ocean biogeochemical models used in this assessment. The eXtreme Gradient Boosting method links this misfit to environmental observations to reconstruct the model misfit across all space and time., which is then added back to model-based fCO2 estimate. The final reconstruction of surface fCO2 is the average across the eight reconstructions.
Gas-exchange parameterization	Wanninkhof 1992. Transfer coefficient k scaled to match a global mean transfer rate of 16.5 cm/hr by (Naegler, 2009)	Wanninkhof 1992. Transfer coefficient k scaled to match a global mean transfer rate of 16.5 cm/hr	Wanninkhof 2014. Transfer coefficient k scaled to match a global mean transfer rate of 16.5 cm/hr (Naegler, 2009)	Nightingale et al 2000	Wanninkhof, 2014. Transfer coefficient k scaled to match a global mean transfer rate of 16.5 cm/hr (Naegler, 2009)	Wanninkhof., 2014. Transfer coefficient k scaled to match a global mean transfer rate of 16.5 cm/hr (Naegler, 2009)	Wanninkhof 1992, averaged and scaled for three reanalysis wind data, to a global mean 16.5 cm/hr (after Naegler 2009; Fay & Gregor et al. 2021)	Wanninkhof 1992, averaged and scaled for three reanalysis wind data, to a global mean 16.5 cm/hr (after Naegler 2009; Fay & Gregor et al. 2021)
Wind product	JMA55-do reanalysis	ERA 5	ERA5	Mean and mean square winds monthly 1x1° from CCMP, 0.25x0.25° x 6-hourly,	ERA5	JRA55	JRA55, ERA5, NCEP1	JRA55, ERA5, CCMP2
Spatial resolution	2.5 degrees longitude x 2 degrees latitude	1x1 degree	1x1 degree	1x1 degree	1x1 degree	1x1 degree	1x1 degree	1x1 degree
Temporal resolution	daily	monthly	monthly	monthly	monthly	monthly	monthly	monthly

<b>Atmospheric CO2</b>	Spatially and temporally varying field based on atmospheric CO2 data from 169 stations (Jena CarboScope atmospheric inversion sEXTALL_v2021)	Spatially varying 1x1 degree atmospheric pCO2_wet calculated from the NOAA GMD marine boundary layer xCO2 and NCEP sea level pressure with the moisture correction by Dickson et al 2007.	Spatially and monthly varying fields of atmospheric pCO2 computed from CO2 mole fraction (CO2 atmospheric inversion from the Copernicus Atmosphere Monitoring Service), and atmospheric dry-air pressure which is derived from monthly surface pressure (ERA5) and water vapour pressure fitted by Weiss and Price 1980	Atmospheric pCO2 (wet) calculated from NOAA marine boundary layer XCO2 and NCEP sea level pressure, with pH2O calculated from Cooper et al, 1998. 2021 XCO2 marine boundary values were not available at submission so we used preliminary values, estimated from 2020 values and increase at Mauna Loa.	NOAA Greenhouse Gas Marine Boundary Layer Reference. <a href="https://gml.noaa.gov/ccgg/mbll/mbll.html">https://gml.noaa.gov/ccgg/mbll/mbll.html</a>	Atmospheric xCO2 fields of JMA-GSAM inversion model (Maki et al. 2010; Nakamura et al. 2015) were used. They were converted to pCO2 by using JRA55 sea level pressure. 2021 xCO2 fields were not available at this stage, and we used global xCO2 increments from 2020 to 2021.	NOAA's marine boundary layer product for xCO2 is linearly interpolated onto a 1x1 degree grid and resampled from weekly to monthly. xCO2 is multiplied by ERA5 mean sea level pressure, where the latter corrected for water vapour pressure using Dickson et al. (2007). This results in monthly 1x1 degree pCO2atm.	NOAA's marine boundary layer product for xCO2 is linearly interpolated onto a 1x1 degree grid and resampled from weekly to monthly. xCO2 is multiplied by ERA5 mean sea level pressure, where the latter corrected for water vapour pressure using Dickson et al. (2007). This results in monthly 1x1 degree pCO2atm.
<b>Total ocean area on native grid (km2)</b>	3.63E+08	3.63E+08	3.50E+08	3.52E+08	3.49E+08	3.10E+08 (2.98E+08 to 3.16E+08, depending on ice cover)	3.55E+08	3.61E+08
<b>method to extend product to full global ocean coverage</b>		Arctic and marginal seas added following Landschützer et al. (2020). No coastal cut.				Fay & Gregor et al. 2021	Method has near full coverage	Fay & Gregor et al. 2021. Gaps were filled with monthly climatology. Interannual variability was added to the climatology based on the temporal evolution of 5 products for years 1985 through 2020 and then only using this product for year 2021.

**Table A4.** Comparison of the inversion set up and input fields for the atmospheric inversions. Atmospheric inversions see the full CO<sub>2</sub> fluxes, including the anthropogenic and pre-industrial fluxes. Hence they need to be adjusted for the pre-industrial flux of CO<sub>2</sub> from the land to the ocean that is part of the natural carbon cycle before they can be compared with SOCEAN and SLAND from process models. See Table 4 for references.

	Copernicus Atmosphere Monitoring Service (CAMS)	Carbon-Tracker Europe (CTE)	Jena CarboScope	UoE	NISMN-CO <sub>2</sub>	CMS-Flux	GONGGA	THU	Copernicus Atmosphere Monitoring Service (CAMS) Satellite
<b>Version number</b>	v21r1	v2022	v2022	UoE v6.1b	v2022.1	v2022	v2022	v2022	FT21r2
<b>Observations</b>									
<b>Atmospheric observations</b>	Hourly resolution (well-mixed conditions) obspack GLOBALVIEWplus v7.0 (a) and NRT_v7.2(b), WDCGG, RAMCES and ICOS ATC	Hourly resolution (well-mixed conditions) obspack GLOBALVIEWplus v7.0 (a) and NRT_v7.2(b)	Flasks and hourly from various institutions (outliers removed by 2 $\sigma$ criterion)	Hourly resolution (well-mixed conditions) obspack GLOBALVIEWplus v7.0(a) and NRT_v7.2(b)	Hourly resolution (well-mixed conditions) obspack GLOBALVIEWplus v7.0(a) and NRT_v7.2(b)	ACOS-GOSAT v9r, OCO-2 v10 scaled to WMO 2019 standard and remote flask observations from ObsPack, GLOBALVIEW puls, v7.0(a) and NRT_v 7.2(b)	OCO-2 v10r data that scaled to WMO 2019 standard	OCO-2 v10r data that scaled to WMO 2019 standard	bias-corrected ACOS GOSAT v9 over land until August 2024 + bias-corrected ACOS OCO-2 v10 over land, both rescaled to X2019
<b>Period covered</b>	1979-2021	2001-2021	1957-2021	2001-2021	1990-2021	2010-2021	2015-2021	2015-2021	2010-2021
<b>Prior fluxes</b>									
<b>Biosphere and fires</b>	ORCHIDEE, GFEDv4.1s	SiB4 and GFAS	Zero	CASA v1.0, climatology after 2016 and GFED4.0	VISIT and GFEDv4.1s	CARDAM OM	CASA and GFEDv4.1s	SiB4.2 and GFEDv4.1s	ORCHIDEE, GFEDv4.1s
<b>Ocean</b>	CMEMS-LSCE-FFNN 2021	CarboScope v2021	CarboScope v2022	Takahashi climatology	JMA global ocean mapping (Iida et al., 2015)	MOM6	Takahashi climatology	Takahashi climatology	CMEMS-LSCE-FFNN 2021
<b>Fossil fuels</b>	GridFED 2021.2(c) with an extrapolation to 2021 based on Carbonmonitor and NO <sub>2</sub>	GridFED 2021.3 + GridFED 2022.2 for 2021 (c)	GridFED v2022.2 (c)	GridFED 2022.1 (c)	GridFED v2022.2 (c)	GridFED2 022.2 (c)	GridFED 2021.3 (c) with an extrapolation to 2021 based on Carbonmonitor	GridFED v2022.1 (c)	GridFED 2021.2 (c) with an extrapolation to 2021 based on Carbonmonitor and NO <sub>2</sub>
<b>Transport and optimization</b>									
<b>Transport model</b>	LMDZ v6	TM5	TM3	GEOS-CHEM	NICAM-TM	GEOS-CHEM	GEOS-Chem v12.9.3	GEOS-CHEM	LMDZ v6

<b>Weather forcing</b>	ECMWF	ECMWF	NCEP	MERRA	JRA55	MERRA	MERRA2	GEOS-FP	ECMWF
<b>Horizontal Resolution</b>	Global 3.75°x1.875°	Global 3°x2°, Europe 1°x1°, North America 1°x1°	Global 3.83°x5°	Global 4°x5°	Isocahedra l grid: ~225km	Global 4°x5°	Global 2°x2.5°	Global 4°x5°	Global 3.75°x1.875°
<b>Optimization</b>	Variational	Ensemble Kalman filter	Conjugate gradient (re-orthonormalization) (d)	Ensemble Kalman filter	Variational	Variational	Nonlinear least squares four-dimensional variation (NLS-4DVar)	Ensemble Kalman filter	Variational
(a) <a href="https://doi.org/10.25925/20210801">https://doi.org/10.25925/20210801</a> . Schuldt et al. Multi-laboratory compilation of atmospheric carbon dioxide data for the period 1957-2020; obspack_co2_1_GLOBALVIEWplus_v7.0_2021-08-18; NOAA Earth System Research Laboratory, Global Monitoring Laboratory. <a href="http://doi.org/10.25925/20210801">http://doi.org/10.25925/20210801</a> .									
(b) <a href="http://doi.org/10.25925/20220624">http://doi.org/10.25925/20220624</a> . Schuldt et al. Multi-laboratory compilation of atmospheric carbon dioxide data for the period 2021-2022; obspack_co2_1_NRT_v7.2_2022-06-28; NOAA Earth System Research Laboratory, Global Monitoring Laboratory. <a href="http://doi.org/10.25925/20220624">http://doi.org/10.25925/20220624</a> .									
(c) GCP-GridFED v2021.2, v2021.3, v2022.1 and v2022.2 (Jones et al., 2022) are updates through the year 2021 of the GCP-GridFED dataset presented by Jones et al. (2021).									
(d) ocean prior not optimised									



**Table A5 Attribution of fCO<sub>2</sub> measurements for the year 2021 included in SOCATv2022 (Bakker et al., 2016, 2022) to inform ocean fCO<sub>2</sub>-based data products.**

Platform Name	Regions	No. of measurements	Principal Investigators	No. of datasets	Platform Type
1 degree	North Atlantic, coastal	71,863	Tanhua, T.	1	Ship
Alawai_158W_21 N	Tropical Pacific	387	Sutton, A.; De Carlo, E. H.; Sabine, C.	1	Mooring
Atlantic Explorer	North Atlantic, tropical Atlantic, coastal	34,399	Bates, N. R.	16	Ship
Atlantic Sail	North Atlantic, coastal	27,496	Steinhoff, T.; Körtzinger, A.	7	Ship
BlueFin	Tropical Pacific	60,606	Alin, S. R.; Feely, R. A.	11	Ship
Cap San Lorenzo	North Atlantic, tropical Atlantic, coastal	44,281	Lefèvre, N.	7	Ship
CCE2_121W_34N	Coastal	1,333	Sutton, A.; Send, U.; Ohman, M.	1	Mooring
Celtic Explorer	North Atlantic, coastal	61,118	Cronin, M.	10	Ship
F.G. Walton Smith	Coastal	38,375	Rodriguez, C.; Millero, F. J.; Pierrot, D.; Wanninkhof, R.	14	Ship
Finnmaid	Coastal	223,438	Rehder, G.; Bittig, H. C.; Glockzin, M.	1	Ship
FRA56	Coastal	5,652	Tanhua, T.	1	Ship
G.O. Sars	Arctic, north Atlantic, coastal	82,607	Skjelvan, I.	9	Ship
GAKOA_149W_60 N	Coastal	402	Monacci, N.; Cross, J.; Musielewicz, S.; Sutton, A.	1	Mooring
Gordon Gunter	North Atlantic, coastal	36,058	Wanninkhof, R.; Pierrot, D.	6	Ship
Gulf Challenger	Coastal	6,375	Salisbury, J.; Vandemark, D.; Hunt, C. W.	6	Ship
Healy	Arctic, north Atlantic, coastal	28,998	Sweeney, C.; Newberger, T.; Sutherland, S. C.; Munro, D. R.	5	Ship
Henry B. Bigelow	North Atlantic, coastal	67,399	Wanninkhof, R.; Pierrot, D.	8	Ship
Heron Island	Coastal	989	Tilbrook, B.; Neill, C.; van Ooijen, E.; Passmore, A.; Black, J.	1	Mooring
Investigator	Southern Ocean, coastal, tropical Pacific, Indian Ocean	120,782	Tilbrook, B.; Akl, J.; Neill, C.	6	Ship
KC_BUOY	Coastal	2,860	Evans, W.; Pocock, K.	1	Mooring
Keifu Maru II	North Pacific, tropical Pacific, coastal	10,053	Kadono, K.	8	Ship
Laurence M. Gould	Southern Ocean	2,604	Sweeney, C.; Newberger, T.; Sutherland, S. C.; Munro, D. R.	1	Ship
Marion Dufresne	Indian Ocean, Southern Ocean, coastal	9,911	Lo Monaco, C.; Metzl, N.	1	Ship
Nathaniel B. Palmer	Southern Ocean	2,376	Sweeney, C.; Newberger, T.; Sutherland, S. C.; Munro, D. R.	1	Ship
New Century 2	North Pacific, tropical Pacific, north Atlantic, coastal	198,293	Nakaoka, S.-I.; Takao, S.	10	Ship
Newrest - Art and Fenetres	North Atlantic, tropical Atlantic, south Atlantic, coastal	17,699	Tanhua, T.	2	Ship
Quadra Island Field Station	Coastal	81,201	Evans, W.; Pocock, K.	1	Mooring
Ronald H. Brown	North Atlantic, coastal	31,661	Wanninkhof, R.; Pierrot, D.	3	Ship
Ryofu Maru III	North Pacific, tropical Pacific, coastal	10,464	Kadono, K.	8	Ship
Sea Explorer	Southern Ocean, north Atlantic, coastal, tropical Atlantic	37,027	Landshützer, P.; Tanhua, T.	2	Ship

Sikuliaq	Arctic, north Pacific, coastal	60,549	Sweeney, C.; Newberger, T.; Sutherland, S. C.; Munro, D. R.	13	Ship
Simon Stevin	Coastal	57,055	Gkritzalis, T.; Theetaert, H.; Cattrijse, A.; T’Jampens, M.	11	Ship
Sitka Tribe of Alaska Environmental Research Laboratory	Coastal	19,086	Whitehead, C.; Evans, W.; Lanphier, K.; Peterson, W.; Kennedy, E.; Hales, B.	1	Mooring
SOFS_142E_46S	Southern Ocean	894	Sutton, A.; Trull, T.; Shadwick, E.	1	Mooring
Soyo Maru	Tropical Pacific, coastal	33,234	Ono, T.	3	Ship
Station M	North Atlantic	447	Skjelvan, I.	1	Mooring
Statsraad Lehmkuhl	North Atlantic, tropical Atlantic, coastal	47,881	Becker, M.; Olsen, A.	3	Ship
TAO125W_ON	Tropical Pacific	241	Sutton, A.	1	Mooring
Tavastland	Coastal	48,421	Willstrand Wranne, A.; Steinhoff, T.	17	Ship
Thomas G. Thompson	North Atlantic, tropical Atlantic, north Pacific, tropical Pacific, coastal	47,073	Alin, S. R. ; Feely, R. A.	5	Ship
Trans Future 5	Southern Ocean, north Pacific, tropical Pacific, coastal	257,424	Nakaoka, S.-I.; Takao, S.	22	Ship
Tukuma Arctica	North Atlantic, coastal	70,033	Becker, M.; Olsen, A.	23	Ship
Wakataka Maru	North Pacific, coastal	13,392	Tadokoro, K.	2	Ship

**Table A6.** Aircraft measurement programs archived by Cooperative Global Atmospheric Data Integration Project (CGADIP; Schuldt et al. 2022a and 2022b) that contribute to the evaluation of the atmospheric inversions (Figure B4).

Site code	Measurement program name in Obspack	Specific doi	Data providers
AAO	Airborne Aerosol Observatory, Bondville, Illinois		Sweeney, C.; Dlugokencky, E.J.
ABOVE	Carbon in Arctic Reservoirs Vulnerability Experiment (CARVE)	<a href="https://doi.org/10.3334/ORNLDAAC/1404">https://doi.org/10.3334/ORNLDAAC/1404</a>	Sweeney, C., J.B. Miller, A. Karion, S.J. Dinardo, and C.E. Miller. 2016. CARVE: L2 Atmospheric Gas Concentrations, Airborne Flasks, Alaska, 2012-2015. ORNL DAAC, Oak Ridge, Tennessee, USA.
ACG	Alaska Coast Guard		Sweeney, C.; McKain, K.; Karion, A.; Dlugokencky, E.J.
ACT	Atmospheric Carbon and Transport - America		Sweeney, C.; Dlugokencky, E.J.; Baier, B.; Montzka, S.; Davis, K.
AIRCO RENOA A	NOAA AirCore		Colm Sweeney (NOAA) AND Bianca Baier (NOAA)
ALF	Alta Floresta		Gatti, L.V.; Gloor, E.; Miller, J.B.;
AOA	Aircraft Observation of Atmospheric trace gases by JMA		ghg_obs@met.kishou.go.jp
BGI	Bradgate, Iowa		Sweeney, C.; Dlugokencky, E.J.
BNE	Beaver Crossing, Nebraska		Sweeney, C.; Dlugokencky, E.J.
BRZ	Berezorechka, Russia		Sasakama, N.; Machida, T.
CAR	Briggsdale, Colorado		Sweeney, C.; Dlugokencky, E.J.
CMA	Cape May, New Jersey		Sweeney, C.; Dlugokencky, E.J.
CON	CONTRAIL (Comprehensive Observation Network for TRace gases by AlrLiner)	<a href="http://dx.doi.org/10.17595/20180208.001">http://dx.doi.org/10.17595/20180208.001</a>	Machida, T.; Matsueda, H.; Sawa, Y. Niwa, Y.
CRV	Carbon in Arctic Reservoirs Vulnerability Experiment (CARVE)		Sweeney, C.; Karion, A.; Miller, J.B.; Miller, C.E.; Dlugokencky, E.J.
DND	Dahlen, North Dakota		Sweeney, C.; Dlugokencky, E.J.
ECO	East Coast Outflow		Sweeney, C.; McKain, K.
ESP	Estevan Point, British Columbia		Sweeney, C.; Dlugokencky, E.J.
ETL	East Trout Lake, Saskatchewan		Sweeney, C.; Dlugokencky, E.J.
FWI	Fairchild, Wisconsin		Sweeney, C.; Dlugokencky, E.J.
GSFC	NASA Goddard Space Flight Center Aircraft Campaign		Kawa, S.R.; Abshire, J.B.; Riris, H.
HAA	Molokai Island, Hawaii		Sweeney, C.; Dlugokencky, E.J.
HFM	Harvard University Aircraft Campaign		Wofsy, S.C.
HIL	Homer, Illinois		Sweeney, C.; Dlugokencky, E.J.
HIP	HIPPO (HIAPER Pole-to-Pole Observations)	<a href="https://doi.org/10.3334/CDIAC/HIPPO_010">https://doi.org/10.3334/CDIAC/HIPPO_010</a>	Wofsy, S.C.; Stephens, B.B.; Elkins, J.W.; Hintsa, E.J.; Moore, F.
IAGOS-CARIBI	In-service Aircraft for a Global Observing System		Obersteiner, F.; Boenisch, H.; Gehrlein, T.; Zahn, A.; Schuck, T.

C			
INX	INFLUX (Indianapolis Flux Experiment)		Sweeney, C.; Dlugokencky, E.J.; Shepson, P.B.; Turnbull, J.
LEF	Park Falls, Wisconsin		Sweeney, C.; Dlugokencky, E.J.
NHA	Offshore Portsmouth, New Hampshire (Isles of Shoals)		Sweeney, C.; Dlugokencky, E.J.
OIL	Oglesby, Illinois		Sweeney, C.; Dlugokencky, E.J.
ORC	ORCAS (O2/N2 Ratio and CO2 Airborne Southern Ocean Study)	<a href="https://doi.org/10.5065/D6SB445X">https://doi.org/10.5065/D6SB445X</a>	Stephens, B.B., Sweeney, C., McKain, K., Kort, E.
PFA	Poker Flat, Alaska		Sweeney, C.; Dlugokencky, E.J.
RBA-B	Rio Branco		Gatti, L.V.; Gloor, E.; Miller, J.B.
RTA	Rarotonga		Sweeney, C.; Dlugokencky, E.J.
SCA	Charleston, South Carolina		Sweeney, C.; Dlugokencky, E.J.
SGP	Southern Great Plains, Oklahoma		Sweeney, C.; Dlugokencky, E.J.; Biraud, S.
TAB	Tabatinga		Gatti, L.V.; Gloor, E.; Miller, J.B.
TGC	Offshore Corpus Christi, Texas		Sweeney, C.; Dlugokencky, E.J.
THD	Trinidad Head, California		Sweeney, C.; Dlugokencky, E.J.
WBI	West Branch, Iowa		Sweeney, C.; Dlugokencky, E.J.

273  
274  
275  
276  
277  
278  
279  
280  
281  
282  
283  
284  
285  
286  
287

**Table A7.** Main methodological changes in the global carbon budget since first publication. Methodological changes introduced in one year are kept for the following years unless noted. Empty cells mean there were no methodological changes introduced that year.

Publication year	Fossil fuel emissions			LUC emissions	Reservoirs			Uncertainty & other changes
	Global	Country (territorial)	Country (consumption)		Atmosphere	Ocean	Land	
2006 (a)		Split in regions						
2007 (b)				ELUC based on FAO-FRA 2005; constant ELUC for 2006	1959-1979 data from Mauna Loa; data after 1980 from global average	Based on one ocean model tuned to reproduced observed 1990s sink		±1σ provided for all components
2008 (c)				Constant ELUC for 2007				
2009 (d)		Split between Annex B and non-Annex B	Results from an independent study discussed	Fire-based emission anomalies used for 2006-2008		Based on four ocean models normalised to observations with constant delta	First use of five DGVMs to compare with budget residual	
2010 (e)	Projection for current year based on GDP	Emissions for top emitters		ELUC updated with FAO-FRA 2010				
2011 (f)			Split between Annex B and non-Annex B					
2012 (g)		129 countries from 1959	129 countries and regions from 1990-2010 based on GTAP8.0	ELUC for 1997-2011 includes interannual anomalies from fire-based emissions	All years from global average	Based on 5 ocean models normalised to observations with ratio	Ten DGVMs available for SLAND; First use of four models to compare with ELUC	
2013 (h)		250 countriesb	134 countries and regions 1990-2011 based on GTAP8.1, with detailed estimates for years 1997, 2001, 2004, and 2007	ELUC for 2012 estimated from 2001-2010 average		Based on six models compared with two data-products to year 2011	Coordinated DGVM experiments for SLAND and ELUC	Confidence levels; cumulative emissions; budget from 1750

2014 (i)	Three years of BP data	Three years of BP data	Extended to 2012 with updated GDP data	ELUC for 1997-2013 includes interannual anomalies from fire-based emissions		Based on seven models	Based on ten models	Inclusion of breakdown of the sinks in three latitude bands and comparison with three atmospheric inversions
2015 (j)	Projection for current year based Jan-Aug data	National emissions from UNFCCC extended to 2014 also provided	Detailed estimates introduced for 2011 based on GTAP9			Based on eight models	Based on ten models with assessment of minimum realism	The decadal uncertainty for the DGVM ensemble mean now uses $\pm 1\sigma$ of the decadal spread across models
2016 (k)	Two years of BP data	Added three small countries; China's emissions from 1990 from BP data (this release only)		Preliminary ELUC using FRA-2015 shown for comparison; use of five DGVMs		Based on seven models	Based on fourteen models	Discussion of projection for full budget for current year
2017 (l)	Projection includes India-specific data			Average of two bookkeeping models; use of 12 DGVMs		Based on eight models that match the observed sink for the 1990s; no longer normalised	Based on 15 models that meet observation-based criteria (see Sect. 2.5)	Land multi-model average now used in main carbon budget, with the carbon imbalance presented separately; new table of key uncertainties

a Raupach et al. (2007)

b Canadell et al. (2007)

c GCP (2008)

d Le Quéré et al. (2009)

e Friedlingstein et al. (2010)

f Peters et al. (2012b)

g Le Quéré et al. (2013), Peters et al. (2013)

h Le Quéré et al. (2014)

i Le Quéré et al. (2015a)

j Le Quéré et al. (2015b)

k Le Quéré et al. (2016)

l Le Quéré et al. (2018a)

3291

**Table A8: Mapping of global carbon cycle models' land flux definitions to the definition of the LULUCF net flux used in national reporting to UNFCCC. Non-intact lands are used here as proxy for "managed lands" in the country reporting, national Greenhouse Gas Inventories (NGHGI) are gap-filled (see Sec. C.2.3 for details). Where available, we provide independent estimates of certain fluxes for comparison. Units are GtC yr<sup>-1</sup>.**

			2002-2011	2012-2021
ELUC from bookkeeping estimates (from Tab. 5)			1.36	1.24
SLAND	Total (from Tab. 5)	from DGVMs	-2.85	-3.10
	in non-forest lands	from DGVMs	-0.74	-0.83
	in non-intact forest	from DGVMs	-1.67	-1.81
	in intact forests	from DGVMs	-0.44	-0.47
	in intact land	from ORCHIDEE-MICT	-1.34	-1.38
ELUC plus SLAND on non-intact lands	considering non-intact forests only	from bookkeeping ELUC and DGVMs	-0.31	-0.56
	considering all non-intact land	from ORCHIDEE-MICT	0.90	0.60
National Greenhouse Gas Inventories (LULUCF)			-0.37	-0.54
FAOSTAT (LULUCF)			0.39	0.24

3292

3293

**Table A9. Funding supporting the production of the various components of the global carbon budget in addition to the authors' supporting institutions (see also acknowledgements).**

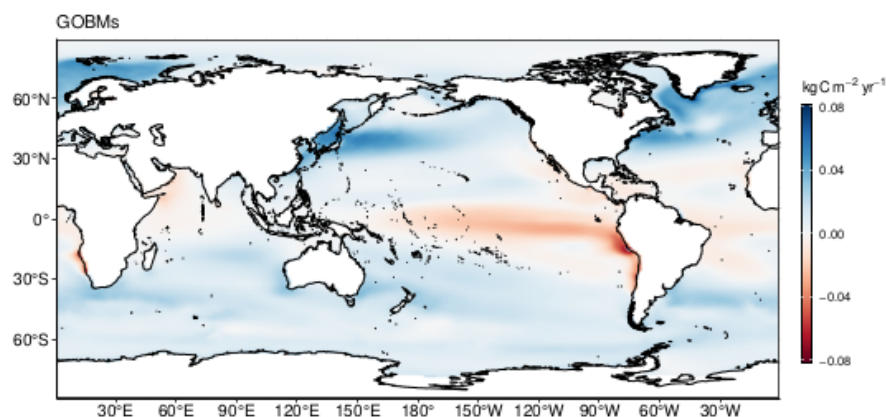
<b>Funder and grant number (where relevant)</b>	<b>Author Initials</b>
Australia, Integrated Marine Observing System (IMOS)	BT
Australian National Environment Science Program (NESP)	JGC
Belgium, FWO (Flanders Research Foundation, contract GN I001821N)	TGk
BNP Paribas Foundation through Climate & Biodiversity initiative, philanthropic grant for developments of the Global Carbon Atlas	PC
Canada, Tula Foundation	WE, KP
China, National Natural Science Foundation (grant no. 41975155)	XY
China, National Natural Science Foundation (grant no. 42141020)	WY
China, National Natural Science Foundation of China (grant no. 41921005)	BZ
China, Scientific Research Start-up Funds (grant no. QD2021024C) from Tsinghua Shenzhen International Graduate School	BZ
China, Second Tibetan Plateau Scientific Expedition and Research Program (SQ2022QZKK0101)	XT
China, Young Elite Scientists Sponsorship Program by CAST (grant no. YESS20200135)	BZ
EC Copernicus Atmosphere Monitoring Service implemented by ECMWF	FC
EC Copernicus Marine Environment Monitoring Service implemented by Mercator Ocean	MG
EC H2020 (4C; grant no 821003)	PF, MOS, RMA, SS, GPP, PC, JIK, TI, LB, AJ, PL, LGr, NG, NMa, SZ
EC H2020 (CoCO2: grant no. 958927)	RMA, GPP, JIK
EC H2020 (COMFORT: grant no. 820989)	LGr, MG, NG
EC H2020 (CONSTRAIN: grant no 820829)	RS, TGa
EC H2020 (ESM2025 – Earth System Models for the Future; grant agreement No 101003536).	RS, TGa, TI, LB, BD
EC H2020 (JERICO-S3: grant no. 871153)	HCB
EC H2020 (VERIFY: grant no. 776810)	MWJ, RMA, GPP, PC, JIK, MJM
Efg International	TT, MG
European Space Agency Climate Change Initiative ESA-CCI RECCAP2 project 655 (ESRIN/4000123002/18/I-NB)	SS, PC
European Space Agency OceanSODA project (grant no. 4000137603/22/I-DT)	LGr, NG
France, French Oceanographic Fleet (FOF)	NMe
France, ICOS (Integrated Carbon Observation System) France	NL
France, Institut National des Sciences de l'Univers (INSU)	NMe
France, Institut polaire français Paul-Emile Victor(IPEV)	NMe
France, Institut de recherche français sur les ressources marines (IFREMER)	NMe
France, Institut de Recherche pour le Développement (IRD)	NL
France, Observatoire des sciences de l'univers Ecce-Terra (OSU at	NMe



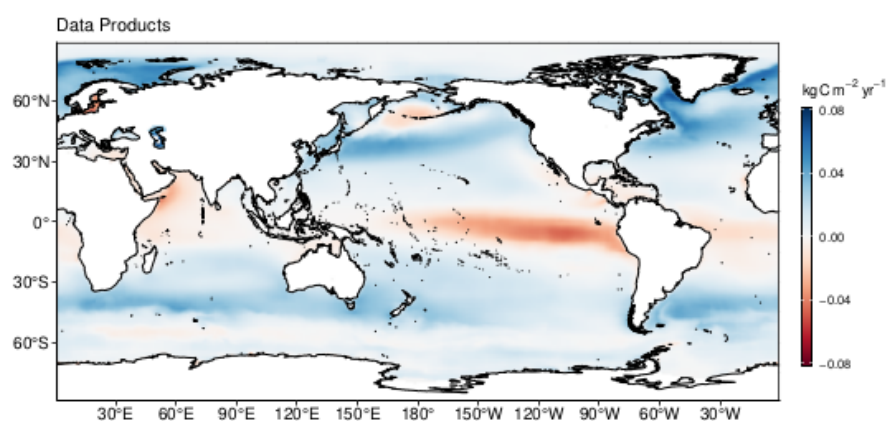
Sorbonne Université)	
Germany, Deutsche Forschungsgemeinschaft (DFG) under Germany's Excellence Strategy – EXC 2037 'Climate, Climatic Change, and Society' – Project Number: 390683824	TI
Germany, Federal Ministry for Education and Research (BMBF)	HCB
Germany, Federal Ministry for Education and Research (BMBF) under project "CDRSynTra" (01LS2101A)	JP
Germany, German Federal Ministry of Education and Research under project "DArgo2025" (03F0857C)	TS
Germany, Helmholtz Association ATMO programme	AA
Germany, Helmholtz Young Investigator Group Marine Carbon and Ecosystem Feedbacks in the Earth System (MarESys), grant number VH-NG-1301	JH, OG
Germany, ICOS (Integrated Carbon Observation System) Germany	HCB
Hapag-Lloyd	TT, MG
Ireland, Marine Institute	MC
Japan, Environment Research and Technology Development Fund of the Ministry of the Environment (JPMEERF21S20810)	YN
Japan, Global Environmental Research Coordination System, Ministry of the Environment (grant number E1751)	SN, ST, TO
Japan, Environment Research and Technology Development Fund of the Ministry of the Environment (JPMEERF21S20800)	HT
Japan, Japan Meteorological Agency	KK
Kuehne + Nagel International AG	TT, MG
Mediterranean Shipping Company (MSc)	TT, MG
Monaco, Fondation Prince Albert II de Monaco	TT, MG
Monaco, Yacht Club de Monaco	TT, MG
Netherlands, ICOS (Integrated Carbon Observation System)	WP
Norway, Research Council of Norway (N-ICOS-2, grant no. 296012)	AO, MB, IS
Norway, Norwegian Research Council (grant no. 270061)	JS
Sweden, ICOS (Integrated Carbon Observation System)	AW
Sweden, Swedish Meteorological and Hydrological Institute	AW
Sweden, The Swedish Research Council	AW
Swiss National Science Foundation (grant no. 200020-200511)	QS
Tibet, Second Tibetan Plateau Scientific Expedition and Research Program (SQ2022QZKK0101)	TX
UK Royal Society (grant no. RP\R1\191063)	CLQ
UK, Natural Environment Research Council (SONATA: grant no. NE/P021417/1)	RW
UK, Natural Environmental Research Council (NE/R016518/1)	PIP
UK, Natural Environment Research Council (NE/V01417X/1)	MWJ
UK, Royal Society: The European Space Agency OCEANFLUX projects	JDS
UK Royal Society (grant no. RP\R1\191063)	CLQ
USA, BIA Tribal Resilience	CW

USA, Cooperative Institute for Modeling the Earth System between the National Oceanic and Atmospheric Administration Geophysical Fluid Dynamics Laboratory and Princeton University and the High Meadows Environmental Institute	LR
USA, Cooperative Institute for Climate, Ocean, & Ecosystem Studies (CIOCES) under NOAA Cooperative Agreement NA20OAR4320271	KO
USA, Department of Energy, Biological and Environmental Research	APW
USA, Department of Energy, SciDac (DESC0012972)	GCH, LPC
USA, Energy Exascale Earth System Model (E3SM) project, Department of Energy, Office of Science, Office of Biological and Environmental Research	GCH, LPC
USA, EPA Indian General Assistance Program	CW
USA, NASA Carbon Monitoring System program and OCO Science team program (80NM0018F0583) .	JL
USA, NASA Interdisciplinary Research in Earth Science (IDS) (80NSSC17K0348)	GCH, LPC, BP
USA, National Center for Atmospheric Research (NSF Cooperative Agreement No. 1852977)	DK
USA, National Oceanic and Atmospheric Administration, Ocean Acidification Program	DP, RW, SRA, RAF, AJS, NMM
USA, National Oceanic and Atmospheric Administration, Global Ocean Monitoring and Observing Program	DRM, CSw, NRB, CRodr, DP, RW, SRA, RAF, AJS
USA, National Science Foundation (grant number 1903722)	HT
USA, State of Alaska	NMM
<b>Computing resources</b>	
ADA HPC cluster at the University of East Anglia	MWJ
CAMS inversion was granted access to the HPC resources of TGCC under the allocation A0110102201	FC
Cheyenne supercomputer (doi:10.5065/D6RX99HX), were provided by the Computational and Information Systems Laboratory (CISL) at NCAR	DK
HPC cluster Aether at the University of Bremen, financed by DFG within the scope of the Excellence Initiative	ITL
MRI (FUJITSU Server PRIMERGY CX2550M5)	YN
NIES (SX-Aurora)	YN
NIES supercomputer system	EK

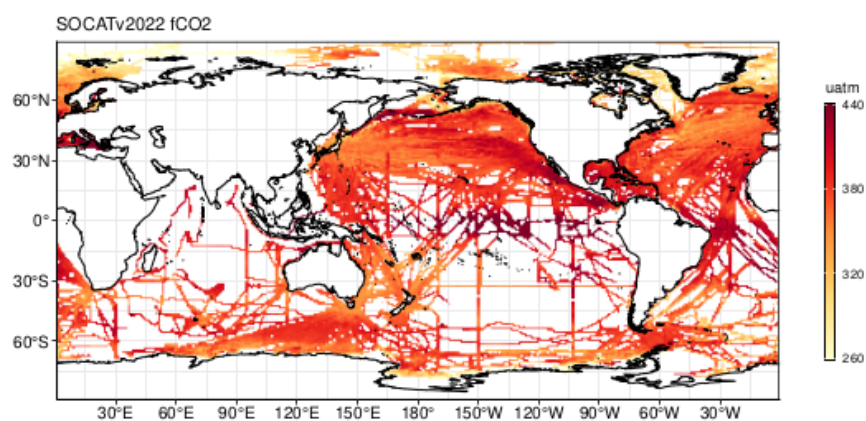
a



b



c



3297  
3298 Figure B1. Ensemble mean air-sea CO<sub>2</sub> flux from a) global ocean biogeochemistry models and b) fCO<sub>2</sub> based data products,  
3299 averaged over 2012-2021 period (kgC m<sup>-2</sup> yr<sup>-1</sup>). Positive numbers indicate a flux into the ocean. c) gridded SOCAT v2022  
3300 fCO<sub>2</sub> measurements, averaged over the 2012-2021 period (uatm). In (a) model simulation A is shown. The data-products  
3301 represent the contemporary flux, i.e. including outgassing of riverine carbon, which is estimated to amount to 0.65 GtC yr<sup>-1</sup>  
3302 globally.

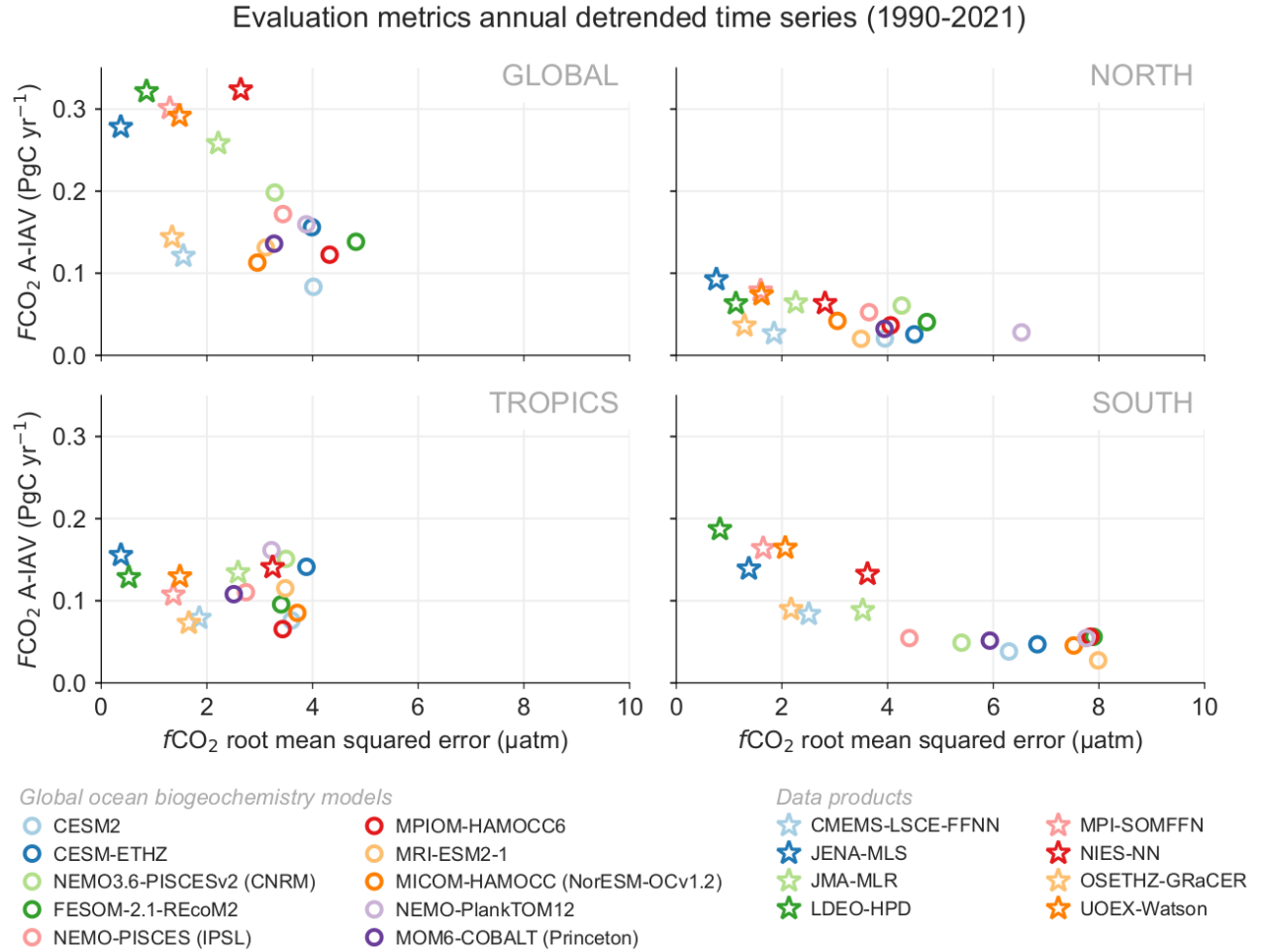


**Figure B2.** Evaluation of the GOBMs and data products using the root mean squared error (RMSE) for the period 1990 to 2021, between the individual surface ocean fCO<sub>2</sub> mapping schemes and the SOCAT v2022 database. The y-axis shows the amplitude of the interannual variability of the air-sea CO<sub>2</sub> flux (A-IAV, taken as the standard deviation of the detrended annual time series). Results are presented for the globe, north (>30°N), tropics (30°S-30°N), and south (<30°S) for the GOBMs (see legend, circles) and for the fCO<sub>2</sub>-based data products (star symbols). The fCO<sub>2</sub>-based data products use the SOCAT database and therefore are not independent from the data (see section 2.4.1).

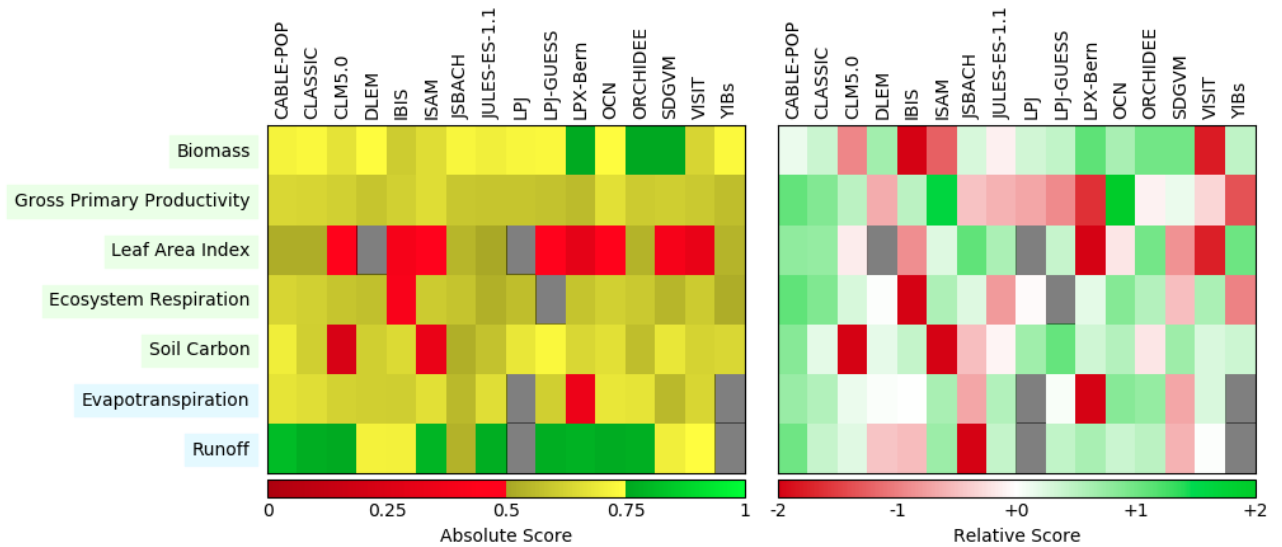


Figure B3. Evaluation of the DGVMs using the International Land Model Benchmarking system (ILAMB; Collier et al., 2018) (left) absolute skill scores and (right) skill scores relative to other models. The benchmarking is done with observations for vegetation biomass (Saatchi et al., 2011; and GlobalCarbon unpublished data; Avitabile et al., 2016), GPP (Jung et al., 2010; Lasslop et al., 2010), leaf area index (De Kauwe et al., 2011; Myneni et al., 1997), ecosystem respiration (Jung et al., 2010; Lasslop et al., 2010), soil carbon (Hugelius et al., 2013; Todd-Brown et al., 2013), evapotranspiration (De Kauwe et al., 2011), and runoff (Dai and Trenberth, 2002). For each model-observation comparison a series of error metrics are calculated, scores are then calculated as an exponential function of each error metric, finally for each variable the multiple scores from different metrics and observational data sets are combined to give the overall variable scores shown in the left panel. Overall variable scores increase from 0 to 1 with improvements in model performance. The set of error metrics vary with data set and can include metrics based on the period mean, bias, root mean squared error, spatial distribution, interannual variability and seasonal cycle. The relative skill score shown in the right panel is a Z-score, which indicates in units of standard deviation the model scores relative to the multi-model mean score for a given variable. Grey boxes represent missing model data.

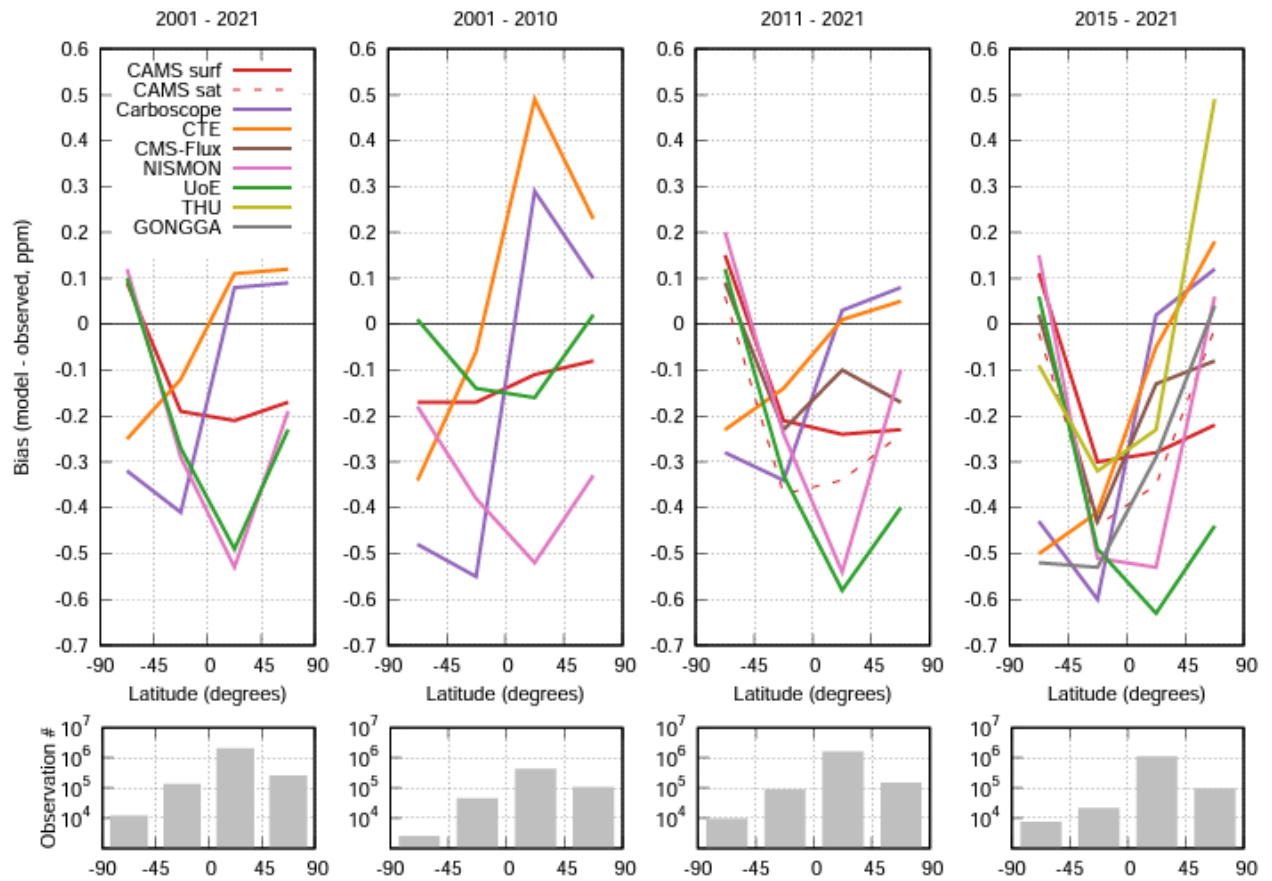
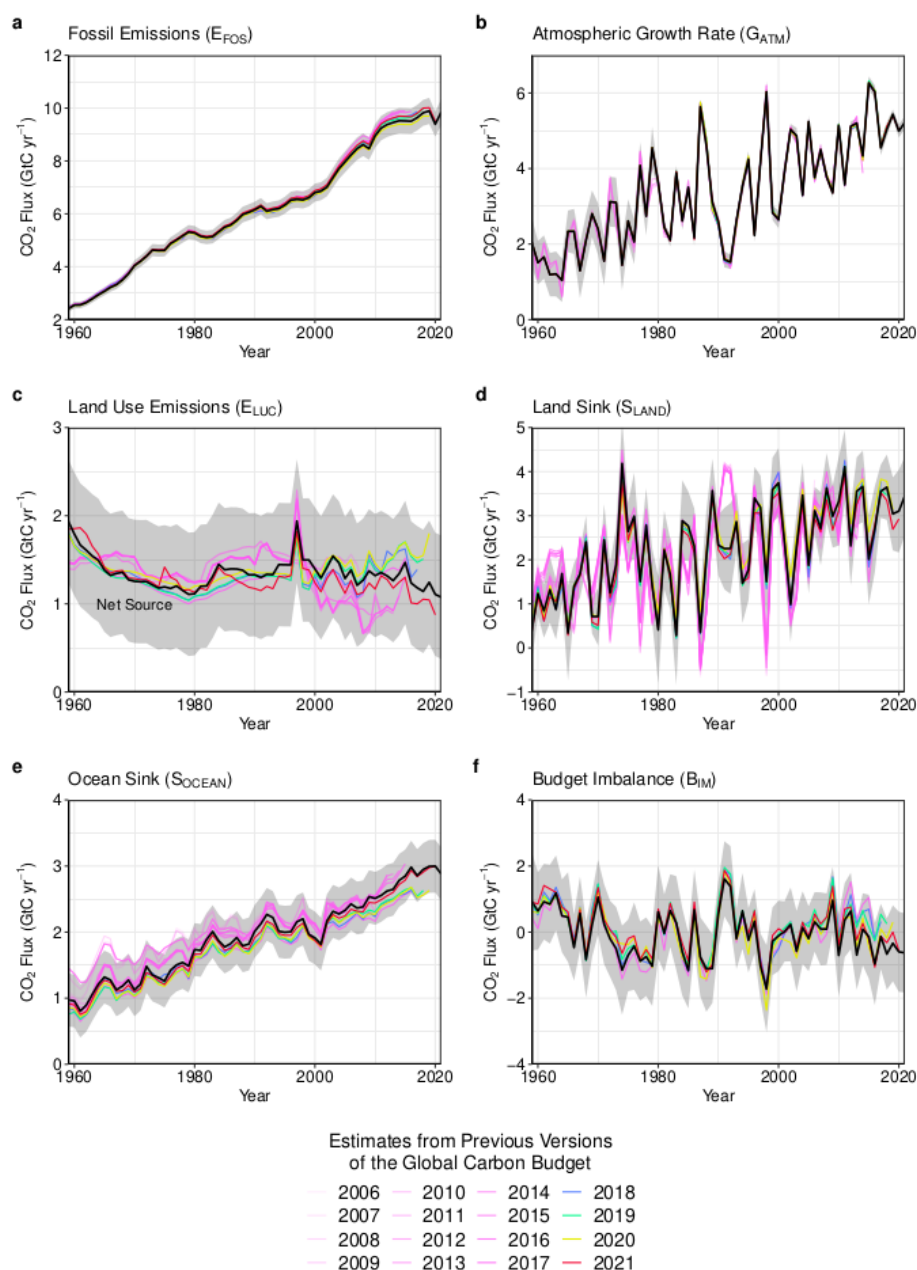


Figure B4. Evaluation of the atmospheric inversion products. The mean of the model minus observations is shown for four latitude bands in four periods: (first panel) 2001-2021, (second panel) 2001-2010, (third panel) 2011-2021, (fourth panel) 2015-2021. The 9 systems are compared to independent CO<sub>2</sub> measurements made onboard aircraft over many places of the world between 2 and 7 km above sea level. Aircraft measurements archived in the Cooperative Global Atmospheric Data Integration Project (Schuldt et al. 2021, Schuldt et al. 2022) from sites, campaigns or programs that have not been assimilated and cover at least 9 months (except for SH programs) between 2001 and 2021, have been used to compute the biases of the differences in four 45° latitude bins. Land and ocean data are used without distinction, and observation density varies strongly with latitude and time as seen on the lower panels.



**Figure B5.** Comparison of the estimates of each component of the global carbon budget in this study (black line) with the estimates released annually by the GCP since 2006. Grey shading shows the uncertainty bounds representing  $\pm 1$  standard deviation of the current global carbon budget, based on the uncertainty assessments described in Appendix C. CO<sub>2</sub> emissions from (a) fossil CO<sub>2</sub> emissions ( $E_{\text{FOS}}$ ), and (b) land-use change ( $E_{\text{LUC}}$ ), as well as their partitioning among (c) the atmosphere ( $G_{\text{ATM}}$ ), (d) the land ( $S_{\text{LAND}}$ ), and (e) the ocean ( $S_{\text{OCEAN}}$ ). See legend for the corresponding years, and Tables 3 and A7 for references. The budget year corresponds to the year when the budget was first released. All values are in GtC yr<sup>-1</sup>.

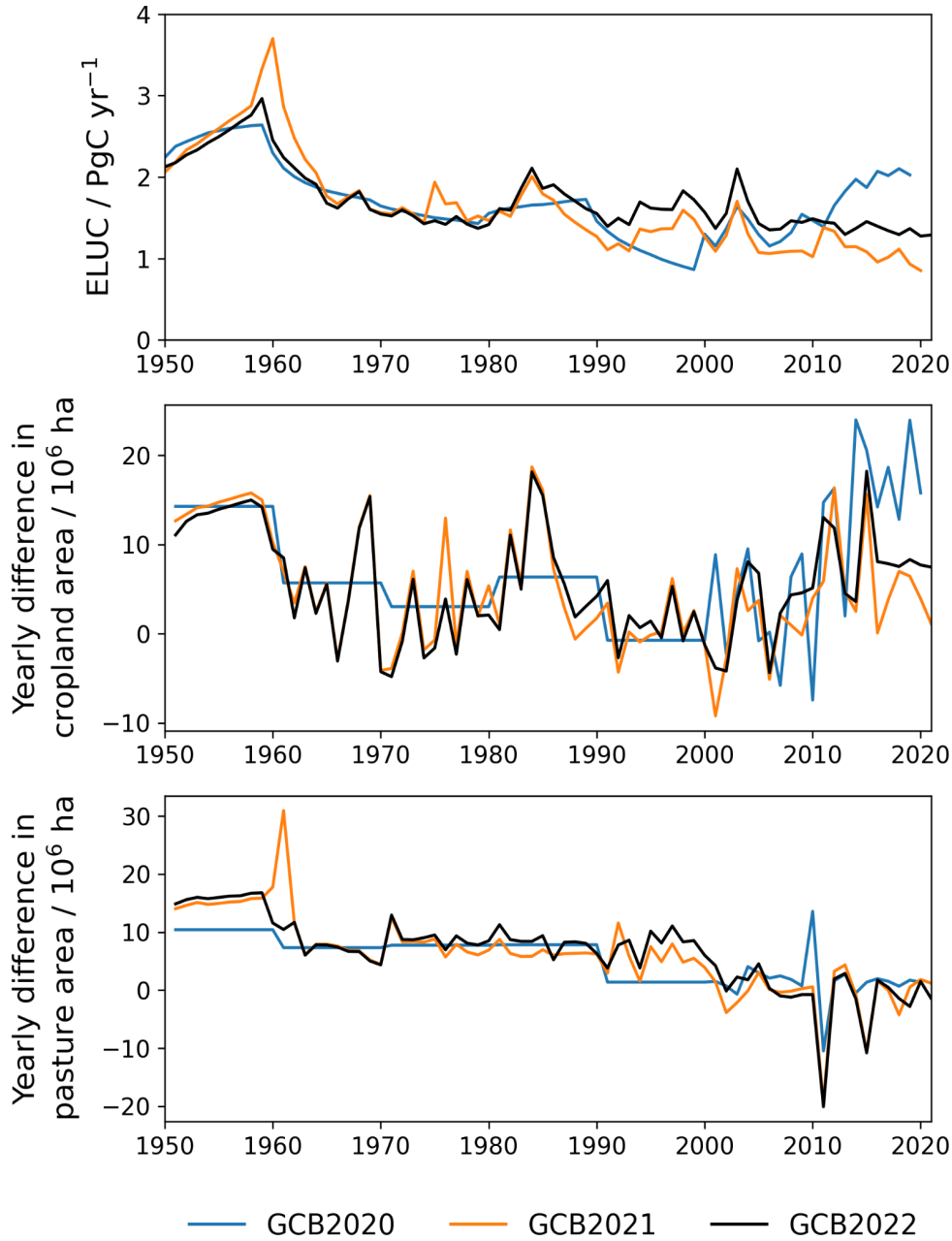


Figure B6. Differences in the HYDE/LUH2 land-use forcing used for the global carbon budgets GCB2020 (Friedlingstein et al., 2021), GCB2021 (Friedlingstein et al., 2022a), and GCB2022 (Friedlingstein et al., 2022b). Shown are year-to-year changes in cropland area (middle panel) and pasture area (bottom panel). To illustrate the relevance of the update in the land-use forcing to the recent trends in  $E_{LUC}$ , the top panel shows the land-use emission estimate from the bookkeeping model BLUE (original model output, i.e. excluding peat fire and drainage emissions).



## 3349 **Appendix C. Extended Methodology**

### 3350 **C.1 Methodology Fossil Fuel CO<sub>2</sub> emissions (E<sub>FOS</sub>)**

#### 3351 **C.1.1 Cement carbonation**

3352 From the moment it is created, cement begins to absorb CO<sub>2</sub> from the atmosphere, a process known as ‘cement  
3353 carbonation’. We estimate this CO<sub>2</sub> sink, from 1931 onwards, as the average of two studies in the literature (Cao et al.,  
3354 2020; Guo et al., 2021). The Global Cement and Concrete Association reports a much lower carbonation rate, but this is  
3355 based on the highly conservative assumption of 0% mortar (GCCA, 2021). Modelling cement carbonation requires  
3356 estimation of a large number of parameters, including the different types of cement material in different countries, the  
3357 lifetime of the structures before demolition, of cement waste after demolition, and the volumetric properties of  
3358 structures, among others (Xi et al., 2016). Lifetime is an important parameter because demolition results in the exposure  
3359 of new surfaces to the carbonation process. The main reasons for differences between the two studies appear to be the  
3360 assumed lifetimes of cement structures and the geographic resolution, but the uncertainty bounds of the two studies  
3361 overlap.

#### 3362 **C.1.2 Emissions embodied in goods and services**

3363 CDIAC, UNFCCC, and BP national emission statistics ‘include greenhouse gas emissions and removals taking place  
3364 within national territory and offshore areas over which the country has jurisdiction’ (Rypdal et al., 2006), and are called  
3365 territorial emission inventories. Consumption-based emission inventories allocate emissions to products that are  
3366 consumed within a country, and are conceptually calculated as the territorial emissions minus the ‘embodied’ territorial  
3367 emissions to produce exported products plus the emissions in other countries to produce imported products  
3368 (Consumption = Territorial – Exports + Imports). Consumption-based emission attribution results (e.g. Davis and  
3369 Caldeira, 2010) provide additional information to territorial-based emissions that can be used to understand emission  
3370 drivers (Hertwich and Peters, 2009) and quantify emission transfers by the trade of products between countries (Peters  
3371 et al., 2011b). The consumption-based emissions have the same global total, but reflect the trade-driven movement of  
3372 emissions across the Earth's surface in response to human activities. We estimate consumption-based emissions from  
3373 1990-2020 by enumerating the global supply chain using a global model of the economic relationships between  
3374 economic sectors within and between every country (Andrew and Peters, 2013; Peters et al., 2011a). Our analysis is  
3375 based on the economic and trade data from the Global Trade and Analysis Project (GTAP; Narayanan et al., 2015), and  
3376 we make detailed estimates for the years 1997 (GTAP version 5), 2001 (GTAP6), and 2004, 2007, 2011, and 2014  
3377 (GTAP10.0a), covering 57 sectors and 141 countries and regions. The detailed results are then extended into an annual  
3378 time series from 1990 to the latest year of the Gross Domestic Product (GDP) data (2020 in this budget), using GDP  
3379 data by expenditure in current exchange rate of US dollars (USD; from the UN National Accounts main Aggregates  
3380 database; UN, 2021) and time series of trade data from GTAP (based on the methodology in Peters et al., 2011a). We  
3381 estimate the sector-level CO<sub>2</sub> emissions using the GTAP data and methodology, add the flaring and cement emissions  
3382 from our fossil CO<sub>2</sub> dataset, and then scale the national totals (excluding bunker fuels) to match the emission estimates  
3383 from the carbon budget. We do not provide a separate uncertainty estimate for the consumption-based emissions, but  
3384 based on model comparisons and sensitivity analysis, they are unlikely to be significantly different than for the  
3385 territorial emission estimates (Peters et al., 2012a).

### 3386 C.1.3 Uncertainty assessment for $E_{FOS}$

3387 We estimate the uncertainty of the global fossil CO<sub>2</sub> emissions at  $\pm 5\%$  (scaled down from the published  $\pm 10\%$  at  $\pm 2\sigma$   
3388 to the use of  $\pm 1\sigma$  bounds reported here; Andres et al., 2012). This is consistent with a more detailed analysis of  
3389 uncertainty of  $\pm 8.4\%$  at  $\pm 2\sigma$  (Andres et al., 2014) and at the high-end of the range of  $\pm 5\text{--}10\%$  at  $\pm 2\sigma$  reported by  
3390 (Ballantyne et al., 2015). This includes an assessment of uncertainties in the amounts of fuel consumed, the carbon and  
3391 heat contents of fuels, and the combustion efficiency. While we consider a fixed uncertainty of  $\pm 5\%$  for all years, the  
3392 uncertainty as a percentage of emissions is growing with time because of the larger share of global emissions from  
3393 emerging economies and developing countries (Marland et al., 2009). Generally, emissions from mature economies  
3394 with good statistical processes have an uncertainty of only a few per cent (Marland, 2008), while emissions from  
3395 strongly developing economies such as China have uncertainties of around  $\pm 10\%$  (for  $\pm 1\sigma$ ; Gregg et al., 2008; Andres  
3396 et al., 2014). Uncertainties of emissions are likely to be mainly systematic errors related to underlying biases of energy  
3397 statistics and to the accounting method used by each country.

### 3398 C.1.4 Growth rate in emissions

3399 We report the annual growth rate in emissions for adjacent years (in percent per year) by calculating the difference  
3400 between the two years and then normalising to the emissions in the first year:  $(E_{FOS}(t+1) - E_{FOS}(t))/E_{FOS}(t) \times 100\%$ . We apply a leap-year adjustment where relevant to ensure valid interpretations of annual  
3401 growth rates. This affects the growth rate by about  $0.3\%$  yr<sup>-1</sup> ( $1/366$ ) and causes calculated growth rates to go up  
3402 approximately  $0.3\%$  if the first year is a leap year and down  $0.3\%$  if the second year is a leap year.

3404 The relative growth rate of  $E_{FOS}$  over time periods of greater than one year can be rewritten using its logarithm  
3405 equivalent as follows:

$$3406 \frac{1}{E_{FOS}} \frac{dE_{FOS}}{dt} = \frac{d(\ln E_{FOS})}{dt} \quad (2)$$

3407 Here we calculate relative growth rates in emissions for multi-year periods (e.g. a decade) by fitting a linear trend to  
3408  $\ln(E_{FOS})$  in Eq. (2), reported in percent per year.

### 3409 C.1.5 Emissions projection for 2022

3410 To gain insight on emission trends for 2022, we provide an assessment of global fossil CO<sub>2</sub> emissions,  $E_{FOS}$ , by  
3411 combining individual assessments of emissions for China, USA, the EU, and India (the four countries/regions with the  
3412 largest emissions), and the rest of the world.

3413 The methods are specific to each country or region, as described in detail below.

3414 **China:** We use a regression between monthly data for each fossil fuel and cement, and annual data for consumption of  
3415 fossil fuels / production of cement to project full-year growth in fossil fuel consumption and cement production. The  
3416 monthly data for each product consists of the following:

- 3417 • Coal: Proprietary estimate for monthly consumption of main coal types, from SX Coal
- 3418 • Oil: Production data from the National Bureau of Statistics (NBS), plus net imports from the China Customs  
3419 Administration (i.e., gross supply of oil, not including inventory changes)
- 3420 • Natural gas: Same as for oil

3421       • Cement: Production data from NBS

3422       For oil, we use data for production and net imports of refined oil products rather than crude oil. This choice is made

3423       because refined products are one step closer to actual consumption, and because crude oil can be subject to large

3424       market-driven and strategic inventory changes that are not captured by available monthly data.

3425       For each fuel and cement, we make a Bayesian linear regression between year-on-year cumulative growth in supply

3426       (production for cement) and full-year growth in consumption (production for cement) from annual consumption data. In

3427       the regression model, the growth rate in annual consumption (production for cement) is modelled as a regression

3428       parameter multiplied by the cumulative year-on-year growth rate from the monthly data through July of each year for

3429       past years (through 2021). We use broad Gaussian distributions centered around 1 as priors for the ratios between

3430       annual and through-July growth rates. We then use the posteriors for the growth rates together with cumulative monthly

3431       supply/production data through July of 2022 to produce a posterior predictive distribution for the full-year growth rate

3432       for fossil fuel consumption / cement production in 2022.

3433       If the growth in supply/production through July were an unbiased estimate of the full-year growth in

3434       consumption/production, the posterior distribution for the ratio between the monthly and annual growth rates would be

3435       centered around 1. However, in practice the ratios are different from 1 (in most cases below 1). This is a result of

3436       various biasing factors such as uneven evolution in the first and second half of each year, inventory changes that are

3437       somewhat anti-correlated with production and net imports, differences in statistical coverage, and other factors that are

3438       not captured in the monthly data.

3439       For fossil fuels, the mean of the posterior distribution is used as the central estimate for the growth rate in 2022, while

3440       the edges of a 68% credible interval (analogous to a 1-sigma confidence interval) are used for the upper and lower

3441       bounds.

3442       For cement, the evolution from January to July has been highly atypical owing to the ongoing turmoil in the

3443       construction sector, and the results of the regression analysis are heavily biased by equally atypical but different

3444       dynamics in 2021. For this reason, we use an average of the results of the regression analysis and the plain growth in

3445       cement production through July 2022, since this results in a growth rate that seems more plausible and in line with

3446       where the cumulative cement production appears to be headed at the time of writing.

3447       **USA:** We use emissions estimated by the U.S. Energy Information Administration (EIA) in their Short-Term Energy

3448       Outlook (STEO) for emissions from fossil fuels to get both YTD and a full year projection (EIA, 2022). The STEO also

3449       includes a near-term forecast based on an energy forecasting model which is updated monthly (last update with

3450       preliminary data through August 2022), and takes into account expected temperatures, household expenditures by fuel

3451       type, energy markets, policies, and other effects. We combine this with our estimate of emissions from cement

3452       production using the monthly U.S. cement clinker production data from USGS for January-June 2022, assuming

3453       changes in cement production over the first part of the year apply throughout the year.

3454       **India:** We use monthly emissions estimates for India updated from Andrew (2020b) through July 2022. These

3455       estimates are derived from many official monthly energy and other activity data sources to produce direct estimates of

3456       national CO<sub>2</sub> emissions, without the use of proxies. Emissions from coal are then extended to August using a regression

3457       relationship based on power generated from coal, coal dispatches by Coal India Ltd., the composite PMI, time, and days

3458       per month. For the last 3-5 months of the year, each series is extrapolated assuming typical trends.

**EU:** We use a refinement to the methods presented by Andrew (2021), deriving emissions from monthly energy data reported by Eurostat. Some data gaps are filled using data from the Joint Organisations Data Initiative (JODI, 2022). Sub-annual cement production data are limited, but data for Germany and Poland, the two largest producers, suggest a small decline. For fossil fuels this provides estimates through July. We extend coal emissions through August using a regression model built from generation of power from hard coal, power from brown coal, total power generation, and the number of working days in Germany and Poland, the two biggest coal consumers in the EU. These are then extended through the end of the year assuming typical trends. We extend oil emissions by building a regression model between our monthly CO<sub>2</sub> estimates and oil consumption reported by the EIA for Europe in its Short-Term Energy Outlook (September edition), and then using this model with EIA's monthly forecasts. For natural gas, the strong seasonal signal allows the use of the bias-adjusted Holt-Winters exponential smoothing method (Chatfield, 1978).

**Rest of the world:** We use the close relationship between the growth in GDP and the growth in emissions (Raupach et al., 2007) to project emissions for the current year. This is based on a simplified Kaya Identity, whereby  $E_{FOS}$  (GtC yr<sup>-1</sup>) is decomposed by the product of GDP (USD yr<sup>-1</sup>) and the fossil fuel carbon intensity of the economy ( $I_{FOS}$ ; GtC USD<sup>-1</sup>) as follows:

$$E_{FOS} = GDP \times I_{FOS} \quad (3)$$

Taking a time derivative of Equation (3) and rearranging gives:

$$\frac{1}{E_{FOS}} \frac{dE_{FOS}}{dt} = \frac{1}{GDP} \frac{dGDP}{dt} + \frac{1}{I_{FOS}} \frac{dI_{FOS}}{dt} \quad (4)$$

where the left-hand term is the relative growth rate of  $E_{FOS}$ , and the right-hand terms are the relative growth rates of GDP and  $I_{FOS}$ , respectively, which can simply be added linearly to give the overall growth rate.

The  $I_{FOS}$  is based on GDP in constant PPP (Purchasing Power Parity) from the International Energy Agency (IEA) up to 2017 (IEA/OECD, 2019) and extended using the International Monetary Fund (IMF) growth rates through 2021 (IMF, 2022). Interannual variability in  $I_{FOS}$  is the largest source of uncertainty in the GDP-based emissions projections. We thus use the standard deviation of the annual  $I_{FOS}$  for the period 2012-2021 as a measure of uncertainty, reflecting a  $\pm 1\sigma$  as in the rest of the carbon budget. For rest-of-world oil emissions growth, we use the global oil demand forecast published by the EIA less our projections for the other four regions, and estimate uncertainty as the maximum absolute difference over the period available for such forecasts using the specific monthly edition (e.g. August) compared to the first estimate based on more solid data in the following year (April).

**World:** The global total is the sum of each of the countries and regions.

## C.2 Methodology CO<sub>2</sub> emissions from land-use, land-use change and forestry ( $E_{LUC}$ )

The net CO<sub>2</sub> flux from land-use, land-use change and forestry ( $E_{LUC}$ , called land-use change emissions in the rest of the text) includes CO<sub>2</sub> fluxes from deforestation, afforestation, logging and forest degradation (including harvest activity), shifting cultivation (cycle of cutting forest for agriculture, then abandoning), and regrowth of forests following wood harvest or abandonment of agriculture. Emissions from peat burning and drainage are added from external datasets (see Appendix C.2.1 below). Only some land-management activities are included in our land-use change emissions estimates (Table A1). Some of these activities lead to emissions of CO<sub>2</sub> to the atmosphere, while others lead to CO<sub>2</sub>

sinks.  $ELUC$  is the net sum of emissions and removals due to all anthropogenic activities considered. Our annual estimate for 1960-2021 is provided as the average of results from three bookkeeping approaches (Appendix C.2.1 below): an estimate using the Bookkeeping of Land Use Emissions model (Hansis et al., 2015; hereafter BLUE) and one using the compact Earth system model OSCAR (Gasser et al., 2020), both BLUE and OSCAR being updated here to new land-use forcing covering the time period until 2021, and an updated version of the estimate published by Houghton and Nassikas (2017) (hereafter updated H&N2017). All three data sets are then extrapolated to provide a projection for 2022 (Appendix C.2.5 below). In addition, we use results from Dynamic Global Vegetation Models (DGVMs; see Appendix 2.5 and Table 4) to help quantify the uncertainty in  $ELUC$  (Appendix C.2.4), and thus better characterise our understanding. Note that in this budget, we use the scientific  $ELUC$  definition, which counts fluxes due to environmental changes on managed land towards  $S_{LAND}$ , as opposed to the national greenhouse gas inventories under the UNFCCC, which include them in  $ELUC$  and thus often report smaller land-use emissions (Grassi et al., 2018; Petrescu et al., 2020). However, we provide a methodology of mapping of the two approaches to each other further below (Appendix C.2.3).

### C.2.1 Bookkeeping models

Land-use change  $CO_2$  emissions and uptake fluxes are calculated by three bookkeeping models. These are based on the original bookkeeping approach of Houghton (2003) that keeps track of the carbon stored in vegetation and soils before and after a land-use change (transitions between various natural vegetation types, croplands, and pastures). Literature-based response curves describe decay of vegetation and soil carbon, including transfer to product pools of different lifetimes, as well as carbon uptake due to regrowth. In addition, the bookkeeping models represent long-term degradation of primary forest as lowered standing vegetation and soil carbon stocks in secondary forests, and include forest management practices such as wood harvests.

BLUE and the updated H&N2017 exclude land ecosystems' transient response to changes in climate, atmospheric  $CO_2$  and other environmental factors, and base the carbon densities on contemporary data from literature and inventory data. Since carbon densities thus remain fixed over time, the additional sink capacity that ecosystems provide in response to  $CO_2$ -fertilisation and some other environmental changes is not captured by these models (Pongratz et al., 2014). On the contrary, OSCAR includes this transient response, and it follows a theoretical framework (Gasser and Ciais, 2013) that allows separating bookkeeping land-use emissions and the loss of additional sink capacity. Only the former is included here, while the latter is discussed in Appendix D4. The bookkeeping models differ in (1) computational units (spatially explicit treatment of land-use change for BLUE, country-level for the updated H&N2017 and OSCAR), (2) processes represented (see Table A1), and (3) carbon densities assigned to vegetation and soil of each vegetation type (literature-based for BLUE and the updated H&N2017, calibrated to DGVMs for OSCAR). A notable difference between models exists with respect to the treatment of shifting cultivation. The update of H&N2017, introduced for the GCB2021 (Friedlingstein et al., 2022) changed the approach over the earlier H&N2017 version: H&N2017 had assumed the "excess loss" of tropical forests (i.e., when the Global Forest Resources Assessment (FRA; FAO 2020) indicated a forest loss larger than the increase in agricultural areas from FAO (FAOSTAT 2021) resulted from converting forests to croplands at the same time older croplands were abandoned. Those abandoned croplands began to recover to forests after 15 years. The updated H&N2017 now assumes that forest loss in excess of increases in cropland and pastures represented an increase in shifting cultivation. When the excess loss of forests was negative, it was assumed that shifting cultivation was returned to forest. Historical areas in shifting cultivation were extrapolated taking into account country-based estimates of areas in fallow in 1980 (FAO/UNEP, 1981) and expert opinion (from Heinimann et al.,

2017). In contrast, the BLUE and OSCAR models include sub-grid-scale transitions between all vegetation types. Furthermore, the updated H&N2017 assumes conversion of natural grasslands to pasture, while BLUE and OSCAR allocate pasture transitions proportionally on all natural vegetation that exists in a grid-cell. This is one reason for generally higher emissions in BLUE and OSCAR. Bookkeeping models do not directly capture carbon emissions from peat fires, which can create large emissions and interannual variability due to synergies of land-use and climate variability in Southeast Asia, particularly during El-Niño events, nor emissions from the organic layers of drained peat soils. To correct for this, we add peat fire emissions based on the Global Fire Emission Database (GFED4s; van der Werf et al., 2017) to the bookkeeping models' output. Emissions are calculated by multiplying the mass of dry matter emitted by peat fires with the C emission factor for peat fires indicated in the GFED4s database. Emissions from deforestation fires used to derive ELUC projections for 2022 are calculated analogously. As these satellite-derived estimates of peat fire emissions start in 1997 only, we follow the approach by Houghton and Nassikas (2017) for earlier years, which ramps up from zero emissions in 1980 to 0.04 Pg C yr<sup>-1</sup> in 1996, reflecting the onset of major clearing of peatlands in equatorial Southeast Asia in the 1980s. Similarly, we add estimates of peat drainage emissions. In recent years, more peat drainage estimates that provide spatially explicit data have become available, and we thus extended the number of peat drainage datasets considered: We employ FAO peat drainage emissions 1990–2019 from croplands and grasslands (Conchedda and Tubiello, 2020), peat drainage emissions 1700–2010 from simulations with the DGVM ORCHIDEE-PEAT (Qiu et al., 2021), and peat drainage emissions 1701–2021 from simulations with the DGVM LPX-Bern (Lienert and Joos, 2018; Müller and Joos, 2021) applying the updated LUH2 forcing as also used by BLUE, OSCAR and the DGVMs. We extrapolate the FAO data to 1850–2021 by keeping the post-2019 emissions constant at 2019 levels, by linearly increasing tropical drainage emissions between 1980 and 1990 starting from 0 GtC yr<sup>-1</sup> in 1980, consistent with H&N2017's assumption (Houghton and Nassikas, 2017), and by keeping pre-1990 emissions from the often old drained areas of the extra-tropics constant at 1990 emission levels. ORCHIDEE-PEAT data are extrapolated to 2011–2021 by replicating the average emissions in 2000–2010 (pers. comm. C. Qiu). Further, ORCHIDEE-PEAT only provides peat drainage emissions north of 30°N, and thus we fill the regions south of 30°N by the average peat drainage emissions from FAO and LPX-Bern. The average of the carbon emission estimates by the three different peat drainage dataset is added to the bookkeeping models to obtain net ELUC and gross sources.

The three bookkeeping estimates used in this study differ with respect to the land-use change data used to drive the models. The updated H&N2017 base their estimates directly on the Forest Resource Assessment of the FAO which provides statistics on forest-area change and management at intervals of five years currently updated until 2020 (FAO, 2020). The data is based on country reporting to FAO and may include remote-sensing information in more recent assessments. Changes in land-use other than forests are based on annual, national changes in cropland and pasture areas reported by FAO (FAOSTAT, 2021). On the other hand, BLUE uses the harmonised land-use change data LUH2-GCB2022 covering the entire 850–2021 period (an update to the previously released LUH2 v2h dataset; Hurtt et al., 2017; Hurtt et al., 2020), which was also used as input to the DGVMs (Appendix C.2.2). It describes land-use change, also based on the FAO data as described in Appendix C.2.2 as well as the HYDE3.3 dataset (Klein Goldewijk et al., 2017a, 2017b), but provided at a quarter-degree spatial resolution, considering sub-grid-scale transitions between primary forest, secondary forest, primary non-forest, secondary non-forest, cropland, pasture, rangeland, and urban land (Hurtt et al., 2020; Chini et al., 2021). LUH2-GCB2022 provides a distinction between rangelands and pasture, based on inputs from HYDE. To constrain the models' interpretation on whether rangeland implies the original natural vegetation to be transformed to grassland or not (e.g., browsing on shrubland), a forest mask was provided with LUH2-

GCB2021; forest is assumed to be transformed to grasslands, while other natural vegetation remains (in case of secondary vegetation) or is degraded from primary to secondary vegetation (Ma et al., 2020). This is implemented in BLUE. OSCAR was run with both LUH2-GCB2022 and FAO/FRA (as used with the updated H&N2017), where the drivers of the latter were linearly extrapolated to 2021 using their 2015–2020 trends. The best-guess OSCAR estimate used in our study is a combination of results for LUH2-GCB2022 and FAO/FRA land-use data and a large number of perturbed parameter simulations weighted against a constraint (the cumulative  $S_{\text{LAND}}$  over 1960–2020 of last year's GCB). As the record of the updated H&N2017 ends in 2020, we extend it to 2021 by adding the difference of the emissions from tropical deforestation and degradation, peat drainage, and peat fire between 2020 and 2021 to the model's estimate for 2020 (i.e. considering the yearly anomalies of the emissions from tropical deforestation and degradation, peat drainage, and peat fire). The same method is applied to all three bookkeeping estimates to provide a projection for 2022.

For  $ELUC$  from 1850 onwards we average the estimates from BLUE, the updated H&N2017 and OSCAR. For the cumulative numbers starting 1750 an average of four earlier publications is added ( $30 \pm 20$  PgC 1750–1850, rounded to nearest 5; Le Quéré et al., 2016).

We provide estimates of the gross land use change fluxes from which the reported net land-use change flux,  $ELUC$ , is derived as a sum. Gross fluxes are derived internally by the three bookkeeping models: Gross emissions stem from decaying material left dead on site and from products after clearing of natural vegetation for agricultural purposes or wood harvesting, emissions from peat drainage and peat burning, and, for BLUE, additionally from degradation from primary to secondary land through usage of natural vegetation as rangeland. Gross removals stem from regrowth after agricultural abandonment and wood harvesting. Gross fluxes for the updated H&N2017 for 2020 and for the 2022 projection of all three models were calculated by the change in emissions from tropical deforestation and degradation and peat burning and drainage as described for the net  $ELUC$  above: As tropical deforestation and degradation and peat burning and drainage all only lead to gross emissions to the atmosphere, only gross (and net) emissions are adjusted this way, while gross sinks are assumed to remain constant over the previous year. .

This year, we provide an additional split of the net  $ELUC$  into component fluxes to better identify reasons for divergence between bookkeeping estimates and to give more insight into the drivers of sources and sinks. This split distinguishes between fluxes from deforestation (including due to shifting cultivation), fluxes from organic soils (i.e., peat drainage and fires), re/afforestation and wood harvest (i.e., fluxes in forests from slash and product decay following wood harvesting; regrowth associated with wood harvesting or after abandonment, including reforestation and in shifting cultivation cycles; afforestation) and fluxes associated with all other transitions.

### C.2.2 Dynamic Global Vegetation Models (DGVMs)

Land-use change  $CO_2$  emissions have also been estimated using an ensemble of 16 DGVMs simulations. The DGVMs account for deforestation and regrowth, the most important components of  $ELUC$ , but they do not represent all processes resulting directly from human activities on land (Table A1). All DGVMs represent processes of vegetation growth and mortality, as well as decomposition of dead organic matter associated with natural cycles, and include the vegetation and soil carbon response to increasing atmospheric  $CO_2$  concentration and to climate variability and change. Most models explicitly simulate the coupling of carbon and nitrogen cycles and account for atmospheric N deposition and N

fertilisers (Table A1). The DGVMs are independent from the other budget terms except for their use of atmospheric CO<sub>2</sub> concentration to calculate the fertilisation effect of CO<sub>2</sub> on plant photosynthesis.

All DGVMs use the LUH2-GCB2022 dataset as input, which includes the HYDE cropland/grazing land dataset (Klein Goldewijk et al., 2017a, 2017b), and additional information on land-cover transitions and wood harvest. DGVMs use annual, half-degree (regridged from 5 minute resolution), fractional data on cropland and pasture from HYDE3.3.

DGVMs that do not simulate subgrid scale transitions (i.e., net land-use emissions; see Table A1) used the HYDE information on agricultural area change. For all countries, with the exception of Brazil and the Democratic Republic of the Congo, these data are based on the available annual FAO statistics of change in agricultural land area available from 1961 up to and including 2017. The FAO retrospectively revised their reporting for the Democratic Republic of the Congo, which was newly available until 2020. In addition to FAO country-level statistics the HYDE3.3 cropland/grazing land dataset is constrained spatially based on multi-year satellite land cover maps from ESA CCI LC (see below). After the year 2017, LUH2 extrapolates, on a gridcell-basis, the cropland, pasture, and urban data linearly based on the trend over the previous 5 years, to generate data until the year 2021. This extrapolation methodology is not appropriate for countries which have experienced recent rapid changes in the rate of land-use change, e.g. Brazil which has experienced a recent upturn in deforestation. Hence, for Brazil we replace FAO state-level data for cropland and grazing land in HYDE by those from in-country land cover dataset MapBiomass (collection 6) for 1985-2020 (Souza et al. 2020). ESA-CCI is used to spatially disaggregate as described below. Similarly, an estimate for the year 2021 is based on the MapBiomass trend 2015-2020. The pre-1985 period is scaled with the per capita numbers from 1985 from MapBiomass, so this transition is smooth.

HYDE uses satellite imagery from ESA-CCI from 1992 – 2018 for more detailed yearly allocation of cropland and grazing land, with the ESA area data scaled to match the FAO annual totals at country-level. The original 300 metre spatial resolution data from ESA was aggregated to a 5 arc minute resolution according to the classification scheme as described in Klein Goldewijk et al (2017a).

DGVMs that simulate subgrid scale transitions (i.e., gross land-use emissions; see Table A1) use more detailed land use transition and wood harvest information from the LUH2-GCB2022 data set. LUH2-GCB2022 is an update of the more comprehensive harmonised land-use data set (Hurtt et al., 2020), that further includes fractional data on primary and secondary forest vegetation, as well as all underlying transitions between land-use states (850-2020; Hurtt et al., 2011, 2017, 2020; Chini et al., 2021; Table A1). This data set is of quarter degree fractional areas of land-use states and all transitions between those states, including a new wood harvest reconstruction, new representation of shifting cultivation, crop rotations, management information including irrigation and fertiliser application. The land-use states include five different crop types in addition to splitting grazing land into managed pasture and rangeland. Wood harvest patterns are constrained with Landsat-based tree cover loss data (Hansen et al. 2013). Updates of LUH2-GCB2022 over last year's version (LUH2-GCB2021) are using the most recent HYDE release (covering the time period up to 2017, revision to Brazil and the Democratic Republic of the Congo as described above). We use the same FAO wood harvest data as last year for all dataset years from 1961 to 2019, and extrapolate to the year 2022. The HYDE3.3 population data is also used to extend the wood harvest time series back in time. Other wood harvest inputs (for years prior to 1961) remain the same in LUH2. These updates in the land-use forcing are shown in comparison to the more pronounced version change from the GCB2020 (Friedlingstein et al., 2020) to GCB2021, which was discussed in Friedlingstein et al. (2022a) in Figure B6 and their relevance for land-use emissions discussed in Section 3.2.2. DGVMs



implement land-use change differently (e.g., an increased cropland fraction in a grid cell can either be at the expense of grassland or shrubs, or forest, the latter resulting in deforestation; land cover fractions of the non-agricultural land differ between models). Similarly, model-specific assumptions are applied to convert deforested biomass or deforested area, and other forest product pools into carbon, and different choices are made regarding the allocation of rangelands as natural vegetation or pastures.

The difference between two DGVMs simulations (see Appendix C4.1 below), one forced with historical changes in land-use and a second with time-invariant pre-industrial land cover and pre-industrial wood harvest rates, allows quantification of the dynamic evolution of vegetation biomass and soil carbon pools in response to land-use change in each model ( $E_{LUC}$ ). Using the difference between these two DGVMs simulations to diagnose  $E_{LUC}$  means the DGVMs account for the loss of additional sink capacity (around  $0.4 \pm 0.3$  GtC yr<sup>-1</sup>; see Section 2.7 and Appendix D4), while the bookkeeping models do not.

As a criterion for inclusion in this carbon budget, we only retain models that simulate a positive  $E_{LUC}$  during the 1990s, as assessed in the IPCC AR4 (Denman et al., 2007) and AR5 (Ciais et al., 2013). All DGVMs met this criterion, although one model was not included in the  $E_{LUC}$  estimate from DGVMs as it exhibited a spurious response to the transient land cover change forcing after its initial spin-up.

### **C.2.3 Mapping of national GHG inventory data to $E_{LUC}$**

An approach was implemented to reconcile the large gap between land-use emissions estimates from bookkeeping models and from national GHG Inventories (NGHGI) (see Tab. A8). This gap is due to different approaches to calculating “anthropogenic” CO<sub>2</sub> fluxes related to land-use change and land management (Grassi et al. 2018). In particular, the land sinks due to environmental change on managed lands are treated as non-anthropogenic in the global carbon budget, while they are generally considered as anthropogenic in NGHGIs (“indirect anthropogenic fluxes”; Eggleston et al., 2006). Building on previous studies (Grassi et al. 2021), the approach implemented here adds the DGVMs estimates of CO<sub>2</sub> fluxes due to environmental change from countries’ managed forest area (part of  $S_{LAND}$ ) to the  $E_{LUC}$  flux. This sum is expected to be conceptually more comparable to LULUCF than  $E_{LUC}$ .

$E_{LUC}$  data are taken from bookkeeping models, in line with the global carbon budget approach. To determine  $S_{LAND}$  on managed forest, the following steps were taken: Spatially gridded data of “natural” forest NBP ( $S_{LAND}$  i.e., due to environmental change and excluding land use change fluxes) were obtained with S2 runs from DGVMs up to 2021 from the TRENDY v11 dataset. Results were first masked with a forest map that is based on Hansen (Hansen et al. 2013) tree cover data. To do this conversion (“tree” cover to “forest” cover), we exclude gridcells with less than 20% tree cover and isolated pixels with maximum connectivity less than 0.5 ha following the FAO definition of forest. Forest NBP are then further masked with the “intact” forest map for the year 2013, i.e. forest areas characterised by no remotely detected signs of human activity (Potapov et al. 2017). This way, we obtained the  $S_{LAND}$  in “intact” and “non-intact” forest area, which previous studies (Grassi et al. 2021) indicated to be a good proxy, respectively, for “unmanaged” and “managed” forest area in the NGHGI. Note that only 4 models (CABLE-POP, CLASSIC, JSBACH and YIBs) had forest NBP at grid cell level. For the other DGVMs, when a grid cell had forest, all the NBP was allocated to forest. However, since S2 simulations use pre-industrial forest cover masks that are at least 20% larger than today’s forest (Hurt et al. 2020), we corrected this NBP by a ratio between observed (based on Hansen) and prescribed (from DGVMs) forest cover. This ratio is calculated for each individual DGVM that provides information on prescribed

forest cover (LPX-Bern, OCN, JULES, VISIT, VISIT-NIES, SDGVM). For the others (IBIS, CLM5.0, ORCHIDEE, ISAM, DLEM, LPJ-GUESS) a common ratio (median ratio of all the 10 models that provide information on prescribed forest cover) is used. The details of the method used are explained here:

[https://github.com/RamAlkama/LandCarbonBudget\\_IntactAndNonIntactForest](https://github.com/RamAlkama/LandCarbonBudget_IntactAndNonIntactForest)

LULUCF data from NGHGs are from Grassi et al. (2022a). While Annex I countries report a complete time series 1990-2020, for Non-Annex I countries gap-filling was applied through linear interpolation between two points and/or through extrapolation backward (till 1990) and forward (till 2020) using the single closest available data. For all countries, the estimates of the year 2021 are assumed to be equal to those of 2020. This data includes all CO<sub>2</sub> fluxes from land considered managed, which in principle encompasses all land uses (forest land, cropland, grassland, wetlands, settlements, and other land), changes among them, emissions from organic soils and from fires. In practice, although almost all Annex I countries report all land uses, many non-Annex I countries report only on deforestation and forest land, and only few countries report on other land uses. In most cases, NGHGs include most of the natural response to recent environmental change, because they use direct observations (e.g., national forest inventories) that do not allow separating direct and indirect anthropogenic effects (Eggleston et al., 2006).

To provide additional, largely independent assessments of fluxes on unmanaged vs managed lands, we include a DGVM that allows diagnosing fluxes from unmanaged vs managed lands by tracking vegetation cohorts of different ages separately. This model, ORCHIDEE-MICT (Yue et al., 2018), was run using the same LUH2 forcing as the DGVMs used in this budget (Section 2.5) and the bookkeeping models BLUE and OSCAR (Section 2.2). Old-aged forest was classified as primary forest after a certain threshold of carbon density was reached again, and the model-internal distinction between primary and secondary forest used as proxies for unmanaged vs managed forests; agricultural lands are added to the latter to arrive at total managed land.

Tab. A8 shows the resulting mapping of global carbon cycle models' land flux definitions to that of the NGHGI (discussed in Section 3.2.2). ORCHIDEE-MICT estimates for SLAND on intact forests are expected to be higher than based on DGVMs in combination with the NGHGI managed/unmanaged forest data because the unmanaged forest area, with about 27 mio km<sup>2</sup>, is estimated to be substantially larger by ORCHIDEE-MICT than, with less than 10 mio km<sup>2</sup>, by the NGHGI, while managed forest area is estimated to be smaller (22 compared to 32 mio km<sup>2</sup>). Related to this, E<sub>LUC</sub> plus S<sub>LAND</sub> on non-intact lands is a larger source estimated by ORCHIDEE-MICT compared to NGHGI. We also show as comparison FAOSTAT emissions totals (FAO, 2021), which include emissions from net forest conversion and fluxes on forest land (Tubiello et al., 2021) as well as CO<sub>2</sub> emissions from peat drainage and peat fires. The 2021 data was estimated by including actual 2021 estimates for peatlands drainage and fire and a carry forward from 2020 to 2021 for the forest land stock change. The FAO data shows a global source of 0.24 GtC yr<sup>-1</sup> averaged over 2012-2021, in contrast to the sink of -0.54 GtC yr<sup>-1</sup> of the gap-filled NGHGI data. Most of this difference is attributable to different scopes: a focus on carbon fluxes for the NGHGI and a focus on area and biomass for FAO. In particular, the NGHGI data includes a larger forest sink for non-Annex I countries resulting from a more complete coverage of non-biomass carbon pools and non-forest land uses. NGHGI and FAO data also differ in terms of underlying data on forest land (Grassi et al., 2022a).

#### C.2.4 Uncertainty assessment for $E_{LUC}$

Differences between the bookkeeping models and DGVMs models originate from three main sources: the different methodologies, which among others lead to inclusion of the loss of additional sink capacity in DGVMs (see Appendix D1.4), the underlying land-use/land cover data set, and the different processes represented (Table A1). We examine the results from the DGVMs models and of the bookkeeping method and use the resulting variations as a way to characterise the uncertainty in  $E_{LUC}$ .

Despite these differences, the  $E_{LUC}$  estimate from the DGVMs multi-model mean is consistent with the average of the emissions from the bookkeeping models (Table 5). However there are large differences among individual DGVMs (standard deviation at around 0.5 GtC yr<sup>-1</sup>; Table 5), between the bookkeeping estimates (average difference 1850-2020 BLUE-updated H&N2017 of 0.8 GtC yr<sup>-1</sup>, BLUE-OSCAR of 0.4 GtC yr<sup>-1</sup>, OSCAR-updated H&N2017 of 0.3 GtC yr<sup>-1</sup>), and between the updated estimate of H&N2017 and its previous model version (Houghton et al., 2012). A factorial analysis of differences between BLUE and H&N2017 attributed them particularly to differences in carbon densities between natural and managed vegetation or primary and secondary vegetation (Bastos et al., 2021). Earlier studies additionally showed the relevance of the different land-use forcing as applied (in updated versions) also in the current study (Gasser et al., 2020). Ganzenmüller et al. (2022) recently showed that  $E_{LUC}$  estimates with BLUE are substantially smaller when the model is driven by a new high-resolution land-use dataset (HILDA+). They identified shifting cultivation and the way it is implemented in LUH2 as a main reason for this divergence. They further showed that a higher spatial resolution reduces the estimates of both sources and sinks because successive transitions are not adequately represented at coarser resolution, which has the effect that—despite capturing the same extent of transition areas—overall less area remains pristine at the coarser compared to the higher resolution.

The uncertainty in  $E_{LUC}$  of  $\pm 0.7$  GtC yr<sup>-1</sup> reflects our best value judgement that there is at least 68% chance ( $\pm 1\sigma$ ) that the true land-use change emission lies within the given range, for the range of processes considered here. Prior to the year 1959, the uncertainty in  $E_{LUC}$  was taken from the standard deviation of the DGVMs. We assign low confidence to the annual estimates of  $E_{LUC}$  because of the inconsistencies among estimates and of the difficulties to quantify some of the processes in DGVMs.

#### C.2.5 Emissions projections for $E_{LUC}$

We project the 2022 land-use emissions for BLUE, the updated H&N2017 and OSCAR, starting from their estimates for 2021 assuming unaltered peat drainage, which has low interannual variability, and the highly variable emissions from peat fires, tropical deforestation and degradation as estimated using active fire data (MCD14ML; Giglio et al., 2016). Those latter scale almost linearly with GFED over large areas (van der Werf et al., 2017), and thus allows for tracking fire emissions in deforestation and tropical peat zones in near-real time.

### C.3 Methodology Ocean CO<sub>2</sub> sink

#### C.3.1 Observation-based estimates

We primarily use the observational constraints assessed by IPCC of a mean ocean CO<sub>2</sub> sink of  $2.2 \pm 0.7$  GtC yr<sup>-1</sup> for the 1990s (90% confidence interval; Ciais et al., 2013) to verify that the GOBMs provide a realistic assessment of  $S_{OCEAN}$ .

This is based on indirect observations with seven different methodologies and their uncertainties, and further using three of these methods that are deemed most reliable for the assessment of this quantity (Denman et al., 2007; Ciais et al., 2013). The observation-based estimates use the ocean/land CO<sub>2</sub> sink partitioning from observed atmospheric CO<sub>2</sub> and O<sub>2</sub>/N<sub>2</sub> concentration trends (Manning and Keeling, 2006; Keeling and Manning, 2014), an oceanic inversion method constrained by ocean biogeochemistry data (Mikaloff Fletcher et al., 2006), and a method based on penetration time scale for chlorofluorocarbons (McNeil et al., 2003). The IPCC estimate of 2.2 GtC yr<sup>-1</sup> for the 1990s is consistent with a range of methods (Wanninkhof et al., 2013). We refrain from using the IPCC estimates for the 2000s ( $2.3 \pm 0.7$  GtC yr<sup>-1</sup>), and the period 2002-2011 ( $2.4 \pm 0.7$  GtC yr<sup>-1</sup>, Ciais et al., 2013) as these are based on trends derived mainly from models and one data-product (Ciais et al., 2013). Additional constraints summarised in AR6 (Canadell et al., 2021) are the interior ocean anthropogenic carbon change (Gruber et al., 2019) and ocean sink estimate from atmospheric CO<sub>2</sub> and O<sub>2</sub>/N<sub>2</sub> (Tohjima et al., 2019) which are used for model evaluation and discussion, respectively.

We also use eight estimates of the ocean CO<sub>2</sub> sink and its variability based on surface ocean fCO<sub>2</sub> maps obtained by the interpolation of surface ocean fCO<sub>2</sub> measurements from 1990 onwards due to severe restriction in data availability prior to 1990 (Figure 10). These estimates differ in many respects: they use different maps of surface fCO<sub>2</sub>, different atmospheric CO<sub>2</sub> concentrations, wind products and different gas-exchange formulations as specified in Table A3. We refer to them as fCO<sub>2</sub>-based flux estimates. The measurements underlying the surface fCO<sub>2</sub> maps are from the Surface Ocean CO<sub>2</sub> Atlas version 2022 (SOCATv2022; Bakker et al., 2022), which is an update of version 3 (Bakker et al., 2016) and contains quality-controlled data through 2021 (see data attribution Table A5). Each of the estimates uses a different method to then map the SOCAT v2022 data to the global ocean. The methods include a data-driven diagnostic method combined with a multi linear regression approach to extend back to 1957 (Rödenbeck et al., 2022; referred to here as Jena-MLS), three neural network models (Landschützer et al., 2014; referred to as MPI-SOMFFN; Chau et al., 2022; Copernicus Marine Environment Monitoring Service, referred to here as CMEMS-LSCE-FFNN; and Zeng et al., 2014; referred to as NIES-NN), one cluster regression approaches (Gregor and Gruber, 2021, referred to as OS-ETHZ-GRaCER), and a multi-linear regression method (Iida et al., 2021; referred to as JMA-MLR), and one method that relates the fCO<sub>2</sub> misfit between GOBMs and SOCAT to environmental predictors using the extreme gradient boosting method (Gloege et al., 2022). The ensemble mean of the fCO<sub>2</sub>-based flux estimates is calculated from these seven mapping methods. Further, we show the flux estimate of Watson et al. (2020) who also use the MPI-SOMFFN method to map the adjusted fCO<sub>2</sub> data to the globe, but resulting in a substantially larger ocean sink estimate, owing to a number of adjustments they applied to the surface ocean fCO<sub>2</sub> data. Concretely, these authors adjusted the SOCAT fCO<sub>2</sub> downward to account for differences in temperature between the depth of the ship intake and the relevant depth right near the surface, and included a further adjustment to account for the cool surface skin temperature effect. The Watson et al. flux estimate hence differs from the others by their choice of adjusting the flux to a cool, salty ocean surface skin. Watson et al. (2020) showed that this temperature adjustment leads to an upward correction of the ocean carbon sink, up to 0.9 GtC yr<sup>-1</sup>, that, if correct, should be applied to all fCO<sub>2</sub>-based flux estimates. A reduction of this adjustment to 0.6 GtC yr<sup>-1</sup> was proposed by Dong et al. (2022). The impact of the cool skin effect on air-sea CO<sub>2</sub> flux is based on established understanding of temperature gradients (as discussed by Goddijn-Murphy et al 2015), and laboratory observations (Jähne and Haussecker, 1998; Jähne, 2019), but in situ field observational evidence is lacking (Dong et al., 2022). The Watson et al flux estimate presented here is therefore not included in the ensemble mean of the fCO<sub>2</sub>-based flux estimates. This choice will be re-evaluated in upcoming budgets based on further lines of evidence.

Typically, data products do not cover the entire ocean due to missing coastal oceans and sea ice cover. The CO<sub>2</sub> flux from each fCO<sub>2</sub>-based product is already at or above 99% coverage of the ice-free ocean surface area in two products (Jena-MLS, OS-ETHZ-GRaCER), and filled by the data-provider in three products (using Fay et al., 2021a, method for JMA-MLR and LDEO-HPD; and Landschützer et al., 2020, methodology for MPI-SOMFFN). The products that remained below 99% coverage of the ice-free ocean (CMEMS-LSCE-FFNN, MPI-SOMFFN, NIES-NN, UOx-Watson) were scaled by the following procedure.

In previous versions of the GCB, the missing areas were accounted for by scaling the globally integrated fluxes by the fraction of the global ocean coverage (361.9e6 km<sup>2</sup> based on ETOPO1, Amante and Eakins, 2009; Eakins and Sharman, 2010) with the area covered by the CO<sub>2</sub> flux predictions. This approach may lead to unnecessary scaling when the majority of the missing data are in the ice-covered region (as is often the case), where flux is already assumed to be zero. To avoid this unnecessary scaling, we now scale fluxes regionally (North, Tropics, South) to match the ice-free area (using NOAA's OISSTv2, Reynolds et al., 2002):

$$FCO_2^{reg-scaled} = \frac{A_{(1-ice)}^{region}}{A_{FCO_2}^{region}} \cdot FCO_2^{region}$$

In the equation,  $A$  represents area,  $(1 - ice)$  represents the ice free ocean,  $A_{FCO_2}^{region}$  represents the coverage of the data product for a region, and  $FCO_2^{region}$  is the integrated flux for a region.

We further use results from two diagnostic ocean models, Khatiwala et al. (2013) and DeVries (2014), to estimate the anthropogenic carbon accumulated in the ocean prior to 1959. The two approaches assume constant ocean circulation and biological fluxes, with  $So_{CEAN}$  estimated as a response in the change in atmospheric CO<sub>2</sub> concentration calibrated to observations. The uncertainty in cumulative uptake of  $\pm 20$  GtC (converted to  $\pm 1\sigma$ ) is taken directly from the IPCC's review of the literature (Rhein et al., 2013), or about  $\pm 30\%$  for the annual values (Khatiwala et al., 2009).

### C.3.2 Global Ocean Biogeochemistry Models (GOBMs)

The ocean CO<sub>2</sub> sink for 1959-20121 is estimated using ten GOBMs (Table A2). The GOBMs represent the physical, chemical, and biological processes that influence the surface ocean concentration of CO<sub>2</sub> and thus the air-sea CO<sub>2</sub> flux. The GOBMs are forced by meteorological reanalysis and atmospheric CO<sub>2</sub> concentration data available for the entire time period. They mostly differ in the source of the atmospheric forcing data (meteorological reanalysis), spin up strategies, and in their horizontal and vertical resolutions (Table A2). All GOBMs except two (CESM-ETHZ, CESM2) do not include the effects of anthropogenic changes in nutrient supply (Duce et al., 2008). They also do not include the perturbation associated with changes in riverine organic carbon (see Section 2.7 and Appendix D.3).

Four sets of simulations were performed with each of the GOBMs. Simulation A applied historical changes in climate and atmospheric CO<sub>2</sub> concentration. Simulation B is a control simulation with constant atmospheric forcing (normal year or repeated year forcing) and constant pre-industrial atmospheric CO<sub>2</sub> concentration. Simulation C is forced with historical changes in atmospheric CO<sub>2</sub> concentration, but repeated year or normal year atmospheric climate forcing. Simulation D is forced by historical changes in climate and constant pre-industrial atmospheric CO<sub>2</sub> concentration. To derive  $So_{CEAN}$  from the model simulations, we subtracted the slope of a linear fit to the annual time series of the control simulation B from the annual time series of simulation A. Assuming that drift and bias are the same in simulations A and B, we thereby correct for any model drift. Further, this difference also removes the natural steady state flux (assumed to be 0 GtC yr<sup>-1</sup> globally without rivers) which is often a major source of biases. This approach works for all model set-ups, including IPSL, where simulation B was forced with constant atmospheric CO<sub>2</sub> but observed historical

changes in climate (equivalent to simulation D). This approach assures that the interannual variability is not removed from IPSL simulation A.

The absolute correction for bias and drift per model in the 1990s varied between  $<0.01 \text{ GtC yr}^{-1}$  and  $0.41 \text{ GtC yr}^{-1}$ , with seven models having positive biases, two having negative biases and one model having essentially no bias (NorESM). The MPI model uses riverine input and therefore simulates outgassing in simulation B. By subtracting simulation B, also the ocean carbon sink of the MPI model follows the definition of  $\text{So}_{\text{OCEAN}}$ . This correction reduces the model mean ocean carbon sink by  $0.04 \text{ GtC yr}^{-1}$  in the 1990s. The ocean models cover 99% to 101% of the total ocean area, so that area-scaling is not necessary.

### C.3.3 GOBM evaluation and uncertainty assessment for $\text{So}_{\text{OCEAN}}$

The ocean  $\text{CO}_2$  sink for all GOBMs and the ensemble mean falls within 90% confidence of the observed range, or 1.5 to  $2.9 \text{ GtC yr}^{-1}$  for the 1990s (Ciais et al., 2013) before and after applying adjustments. An exception is the MPI model, which simulates a low ocean carbon sink of  $1.38 \text{ GtC yr}^{-1}$  for the 1990s in simulation A owing to the inclusion of riverine carbon flux. After adjusting to the GCB's definition of  $\text{So}_{\text{OCEAN}}$  by subtracting simulation B, the MPI model falls into the observed range with an estimated sink of  $1.69 \text{ GtC yr}^{-1}$ .

The GOBMs and data products have been further evaluated using the fugacity of sea surface  $\text{CO}_2$  ( $\text{fCO}_2$ ) from the SOCAT v2022 database (Bakker et al., 2016, 2022). We focused this evaluation on the root mean squared error (RMSE) between observed and modelled  $\text{fCO}_2$  and on a measure of the amplitude of the interannual variability of the flux (modified after Rödenbeck et al., 2015). The RMSE is calculated from detrended, annually and regionally averaged time series calculated from GOBMs and data-product  $\text{fCO}_2$  subsampled to SOCAT sampling points to measure the misfit between large-scale signals (Hauck et al., 2020). To this end, we apply the following steps: (i) subsample data points for where there are observations (GOBMs/data-products as well as SOCAT), (ii) average spatially, (iii) calculate annual mean, (iv) detrend both time-series (GOBMs/data-products as well as SOCAT), (v) calculate RMSE. This year, we do not apply an open ocean mask of 400 m, but instead a mask based on the minimum area coverage of the data-products. This ensures a fair comparison over equal areas. The amplitude of the  $\text{So}_{\text{OCEAN}}$  interannual variability (A-IAV) is calculated as the temporal standard deviation of the detrended annual  $\text{CO}_2$  flux time series after area-scaling (Rödenbeck et al., 2015, Hauck et al., 2020). These metrics are chosen because RMSE is the most direct measure of data-model mismatch and the A-IAV is a direct measure of the variability of  $\text{So}_{\text{OCEAN}}$  on interannual timescales. We apply these metrics globally and by latitude bands. Results are shown in Figure B2 and discussed in Section 3.5.5.

We quantify the 1- $\sigma$  uncertainty around the mean ocean sink of anthropogenic  $\text{CO}_2$  by assessing random and systematic uncertainties for the GOBMs and data-products. The random uncertainties are taken from the ensemble standard deviation ( $0.3 \text{ GtC yr}^{-1}$  for GOBMs,  $0.3 \text{ GtC yr}^{-1}$  for data-products). We derive the GOBMs systematic uncertainty by the deviation of the DIC inventory change 1994-2007 from the Gruber et al (2019) estimate ( $0.4 \text{ GtC yr}^{-1}$ ) and suggest these are related to physical transport (mixing, advection) into the ocean interior. For the data-products, we consider systematic uncertainties stemming from uncertainty in  $\text{fCO}_2$  observations ( $0.2 \text{ GtC yr}^{-1}$ , Takahashi et al., 2009; Wanninkhof et al., 2013), gas-transfer velocity ( $0.2 \text{ GtC yr}^{-1}$ , Ho et al., 2011; Wanninkhof et al., 2013; Roobaert et al., 2018), wind product ( $0.1 \text{ GtC yr}^{-1}$ , Fay et al., 2021a), river flux adjustment ( $0.3 \text{ GtC yr}^{-1}$ , Regnier et al., 2022, formally 2- $\sigma$  uncertainty), and  $\text{fCO}_2$  mapping ( $0.2 \text{ GtC yr}^{-1}$ , Landschützer et al., 2014). Combining these uncertainties as their

squared sums, we assign an uncertainty of  $\pm 0.5 \text{ GtC yr}^{-1}$  to the GOBMs ensemble mean and an uncertainty of  $\pm 0.6 \text{ GtC yr}^{-1}$  to the data-product ensemble mean. These uncertainties are propagated as  $\sigma(\text{SoCEAN}) = (1/2^2 * 0.5^2 + 1/2^2 * 0.6^2)^{1/2} \text{ GtC yr}^{-1}$  and result in an  $\pm 0.4 \text{ GtC yr}^{-1}$  uncertainty around the best estimate of  $\text{SoCEAN}$ .

We examine the consistency between the variability of the model-based and the  $\text{fCO}_2$ -based data products to assess confidence in  $\text{SoCEAN}$ . The interannual variability of the ocean fluxes (quantified as A-IAV, the standard deviation after detrending, Figure B2) of the seven  $\text{fCO}_2$ -based data products plus the Watson et al. (2020) product for 1990-2021, ranges from 0.12 to 0.32  $\text{GtC yr}^{-1}$  with the lower estimates by the two ensemble methods (CMEMS-LSCE-FFNN, OS-ETHZ-GRaCER). The inter-annual variability in the GOBMs ranges between 0.09 and 0.20  $\text{GtC yr}^{-1}$ , hence there is overlap with the lower A-IAV estimates of two data-products.

Individual estimates (both GOBMs and data products) generally produce a higher ocean  $\text{CO}_2$  sink during strong El Niño events. There is emerging agreement between GOBMs and data-products on the patterns of decadal variability of  $\text{SoCEAN}$  with a global stagnation in the 1990s and an extra-tropical strengthening in the 2000s (McKinley et al., 2020, Hauck et al., 2020). The central estimates of the annual flux from the GOBMs and the  $\text{fCO}_2$ -based data products have a correlation  $r$  of 0.94 (1990-2021). The agreement between the models and the data products reflects some consistency in their representation of underlying variability since there is little overlap in their methodology or use of observations.

## **C.4 Methodology Land $\text{CO}_2$ sink**

### **C.4.1 DGVM simulations**

The DGVMs model runs were forced by either the merged monthly Climate Research Unit (CRU) and 6 hourly Japanese 55-year Reanalysis (JRA-55) data set or by the monthly CRU data set, both providing observation-based temperature, precipitation, and incoming surface radiation on a  $0.5^\circ \times 0.5^\circ$  grid and updated to 2021 (Harris et al., 2014, 2020). The combination of CRU monthly data with 6 hourly forcing from JRA-55 (Kobayashi et al., 2015) is performed with methodology used in previous years (Viovy, 2016) adapted to the specifics of the JRA-55 data.

Introduced in GCB2021 (Friedlingstein et al., 2022a), incoming short-wave radiation fields to take into account aerosol impacts and the division of total radiation into direct and diffuse components as summarised below.

The diffuse fraction dataset offers 6-hourly distributions of the diffuse fraction of surface shortwave fluxes over the period 1901-2021. Radiative transfer calculations are based on monthly-averaged distributions of tropospheric and stratospheric aerosol optical depth, and 6-hourly distributions of cloud fraction. Methods follow those described in the Methods section of Mercado et al. (2009), but with updated input datasets.

The time series of speciated tropospheric aerosol optical depth is taken from the historical and RCP8.5 simulations by the HadGEM2-ES climate model (Bellouin et al., 2011). To correct for biases in HadGEM2-ES, tropospheric aerosol optical depths are scaled over the whole period to match the global and monthly averages obtained over the period 2003-2020 by the CAMS Reanalysis of atmospheric composition (Inness et al., 2019), which assimilates satellite retrievals of aerosol optical depth.

The time series of stratospheric aerosol optical depth is taken from the by Sato et al. (1993) climatology, which has been updated to 2012. Years 2013-2020 are assumed to be background years so replicate the background year 2010. That assumption is supported by the Global Space-based Stratospheric Aerosol Climatology time series (1979-2016;

Thomason et al., 2018). The time series of cloud fraction is obtained by scaling the 6-hourly distributions simulated in the Japanese Reanalysis (Kobayashi et al., 2015) to match the monthly-averaged cloud cover in the CRU TS v4.06 dataset (Harris et al., 2020). Surface radiative fluxes account for aerosol-radiation interactions from both tropospheric and stratospheric aerosols, and for aerosol-cloud interactions from tropospheric aerosols, except mineral dust. Tropospheric aerosols are also assumed to exert interactions with clouds.

The radiative effects of those aerosol-cloud interactions are assumed to scale with the radiative effects of aerosol-radiation interactions of tropospheric aerosols, using regional scaling factors derived from HadGEM2-ES. Diffuse fraction is assumed to be 1 in cloudy sky. Atmospheric constituents other than aerosols and clouds are set to a constant standard mid-latitude summer atmosphere, but their variations do not affect the diffuse fraction of surface shortwave fluxes.

In summary, the DGVMs forcing data include time dependent gridded climate forcing, global atmospheric CO<sub>2</sub> (Dlugokencky and Tans, 2022), gridded land cover changes (see Appendix C.2.2), and gridded nitrogen deposition and fertilisers (see Table A1 for specific models details).

Four simulations were performed with each of the DGVMs. Simulation 0 (S0) is a control simulation which uses fixed pre-industrial (year 1700) atmospheric CO<sub>2</sub> concentrations, cycles early 20th century (1901-1920) climate and applies a time-invariant pre-industrial land cover distribution and pre-industrial wood harvest rates. Simulation 1 (S1) differs from S0 by applying historical changes in atmospheric CO<sub>2</sub> concentration and N inputs. Simulation 2 (S2) applies historical changes in atmospheric CO<sub>2</sub> concentration, N inputs, and climate, while applying time-invariant pre-industrial land cover distribution and pre-industrial wood harvest rates. Simulation 3 (S3) applies historical changes in atmospheric CO<sub>2</sub> concentration, N inputs, climate, and land cover distribution and wood harvest rates.

S2 is used to estimate the land sink component of the global carbon budget ( $S_{LAND}$ ). S3 is used to estimate the total land flux but is not used in the global carbon budget. We further separate  $S_{LAND}$  into contributions from CO<sub>2</sub> ( $=S1-S0$ ) and climate ( $=S2-S1+S0$ ).

#### **C.4.2 DGVM evaluation and uncertainty assessment for $S_{LAND}$**

We apply three criteria for minimum DGVMs realism by including only those DGVMs with (1) steady state after spin up, (2) global net land flux ( $S_{LAND} - E_{LUC}$ ) that is an atmosphere-to-land carbon flux over the 1990s ranging between -0.3 and 2.3 GtC yr<sup>-1</sup>, within 90% confidence of constraints by global atmospheric and oceanic observations (Keeling and Manning, 2014; Wanninkhof et al., 2013), and (3) global  $E_{LUC}$  that is a carbon source to the atmosphere over the 1990s, as already mentioned in Appendix C.2.2. All DGVMs meet these three criteria.

In addition, the DGVMs results are also evaluated using the International Land Model Benchmarking system (ILAMB; Collier et al., 2018). This evaluation is provided here to document, encourage and support model improvements through time. ILAMB variables cover key processes that are relevant for the quantification of  $S_{LAND}$  and resulting aggregated outcomes. The selected variables are vegetation biomass, gross primary productivity, leaf area index, net ecosystem exchange, ecosystem respiration, evapotranspiration, soil carbon, and runoff (see Figure B3 for the results and for the list of observed databases). Results are shown in Figure B3 and discussed in Section 3.6.5.

For the uncertainty for  $S_{LAND}$ , we use the standard deviation of the annual CO<sub>2</sub> sink across the DGVMs, averaging to about  $\pm 0.6$  GtC yr<sup>-1</sup> for the period 1959 to 2021. We attach a medium confidence level to the annual land CO<sub>2</sub> sink and



its uncertainty because the estimates from the residual budget and averaged DGVMs match well within their respective uncertainties (Table 5).

## **C.5 Methodology Atmospheric Inversions**

### **C.5.1 Inversion System Simulations**

Nine atmospheric inversions (details of each in Table A4) were used to infer the spatio-temporal distribution of the CO<sub>2</sub> flux exchanged between the atmosphere and the land or oceans. These inversions are based on Bayesian inversion principles with prior information on fluxes and their uncertainties. They use very similar sets of surface measurements of CO<sub>2</sub> time series (or subsets thereof) from various flask and in situ networks. One inversion system also used satellite xCO<sub>2</sub> retrievals from GOSAT and OCO-2.

Each inversion system uses different methodologies and input data but is rooted in Bayesian inversion principles. These differences mainly concern the selection of atmospheric CO<sub>2</sub> data and prior fluxes, as well as the spatial resolution, assumed correlation structures, and mathematical approach of the models. Each system uses a different transport model, which was demonstrated to be a driving factor behind differences in atmospheric inversion-based flux estimates, and specifically their distribution across latitudinal bands (Gaubert et al., 2019; Schuh et al., 2019).

The inversion systems all prescribe similar global fossil fuel emissions for E<sub>FOS</sub>; specifically, the GCP's Gridded Fossil Emissions Dataset version 2022 (GCP-GridFEDv2022.2; Jones et al., 2022), which is an update through 2021 of the first version of GCP-GridFED presented by Jones et al. (2021), or another recent version of GCP-GridFED (Table A4). All GCP-GridFED versions scale gridded estimates of CO<sub>2</sub> emissions from EDGARv4.3.2 (Janssens-Maenhout et al., 2019) within national territories to match national emissions estimates provided by the GCP for the years 1959-2021, which are compiled following the methodology described in Appendix C.1. GCP-GridFEDv2022.2 adopts the seasonality of emissions (the monthly distribution of annual emissions) from the Carbon Monitor (Liu et al., 2020a,b; Dou et al., 2022) for Brazil, China, all EU27 countries, the United Kingdom, the USA and shipping and aviation bunker emissions. The seasonality present in Carbon Monitor is used directly for years 2019-2021, while for years 1959-2018 the average seasonality of 2019 and 2021 are applied (avoiding the year 2020 during which emissions were most impacted by the COVID-19 pandemic). For all other countries, seasonality of emissions is taken from EDGAR (Janssens-Maenhout et al., 2019; Jones et al., 2022), with small annual correction to the seasonality present in year 2010 based on heating or cooling degree days to account for the effects of inter-annual climate variability on the seasonality of emissions (Jones et al., 2021). Earlier versions of GridFED used Carbon Monitor-based seasonality only during the years 2019 onwards. In addition, we note that GCP-GridFEDv2022.1 and v2022.2 include emissions from cement production and the cement carbonation CO<sub>2</sub> sink (Appendix C.1.1), whereas earlier versions of GCP-GridFED did not include the cement carbonation CO<sub>2</sub> sink.

The consistent use of recent versions of GCP-GridFED for E<sub>FOS</sub> ensures a close alignment with the estimate of E<sub>FOS</sub> used in this budget assessment, enhancing the comparability of the inversion-based estimate with the flux estimates deriving from DGVMs, GOBMs and fCO<sub>2</sub>-based methods. To ensure that the estimated uptake of atmospheric CO<sub>2</sub> by the land and oceans was fully consistent with the sum of the fossil emissions flux from GCP-GridFEDv2022.2 and the atmospheric growth rate of CO<sub>2</sub>, small corrections to the fossil fuel emissions flux were applied to inversions systems using other versions of GCP-GridFED.

The land and ocean CO<sub>2</sub> fluxes from atmospheric inversions contain anthropogenic perturbation and natural pre-industrial CO<sub>2</sub> fluxes. On annual time scales, natural pre-industrial fluxes are primarily land CO<sub>2</sub> sinks and ocean CO<sub>2</sub> sources corresponding to carbon taken up on land, transported by rivers from land to ocean, and outgassed by the ocean. These pre-industrial land CO<sub>2</sub> sinks are thus compensated over the globe by ocean CO<sub>2</sub> sources corresponding to the outgassing of riverine carbon inputs to the ocean, using the exact same numbers and distribution as described for the oceans in Section 2.4. To facilitate the comparison, we adjusted the inverse estimates of the land and ocean fluxes per latitude band with these numbers to produce historical perturbation CO<sub>2</sub> fluxes from inversions.

### **C.5.2 Inversion System Evaluation**

All participating atmospheric inversions are checked for consistency with the annual global growth rate, as both are derived from the global surface network of atmospheric CO<sub>2</sub> observations. In this exercise, we use the conversion factor of 2.086 GtC/ppm to convert the inverted carbon fluxes to mole fractions, as suggested by Prather (2012). This number is specifically suited for the comparison to surface observations that do not respond uniformly, nor immediately, to each year's summed sources and sinks. This factor is therefore slightly smaller than the GCB conversion factor in Table 1 (2.142 GtC/ppm, Ballantyne et al., 2012). Overall, the inversions agree with the growth rate with biases between 0.03-0.08 ppm (0.06-0.17 GtCyr<sup>-1</sup>) on the decadal average.

The atmospheric inversions are also evaluated using vertical profiles of atmospheric CO<sub>2</sub> concentrations (Figure B4). More than 30 aircraft programs over the globe, either regular programs or repeated surveys over at least 9 months, have been used in order to draw a robust picture of the system performance (with space-time data coverage irregular and denser in the 0-45°N latitude band; Table A6). The nine systems are compared to the independent aircraft CO<sub>2</sub> measurements between 2 and 7 km above sea level between 2001 and 2021. Results are shown in Figure B4, where the inversions generally match the atmospheric mole fractions to within 0.7 ppm at all latitudes, except for CT Europe in 2011-2021 over the more sparsely sampled southern hemisphere.

## **Appendix D: Processes not included in the global carbon budget**

### **D.1 Contribution of anthropogenic CO and CH<sub>4</sub> to the global carbon budget**

Equation (1) includes only partly the net input of CO<sub>2</sub> to the atmosphere from the chemical oxidation of reactive carbon-containing gases from sources other than the combustion of fossil fuels, such as: (1) cement process emissions, since these do not come from combustion of fossil fuels, (2) the oxidation of fossil fuels, (3) the assumption of immediate oxidation of vented methane in oil production. However, it omits any other anthropogenic carbon-containing gases that are eventually oxidised in the atmosphere, forming a diffuse source of CO<sub>2</sub>, such as anthropogenic emissions of CO and CH<sub>4</sub>. An attempt is made in this section to estimate their magnitude and identify the sources of uncertainty. Anthropogenic CO emissions are from incomplete fossil fuel and biofuel burning and deforestation fires. The main anthropogenic emissions of fossil CH<sub>4</sub> that matter for the global (anthropogenic) carbon budget are the fugitive emissions of coal, oil and gas sectors (see below). These emissions of CO and CH<sub>4</sub> contribute a net addition of fossil carbon to the atmosphere.

In our estimate of  $E_{FOS}$  we assumed (Section 2.1.1) that all the fuel burned is emitted as  $CO_2$ , thus CO anthropogenic emissions associated with incomplete fossil fuel combustion and its atmospheric oxidation into  $CO_2$  within a few months are already counted implicitly in  $E_{FOS}$  and should not be counted twice (same for  $E_{LUC}$  and anthropogenic CO emissions by deforestation fires). The diffuse atmospheric source of  $CO_2$  deriving from anthropogenic emissions of fossil  $CH_4$  is not included in  $E_{FOS}$ . In reality, the diffuse source of  $CO_2$  from  $CH_4$  oxidation contributes to the annual  $CO_2$  growth. Emissions of fossil  $CH_4$  represent 30% of total anthropogenic  $CH_4$  emissions (Saunois et al. 2020; their top-down estimate is used because it is consistent with the observed  $CH_4$  growth rate), that is  $0.083 \text{ GtC yr}^{-1}$  for the decade 2008-2017. Assuming steady state, an amount equal to this fossil  $CH_4$  emission is all converted to  $CO_2$  by OH oxidation, and thus explain  $0.083 \text{ GtC yr}^{-1}$  of the global  $CO_2$  growth rate with an uncertainty range of 0.061 to  $0.098 \text{ GtC yr}^{-1}$  taken from the min-max of top-down estimates in Saunois et al. (2020). If this min-max range is assumed to be  $2 \sigma$  because Saunois et al. (2020) did not account for the internal uncertainty of their min and max top-down estimates, it translates into a  $1\text{-}\sigma$  uncertainty of  $0.019 \text{ GtC yr}^{-1}$ .

Other anthropogenic changes in the sources of CO and  $CH_4$  from wildfires, vegetation biomass, wetlands, ruminants, or permafrost changes are similarly assumed to have a small effect on the  $CO_2$  growth rate. The  $CH_4$  and CO emissions and sinks are published and analysed separately in the Global Methane Budget and Global Carbon Monoxide Budget publications, which follow a similar approach to that presented here (Saunois et al., 2020; Zheng et al., 2019).

## **D.2 Contribution of other carbonates to $CO_2$ emissions**

Although we do account for cement carbonation (a carbon sink), the contribution of emissions of fossil carbonates (carbon sources) other than cement production is not systematically included in estimates of  $E_{FOS}$ , except for Annex I countries and lime production in China (Andrew and Peters, 2021). The missing processes include  $CO_2$  emissions associated with the calcination of lime and limestone outside of cement production. Carbonates are also used in various industries, including in iron and steel manufacture and in agriculture. They are found naturally in some coals.  $CO_2$  emissions from fossil carbonates other than cement not included in our dataset are estimated to amount to about 0.3% of  $E_{FOS}$  (estimated based on Crippa et al., 2019).

## **D.3 Anthropogenic carbon fluxes in the land-to-ocean aquatic continuum**

The approach used to determine the global carbon budget refers to the mean, variations, and trends in the perturbation of  $CO_2$  in the atmosphere, referenced to the pre-industrial era. Carbon is continuously displaced from the land to the ocean through the land-ocean aquatic continuum (LOAC) comprising freshwaters, estuaries, and coastal areas (Bauer et al., 2013; Regnier et al., 2013). A substantial fraction of this lateral carbon flux is entirely ‘natural’ and is thus a steady state component of the pre-industrial carbon cycle. We account for this pre-industrial flux where appropriate in our study (see Appendix C.3). However, changes in environmental conditions and land-use change have caused an increase in the lateral transport of carbon into the LOAC – a perturbation that is relevant for the global carbon budget presented here.

The results of the analysis of Regnier et al. (2013) can be summarised in two points of relevance for the anthropogenic  $CO_2$  budget. First, the anthropogenic perturbation of the LOAC has increased the organic carbon export from terrestrial ecosystems to the hydrosphere by as much as  $1.0 \pm 0.5 \text{ GtC yr}^{-1}$  since pre-industrial times, mainly owing to enhanced carbon export from soils. Second, this exported anthropogenic carbon is partly respired through the LOAC, partly

sequestered in sediments along the LOAC and to a lesser extent, transferred to the open ocean where it may accumulate or be outgassed. The increase in storage of land-derived organic carbon in the LOAC carbon reservoirs (burial) and in the open ocean combined is estimated by Regnier et al. (2013) at  $0.65 \pm 0.35 \text{ GtC yr}^{-1}$ . The inclusion of LOAC related anthropogenic  $\text{CO}_2$  fluxes should affect estimates of  $S_{\text{LAND}}$  and  $S_{\text{OCEAN}}$  in Eq. (1) but does not affect the other terms. Representation of the anthropogenic perturbation of LOAC  $\text{CO}_2$  fluxes is however not included in the GOBMs and DGVMs used in our global carbon budget analysis presented here.

#### **D.4 Loss of additional land sink capacity**

Historical land-cover change was dominated by transitions from vegetation types that can provide a large carbon sink per area unit (typically, forests) to others less efficient in removing  $\text{CO}_2$  from the atmosphere (typically, croplands). The resultant decrease in land sink, called the ‘loss of additional sink capacity’, can be calculated as the difference between the actual land sink under changing land-cover and the counterfactual land sink under pre-industrial land-cover. This term is not accounted for in our global carbon budget estimate. Here, we provide a quantitative estimate of this term to be used in the discussion. Seven of the DGVMs used in Friedlingstein et al. (2019) performed additional simulations with and without land-use change under cycled pre-industrial environmental conditions. The resulting loss of additional sink capacity amounts to  $0.9 \pm 0.3 \text{ GtC yr}^{-1}$  on average over 2009-2018 and  $42 \pm 16 \text{ GtC}$  accumulated between 1850 and 2018 (Obermeier et al., 2021). OSCAR, emulating the behaviour of 11 DGVMs finds values of the loss of additional sink capacity of  $0.7 \pm 0.6 \text{ GtC yr}^{-1}$  and  $31 \pm 23 \text{ GtC}$  for the same time period (Gasser et al., 2020). Since the DGVM-based ELUC estimates are only used to quantify the uncertainty around the bookkeeping models' ELUC, we do not add the loss of additional sink capacity to the bookkeeping estimate.